FEM analysis of a Mode III fracture mechanics test specimens for cohesive law determination of fibre composite

Department of Wind Energy Master Report

Amir Baharvand

DTU Wind Energy-M-0218

July 2018

DTU Wind Energy
Department of Wind Energy

Authors: Amir Baharvand

Title: FEM analysis of a Mode III fracture mechanics test specimens for cohesive law determination of fibre composite

DTU Wind Energy-M-0218
July 2018

Project Period:
November 2017 – July 2018

ECTS: 45

Education: Master of Science

Supervisors:
Bent F. Sørensen, **DTU Wind Energy**
Stergios Goutianos, **DTU Wind Energy**
Helmuth L.Toftegaard, **DTU Wind Energy**
Julie Teuwen, **TU Delft**
Jeppe Bjørn Jørgensen, **LM Wind Power**

Remarks:
This report is submitted as partial fulfillment of the requirements for graduation in the above education at the Technical University of Denmark.

DTU Wind Energy is a department of the Technical University of Denmark with a unique integration of research, education, innovation and public/private sector consulting in the field of wind energy. Our activities develop new opportunities and technology for the global and Danish exploitation of wind energy. Research focuses on key technical-scientific fields, which are central for the development, innovation and use of wind energy and provides the basis for advanced education at the education.

We have more than 240 staff members of which approximately 60 are PhD students. Research is conducted within nine research programmes organized into three main topics: Wind energy systems, Wind turbine technology and Basics for wind energy.

Technical University of Denmark
Department of Wind Energy
Frederiksborgvej 399
2800 Kgs. Lyngby
Denmark
www.vindenergi.dtu.dk

FEM analysis of a Mode III fracture mechanics test specimens for cohesive law determination of fibre composite

Amir Baharvand
European Wind Energy Master (EWEM)
Rotor Design - Structures and Composites

M.Sc. European Wind Energy
Technical University of Denmark
M.Sc. Aerospace Engineering
Delft University of Technology

Student number: s163506 (DTU), 4625889 (TU Delft)
Project duration: November 1, 2017 - July 31, 2018
Defence date: Friday, September 28, 2018 - Risø, Denmark

Thesis committee:

Prof. Bent F. Sørensen	Supervisor (DTU)
Dr. Stergios Goutianos	Co-supervisor (DTU)
Dr. Helmuth Langmaack Toftegaard	Co-supervisor (DTU)
Dr. Julie Teuwen	Supervisor (TU Delft)
Prof. Rinze Benedictus	Chairman (TU Delft)
Prof. Henrik M. Jensen	Aarhus University

Summary

Delamination is one of the common failure types in the fiber composites. The trailing edge in the wind turbine blades, for example, is one of the structural components where the delamination is driven by mode III under predominantly flapwise loading. There has been an extensive effort in developing test procedures and test specimens for determination of the delamination toughness in mode I and mode II delamination while the mode III is neglected due to its complexity, on the one hand, and the lack of a reliable test procedure and numerical model for the mode III delamination toughness testing on the other hand. Therefore, the current project aims for developing an experimental test specimen capable of extracting cohesive laws using the *J* integral approach. To this end, the FEM is utilized for the analyses of various parameters.

Delamination can be modeled using Progressive Failure Analysis where the crack initiation and crack evolution are studied. The present thesis covers both aspects of the Progressive Failure Analysis in the unidirectional fiber composites. Before starting the mode III, mode I and II test specimens are analyzed to establish requirements for proper three-dimensional simulation. The reliable numerical model from this step is the fundamental model for the mode III delamination analysis. In the first part of the project, the Double Cantilever Beam cross-section is optimized to give the pure mode III. LEFM is invoked for the analyses of this section (Small Fracture Process Zone). The results have shown that the pure mode III cannot be accomplished and there always exists an induced coupling mode II under anti-plane loading. Furthermore, the results suggest higher mesh density is required at the free surface to further investigate the $1/\sqrt{r}$-singularity at this location.

The second part of the thesis covers the Cohesive Zone Modeling (Large Fracture Process Zone) whereby the crack evolution is simulated by the cohesive elements. The implemented cohesive law is validated by the *J* integral. The bilinear cohesive law has been successful in simulating the crack extension for Large-Scale Bridging condition. The traction-separation law has been validated through the resistance curve generated by the FEM and derivation of the resistance w.r.t the tangential end-opening.

The commercial code, ABAQUS, is utilized in this study for the Finite Element Analyses.

Acknowledgements

This thesis would never have been completed without the unfailing support and assistance from my supervisors at DTU. I am eternally grateful for the patience, recommendations and comments from Professor Bent F. Sørensen during the presentations and meetings. My special and sincerest gratitude to Dr. Stergios Goutianos who has always been eager to discuss my findings and problems in Finite Element Modeling. I would like to sincerely appreciate the support and guidance from Dr. Helmuth L.Toftegaard.

I would like to truly appreciate my supervisor at TU Delft, Dr. Julie Teuwen, for the support and her kindness during my master project.

I really like to thank Jeppe Bjørn Jørgensen from LM Wind Power for accepting being my supervisor.

I am so grateful to Professor Rinze Benedictus from Delft University of Technology and Professor Henrik M. Jensen from Aarhus University for being a part of my thesis committee.

I appreciate the help from Marianne Hjorthede Arbirk, Secretary for Fluid Mechanics & Study Board Secretary.

Finally, I would like to express my special and heartfelt thanks to my family for their support and encouragement.

Copenhagen, Denmark, September 14, 2018
Amir Baharvand

Contents

List of Figures

List of Tables

Nomenclature

Abbreviations

4PBP	4-point Bending Plate
6ECT	6-point Edge Crack Tension
CZM	Cohesive Zone Modeling
DCB	Double Cantilever Beam
ECT	Edge Crack Tension
ERCT	Edge Ring Crack Torsion
ERR	Energy Release Rate
FEM	Finite Element Method
FE	Finite Element
FPZ	Fracture Process Zone
LEFM	Linear Elastic Fracture Mechanics
LSB	Large-Scale Bridging
MSCB	Modified Split Cantilever Beam
ne	number of elements
RP	Reference Point
SCB	Split Cantilever Beam
SIF	Stress Intensity Factor
SSB	Small-Scale Bridging
SSCB	Simplified Split Cantilever Beam
SST	Split Shear Torsion
SSY	Small-Scale Yielding
TSL	Traction-Separation Law
TS	Torque Shell

Greek Symbols

δ	Opening
δ^*	End-opening
δ^e	End-opening in the elastic regime
δ_c	Opening at the steady-state of the R-curve
δ_{ij}	The Kronecker delta
δ_{max}	End beam deflection
ε	Strain
Γ	Integral path/contour

γ	Shear strain
κ	Curvature
Λ	Scaling factor for the orthotropy
λ	Singularity exponent
ν	Poisson's ratio
ν_{12}	In-plane Poisson's ratio
ν_{23}	Out-of-plane Poisson's ratio
ρ	Radius of curvature
σ	Stress
σ_b	Maximum bending stress
θ	Polar coordinate

Latin Symbols

$\boldsymbol{E}$	Elasticity matrix
$\boldsymbol{K}$	Stiffness matrix
$\boldsymbol{n}$	Normal vector
$\boldsymbol{S'}$	Secondary Compliance matrix
$\boldsymbol{S}$	Compliance matrix
$\boldsymbol{T}$	Traction
$\mathcal{G}$	Energy release rate
ℓ	Length of the fine mesh region
$\overline{T}$	Traction from the elastic cohesive law
$\overline{T}_c$	Corresponding cohesive traction
$\overline{x}$	Neutral axis
ne_c^0	Prescribed number of cohesive elements
A	Area
a_0	Length of pre-existing crack
B	Width
d	Distance from free surface in three-dimensions
dS	Infinitesimally element of the surface
ds	Infinitesimally element of the contour
E	Young's modulus
e	Element
E_{11}	Longitudinal Young's modulus
E_{22}	Transverse Young's modulus
G	Shear modulus
G_{12}	In-plane shear modulus
G_{23}	Out-of-plane shear modulus
H	Height
h_s	Cohesive element thickness
I	Second moment of area
J	J integral
J_0	J integral evaluated at the crack tip

J_c	Work of separation in the cohesive zone
J_R	Resistance in the form of the J integral
K	Stress Intensity Factor
L	Length
M	Moment
R	Radius of the fine mesh region
r	Polar coordinate
S	Surface
T_c	Cohesive strength
U	Cohesive element displacement
u	Displacement
ur	Rotational degree of freedom
V_f	Fiber volume fraction
W	Strain energy density
X_i	Cohesive Element Cartesian coordinate system ($i = 1,2,3$)
x_i	Cartesian coordinate system ($i = 1,2,3$)
D	Damage

Superscript/Subscript

#1	Double Cantilever Beam
#2	Elastic Beam
C	Critical
c	Cohesive / Critical / Coupling
FE	Finite Element
i	Unit vector in the x-direction
ii	Time increment
j	Unit vector in the y-direction
k	Unit vector in the z-direction
n	Direction normal to the crack surface corresponding to mode I
s	Direction transverse to the crack surface corresponding to mode II (sliding)
t	Direction transverse to the crack surface corresponding to mode III (tangential)
th	Theoretical
1	Longitudinal direction / Parallel to crack surface
2	Upward direction / Orthogonal to crack surface
3	Transverse direction / Tangential to crack front
eff	Effective
h	Height / thickness
I	First mode of fracture
II	Second mode of fracture
III	Third mode of fracture
l	Length
R	Resistance

tip	Crack tip
w	Width
y	Yielding

CHAPTER 1

Introduction

1.1 Motivation

Offering light-weight and high stiffness and strength compared to metals have made fiber-reinforced composites (from now on fiber composites) a suitable choice for the aerospace and wind turbine industry. Versatile mechanical properties, as well as strength to weight ratio can be obtained by changing fiber lay-up, fiber/matrix volume fraction, etc. Advanced carbon fibers, for example, have zero thermal expansion which makes them a good choice for space projects. Due to high fatigue resistance, composites are utilized in high frequency rotating parts such as wind turbine blades and helicopter blades. Despite these advantages, there are several shortcomings regarding fiber composites, for instance, the presence of the voids and impurities inherited from the manufacturing process and the complexity in both material and mechanical aspects. The weak interface and anisotropy have made the failure mechanism of fiber composites entirely different from metals.

One of the most current failures in fiber composites is delamination. Delamination is the separation of two adjacent composite layers due to the weakness of interface bonding (figure 1.1). The frequent causes of delamination are the manufacturing process, impact (for example dropping a tool during inspection), matrix cracking, free edges and holes, resin pockets and geometrical discontinuities such as ply-drops (Kassapoglou, 2015). The existence of voids and impurities during the manufacturing process creates pre-existing internal cracks that can extend under static and cyclic loading. Usually, the matrix is more prone to failure in the transverse loading because of lower stiffness and strength compared to the fibers. Transverse stresses that exceed the interlaminar strength cause the delamination.

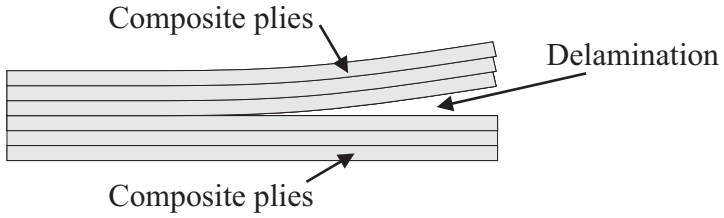

Figure 1.1: Delamination.

Delamination crack growth is a mixed-mode crack extension; therefore, it is analyzed through fracture mechanics and a damage model (for instance, Cohesive Zone Modeling in the present thesis). Fracture mechanics started in the early 1950s parallel to the manifestation

of larger and more complicated structures. In fact, catastrophic failure in structures due to the existence of micro-voids and their propagation under fatigue led to the development of a new field in the Material Science known as the Fracture Mechanics. Generally speaking, crack surface displacement can be divided into three modes (Irwin and Kies, 1954) as illustrated in figure 1.2. Unlike metals, where the crack tends to grow in mode I (Pook, 2013), delamination could occur in each one of these three modes; mode I, mode II, mode III or a combination of them, known as the mixed-modes, e.g., mode I+II.

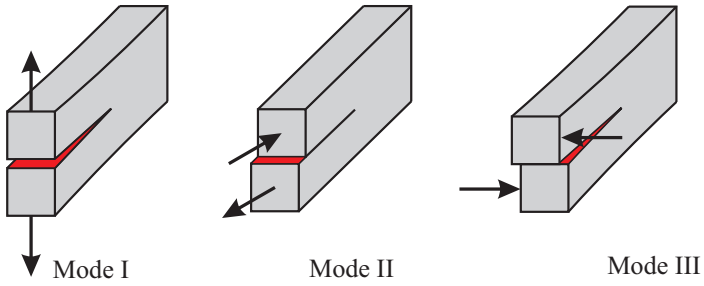

Figure 1.2: Fracture modes. Arrows show the loading condition. The crack surfaces are shown in red.

The prediction of crack growth is the backbone of the fracture mechanics. Damage in form of crack evolution, which results in material degradation, is the principle of the damage tolerant design. Not all the damages can cause failure, only the ones with a critical size can grow and turn into material separation. Thus, it is of paramount importance to identify

1. The crack initiation or its critical size which stays within the scope of fracture mechanics.

2. The crack extension and the residual strength (the load-bearing capacity after crack growth) of the structure[1].

In the unidirectional composite laminates, the fibers have higher strength in the longitudinal direction and lower in the transverse directions which makes the unidirectional fiber composites susceptible to delamination under anti-plane loading. In the present work, the out-of-plane delamination, equivalent to mode III in fracture mechanics, in the unidirectional fiber composites will be investigated.

The Finite Element Method (FEM) has had a substantial influence on the fracture mechanics improvement and this project is no exception. ABAQUS as an accepted and powerful Finite Element (FE) package is utilized for the FE analyses in this project. Notes regarding the FE implementation in ABAQUS will be explained where applicable.

[1]The residual strength is not covered in this study.

CHAPTER 2

Background

In this chapter, the essential theoretical background in the Linear Elastic Fracture Mechanics (LEFM) in two-dimension and three-dimension as well as the Cohesive Zone Modeling (CZM) are explained. Next, the research objective, questions, test method, and the state-of-the-art research regarding mode III delamination toughness testing along with the thesis outline are presented.

2.1 LEFM

LEFM is a division of fracture mechanics that assumes a very small Fracture Process Zone (FPZ) (the gray-shaded area in figure 2.1) compared to the other geometrical dimensions, e.g. width, length and crack length. As the name indicates, LEFM is based on the assumptions of linear relation between the stress and strain, a brittle, homogeneous material and a continuous crack front[1]. In fracture mechanics, the region where the LEFM is applicable is called the "K-dominated zone" (figure 2.1). The K-dominated zone can be understood as a universal stress field that communicates the load and geometry under the condition of the LEFM of the Small-Scaled Fracture Process Zone (Bao and Suo, 1992).

The Stress Intensity Factor (SIF), K, concept was firstly developed by Irwin (1957) based on Westergaard (1939) solution. K is the first term of a series expansion of stresses and includes a $1/\sqrt{r}$-singularity (blue curve in figure 2.2) close to the crack tip where r is the distance in front of the crack tip. The rest of the terms are neglected since they are not singular and their values tend to zero at the crack tip. In the LEFM, the stress in the "K-dominated zone" tends to infinity and therefore, the solution fails in the vicinity of the crack tip. Far from the crack tip, the stress falls and the solution equals to zero where the K-dominated zone vanishes. Under Small-Scaled Fracture Process Zone or the so-called Small-Scale Yielding (SSY) the crack tip load distribution and geometry can be described only by a single parameter, K. K_{I}, K_{II} and K_{III} indicate the SIF for mode I, mode II and mode III, respectively.

In the LEFM, the stress field at the vicinity of a crack in terms of K and the distance from the crack tip can be written as (Irwin (1957), Williams (1961))

$$\sigma_{ij} = \frac{K}{\sqrt{r}} f_{ij}(\theta) \quad , \quad i,j = 1,2,3 \tag{2.1}$$

[1]The conventional definition of crack is used in the present work. Crack in two-dimension is addressed by the "crack tip" and in three-dimension by the "crack front".

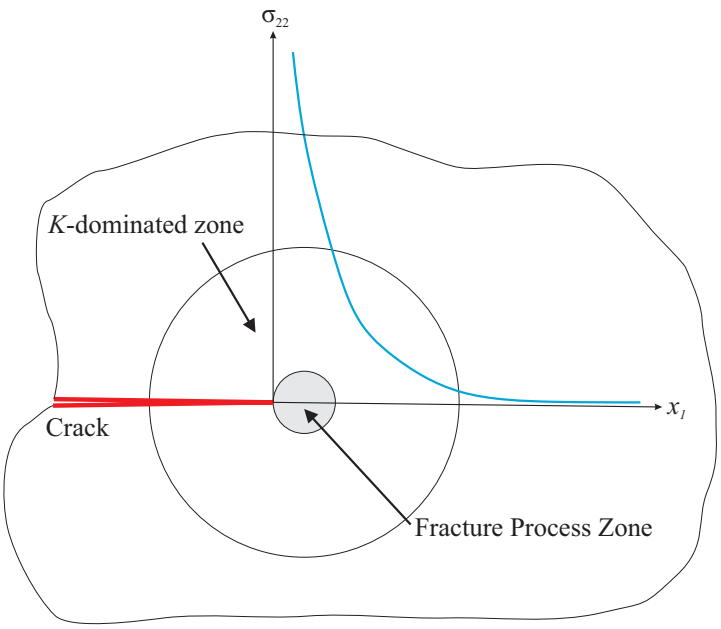

Figure 2.1: K-dominated zone shown in mode I (θ=0).

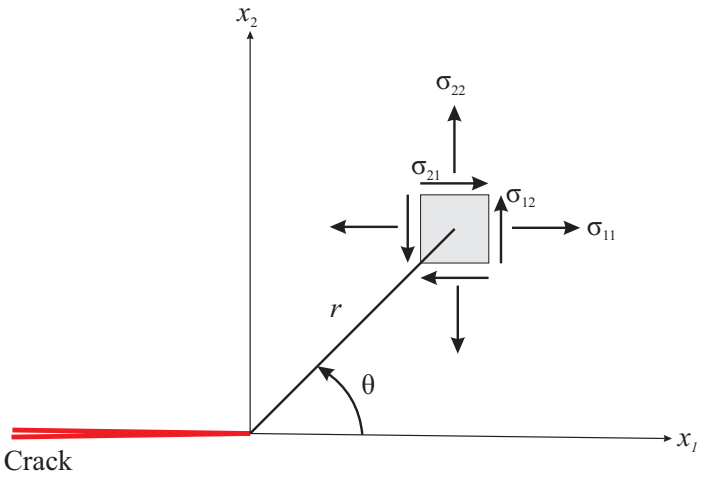

Figure 2.2: The crack tip coordinate system. θ=0 corresponds to the crack plane.

where σ_{ij} denotes the stress tensor (i is the normal vector of the surface that the stress acts on and j is the direction of the stress), $f_{ij}(\theta)$ is a function of angle, θ, around the crack tip and r is the distance from the crack tip. r and θ are the polar coordinates depicted in figure 2.2.

The Displacement vector can be written as

$$u_i = \frac{K\sqrt{r}}{G} g_i(\theta) \quad , \quad i = 1,2,3 \tag{2.2}$$

where u_i is the displacement, G is the shear modulus and $g_i(\theta)$ is a function of θ which determines the displacement field for various angles around the crack tip. Irwin's solution

from (Tada et al., 2000) for an isotropic material is presented in Appendix A.

Since K describes the strength of the stress field in the K-dominated zone, it could be utilized as a fracture criterion. The critical value of the SIF is called the fracture toughness and is denoted for example by K_{IC} for mode I. If $K_I \geq K_{IC}$, fracture occurs. Hence, the crack growth, for instance, in a wind turbine blade can be predicted by extracting the SIF and comparing it with the fracture toughness from the experiment based on the principle of autonomy. According to the principle of autonomy, two different bodies under distinct loading conditions and pre-crack lengths but identical materials have similar behavior at the crack tip/front under SSY (Broberg (1999), Rice (1968b)).

2.2 J integral

Energy Release Rate (ERR), $\mathcal{G}$, is another alternative concept to K in the LEFM and is defined as the decrease in the potential energy during the crack extension. The $\mathcal{G}$ nonlinear companion is the J integral which enables the material to be nonlinear elastic. In the linear elastic materials, the J and $\mathcal{G}$ are equal; therefore, in the following the J integral in the two and three-dimension will be explained.

2.2.1 The two-dimensional J integral

J integral is a path-independent integral on a contour that encloses the crack (figure 2.3) and in two-dimension is defined as (Rice, 1968a)

$$J = \int_{\Gamma} \left(W dx_2 - T_i \frac{\partial u_i}{\partial x_1} ds \right) \tag{2.3}$$

where

$$W = \int_0^{\varepsilon} \sigma_{ij} d\varepsilon_{ij} \quad , \quad T_i = \sigma_{ij} n_j \quad , \quad dx_2 = n_1 ds \quad \text{and} \quad dx_1 = n_2 ds$$

i is a free and j is a dummy index according to the Einstein's summation convention and they take 1 and 2, Γ is the closed integral contour, W is the strain energy density, σ_{ij} is the stress tensor, n_j is the outward unit vector normal to the contour (figure 2.3), u_i is the displacement vector, ds is a small element of the contour and ε_{ij} is the strain tensor. Under LEFM conditions, J and K for an isotropic material with a straight crack extension can be related through the set of Eq.(2.4).

$$
\begin{aligned}
J_{\mathrm{I}} &= \frac{K_{\mathrm{I}}^2}{E'} \\
J_{\mathrm{II}} &= \frac{K_{\mathrm{II}}^2}{E'} \\
J_{\mathrm{III}} &= \frac{K_{\mathrm{III}}^2}{2G}
\end{aligned}
\tag{2.4}
$$

where

$$
\begin{aligned}
E' &= E && \text{For plane stress} \\
E' &= \frac{E}{1-\nu^2} && \text{For plane strain} \\
G &= \frac{E}{2(1+\nu)}
\end{aligned}
\tag{2.5}
$$

and ν is the Poisson's ratio.

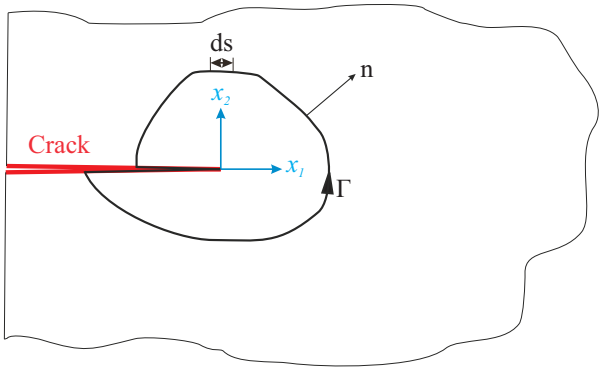

Figure 2.3: Definition of the coordinate system and integration path, Γ, for the J integral in two-dimension.

ABAQUS uses the rings of elements (surface integral) to calculate the J integral. The first contour includes the crack tip. The second contour embraces not only the crack tip but also the first row of the elements around the crack tip. The next subsequent contour is defined by adding the previous contours (ABAQUS, 2017). The 10th contour is illustrated in figure 2.4 which encompasses the previous contours and the 10th ring of elements.

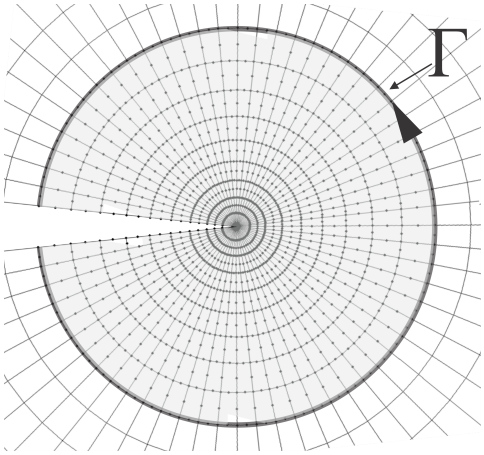

Figure 2.4: ABAQUS uses surface integral to calculate the J integral. The 10th surface contour is shown in gray.

2.2.2 The three-dimensional J integral

Bakker (1984) showed that the J integral in three-dimension is a path-independent integral and can be written as

$$J = \int_{\Gamma} (W n_1 - T_i \frac{\partial u_i}{\partial x_1}) ds = \int_{\Gamma} (W n_1 - \sigma_{ij} n_j \frac{\partial u_i}{\partial x_1}) ds \tag{2.6}$$

if the crack front is orthogonal to x_1-direction and the crack plane is parallel to the x_1x_3 plane. In the above equation, ds is a small element of the contour Γ that lies on the plane x_1x_2. If the J integral is not constant along the crack front, a more generalized form of the J integral can be given according to Eq.(2.7) (Amestoy et al. (1981), Bakker (1984), Chiarelli and Frediani (1993)).

$$J_k = \int_{\Gamma} (W n_k - T_i \frac{\partial u_i}{\partial x_k}) ds + \int_S \frac{\partial}{\partial x_3} (W \delta_{k3} - \sigma_{i3} \frac{\partial u_i}{\partial x_k}) dS \quad , \quad k = 1,2,3 \tag{2.7}$$

in which δ_{ij} is the Kronecker delta, S is a closed surface and dS is a small element of the surface (figure 2.5). The integration domain for dS is defined in the crack plane (indicated by yellow color in figure 2.5) and bounded from one traction free (S_0) to another traction free surface (S_1) as illustrated in figure 2.5. The value for the J_k integral in Eq.(2.7) is calculated locally for each contour, Γ, which belongs to the plane P_2 and is always normal to a unit vector tangent to the crack front and parallel to x_3-axis (figure 2.5). As a result, the J integral is the summation of the two integrals on path Γ and domain S and independent of both path Γ and domain S. For a straight crack front and symmetric body, $k = 1$ in Eq.2.7 and the second term vanishes. In addition, for a non-straight crack front when $k = 1,2$; δ_{13} and δ_{23} is zero; hence, there will be no contribution of W to J_1 and J_2.

Kitagawa et al. (1980) suggested an average value for the J integral analogous to Eq.(2.6) where the local J values are integrated and then divided by the length of the crack front. If the crack front is the same as the specimen width, B then

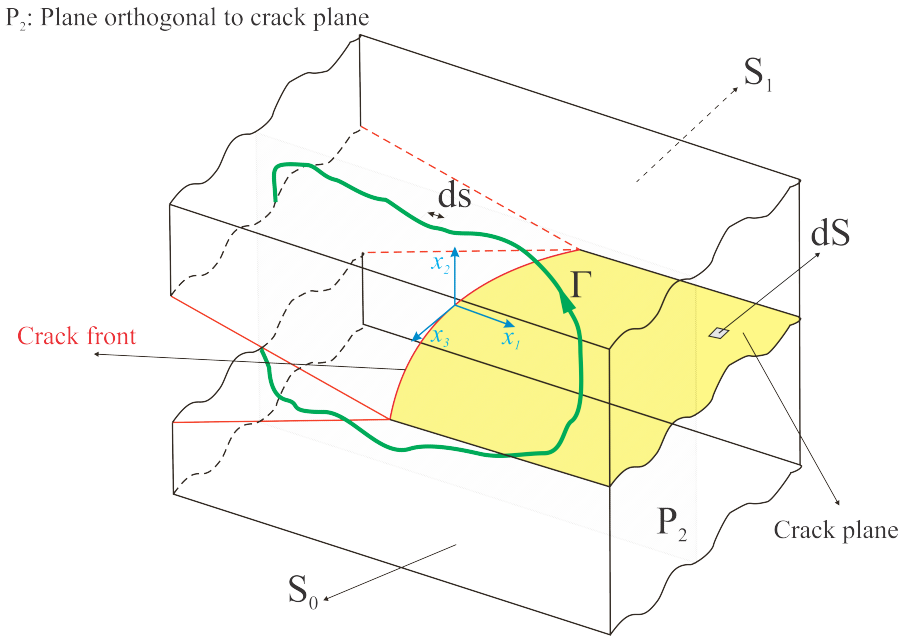

Figure 2.5: Definition of the local coordinate system and integration path, Γ, and domain S for the three-dimensional J integral.

$$J = \frac{1}{B}\int_{S_2}(Wn_1 - T_i\frac{\partial u_i}{\partial x_1})dA \tag{2.8}$$

The coordinate system for Eq.(2.8) is shown in figure 2.6. Kitagawa et al. (1980) assumed a straight plane for the crack extension and traction free surfaces S_0 and S_1. It looks that Eq.(2.8) is suitable for the analytic solution since it sums up the local J integrals and then divides them by the width to determine the global J value. Consequently, the J integral unit becomes $\frac{\mathrm{J}}{\mathrm{m}^2}$.

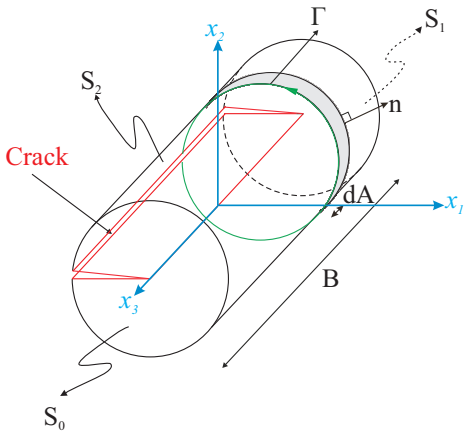

Figure 2.6: Surface contour for the J integral in three-dimension.

In three-dimension, ABAQUS uses Eq.(2.7) to compute the J integral locally (volume integral); hence, in contrast to the two-dimensional case where the output for the J integral is one value, a series of J values along the crack front coordinate will be obtained. The final value of the J from FEM can be calculated by integrating the surface under the J-x_3 plot and dividing it by the length of the crack front.

2.3 Fracture Mechanics of Unidirectional Fiber Composites

As mentioned, the fracture of the fiber composites is too complex as it depends on various parameters. Toubal et al. (2013) observed that the effect of anisotropy decreases as the ratio of the longitudinal to the transverse Young's modulus, $\frac{E_{11}}{E_{22}}$, increases. The fiber orientation also has a considerable effect on K. Sih et al. (1965) showed that the $1/\sqrt{r}$-singularity in an isotropic material can be extended to the orthotropic one. In an orthotropic material, despite the fact of crack growth in the direction of fibers and mixed-mode displacements in case of fiber misalignment with the crack, the principles of the LEFM are applicable conditionally since the distribution of the stresses at the crack tip is much important (Parhizgar, 1979).

2.4 Large-Scale Bridging

Under SSY condition, the stresses can be described by the K and R-curve (section 2.5.2); however, by further increase in the size of the FPZ, the K and R-curve lose their meanings (Bao and Suo, 1992). The LEFM is no more applicable and the R-curve will be different according to the geometry and stiffness (Spearing and Evans, 1992). In addition to the SSY and Large-Scale Yielding (LSY), there is an intermediate FPZ in composites, known as Large-Scale Bridging (LSB) (Sørensen and Jacobsen, 2000). The length of this FPZ, L_c, is longer and its height is shorter than the size of the K-dominated zone, forming a long narrow strip FPZ (figure 2.9(a)). Therefore, to explain the LSB problems, it is essential to establish a parameter which is (a) a material property and (b) independent of the size and geometry so that it can be utilized in complex structures. It has been shown that the Cohesive Zone Modeling (CZM) is able to model the failure process zone for the LSB condition (Sørensen and Jacobsen, 2003). This topic will be covered in the next section.

2.5 Cohesive Zone Modeling

To overcome the peculiar stress singularity in the LEFM and provide a more realistic model for the material separation, Dugdale (1960) proposed a yield strip model to realistically present the details of the physics of the fracture. Dugdale set the maximum value of the cohesive force equal to the material yielding strength, σ_y. Subsequently, the maximum local stress value was limited to σ_y and the stress singularity vanished. The result was the length

of a narrow strip of a plastic zone ahead of a crack in an infinite plate under mode I. Later, Barenblatt (1962) introduced the "cohesive zone" based on the atomic force and coalescence of the micro-voids. In contrast to Dugdale's model where the cohesive force was restricted to σ_y, Barenblatt assumed a cohesive law in which the cohesive traction, T, was defined as a function of the crack ligament, for example x, $T(x)$. Through the years Barenblatt's model was evolved and the crack ligament coordinate was replaced with the crack opening, δ, $T(\delta)$. Since then, Cohesive Zone Modeling (CZM) has drawn much attention and has been used extensively in crack extension, delamination, crack path prediction and so on. Along with the CZM, Virtual Crack Closure Technique (VCCT) has been exploited for simulating the failure process zone in fiber composite laminae. Table 2.1 provides an overview of both VCCT and CZM. The main advantages of CZM like damage onset prediction, independency of a pre-existing crack and its proved ability in progressive failure analysis in layered composites have made the CZM an attractive tool for the delamination analysis.

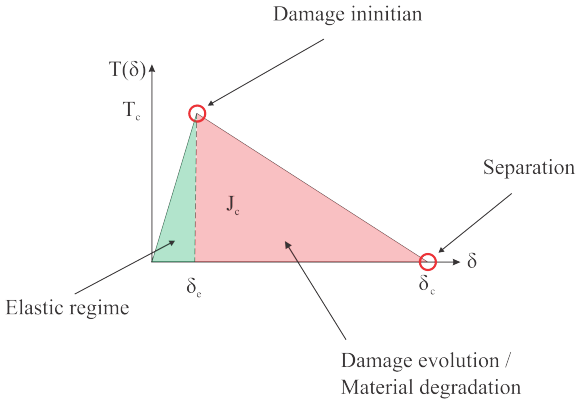

Figure 2.7: An schematic of a bilinear cohesive law.

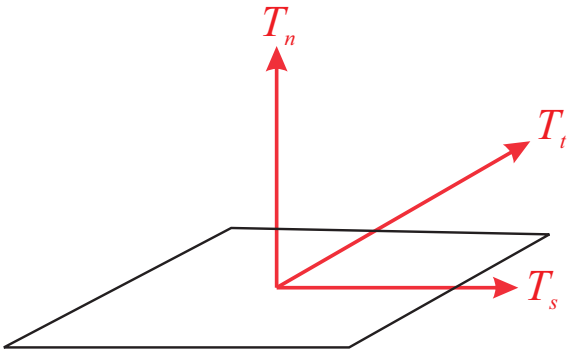

Figure 2.8: Cohesive traction decomposition.

Figure 2.7 illustrates a bilinear cohesive law (or traction-separation law), frequently used for the delamination in composites. The stress increases until a certain level, T_c or the cohesive strength (the green area in figure 2.7). At this point, there is a loss in the stiffness of the material (crack initiation) and the damage, D, is zero. The cohesive stress reduces as the material stiffness degrades, D=1, until the critical separation, δ_c, occurs; when the cohesive traction vanishes (the red area in figure 2.7). At this level, the length of the FPZ is known as the cohesive length, L_c. It is worth-mentioning to note that the cohesive element used in the present work has an infinite thickness. There is an alternative in CZM by ABAQUS without the cohesive element that is not covered here. Some features of the cohesive law presented in figure 2.7 are listed below:

- To minimize any unwanted crack opening before the crack initiation, the slope of the line in the elastic regime should be set to a high value. The opening in the elastic regime is undesired since it causes the crack opening before reaching the cohesive strength. Very high values for the slope of the elastic region will lead to computational error in FEM; hence, it is preferred to opt for a value that is neither too high to circumvent FE error

Table 2.1: VCCT against CZM ABAQUS (2017).

VCCT	CZM
Requires a pre-existing crack	No need for a pre-existing crack
Cannot predict the crack onset	Crack initiation can be determined
Dedicated to brittle fracture	Suitable for both the brittle and LSB fracture
Requires ERR for mode I, II and III	Requires ERR for mode I, II and III, elastic modulus, cohesive traction and elasticity matrix
Crack propagates when the ERR exceed the fracture energy	Crack propagates when the stress exceeds the cohesive strength and fully developed when the cohesive traction is zero
Initially the uncracked regions are bonded rigidly	Initially the uncracked regions are bonded according to the elastic cohesive law
Highly-dependent on mesh size	Highly-dependent on mesh size
Difficult to apply for complex structures	Can be applied to complex structures
Need to know the crack front in advance	Need to know the crack path (Needless of crack front in three-dimension)

nor too low to make the interface less stiff. Generally speaking, the traction-separation can be explained through Eq.(2.9).

$$\boldsymbol{T} = \begin{Bmatrix} T_n \\ T_s \\ T_t \end{Bmatrix} = \begin{bmatrix} K_{nn} & K_{ns} & K_{nt} \\ K_{ns} & K_{ss} & K_{st} \\ K_{nt} & K_{st} & K_{tt} \end{bmatrix} \begin{Bmatrix} \delta_n \\ \delta_s \\ \delta_t \end{Bmatrix} = \boldsymbol{K}\boldsymbol{\delta} \tag{2.9}$$

where $\boldsymbol{T}$ is the traction vector, $\boldsymbol{K}$ is the stiffness matrix and $\boldsymbol{\delta}$ is the separation. The subscripts n, s and t are the traction components (figure 2.8) referring to the normal and the two transverse directions. Considering the cohesive elements with finite thickness, h_c, the strains in the n, s and t directions can be written as

$$\varepsilon_n = \frac{\delta_n}{h_c} \quad \varepsilon_s = \frac{\delta_s}{h_c} \quad \varepsilon_t = \frac{\delta_t}{h_c}$$

Replacing the stiffness matrix components with the suitable values to mimic the elastic behavior in different directions, finally for a finite thickness cohesive element, the elastic behavior in the cohesive zone can be explained by Eq.(2.10).

$$\boldsymbol{T} = \begin{Bmatrix} T_n \\ T_s \\ T_t \end{Bmatrix} = \begin{bmatrix} E_{nn} & E_{ns} & E_{nt} \\ E_{ns} & E_{ss} & E_{st} \\ E_{nt} & E_{st} & E_{tt} \end{bmatrix} \begin{Bmatrix} \varepsilon_n \\ \varepsilon_s \\ \varepsilon_t \end{Bmatrix} = \boldsymbol{E}\boldsymbol{\epsilon} \tag{2.10}$$

where $\boldsymbol{E}$ is the elasticity matrix. One should notice that the elastic parameters in the elasticity matrix are given as interface properties. They are not the material properties since, for example, the effect of the Poisson's ratio is neglected and all the element of the stiffness matrix are chosen based on the experience and observation.

- As a rule of thumb the end-opening in the elastic region, δ^e, should not exceed $0.05\delta_e$ (Schwalbe et al., 2012).
- The area under the curve determines the fracture toughness, J_c. According to Rice (1968a), by shrinking the integration path to the crack surfaces (figure 2.9(b)), the J integral in the form of cohesive law can be written as

$$J_c = \int_0^{\delta_c} T(\delta) d\delta \tag{2.11}$$

where δ_c is the critical separation when the traction is vanished depicted in figure 2.9(a) and J_c is the fracture toughness. The derivation is shown in Appendix B.

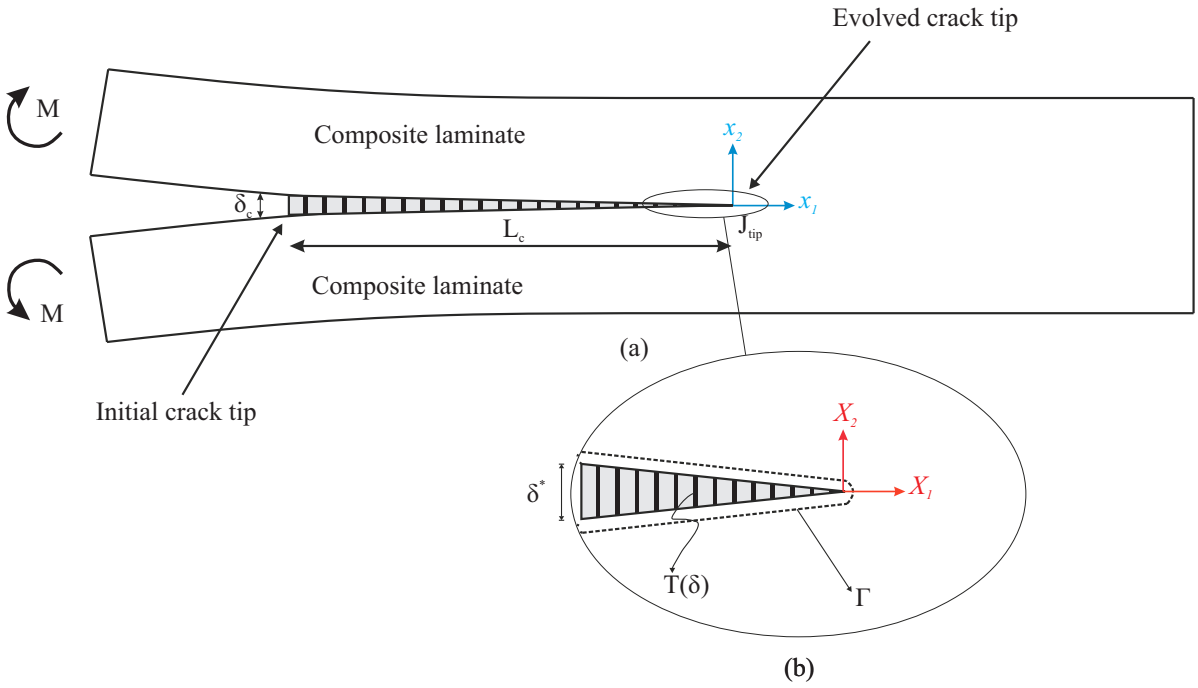

Figure 2.9: (a) LSB in a Double Cantilever Beam specimen loaded by bending moments(b) Integration path, Γ, for the cohesive zone.

- A bilinear cohesive law can be defined by two out of these three parameters: T_c, δ^* and J_c. According to the cohesive law shape, ABAQUS is able to calculate the third parameter.

2.5.1 Cohesive element

In order to mimic the crack growth, certain elements apart from the bulk elements are required for the cohesive zone. Cohesive elements behave according to the defined cohesive law and are placed in all the possible locations where the crack may propagate.

Since cohesive elements are not a part of the bulk material, it is desired to model the cohesive elements with a finite thickness. If the element thickness is sufficiently small, the volume is negligible. In addition, the displacements as the output varies only between the top and the bottom surface of the element (Schwalbe et al., 2012). Figure 2.10 shows a cohesive element with its local coordinate system. The coordinate system is necessary so that the normal and transverse directions can be identified before the mesh generation. The cohesive element includes a top and a bottom surface which are at an initial distance from each other, h_c. Only the rotational degrees of freedom, ur of the cohesive element are limited meaning that they can only translate in the normal and transverse directions ($u_n \neq 0$, $u_s \neq 0$ and $u_t \neq 0$ while $ur_n = ur_s = ur_t = 0$). It is also worth mentioning that the cohesive elements only describe the material separation not the material deformation (i.e. the cohesive element does not include the effect of the Poisson's ratio).

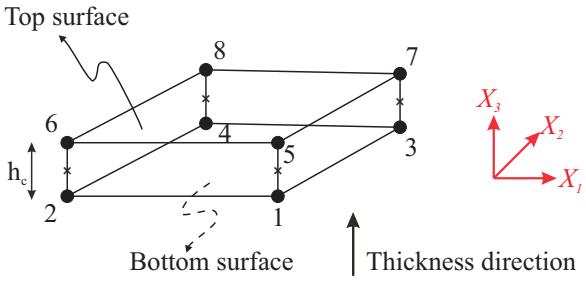

Figure 2.10: A linear three-dimensional cohesive element with 8-nodes (black dots) and 4 integration points (crosses) with its local coordinate system.

The deformed state of a cohesive element in the two-dimensional is shown in figure 2.11. The local coordinate system rotates as the cohesive element deforms and the opening can be written as

$$\boldsymbol{\delta}^* = \begin{Bmatrix} {U_n}^4 - {U_n}^2 \\ {U_t}^4 - {U_t}^2 \end{Bmatrix}$$

where the superscripts denotes the node numbers and U is the local displacement of the cohesive element.

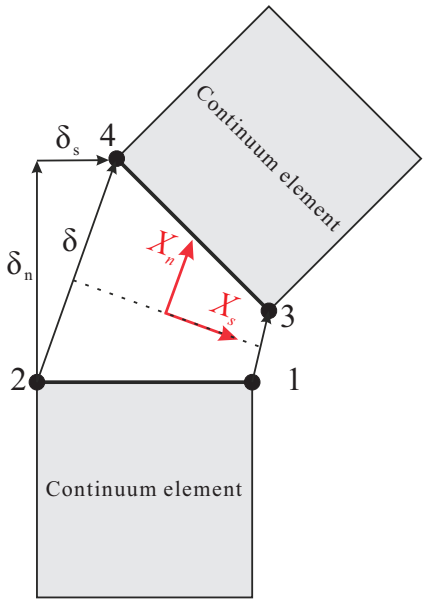

Figure 2.11: Deformed state of a cohesive element in the two-dimensional with the local coordinate system in the presence of continuum elements from the bulk material (Brocks et al., 2003).

Another critical parameter regarding the cohesive elements is their length (or quantity) in the cohesive zone. This is important from two perspectives: (a) too few cohesive elements cannot capture the correct displacement and stress required for the fracture energy calculation (b) too many cohesive elements make the FE analysis much time-consuming. Falk et al. (2001) recommended 4 to 6 number of cohesive elements along the cohesive length, L_c. Moës and Belytschko (2002) suggested at least 10 cohesive elements within the active cohesive zone. Dávila et al. (2001) used the cohesive elements with the length of 1.25 mm for the analysis of a composite Double Cantilever Beam (DCB) specimen. Turon et al. (2007) opted for an adaptive mesh approach whereby pre-defining the number of cohesive elements, ne_c^0, together with the corresponding cohesive strength , $\overline{T}_c$, from Hillerborg et al. (1976), the minimum cohesive strength was calculated to be used in the cohesive law.

$$T = min\{T_c, \overline{T}_c\} = min\{T_c, \sqrt{\frac{E\mathcal{G}_c}{ne_c^0 L_c}}\}$$

In the above equation, $\mathcal{G}_c$ is the fracture toughness and can be replaced according to its corresponding value for mode I, II and III. As a result, the length of the active cohesive zone lengthened by picking the minimum value of T and well-suited for capturing the stress. Schwalbe et al. (2012) preferred to provide some guidelines rather than giving an exact solution for the number of elements. The guidelines are

- h_c should be much smaller than the cohesive element length in two-dimension and the cohesive element area in three-dimension.
- $h_c << \delta^*$

- h_c should be much smaller than any geometrical dimension ,e.g, height, width and length.

Concerning the previous research in the field of the number of the cohesive elements in the cohesive zone, it is concluded that for the purpose of the delamination where the crack path is straight, determined in advance and along the crack plane; the above guidelines from Schwalbe et al. (2012) will be efficient. Furthermore, a mesh convergence study of the stress can reassure the selected cohesive element size.

2.5.2 The R-curve

Usually, failure does not catastrophically occur in materials. There is a material resistance to the crack growth which is well-described by the concept of "Resistance curve" or R-curve (figure 2.12). Crack blunting by plasticity and fiber bridging (figure 2.9(a)) are the main reasons for resistance in metals and fiber composites. In fact, the R-curves shows the dissipated energy, J_R, versus the crack extension. The subscript R is used to differentiate the R-curve. Before the initiation of the crack growth, energy is required to separate the two surfaces at the crack tip and subsequently to overcome the fiber bridging. Therefore, the specimen can sustain the applied load until a certain level, J_0. Further increase in the load causes the crack onset and the crack length extends where both the J and crack length increase. In composites, this step usually starts by matrix fracture which has a lower strength compared to the fibers. In the meanwhile, the fibers do not break and still carry the load behind the crack tip/front while the crack tip/front is dynamically moving from one interface to another (the "Initial" and "Evolved" crack tips in figure 2.9). If the load level becomes sufficiently large to break the fibers, there exists a critical opening displacement, δ^*, where the fibers do not carry any load, T=0, and the FPZ takes a self-similar opening profile, δ_c, and length, L_c. Consequently, the R-curve attains a constant value (steady-state), J_{ss}.

When the integral path is shrunken to include the lower and upper crack surfaces and the crack tip, by applying the energy balance through the J integral equation one can write the J integral in the form of resistance (Rice, 1968a).

$$J_R = \int_0^{\delta^*} T(\delta) d\delta + J_{\text{tip}} \tag{2.12}$$

where J_{tip} is the J value at the crack tip and in fact is equal to J_0 in the R-curve in figure 2.12. If $J_R = J_0$, the crack propagates.

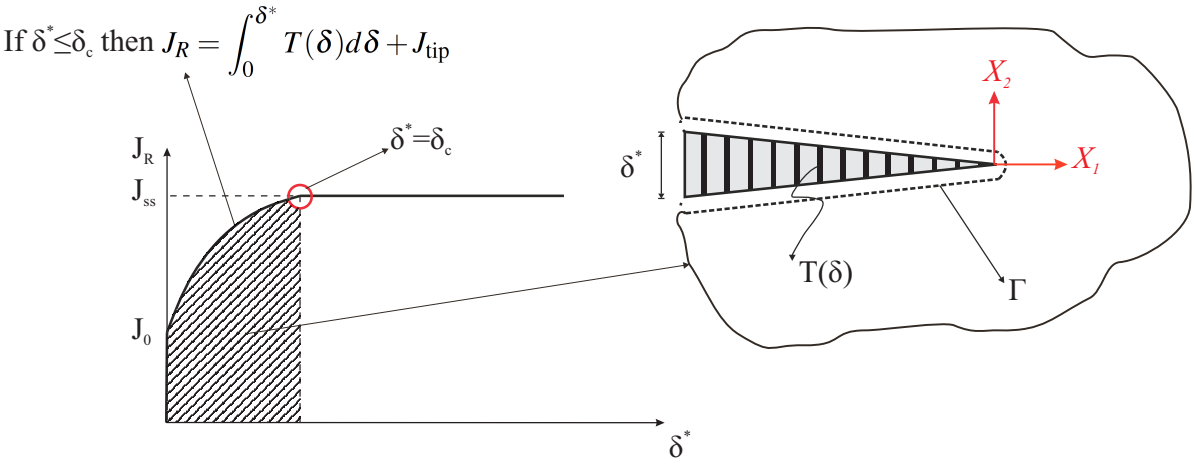

Figure 2.12: An schematic of the *R*-curve.

2.5.3 Determination of the cohesive law

The cohesive law can be determined either from the micro-mechanical or phenomenological model. The micro-mechanical model involves different micro-mechanisms and scattered input variables (for the case of brittle fracture) while the phenomenological model are independent of the geometry, loading and failure mechanisms. Therefore, the phenomenological models are widely-used for the cohesive law.

There has been several approaches for verification of the cohesive law based on the phenomenological model such as fitting the *R*-curves from the experiment with the theory or adjusting the cohesive strength to give the same value of end-opening from the experiment. Another method, also used in this thesis, is by recording the resistance, J_R, and local opening from the *R*-curve (Li and Ward (1989), Z. Suo and FAN (1992)). One can show that the cohesive law then can be determined by Eq.(2.11)

$$T(\delta^*) = \frac{dJ_R}{d\delta^*} \tag{2.13}$$

The derivation of Eq.(2.13) is given in Appendix B.

2.6 Research Objectives and Questions

The objective of the present project is to optimize a unidirectional fiber composite fracture mechanics test specimen for Mode III, with the aim of developing a test specimen geometry that allows stable crack growth and can be analyzed in the framework of the *J* integral so that it can be used also for the Large-Scale Bridging problems.

The proposed project can be divided into three phases:

- **Phase 0:** Developing the LEFM Finite Element model in two-dimension and three-dimension with sufficiently fine mesh focused at the crack tip/front to extract the K_{I} and K_{II} and comparing them with the available results from literature.
- **Phase 1:** The LEFM Finite Element modeling to find a cross-section capable of giving K_{III}.
- **Phase 2:** The cohesive zone Finite Element modeling and testing the accuracy of the implemented cohesive law by recording the crack growth resistance (in the form of the J integral) and the local opening.

In the proceeding, the detailed explanation regarding each phase together with the research questions will be discussed.

2.6.1 Phase 0: Mode I and II FE modeling

The phase naming justifies the reason why "Phase 0" is not included in the objective but is essential since the whole study will be performed on the evolved model from this phase. Fundamental research questions for "Phase 0" are

1. What is the best geometry, based on the previous works, for the delamination toughness testing in mode I and II that primarily can be further developed to mode III and is secondly equipped with a closed-form solution for the J integral independent of the cohesive parameters that can be later compared with the J integral from Eq.(2.11)?
2. How to implement the LEFM model in ABAQUS?
3. Is there any analytic solution in the literature which removes the dependency of the K_{III} from the initial crack length and applied boundary condition?

2.6.2 Phase 1: Mode III FE modeling

After accomplishing the sophisticated LEFM Finite Element model, the effect of several geometrical modifications, listed below, on K_{IIIC} will be investigated.

- Variation in the width and height
- Side-grooves
- Added beams
- Orthotropy

The material in the first three cases has isotropic mechanical properties. The mechanical properties only change in the last case where the effect of orthotropy will be studied.

The research questions regarding "Phase 1" are

1. How do the geometry modifications like side-grooves affect the mesh generation in the three-dimensional model?
2. What are the possible approaches to assure a reliable FE model for each scenario?
3. How to compare the K_{IIIC} obtained from the FE model to the analytic solution?

2.6.3 Phase 2: CZM and cohesive law determination

The CZM includes the cohesive law formulation, the crack preparation simulation and the cohesive law determination. The cohesive law and parameters for the present project are formulated through a series of experiments at the Technical University of Denmark (DTU). In this study thus "Phase 2" only involves the crack extension simulation and cohesive cohesive determination. The J_R values along with the local opening are extracted from ABAQUS.

The research questions regarding "Phase 2" are

1. What are the required parameters for the cohesive law?
2. How to characterize the LSB condition in ABAQUS?

2.7 State of the art

There has been an extensive tendency towards the determination of the delamination toughness, FE analysis and standardization for mode I, II and the mixed-mode I-II of the fiber composites. In contrast, mode III delamination toughness, $\mathcal{G}_{\mathrm{IIIC}}$, due to its complexity and difficulty in the experimental setup on the one hand, and the lack of a robust FE code, on the other hand, has been considered to a lesser extent. In this section, an overview of the recent researches in the field of delamination toughness testing under anti-plane loading in composites will be presented. Figure 2.13 illustrates the specimen geometries that have been used in the fracture toughness testing.

The Split Cantilever Beam (SCB) (Donaldson, 1988) is one of the first specimens used to analyze the delamination in mode III and fracture toughness testing (figure 2.13(a)). The complete setup includes two aluminum plates attached to the specimen to remove the torsional moment around the longitudinal axis. The result showed a higher portion of mode II compared to mode III. Hwang and Hu (2001) suggested the Simplified Split Cantilever Beam (SSCB) (figure 2.13(a)) where the aluminum plates were replaced with the aluminum blocks at the end of the specimen. Good results were obtained using this specimen, even though the mode II further increased from the center to the edges.

The Modified Split Cantilever Beam (MSCB) (figure 2.13(a)) utilized a secondary pair of the loads at the delamination front to create the pure out-of-plane shear. Khoshravan and Moslemi (2014) obtained 97% of the total ERR, driven by the mode III; however, the mode II

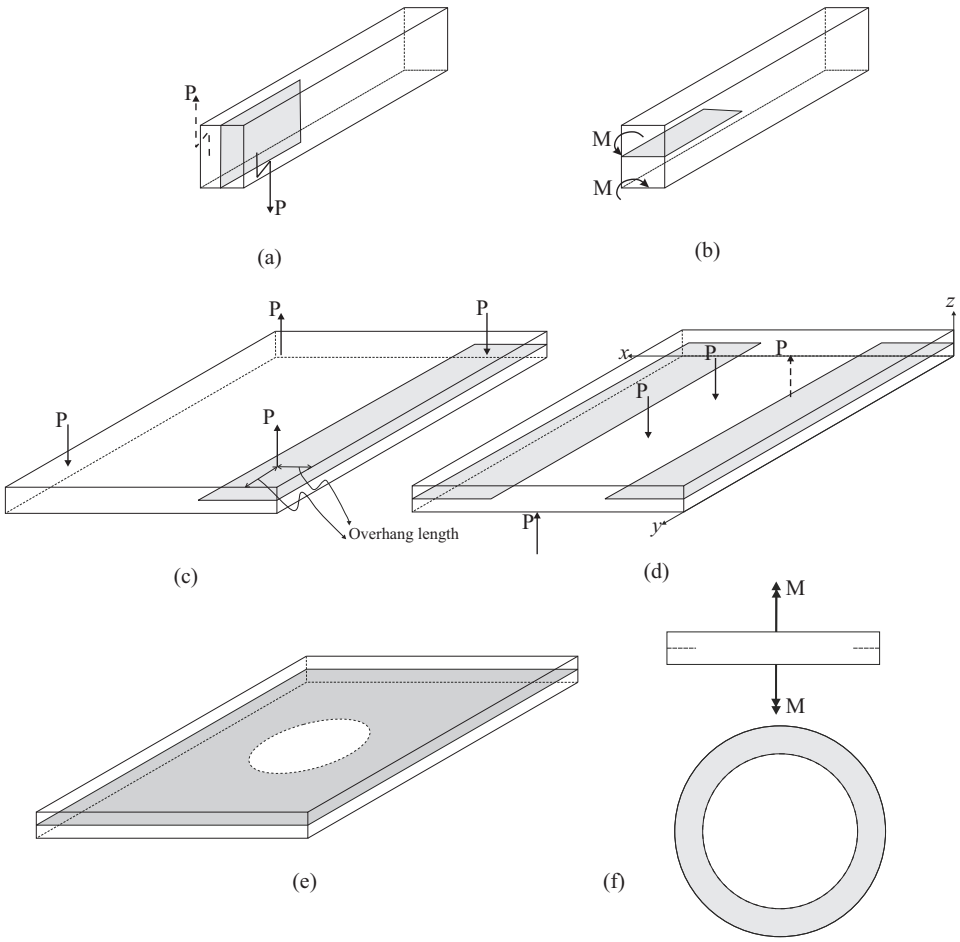

Figure 2.13: (a) SCB, SSCB, MSCB, SST (b) DCB (c) ECT, ECT-a, 6ECT (d) 4PBP (e) ERCT (f) TS test specimen geometries.

was still dominant at the crack edges.

Another test method performed by the Split Shear Torsion (SST) (figure 2.13(a)) specimen. The SST is identical to the MSCB specimen but thinner. The result showed a highly elevated mode II at the edges (Horner et al., 2015).

A novel test for two composite laminates (López-Menéndez et al. (2016), López-Menéndez et al. (2017)) was designed by placing a Double Cantilever Beam (DCB) specimen (figure 2.13(b)) between to horizontal rails. The mode III loading was created via the torque. As a result, the anti-plane shear was accomplished by sliding the gripper along the rails. The $\mathcal{G}_{\mathrm{IIC}}$ was dominated close to the delamination front. Farther away from the delamination front, the $\mathcal{G}_{\mathrm{IIIC}}$ was more pronounced.

One of the test methods which has drawn much attention recently is the Edge Crack Ten-

sion (ECT) (figure 2.13(c)) (Lee, 1993)[2]. PENNAS D. et al. (2007), Browning et al. (2010), Browning et al. (2011) ,Mehrabadi and Khoshravan (2012) did a comprehensive study on the ECT specimen to optimize the geometry for the mode III delamination toughness testing. In this test, the $\mathcal{G}_{\mathrm{IIIC}}$ fell from the specimen center to the edges and was reported between 90%-97%. Being highly dependent on the pre-existing crack length, a_0, and the overhang length (the distance from the applied load to the edges) in the fiber longitudinal direction are the two main drawbacks of the ECT specimen. Other ECT-derived specimens like the 6-point Edge Crack Torsion (6ECT) (Pereira et al., 2011) and ECT-a ((Suemasu, 1999), (Ge et al., 2016)) yielded the same mode-mixity at the edges with predominantly mode II.

The 4-point Bending Plate (4PBP), figure 2.13(d) (Morais and Pereira, 2009) is the less expensive version of the ECT test with two delamination fronts. Despite the good results for the $\mathcal{G}_{\mathrm{IIIC}}$, the 4PBP exhibited the same dependency on the overhang length and specimen length in the y-direction. Furthermore, there is always a possibility of the asynchronous delamination at the loading points that makes the reproducibility of this test questionable.

In another category of the mode III delamination toughness testing, the delamination front has a circular shape. The Edge Ring Crack Torsion (ERCT) (Ge et al., 2016), figure 2.13(e), and the Torque Shell (TS) tests (Cricrì and Perrella, 2017), figure 2.13(f), are listed in this category. The disadvantage of both methods is the susceptibility of the $\mathcal{G}_{\mathrm{IIIC}}$ to the initial delamination size.

Some authors have focused on the evaluation of the theory and the available FE tools. Kotousov et al. (2013), Berto et al. (2015) and Campagnolo et al. (2015) proposed a study on the stress state under the tearing mode. They shrank the specimen to a half-disk (and a rectangular plate in another case) to further include the behavior of all the possible test specimens. They found out that in addition to the three conventional fracture modes, there were two other coupled modes which could initiate the crack even when the $K_{\mathrm{II}} = K_{\mathrm{III}} = 0$. Additionally, in the three-dimensional, there was an infinite number of terms in the classical two-dimensional approach for the SIF the that were able to generate the singularity.

Table 2.2 categorizes the specimens that have been mentioned above for the fracture toughness testing.

Table 2.2: Mode III delamination toughness testing test methods.

Group name	Covered specimens
DCB-type	SCB, SSCB, MSCB, SST, DCB
ECT-type	ECT(MECT), ECT-a, 6ECT, 4PBP
Torsional-type	ERCT, TS

In conclusion, there is a dependency on the initial crack length as well as the geometry in

[2]This test is also known as the Modified Edge Crack Tension (MECT) test.

all the specimen types and yet no robust testing approach has been established for characterizing the $\mathcal{G}_{\text{IIIC}}$ in composites. This gave rise to investigate the delamination front of the SST, MSCB and ECT specimens in the micro-scale (Johnston et al. (2014), Johnston and Davidson (2014), Horner et al. (2015)). The Photomicroscopy revealed the existence of the transverse cracks in the matrix due to the embedded insert (for the sake of seam creation). These matrix cracks initiated in advance to the delamination; therefore, the pure mode III delamination was not accomplished. As a result, the data reduction method (ASTM D5528-01, 2014), frequently used in the fracture toughness testing which is based on the hypothesis of a crack extension under pure delamination becomes invalid. Since the dissipated energy from the delamination and matrix cracking are not distinguishable. To arrest these transverse cracks in the matrix, the plies on the top and bottom of the delamination interface should be stacked such that the plies prevent the matrix cracks from opening. From another point of view, it has been observed that in all the tests under prescribed loading condition can cause unstable crack extension (Anderson, 2005).

To the knowledge of the author, there has not been conducted a research topic analogous to the present work to explore the effect of various parameters on mode III delamination toughness. A DCB specimen is chosen in this study for two reasons.

1. The crack growth for the DCB specimen is stable which is an essential requirement for the CZM (Z. Suo and FAN, 1992). By applying the prescribed displacement, not only a stable crack growth is obtained but also The J integral solution will be independent of the initial delamination length.

2. Under the LSB, the J integral depends on the cohesive parameters. The DCB specimen benefits from a closed-form solution for the J integral in both LEFM and LSB condition.

The researches in the field of fiber composites mode III CZM are limited. Israr et al. (2017) and Cricrì and Perrella (2017) suggested a bilinear cohesive law for the mode III delamination under the ECT and TS test methods. Cricrì et al. (2015) utilized the TS test to compare the results from the experiment with an exponential cohesive law. The aforementioned works were performed by the specimens that the result was proved to be geometrically-dependent. Additionally, they fundamentally lack a systematic procedure for the cohesive law validation which raises the doubt about the obtained result.

The approach based on the potential function by Sørensen and Kirkegaard (2006) can be extended to mode III and thus suggests an approach to determine mode III and mixed-mode cohesive laws.

2.8 What Remains to Be Done?

The delamination toughness is required for the calculations regarding the residual strength and the number of cycles a structure can withstand under fatigue. Material degradation and load-bearing capacity of the structures are of paramount importance when a composite lamina

undergoes mode I-II-III simultaneously. Wang (1983) showed that the contribution of mode III under simultaneous mode I-II-III was several times larger than mode I and II and its value was more pronounced at the hole, free edges and corners (Tvergaard and Hutchinson, 2008). It was discussed in the former section that the obtained results for the delamination toughness determination are more or less under question due to the existence of transverse cracks in the matrix; therefore, it is needed to study various possible factors which may influence the mode III delamination toughness in the absence of all possible phenomena such as matrix cracks. Next, the cohesive law should be determined with a proven method so that it can be extend to real structures.

2.9 Relevance to Wind Industry

Wind turbine blades, as the largest rotating components of a wind turbine, are more prone to damage during their service life. The blade gravitational and bending moments scale by power 3 and power 1 of the rotor diameter, respectively (Jamieson, 2011). Therefore, the overall structural load is proportional to the rotor diameter to the power of 4. Furthermore, longer blades impose higher manufacturing and repairing cost to the manufacturers.

According to Sørensen et al. (2004) and Branner, Kim; Ghadirian (2014), delamination is one of the most frequent failures in the aerodynamic skin and spar sandwich panel laminates of the wind turbine blades. For instance, mode I delamination due to buckling or compression in the flange and the web of the main spar and mode III at the trailing edge when the flapwise and out-of-plane shear loading are the most dominant load cases (Eder et al., 2014). The lines mentioned above highlight the importance of developing reliable design tools which lower the blade weight while enhance the damage tolerance of the wind turbine blades.

2.10 Relevance to Aerospace Industry

Unique mechanical properties along with noticeable weight reduction and better fuel economy have made composites a good choice for the airplane primary structures such as fuselage, wings and control surfaces. Using composites, new AIRBUS A380 and Boeing 787 Dreamliner could have accomplished 25% (AIRBUS, 2018) and 20% (Boeing, 2008) weight reduction, respectively. This rising trend in replacing airplanes metallic components with fiber composites requires robust damage analysis theories. The lack of a reliable model for damage initiation and evolution along with the fail-safe criterion in aeronautic parts lead to more conservative designs. As a result, due to the restrictive certification and inspection standards for the aerospace structures, the manufacturing cost will increase and inspections are performed within short intervals. In conclusion, the current study contributes to the progressive analysis failure of the fiber composites in the aerospace industry where the delamination is more likely due to severe structural loading and complex geometries. The current researches in the field of damage and structural reliability in Instituto Nacional de Tècnica Aeroespacial (INTA) (Javier S. Millàn (2016), Millàn and Armendàriz (2015)) also emphasizes the importance of delami-

nation in the composite aeronautical parts.

2.11 Thesis Outline

The background, required tools, research objectives, approaches and the literature review were explained. In the remainder, the chapters are organized such that in chapter 3 and 4, the mode I and II FE model in two-dimension and three-dimension are developed and verified with the analytic solutions. Chapter 5 and 6 cover the effect of the geometrical changes to the DCB specimen that may affect K_{III}. Chapter 7 and 8 provide an overview of the added elastic beams and orthotropy on K_{III}. Chapter 9 covers the CZM. Finally, the conclusion and the future perspective will be discussed in chapter 10.

CHAPTER 3

Two-dimensional analysis of Mode I and Mode II

In this chapter and the subsequent, the FE modeling for the mode I and II in two-dimension and three-dimension will be explained. This is important for two main reasons: (a) to reassure of the developed FE model by comparing the result with the literature. (b) reasonable mesh quality which is the driving parameter in capturing singularity and computational time. The FE models for the mode I and mode II in two-dimension are covered in this chapter.

3.1 Mode I

3.1.1 Finite Element Model

The geometry of the DCB specimen, shown in figure 3.1, with the applied moments on the top and bottom ends create a symmetric condition whereby for the FE model only half of the specimen suffices (figure 3.2).

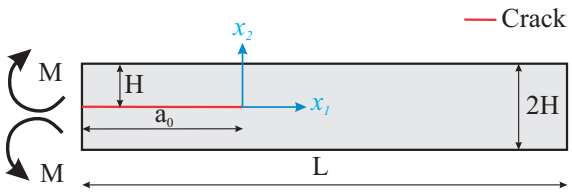

Figure 3.1: The geometry and loading of the two-dimensional DCB specimen under mode I.

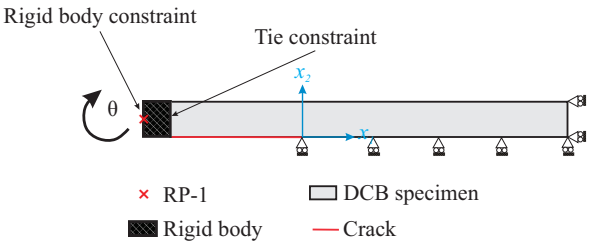

Figure 3.2: The two-dimensional DCB specimen FE model under mode I.

The geometrical dimensions are $a_0 = 5H$ and $L = 5a_0$ where a_0 is the length of the pre-existing crack, H is the specimen height and L is the specimen length. The criteria for selecting the aforementioned dimensions are first, to create a long specimen where the beam theory is applicable and secondly, to remove the effect of the boundary condition on the stress field on the crack tip.

3.1.1.1 Rigid body versus Rigid body constraint

A **rigid body** can be defined in ABAQUS either as discrete or analytical. However, a **rigid body constraint** is used to transfer the motion or constraint (here a point known as the "Reference Point"(RP)) to a system (ABAQUS, 2017).

In order to apply the rotation at the end of the DCB specimen, the **rigid body constraint** is utilized. The **RP-1** is created and connected to the rigid body through a **Rigid body constraint**. Consequently, the **RP-1** rotation can be conveyed through the rigid body. The rigid body is then attached to the end of the DCB specimen through a **Tie** constraint. The translational degree of freedom in the x_1-direction, u_1, and x_2-direction, u_2, at the right end of the specimen and along the crack ligament are limited.

An isotropic material with the Young's modulus, E=200GPa, the shear modulus, G=80GPa and the Poisson's ratio, ν=0.3 is assumed.

3.1.2 Element

Capturing the singularity at the crack tip requires an element capable of calculating the stress accurately. The second-order quadrilateral element is therefore selected (reasoning will be provided in the next section). The second-order quadrilateral element family, figure 3.3, for both the plane stress and plane strain, are listed below.

CPS8: 8-node biquadratic plane stress quadrilateral

CPS8R: 8-node biquadratic plane stress quadrilateral Reduced integration

CPE8: 8-node biquadratic plane strain quadrilateral

CPE8R: 8-node biquadratic plane strain quadrilateral Reduced integration

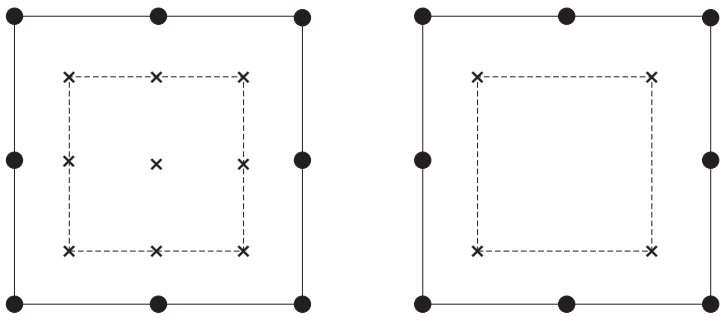

Figure 3.3: CPS8 and CPE8 elements (left). CPS8R and CPE8R elements (right).

The reduced integration versions of the elements are chosen for the plane stress and the plane strain studies. Both elements have eight nodes and four integration points.

3.1.3 Elements at the crack tip

In the FEM, there are two common types of the elements for the LEFM analysis in literature. The collapsed element, figure 3.4(c), which generates triangular elements, figure 3.4(a), and the non-collapsed element, figure 3.4(d) which forms rectangular elements, figure 3.4(b), at the crack tip. In the collapsed elements, the coordinate of the nodes at the crack tip are the same. For example, nodes 1, 8 and 3 share a common coordinate while this is not the case for the non-collapsed elements.

In addition, it is required to shift the mid-nodes of the elements surrounding the crack to the quarter point in the direction of the crack tip as demonstrated in figure 3.4 (Henshell and Shaw (1975), Barsoum (1976)). By moving the nodes, the $1/\sqrt{r}$-singularity appears in the Jacobian matrix.

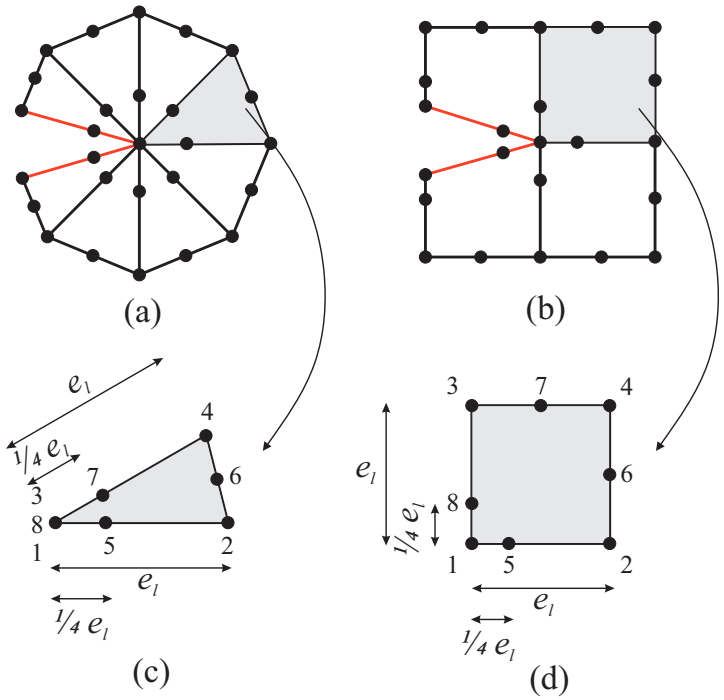

Figure 3.4: Elements configuration at the crack tip for the (a) collapsed (b) non-collapsed elements. Crack surfaces are shown in red. ABAQUS node numbering and the quarter shift in the mid-nodes for the single (c) collapsed and (d) non-collapsed element.

The collapsed and triangular elements, as well as the non-collapsed and rectangular elements, may be used interchangeably. The analyses will be done by both the triangular and rectangular elements to opt for the best choice of the element at the crack tip. The Number of contours for extracting the SIF is set to 10 and the "Maximum tangential stress" is selected as the crack initiation criterion (Erdogan and Sih, 1963). According to, this criterion that is based on the hypothesis originated from the brittle fracture, the crack starts to grow in a direction

where the tangential stress is maximum and the shear stress is zero. The maximum of the tangential stress can be calculated by differentiating it w.r.t to the angle, θ.

3.1.4 Mesh

Before selecting the proper mesh size, several criteria are required for the mesh study. To this end, the convergence of the SIF or J integral is chosen in fracture mechanics (Kuna, 2013) FE analysis. In addition to the SIF, two other measures, one regarding the stress and the other based on the normal opening are added to guarantee the mesh quality around the crack tip.

The "10% stress field" is the length in front of the crack where the maximum relative error between the theoretical and FEM stress (for example σ_{22} for mode I) is equal or less than 10%. In other words, Eq.(3.1) holds.

$$K\text{-field}_{(10\%)} = \left| \left(\frac{\sigma_{22,\text{th}} - \sigma_{22,\text{FE}}}{\sigma_{22,\text{th}}} \right) \times 100 \right| \leq 10\% \tag{3.1}$$

The subscript "th" and "FE" denote the results from the theory and FEM, respectively. Eq.(3.1) is presented for mode I and also can be used as a definition for the K-dominated zone in two-dimension (Sørensen and Jacobsen, 2000). Figure 3.5 illustrates the definition of the K-dominated zone according to Eq.(3.1).

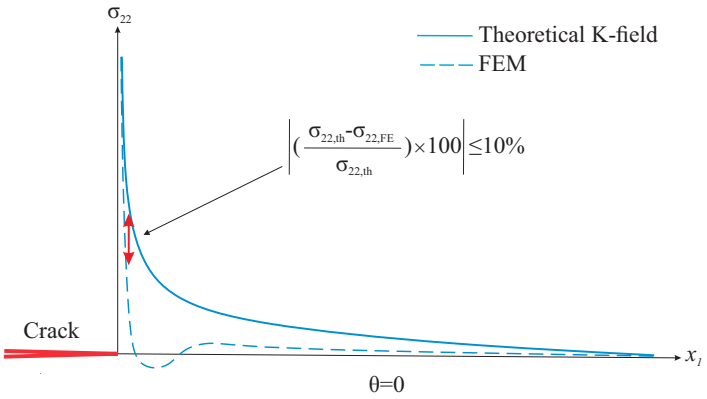

Figure 3.5: Schematic of the 10% stress field.

The displacement of a node in the distance of $x_1 = 0.02H$ behind the crack in the x_2-direction (figure 3.6) is chosen as another mesh criterion. Charalambides et al. (1992) discovered that the K-dominated zone for the DCB specimen is approximately within a distance of $0.01H$ or one percent of the specimen height. Hence, the mesh is fined within a distance of $x_1 = 0.02H$ on both the front and behind the crack tip (the yellow-shared area in figure 3.7). R is the radius of the half-circle centered at the crack tip and ℓ is the length of the rectangular placed on the crack tip.

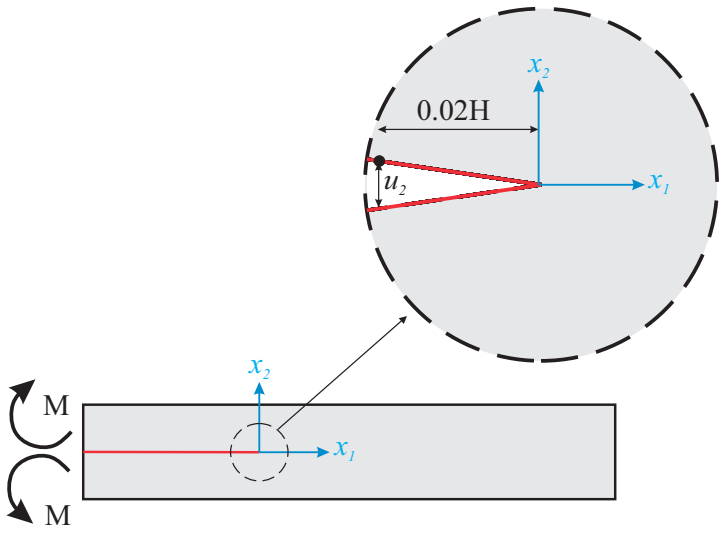

Figure 3.6: Definition of the crack opening for the mesh convergence in mode I.

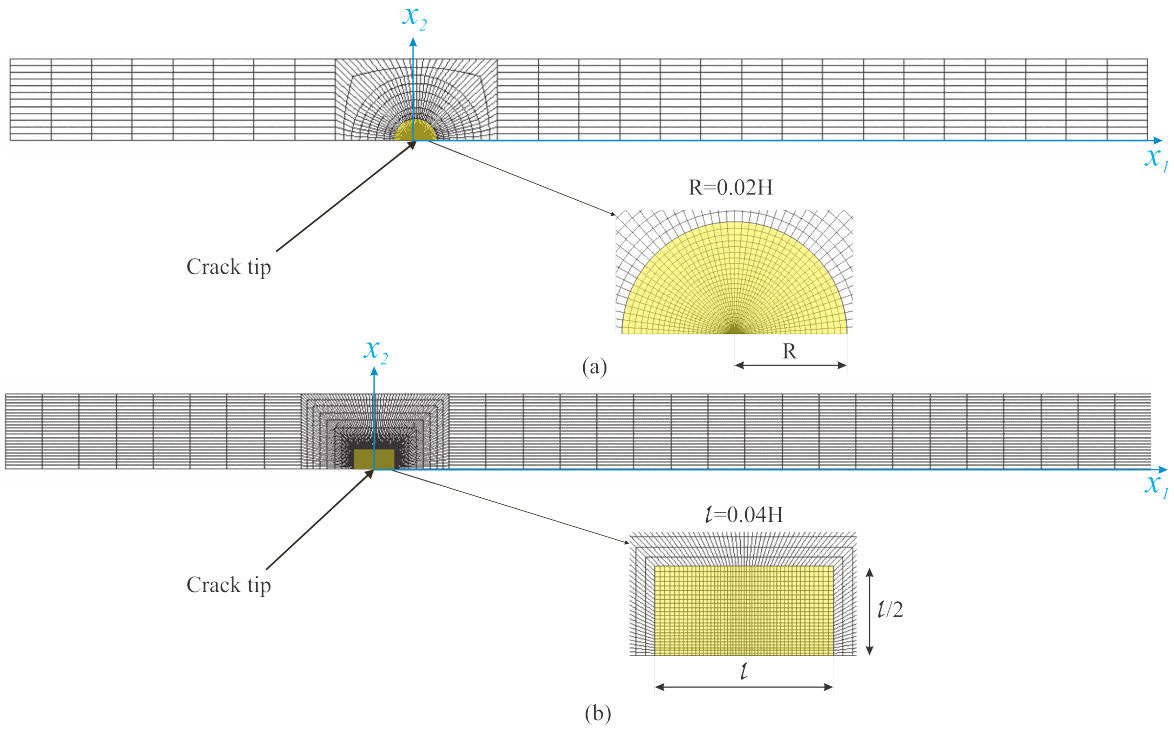

Figure 3.7: The mesh quality around the crack tip (a) triangular elements (b) rectangular elements. $R = 0.02H$ is the radius of the yellow half-circle centered at the crack tip. $\ell = 0.04H$ is the length of the yellow rectangular placed on the crack tip.

3.1.4.1 Mesh convergence

The results for the FE model with the triangular elements at the crack tip are presented in table 3.1 and figure 3.8 whereas the results for the rectangular elements are shown in table 3.2

and figure 3.9. *ne* refers to the number of elements in front of the crack within the length of $0.02H$ as illustrated in figure 3.7.

According to figures 3.8 and 3.9, for both element types at the crack tip, by increasing *ne* to more than 16 no more noticeable improvement will be observed. Although *ne*=8 gives good results for the stress and displacement, it does not create enough number of elements in the *K*-dominated zone (as a rule of thumb there should be at least 10 elements within this domain). Therefore, *ne*=16 is chosen for the FE analysis. The rest of the specimen is meshed with a maximum mesh transition of 1:4.

Table 3.1: The mode I mesh convergence study with the triangular elements at the crack tip.

	Plane stress			Plane strain		
ne	$\left\|\frac{K_{\mathrm{I,th}}-K_{\mathrm{I,FE}}}{K_{\mathrm{I,th}}}\right\| \times 100$	**10% stress field / H relative error [%]**	$u_2/u_{2,th}$ **relative error [%]**	$\left\|\frac{K_{\mathrm{I,th}}-K_{\mathrm{I,FE}}}{K_{\mathrm{I,th}}}\right\| \times 100$	**10% stress field / H relative error [%]**	$u_2/u_{2,th}$ **relative error [%]**
2	0.3847	-	-	0.3830	-	-
4	0.0108	0.0054	0.0047	0.0140	0.0054	0.0193
8	0.0348	0.0201	0.0046	0.0352	0.0201	0.0146
16	0.0368	0.0227	0.0030	0.0373	0.0227	0.0067
24	0.0384	0.0226	0.0006	0.0383	0.0226	0.0015

Table 3.2: The mode I mesh convergence study with the rectangular elements at the crack tip.

	Plane stress			Plane strain		
ne	$\left\|\frac{K_{\mathrm{I,th}}-K_{\mathrm{I,FE}}}{K_{\mathrm{I,th}}}\right\| \times 100$	**10% stress field / H relative error [%]**	$u_2/u_{2,th}$ **relative error [%]**	$\left\|\frac{K_{\mathrm{I,th}}-K_{\mathrm{I,FE}}}{K_{\mathrm{I,th}}}\right\| \times 100$	**10% stress field / H relative error [%]**	$u_2/u_{2,th}$ **relative error [%]**
2	0.0428	-	-	0.0443	-	-
4	0.0137	0.0123	0.0116	0.0134	0.0097	0.0061
8	0.0173	0.0201	0.0008	0.0172	0.0201	0.0042
16	0.0184	0.0220	0.0002	0.0184	0.0220	0.0010
24	0.0179	0.0226	0.0004	0.0181	0.0226	0.0007

3.1.4.2 Element size

The smallest element dimensions that are available around the crack tip for both types are given in table 3.3. The dimensions are also illustrated in figure 3.10.

Table 3.3: Two-dimensional mode I smallest element dimension.

Parameter	**Triangular element**	**Rectangular element**
Aspect ratio (e_h/e_l)	0.1000	0.9984
Smallest element size (e_l) [mm]	4.953E-03	4.953E-03
Smallest element size/H	4.953e-04	4.953e-04

3.1.5 Result and discussion

Figure 3.11 depicts the steps for calculating the theoretical mode I SIF, $K_{\mathrm{I,th}}$. The reaction moment, M, from the FEM is used in the J integral equation. The J integral can be determined

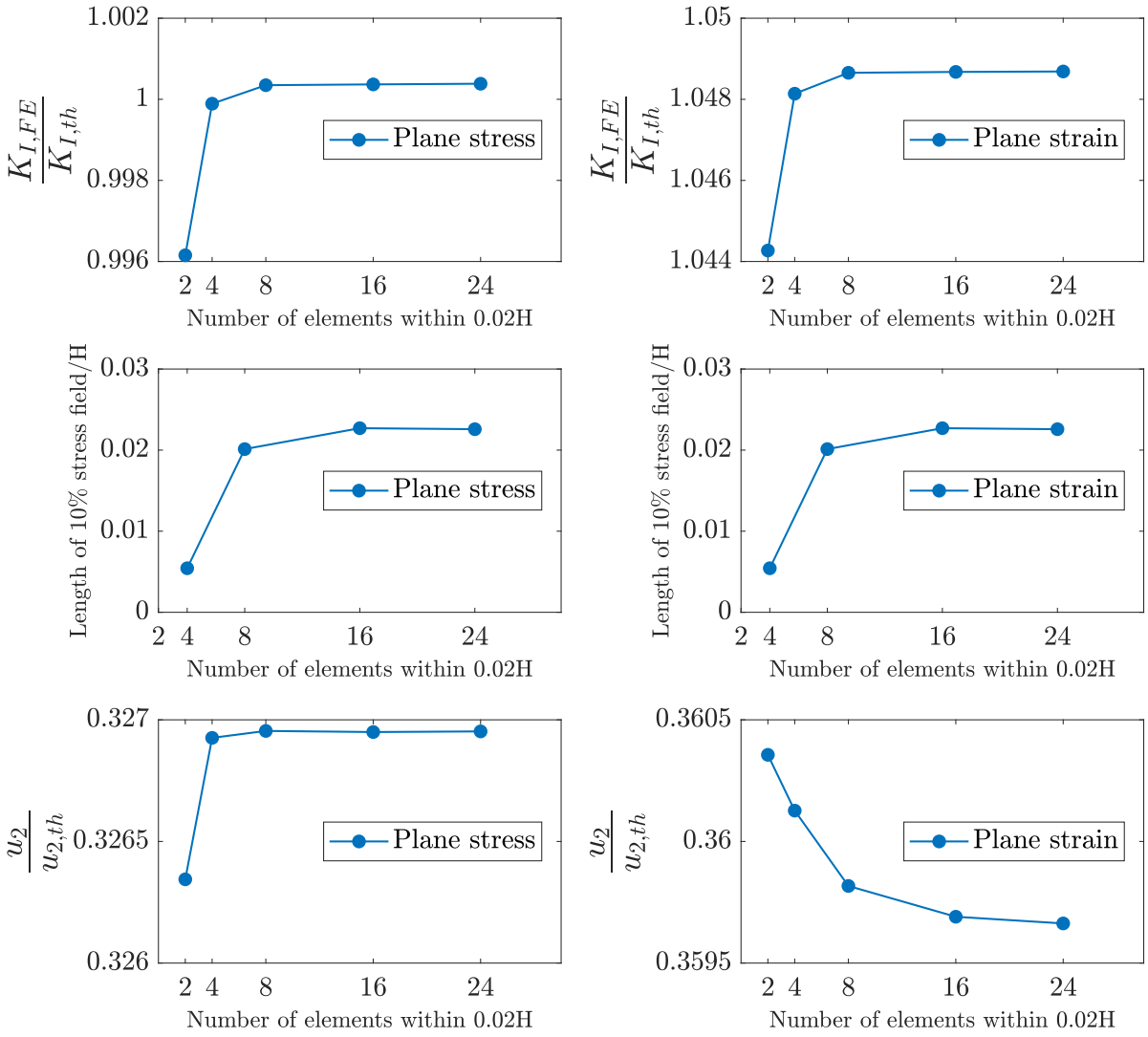

Figure 3.8: The mode I mesh convergence study with the triangular elements at the crack tip (u_2 and $u_{2,th}$ are extracted from a distance of $x_1 = 0.02H$ and θ=0).

for pure mode I either for the plane stress or plane strain condition from Eq.(3.2). Finally, Irwin's equation, Eq.(2.4), is invoked to calculate $K_{\mathrm{I,th}}$. The results are presented in table 3.4.

$$J = \frac{12M^2}{E'B^2H^3} \tag{3.2}$$

where E' is selected from Eq.(2.5). The derivation is provided in Appendix C for an isotropic material..

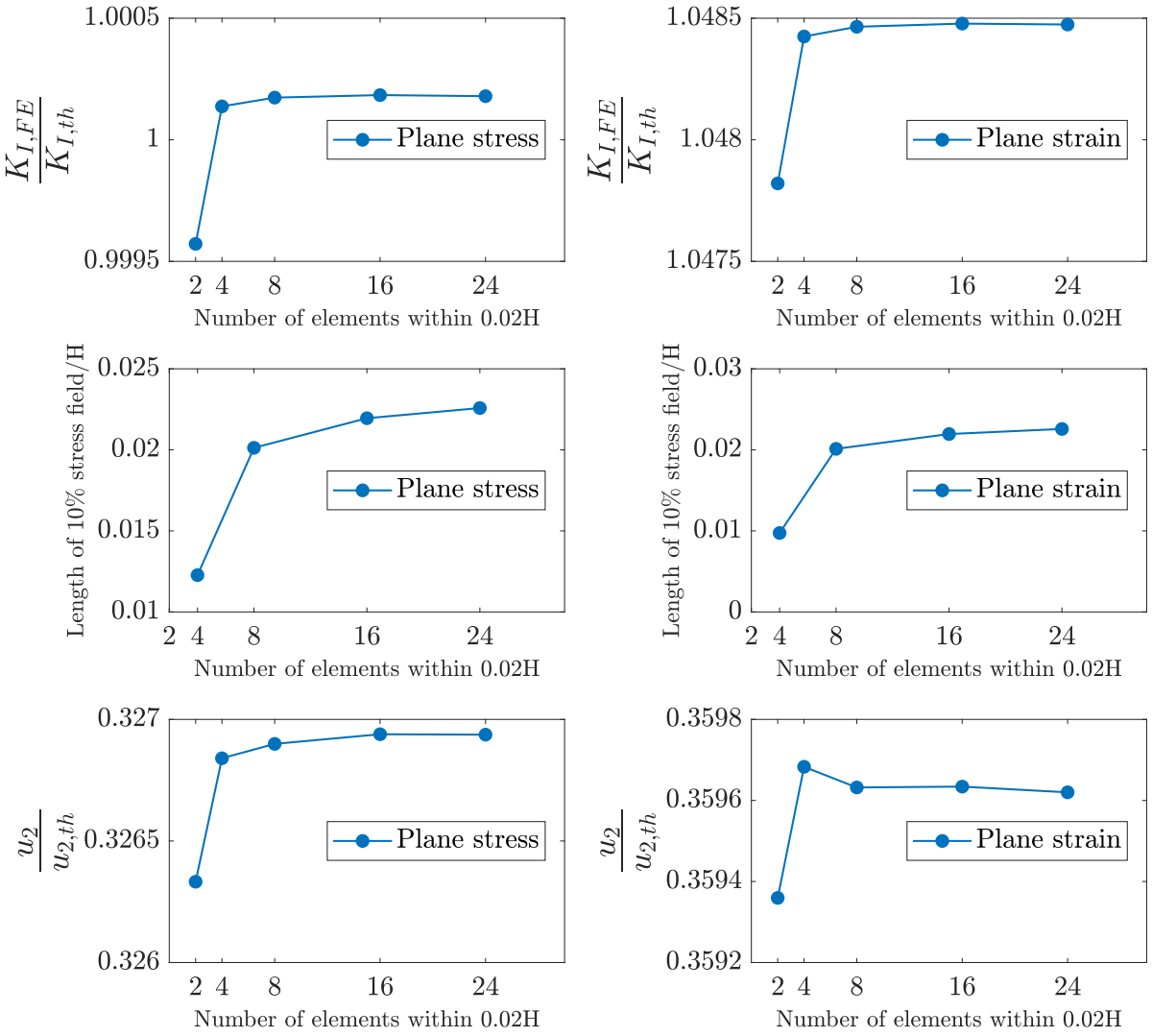

Figure 3.9: The mode I mesh convergence study with the rectangular elements at the crack tip (u_2 and $u_{2,th}$ are extracted from a distance of $x_1 = 0.02H$ and θ=0).

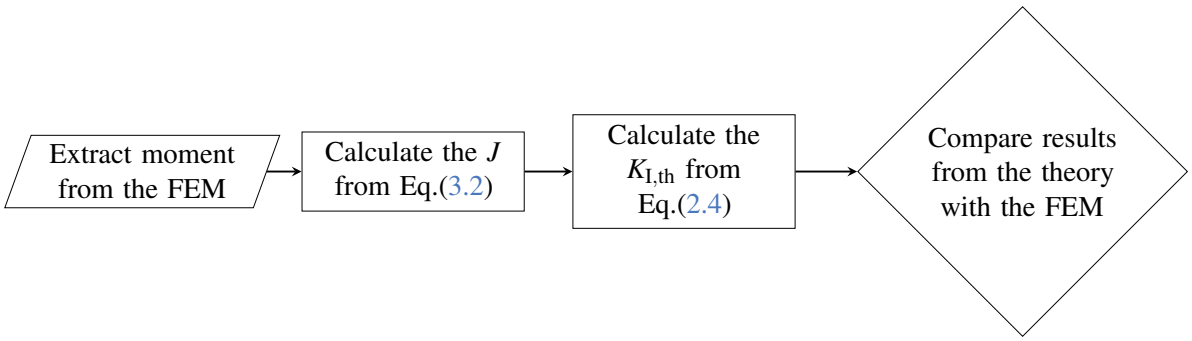

Figure 3.11: The flowchart for calculating $K_{\mathrm{I,th}}$ from the J integral.

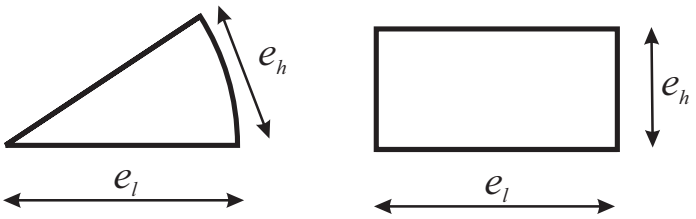

Figure 3.10: The geometry and dimensions of the two-dimensional triangular (left) and rectangular (right) elements at the crack tip.

Table 3.4: The J integral and SIF values for mode I.

Problem condition	**Element at the crack tip**	$J/\sigma_b H$	$K_{\mathrm{I,th}}/K_{\mathrm{I,FE}}$	K_{II}
Plane stress	Triangular	0.0018	0.9996	0
	Rectangular	0.0018	0.9998	0
Plane strain	Triangular	0.0018	0.9996	0
	Rectangular	0.0018	0.9998	0

In table 3.4, the J integral is normalized with the product of the maximum bending stress, σ_b, at the end of the specimen and the specimen height, H. σ_b is defined according to Eq.(3.3)

$$\sigma_b = \frac{Mx_i}{I} \tag{3.3}$$

where M is the applied moment, x_i is the maximum distance from the neutral axis and for mode I and II is x_2 while it is defined as x_3 for mode III. I is the second moment of area of the cross-section. In table 3.4, the values for the FE mode I SIF, $K_{\mathrm{I,FE}}$, is extracted from the 10th contour. The results for K_{I} from both the theoretical solution and FEM are very close and the pure mode I is accomplished.

The size of the K-dominated zone can be determined from one of the criteria mentioned below:

- **K-field$_{(\mathbf{r}/\mathbf{H}\cong 0.01)}$:** The one percent specimen height based on Charalambides et al. (1992)
- **K-field$_{(10\%)}$:** The 10% deviation between the theoretical and FEM solution mentioned in section 3.1.4
- **Singularity exponent:** The first term in the series expansion of the stress at the crack tip has a power of -0.5. It can be written as Eq.(3.6).

$$\sigma_{22} = r^{\lambda} \tag{3.4}$$

where λ is the singularity exponent.

The normalized σ_{22} is plotted along the normalized crack ligament coordinate[1] for the plane stress to compare the results from the theory (Eq. (A.1)) and FE with the triangular (figure 3.12) and rectangular elements (figure 3.13) at the crack tip. The logarithmic scale is also presented to provide a better insight of the LEFM solution.

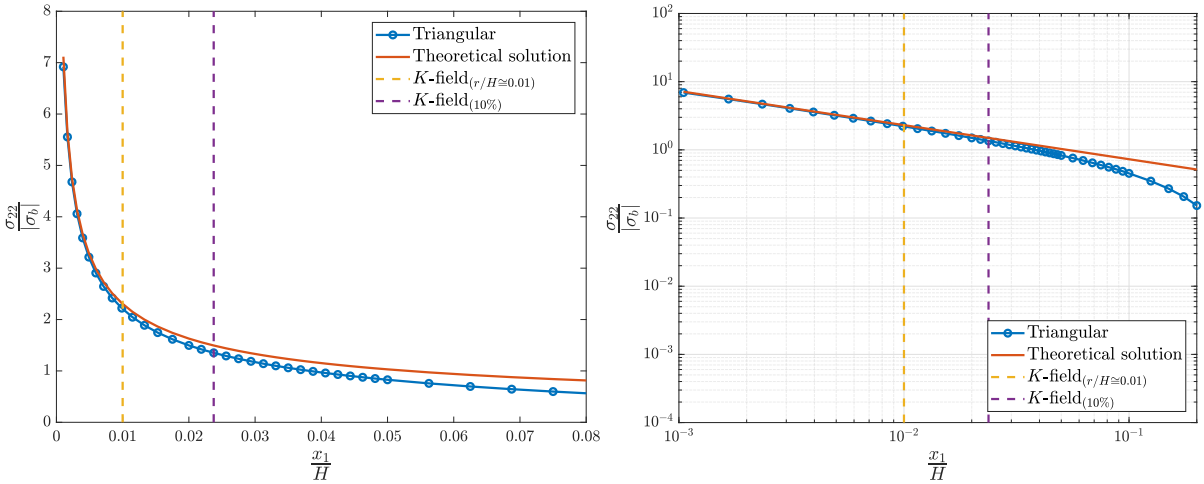

Figure 3.12: (a) Asymptotic (b) Logarithmic σ_{22} along the crack ligament for the plane stress condition with the triangular elements at the crack tip ($\theta = 0$).

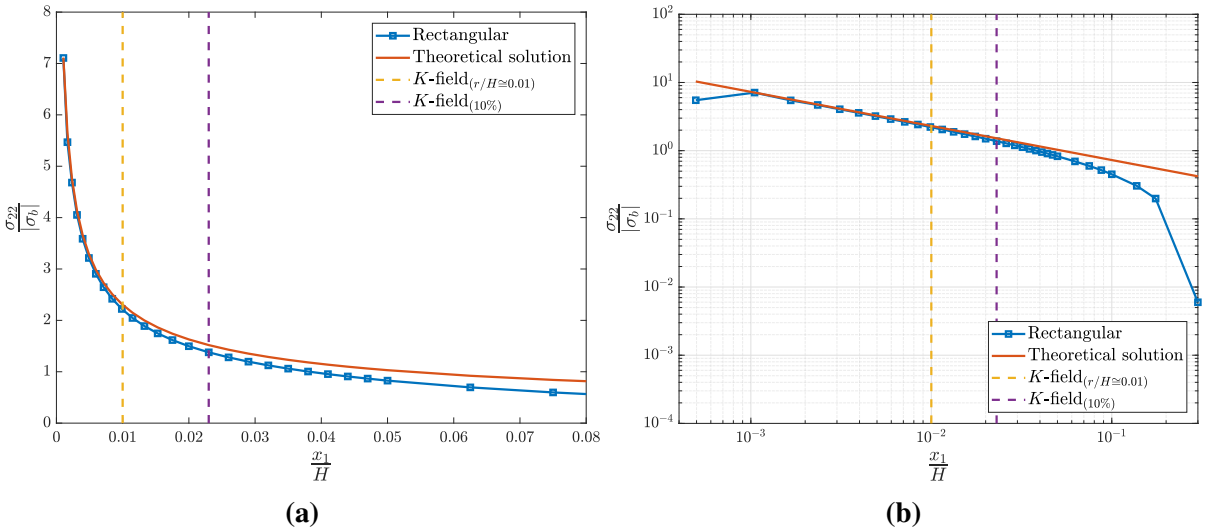

Figure 3.13: (a) Asymptotic (b) Logarithmic σ_{22} along the crack ligament for the plane stress condition with the rectangular elements at the crack tip ($\theta = 0$).

[1]The term Asymptotic refers to the situation where a quantity or parameter is getting close to another one via a curve. In this essence, the stress component, e.g., σ_{22} in mode I, gets closer to the crack tip and tends to nonphysical infinite stress at the crack tip.

The length of the K-dominated zone predicted by the K-field$_{(10\%)}$ is virtually two time larger than K-field$_{(\mathrm{r/H}\cong 0.01)}$. It appears that the stress in the first rectangular element fails to capture the correct stress value.

The plane strain plots for the triangular and rectangular elements at the crack tip are shown in figures 3.14 and 3.15. Once more the very first rectangular element is not able to give the correct stress at the crack tip.

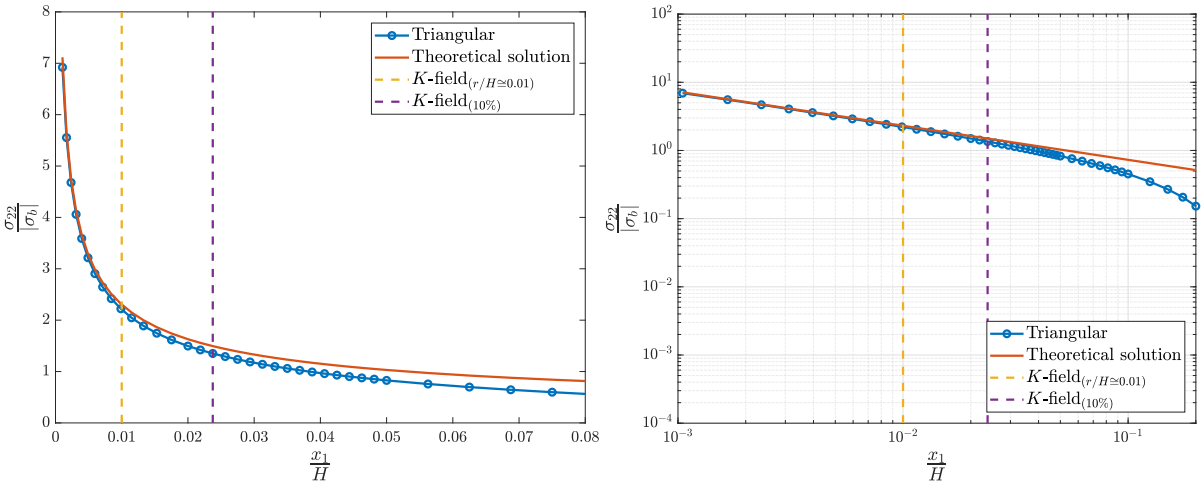

(a) **(b)**

Figure 3.14: (a) Asymptotic (b) Logarithmic σ_{22} along the crack ligament for the plane strain condition with the triangular elements at the crack tip ($\theta = 0$).

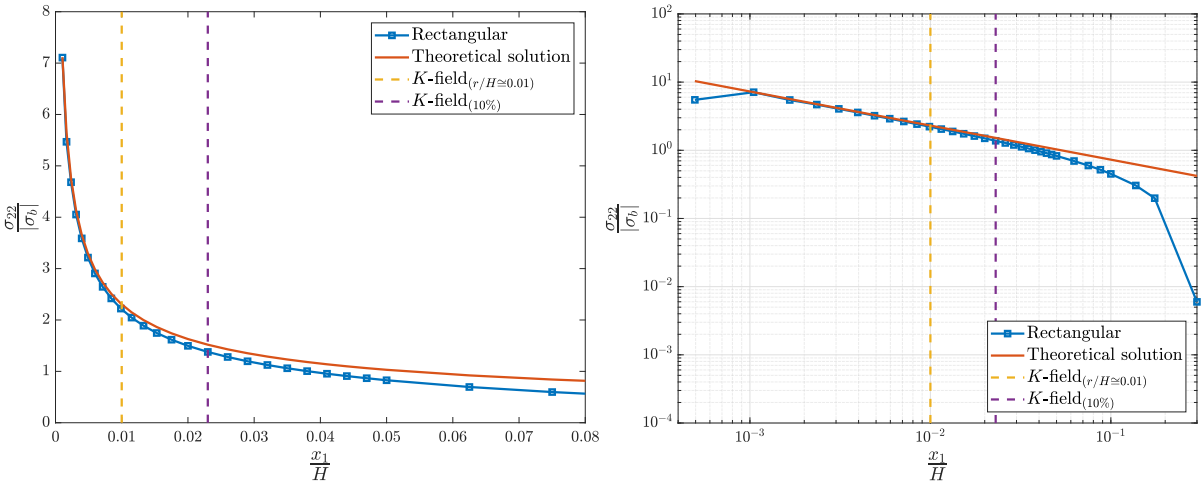

(a) **(b)**

Figure 3.15: (a) Asymptotic (b) Logarithmic σ_{22} along the crack ligament for the plane strain condition with the rectangular elements at the crack tip ($\theta = 0$).

A power curve is fitted to the first 20 elements (ignoring the first element at the crack tip) in front of the crack to find λ. The values are reported in table 3.5 for *ne*=16 and *ne*=24. The λ from the collapsed elements are closer to -0.5. Better λ values are obtained with the finer mesh (*ne*=24); however, by further reducing the element size, ABAQUS is not able to generate the triangular elements at the crack tip. The minimum difference between the obtained results and the known solution (-0.5) is 1.23%.

Table 3.5: λ values for the two-dimensional mode I.

Problem condition	**Element at the crack tip**	λ(*ne*=16)	λ(*ne*=24)
Plane stress	Triangular	-0.5175	-0.5123
	Rectangular	-0.5273	-0.5123
Plane strain	Triangular	-0.5176	-0.5123
	Rectangular	-0.5226	-0.5123

The stress contours for the triangular (figure 3.16) and rectangular (figure 3.17) elements at the crack tip show higher σ_{22} values for the plane strain condition. This reveals that the stress state at the crack tip under mode I for a thin specimen is lower than a thick specimen.

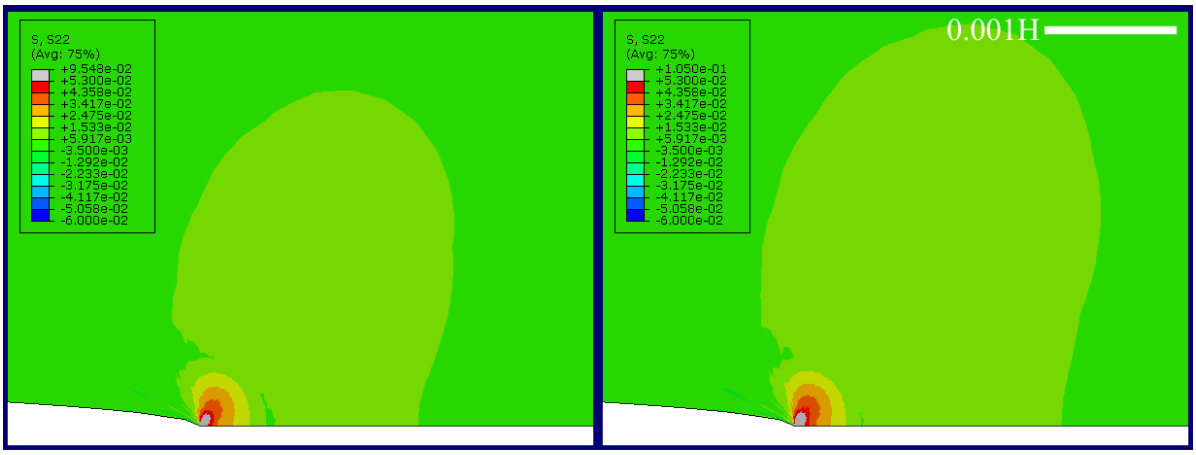

Figure 3.16: The σ_{22} contours under plane stress (left) plane strain (right) using the triangular element at the crack tip.

3.2 Mode II

3.2.1 Finite Element Model

The full DCB specimen is modeled for mode II (figure 3.18). For the FE model, figure 3.19, two identical moments in the form of prescribed rotations are applied in the same direction at the end of the specimen, on the two **RP-1** and **RP-2** reference points. All the translational

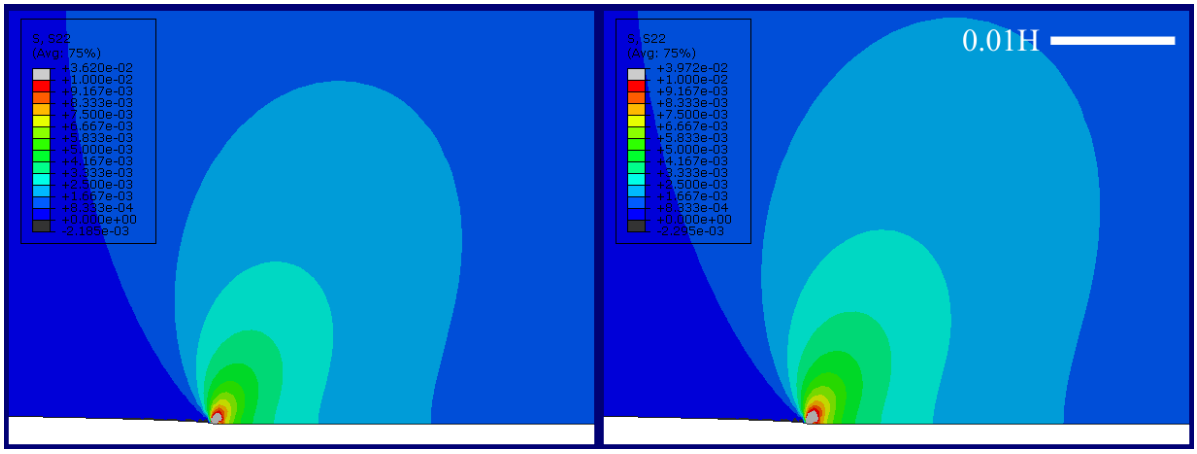

Figure 3.17: The σ_{22} contours under plane stress (left) plane strain (right) using the rectangular element at the crack tip.

and rotational degree of freedom are limited at the right end (cantilever beam). The geometry, material and elements are similar to the mode I.

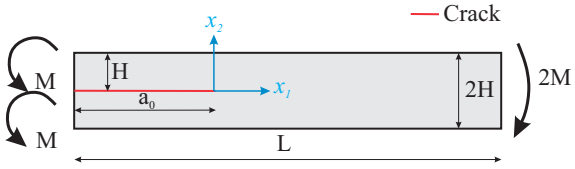

Figure 3.18: The geometry and loading of the two-dimensional DCB specimen under mode II.

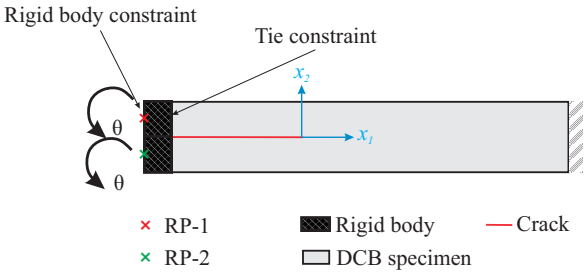

Figure 3.19: The two-dimensional DCB specimen FE model under mode II.

3.2.2 Mesh

The similar mesh convergence criteria from section 3.1.4 are borrowed except for the normal opening. For the mode II, the horizontal distance of the two nodes, Δu_1, one on the top and another on the bottom part of the pre-cracked region of the specimen at the distance of $x_1 = 0.02H$ behind the crack tip are chosen. A schematic of Δu_1 is illustrated in figure 3.20.

3.2.2.1 Mesh convergence

ne=2 cannot capture the stress and displacement adequately; therefore, it is excluded from the mesh convergence study. The mesh convergence with the triangular elements at the crack tip for both the plane stress and plane strain is presented in table 3.6 and figure 3.22. The result for the rectangular elements at the crack tip are presented in table 3.6 and figure 3.22. With respect to the previous explanation and justification in section 3.1.4.1, *ne*=16 is selected for the mode II analysis.

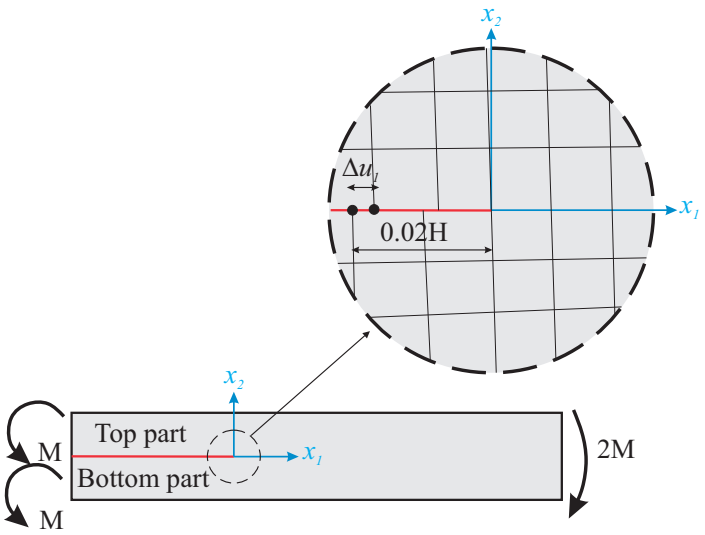

Figure 3.20: Definition of Δu_1 for the mesh convergence in mode II.

Table 3.6: The mode II mesh convergence study with the triangular elements at the crack tip.

	Plane stress			Plane strain		
ne	$\left\lvert\frac{K_{\mathrm{II,th}}-K_{\mathrm{II,FE}}}{K_{\mathrm{II,th}}}\right\rvert \times 100$	**10% stress field / H relative error [%]**	$\Delta u_1/u_{1,th}$ **relative error [%]**	$\left\lvert\frac{K_{\mathrm{II,th}}-K_{\mathrm{II,FE}}}{K_{\mathrm{II,th}}}\right\rvert \times 100$	**10% stress field / H relative error [%]**	$\Delta u_1/u_{1,th}$ **relative error [%]**
4	0.0472	0.0673	-	0.0532	0.0673	-
8	0.0185	0.0678	0.2442	0.0176	0.0678	0.2683
16	0.0186	0.0697	0.8440	0.0089	0.0697	0.9275
24	0.0279	0.0703	0.2648	0.0263	0.0703	0.2910

Table 3.7: The mode II mesh convergence study with the rectangular elements at the crack tip.

	Plane stress			Plane strain		
ne	$\left\lvert\frac{K_{\mathrm{II,th}}-K_{\mathrm{II,FE}}}{K_{\mathrm{II,th}}}\right\rvert \times 100$	**10% stress field / H relative error [%]**	$\Delta u_1/u_{1,th}$ **relative error [%]**	$\left\lvert\frac{K_{\mathrm{II,th}}-K_{\mathrm{II,FE}}}{K_{\mathrm{II,th}}}\right\rvert \times 100$	**10% stress field / H relative error [%]**	$\Delta u_1/u_{1,th}$ **relative error [%]**
4	0.0068	0.0466	-	0.0068	0.0466	-
8	0.0008	0.0483	1.1234	0.0007	0.0483	1.2345
16	0.0185	0.0491	0.5489	0.0202	0.0495	0.8620
24	0.0187	0.0494	0.1804	0.0182	0.0494	0.0556

3.2.2.2 Element size

The dimension of the smallest element (figure 3.10), available at the crack tip, for both the triangular and rectangular elements, is given in table 3.8.

Table 3.8: Two-dimensional mode II smallest element dimension.

Parameter	**Triangular element**	**Rectangular element**
Aspect ratio (e_h/e_l)	0.0982	1.000
Smallest element size (e_l) [mm]	4.953E-03	4.961E-03
Smallest element size/H	4.953E-04	4.961E-04

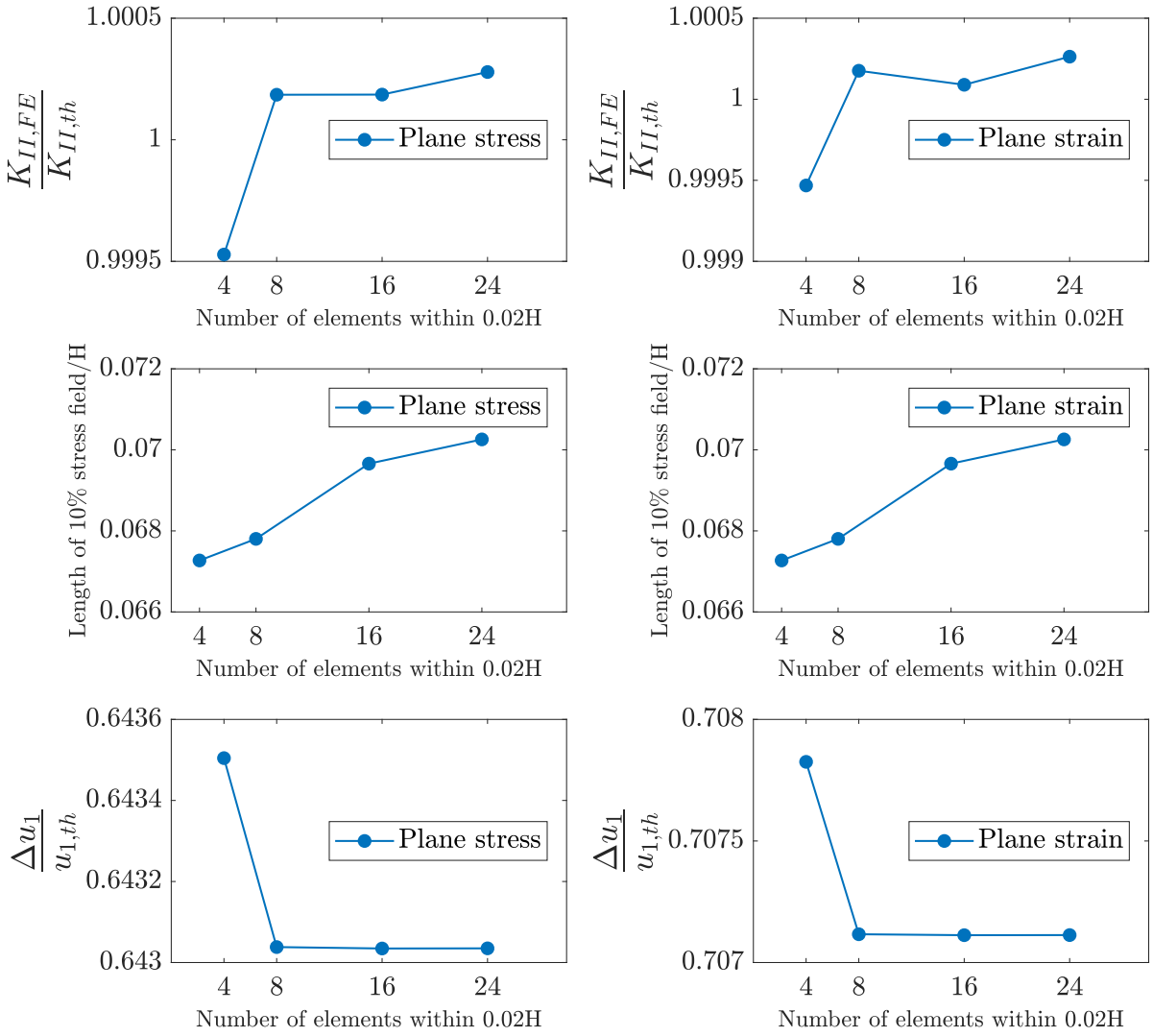

Figure 3.21: The mode II mesh convergence study with the triangular elements at the crack tip (Δu_1 and $u_{1,th}$ are extracted from a distance of $x_1 = 0.02H$ and θ=0).

3.2.3 Result and discussion

Eq.(3.5) provides the closed-form solution of the J integral in pure mode II. The steps for deriving the theoretical mode II SIF, $K_{\text{II,th}}$, are identical to the mode I and is shown in figure 3.23.

$$J = \frac{9M^2}{E'B^2H^3} \tag{3.5}$$

E' can be determined based on the plane stress or plane strain condition from Eq.(2.5). The derivation is given in Appendix D for an isotropic material. The FE mode II SIF, $K_{\text{II,FE}}$, is extracted from the 10th contour. The results for the J integral and the SIF from the theory and FEM are presented in table 3.9. The obtained values show a pure mode II and negligible difference between the $K_{\text{II,th}}$ and $K_{\text{II,FE}}$.

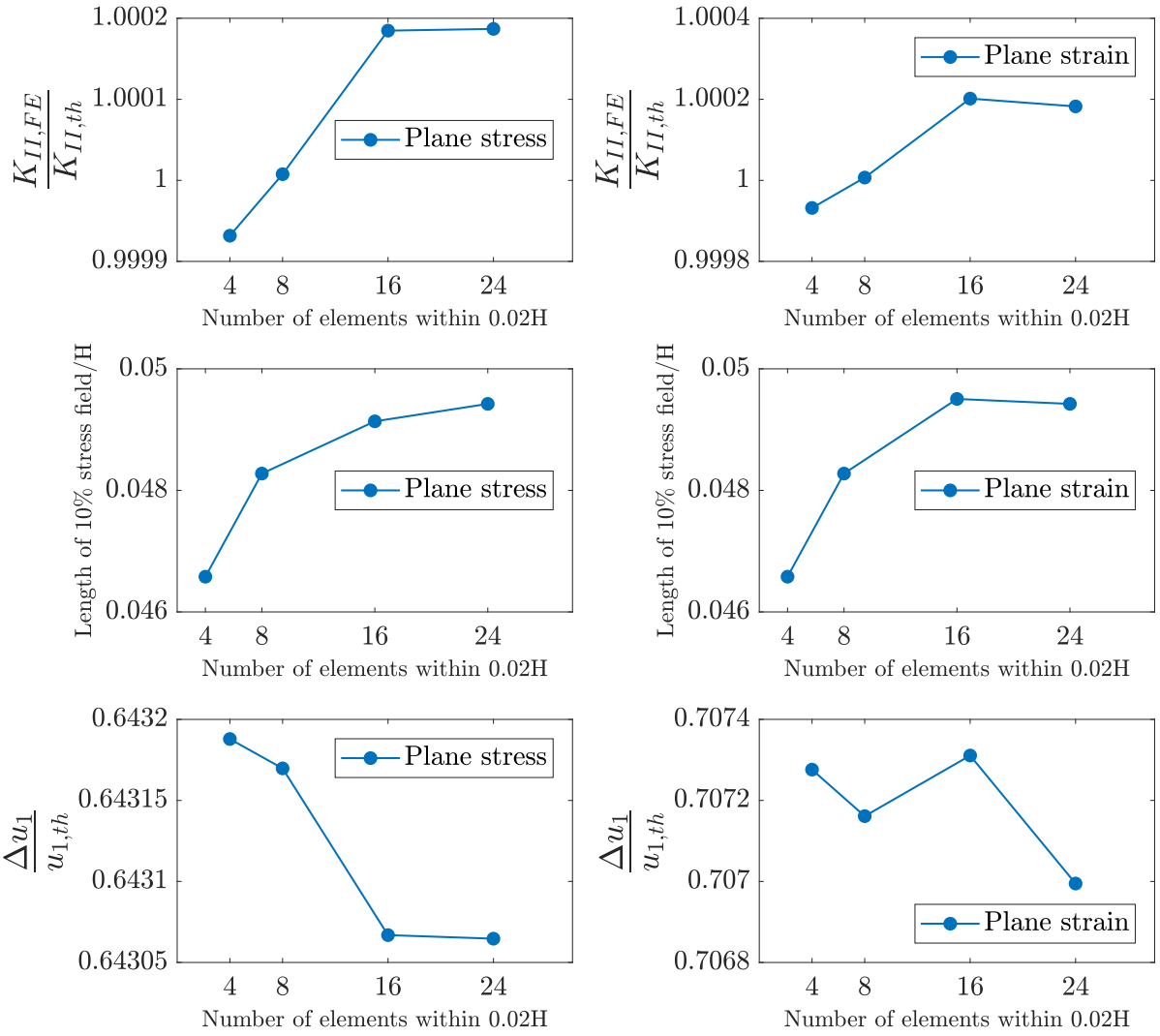

Figure 3.22: The mode II mesh convergence study with the rectangular elements at the crack tip (Δu_1 and $u_{1,th}$ are extracted from a distance of $x_1 = 0.02H$ and $\theta = 0$.

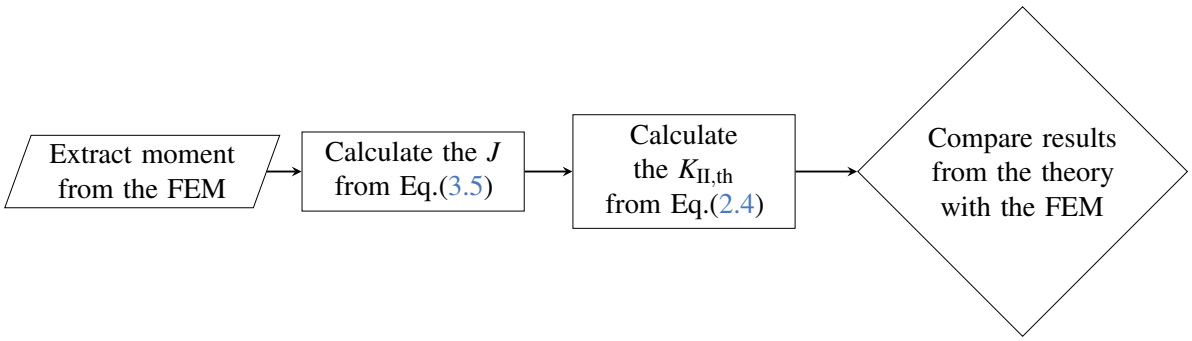

Figure 3.23: The flowchart for calculating $K_{\text{II,th}}$ from the J integral.

Table 3.9: The J integral and SIF values for mode II.

Problem condition	Element at the crack tip	$J/\sigma_b H$	K_{I}	$K_{\mathrm{II,th}}/K_{\mathrm{II,FE}}$
Plane stress	Triangular	0.0005	0	0.9998
	Rectangular	0.0005	0	0.9998
Plane strain	Triangular	0.0005	0	0.9999
	Rectangular	0.0005	0	0.9998

The normalized in-plane shear stress, σ_{12}, versus the normalized crack ligament coordinate for the plane stress are plotted in figures 3.24 and 3.25

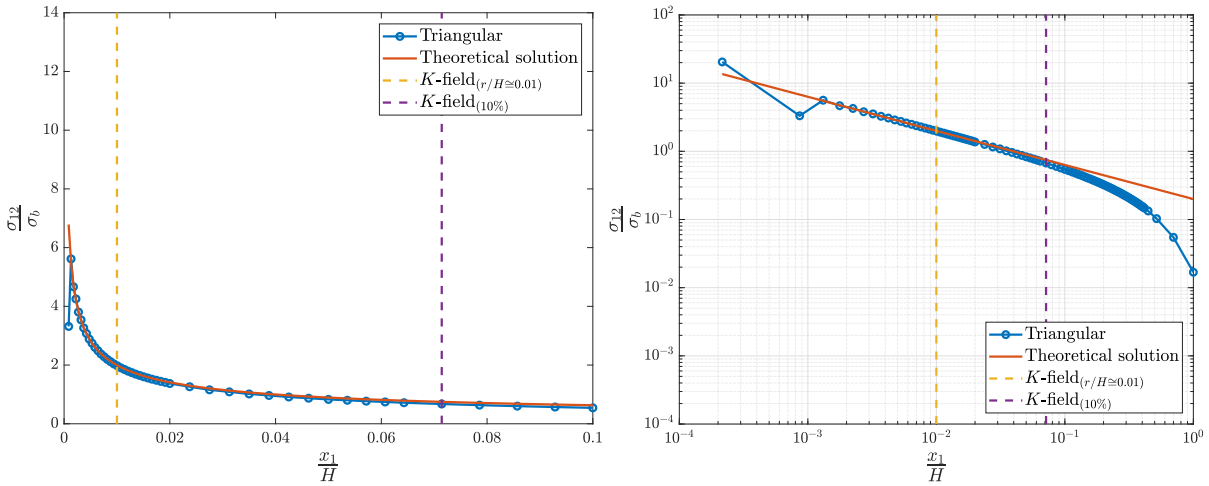

Figure 3.24: (a) Asymptotic (b) Logarithmic σ_{12} along the crack ligament for the plane stress condition with the triangular elements at the crack tip ($\theta = 0$).

Figure 3.26 and 3.27 provide an overview of the asymptotic and logarithmic of σ_{12} along the crack ligament.

As the plots indicate, with the same number of elements around the crack tip, the rectangular elements are able to capture the singularity better than the triangular, where the triangular elements fail to follow the theoretical asymptotic solution. In the logarithmic scale from the very first elements, the rectangular elements can create a linear behavior while at least, the first element in the triangular elements, σ_{12} does not correspond to the theory.

The singularity exponent for the mode II can be defined by Eq.(3.6).

$$\sigma_{12} = r^{\lambda} \tag{3.6}$$

The obtained values for λ are presented in table 3.10. The values are extracted by a power curve fit to the first 30 elements (ignoring the first element at the crack tip) in front of the crack tip. Another curve fitting study with a finer mesh ,*ne*=24, produces better results for the λ with the triangular elements, although no improvement is observed in the asymptotic solution.

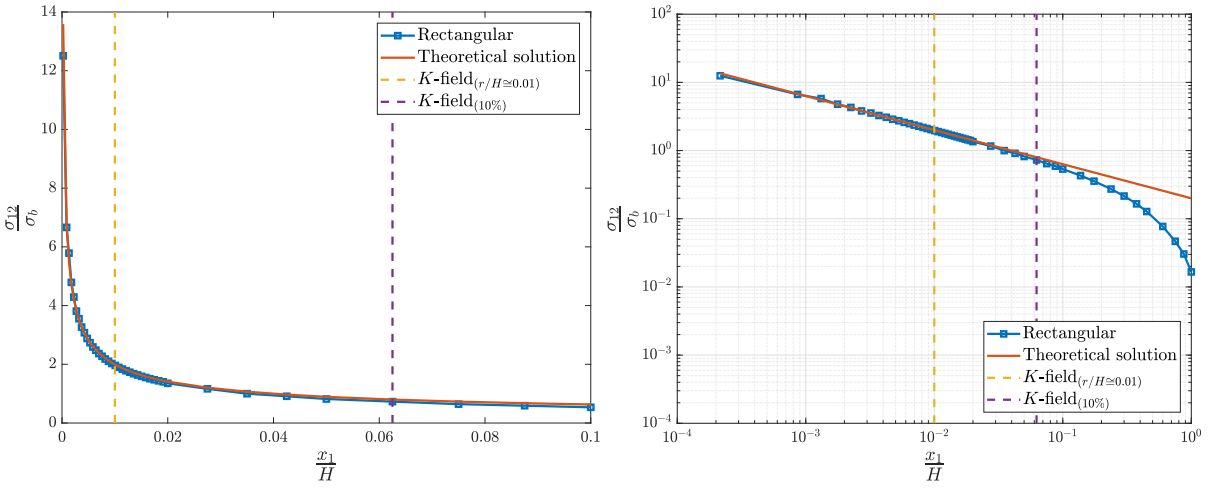

Figure 3.25: (a) Asymptotic (b) Logarithmic σ_{12} along the crack ligament for the plane stress condition with the rectangular elements at the crack tip ($\theta = 0$).

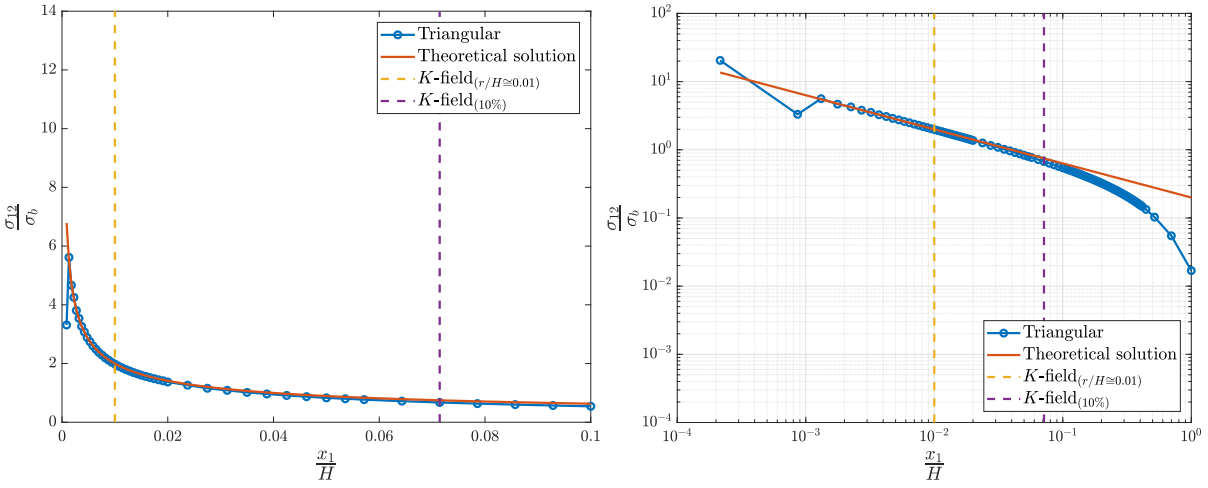

Figure 3.26: (a) Asymptotic (b) Logarithmic σ_{12} along the crack ligament for the plane strain condition with the triangular elements at the crack tip ($\theta = 0$).

Table 3.10: λ values for the two-dimensional mode II.

Problem condition	**Element at the crack tip**	$\lambda(ne = 16)$	$\lambda(ne = 24)$
Plane stress	Triangular	-0.5202	-0.5083
	Rectangular	-0.4891	-0.5239
Plane strain	Triangular	-0.5200	-0.5082
	Rectangular	-0.4866	-0.5260

A comparison between the σ_{12} contours for the plane stress and plane strain, figures 3.28

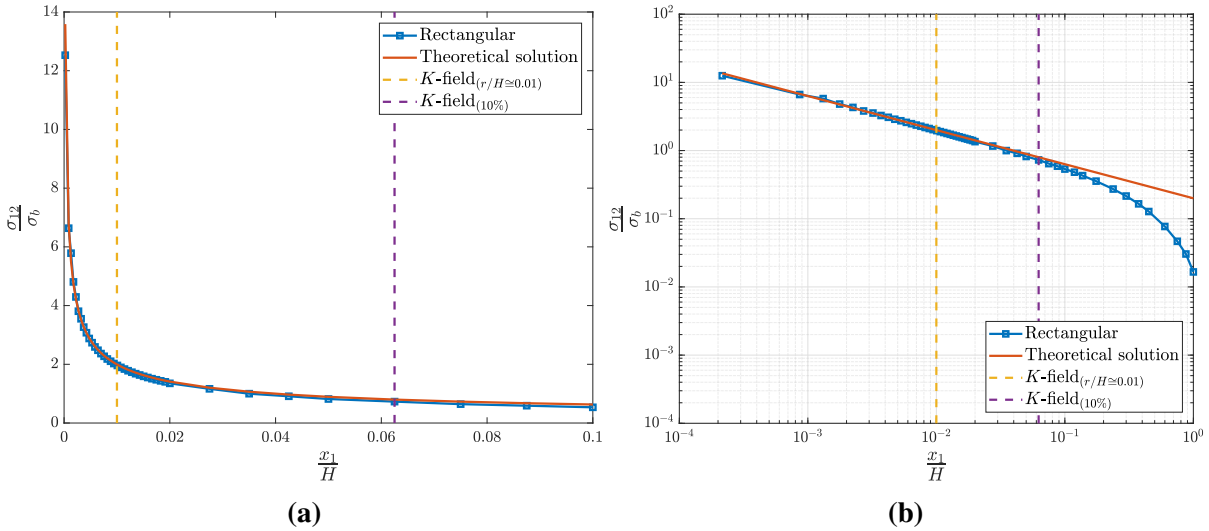

Figure 3.27: (a) Asymptotic (b) Logarithmic σ_{12} along the crack ligament for the plane strain condition with the rectangular elements at the crack tip ($\theta = 0$).

and 3.29, implies higher stress values for the thicker specimen.

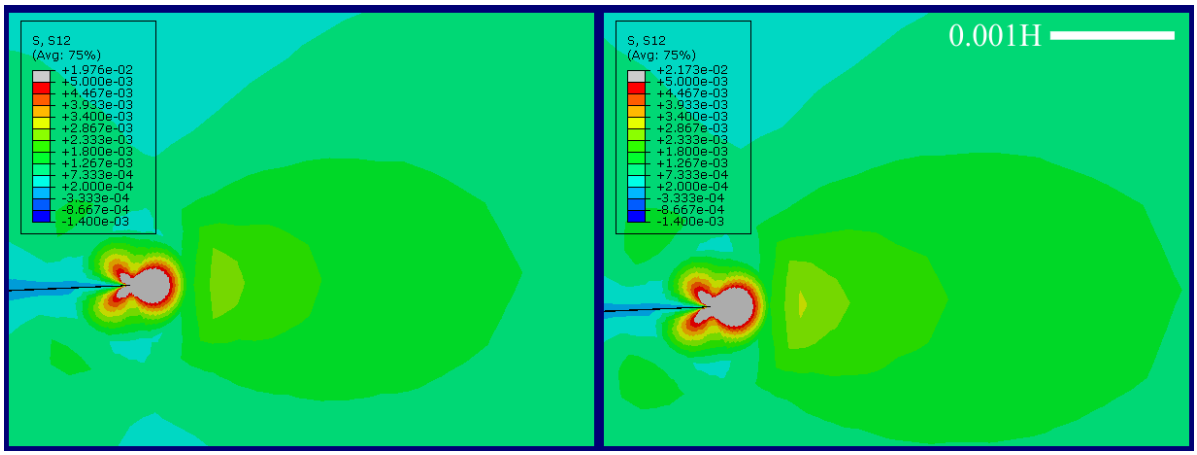

Figure 3.28: The σ_{12} contours under lane stress (left) plane strain (right) conditions using the triangular element at the crack tip.

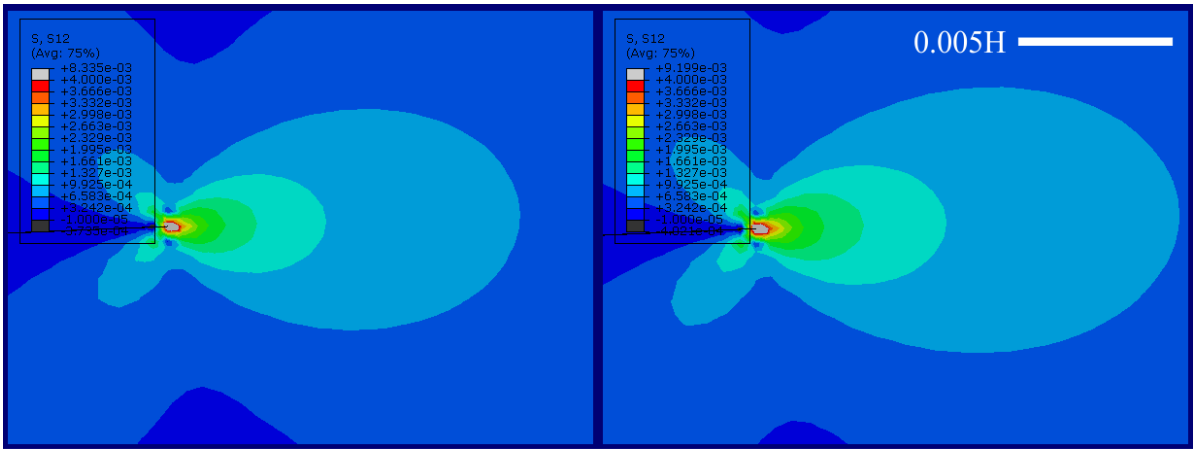

Figure 3.29: The σ_{12} contours under lane stress (left) plane strain (right) conditions using the rectangular element at the crack tip.

3.3 Collapsed against non-collapsed elements at the crack tip

Achieving asymptotic solution, Barsoum (1977) suggested not only to shift the mid-nodes of the elements at the crack tip to the quarter point in the direction of the crack but also to collapse the nodes at the crack tip. He also attributed the poor result of the rectangular elements to the generation of singularity on the boundary of these elements.

The two-dimensional analysis of the mode I and II provided the opportunity to explicitly compare the collapsed (triangular) and non-collapsed (rectangular) elements at the crack tip. To study the effect of each element type at the crack tip, all the stress components are extracted on the crack plane (θ=0) for pure mode I, figure 3.31, for a very small distance ahead of the crack tip where the K-dominated zone is guaranteed. According to the theory (Eq. (A.1)) under mode I, $\sigma_{11} = \sigma_{22}$ in the K-dominated zone on the crack plane (θ=0). Comparing the stress from the FEM to the theory, figure 3.31, clearly shows that for the triangular elements at the crack tip, $\sigma_{22,FE} = \sigma_{22,th}$ follow each other while a difference between the obtained $\sigma_{11,FE}$ and $\sigma_{22,th}$ is visible (figure 3.31(a) and (b)) that is not vanished with a higher mesh density around the crack tip. In contrast to the analytic solution for the triangular elements , $\sigma_{11,FE} \neq \sigma_{22,FE}$. There is no agreement among $\sigma_{11,FE}$, $\sigma_{22,FE}$ and $\sigma_{22,th}$ for the rectangular elements at the crack tip (figure 3.31(c) and (d)).

Another weak point about the rectangular elements is the presence of maximum four elements around the crack tip (figure 3.4(b)) which provides poor calculation of the stresses at different angles around the crack tip. However, the triangular elements can be generated in higher numbers at the crack tip (figure 3.4(a)) that comes with the shortcoming of poor aspect ratios for the triangular elements. To provide an overview of the above-mentioned lines, σ_{22} is plotted for mode I-plane stress condition in figure 3.30. The rectangular elements are un-

able to provide good results for σ_{22} while the triangular elements can follow the theoretical solution from Eq.(A.1).

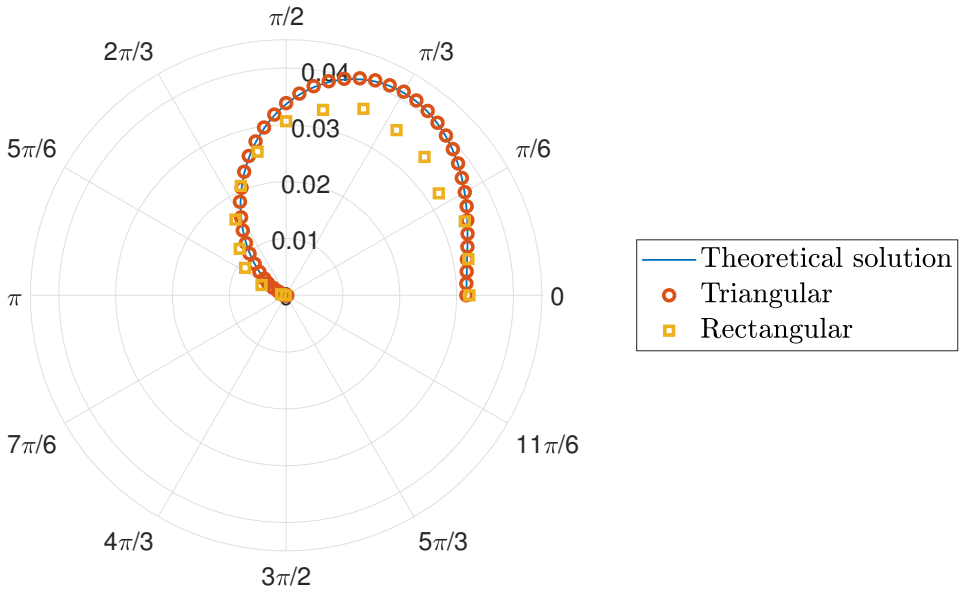

Figure 3.30: The normalized σ_{22} with E extracted in the x_1-direction within a radial distance of r=14.77μm around the crack tip from mode I-plane stress.

ABAQUS counters the mesh generation for the triangular elements at the crack tip with a higher mesh density; therefore, a finer mesh (ne >24) cannot be accomplished with this type of elements at the crack tip. Based on the above-mentioned observations and the suitability of the triangular elements at the crack tip, shown by Barsoum (1977), Barsoum (1976), Pontjo Utomo and Hamid R. Nikraz (2007), the analysis in the next chapter for the three-dimensional case of the mode I and II will be continued by the triangular elements at the crack tip (this topic will be further discussed in section 4.1.3).

Barsoum (1977) attributed the inappropriateness of the rectangular elements at the crack tip to their poor calculation of the SIF, although according to the aforementioned lines, the weakness of the rectangular elements at the crack tip might be due to their weakness in the stress calculation which requires further research in this field. Table 3.11 summarizes the finding from the FE analysis of the DCB specimen under pure mode I and II loading.

Despite the poor aspect ratio (but not larger than 1:10) in the triangular elements compared to the rectangular, the triangular elements capture the singularity and the SIF accurately. It is also noteworthy that the element aspect ratio differs from one problem to another and as to the author's knowledge, does not always result in wrong FE calculation.

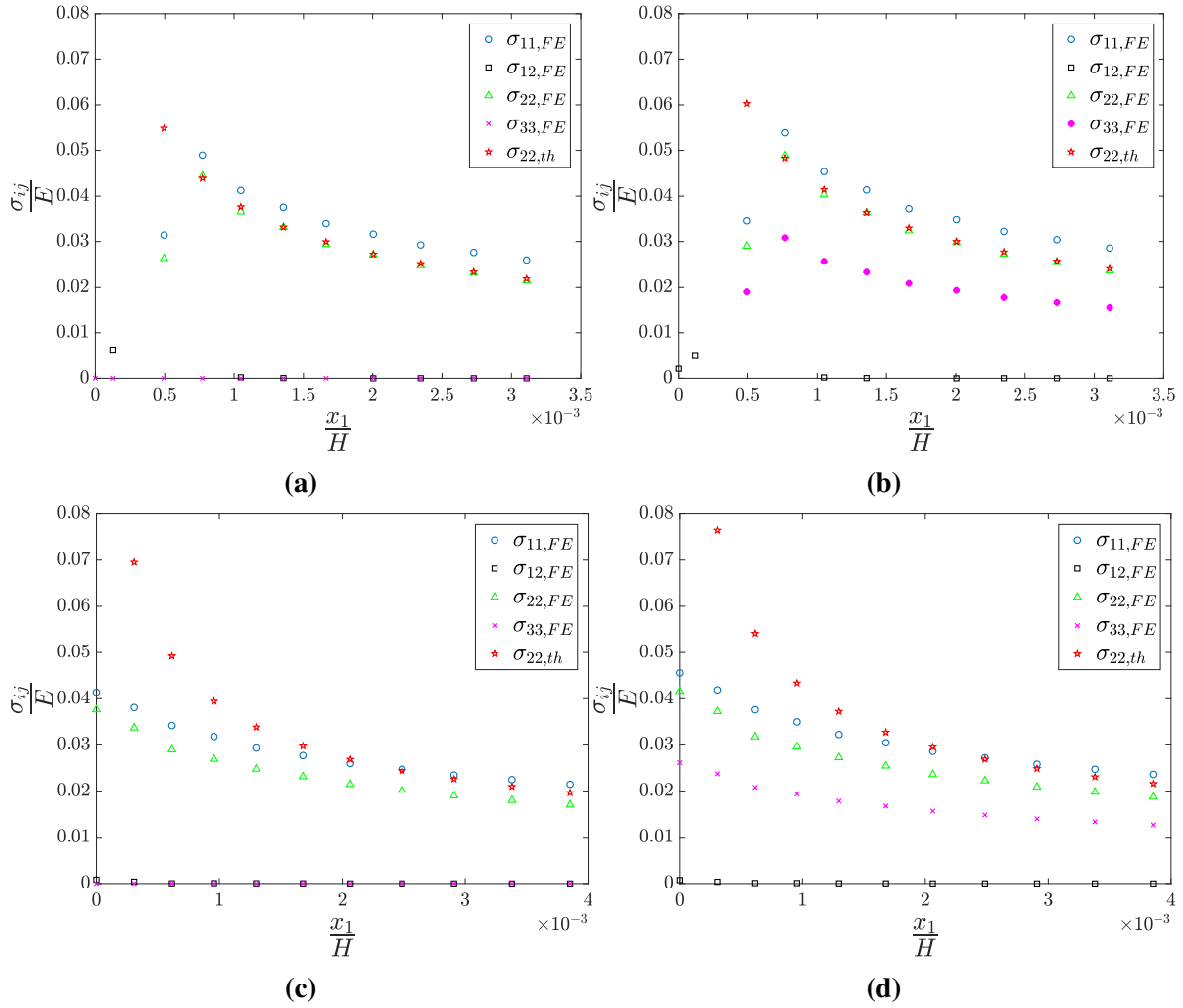

Figure 3.31: Stress components along the crack ligament in the mode I. (a) Triangular elements-plane stress (b) Triangular elements-plane strain (c) Rectangular elements-plane stress (d) Rectangular elements-plane strain.

Parameter	Triangular element	Rectangular element
Stress calculation along the ligament	Good	Poor
Aspect ratio	Poor	Good
Capturing singularity	Good	Good
Near-crack mesh generation	Medium	Good
Stress for different angles at the crack tip	Good	Poor

Table 3.11: The collapsed against the non-collapsed elements at the crack tip.

CHAPTER 4
Three-dimensional analysis of Mode I and Mode II

This chapter covers the three-dimensional FE model for the mode I and II. After achieving the proper mesh size in two-dimensions, the proper mesh size in the width direction needs to be determined. Furthermore, the SIF which is a two-dimensional concept can be evaluated in the three-dimensional. The developed FE model from this chapter will be used in the subsequent chapters as the fundamental model for the analyses of mode III.

4.1 Mode I

4.1.1 Finite Element Model

First, to avoid the effect of boundary condition on the crack front and secondly, to create a beam-like specimen, the specimen dimensions are set to $a_0 = 5H$, $L = 30H$ and $B = 10H$ where B is the specimen width depicted in figure 4.1. Due to symmetry in both geometry and loading, only a quarter of the DCB specimen is enough for the FE model (figure 4.2). In the FE model, the translational degree of freedom at the right end and along the crack ligament are limited in the x_1 and x_2-direction, respectively. In addition, the symmetry in the x_3-direction is fulfilled by applying u_3=0. Similar to the two-dimensional model, the Reference Point (**RP-1**) rotation, indicated in figure 4.2, is transferred through the **Rigid body constraint** to the specimen. The reaction moment will be extracted from the **RP-1** in the post-processing.

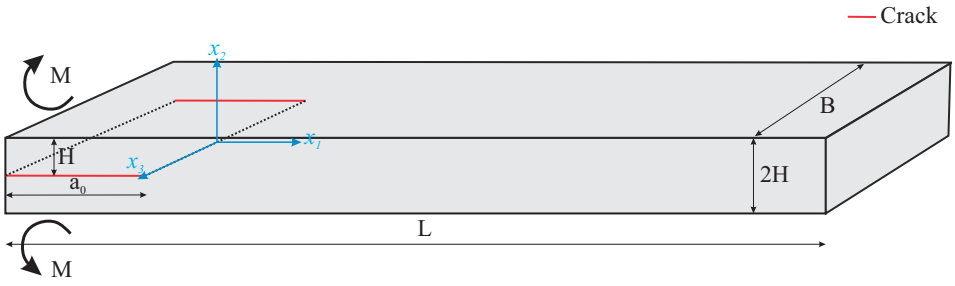

Figure 4.1: The geometry and loading of the three-dimensional DCB specimen under mode I.

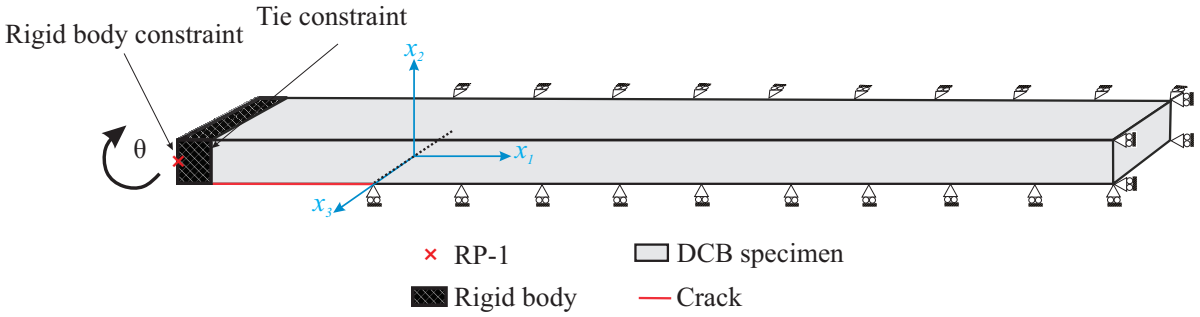

Figure 4.2: The three-dimensional DCB specimen FE model under mode I.

An isotropic material with the same mechanical properties from the two-dimensional analysis is assumed (E=200GPa, G=80GPa and ν=0.3).

4.1.2 Element

The plane stress and plane strain conditions cannot be differentiated in the three-dimensional model since the specimen undergoes a combination of both of them. Hence, an element from the quadratic **3D Stress** family is selected. There are two elements in this family shown in figure 4.3.

C3D20: 20-node quadratic

C3D20R: 20-node quadratic Reduced integration

The quadratic elements are suitable for contour integrals as well as Linear Elastic problems. In this study, the reduced version, C3D20R, will be used. C3D20R has 20 nodes and 8 integration points and by fining the mesh close to the crack front, the reduced version can succeed in calculating the stress accurately.

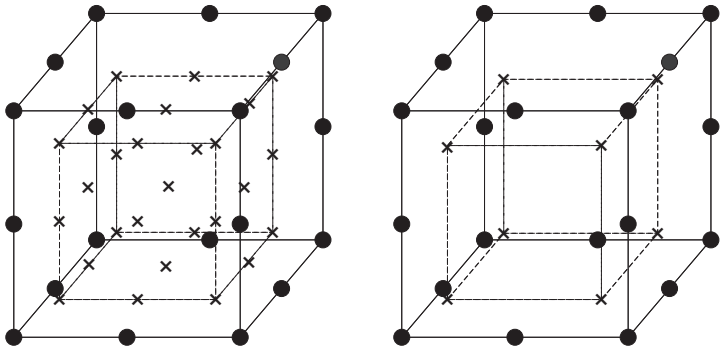

Figure 4.3: C3D20 (left) and C3D20R (right) elements.

4.1.3 Triangular (Collapsed) elements at the crack front revisited

For the elements at the crack front, there are two possible choices similar to the two-dimensional. One is the triangular (collapsed) and another is the rectangular (non-collapsed) element. After accomplishing reasonably-fine mesh (which will be elaborated in the next section), the stress components are plotted along the crack width, figure 4.4. "0" and "1" on the horizontal axis correspond to the specimen center and the free surface, respectively.

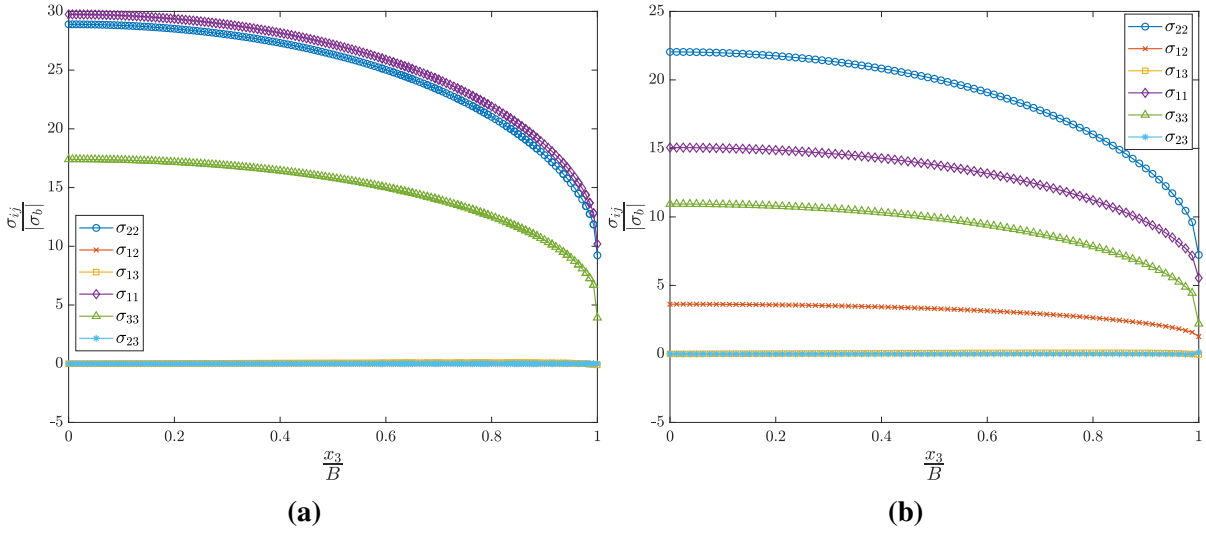

Figure 4.4: Different stress components along the crack width in mode I. (a) triangular (collapsed) and (b) rectangular (non-collapsed) elements. The results are extracted from the distance of x_1=3.125μm from the crack front and at the crack plane (x_2=0).

According to the explanation provided in section 3.3, and figure 4.4(a), σ_{11} and σ_{22} are very close along the crack front for the triangular elements. In contrast, for the rectangular elements at the crack front (figure 4.4(b)), σ_{11} and σ_{22} discrepancy increases from the free surface to the center along the specimen width. The stresses have been plotted for several coordinates (x_1=3.125μm, 2.5μm and 1.66μm) in front of the crack, along the crack plane for the rectangular elements and every time they yield the same trend as shown in figure 4.4(b)[1]. From now on, according to the above-mentioned lines and discussion in section 3.3, the analyses will be performed by the triangular (collapsed) elements at the crack front.

[1] Although it is clear that by getting far from the crack tip, the K-dominated zone vanishes and LEFM is not applicable.

4.1.4 Mesh

4.1.4.1 Mesh strategy

To apply the mesh transition along the width and height simultaneously, the specimen is broken into several parts that are assembled using the **Tie** constraint, as shown in figure 4.5. The red lines indicate the applied **Tie** constraints. To remove the possibility of discontinuities in the contour integral calculated by ABAQUS, all the first 10 integral contours stays within the first part. The maximum mesh transition is 1:4. Figure 4.6 provides an overview of the mesh quality in the vicinity of the crack and mesh transition.

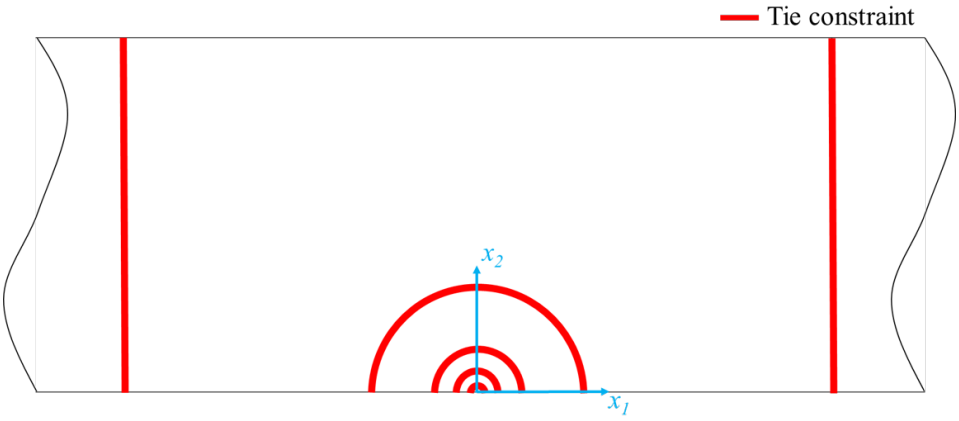

Figure 4.5: The three-dimensional DCB specimen consists of several parts assembled by the **Tie** constraint.

4.1.4.2 Mesh convergence

Due to the failure of the "10% stress field" criterion (Eq.(3.1)) in the three-dimensional, it is replaced with the "Stress triaxiality coefficient", T_z, and is defined according to Eq.(4.1).

$$T_z = \frac{\sigma_{33}}{\sigma_{11}+\sigma_{22}} = \begin{cases} \dfrac{\nu(\sigma_{11}+\sigma_{22})}{\sigma_{11}+\sigma_{22}} = \nu & \text{For mode I if } \theta = 0 \\ \dfrac{\nu(\sigma_{11}+\sigma_{22})}{\sigma_{11}+\sigma_{22}} = \nu & \text{For mode II if } \theta = 90^{o} \end{cases} \tag{4.1}$$

T_z for mode I and in the crack plane ($\theta = 0$) is equal to the Poisson's ratio (Eq. (A.1)) under the plane strain condition. If the plane strain prevails, for mode II when θ =90^{o}, T_z and ν are equal (Eq. (A.2)). In addition, T_z is a measure of the sufficient number of elements, especially at the free surface which will be discussed later in this section.

Performing the mesh study for K_{I} with two lengths of the pre-existing crack, (a) $a_0 = 15H$ and (b) $a_0 = 5H$, it is conceded that for a thin specimen with the longer pre-crack length, K_{I} becomes negative at the free surface which implies undesired crack closure in mode I. After

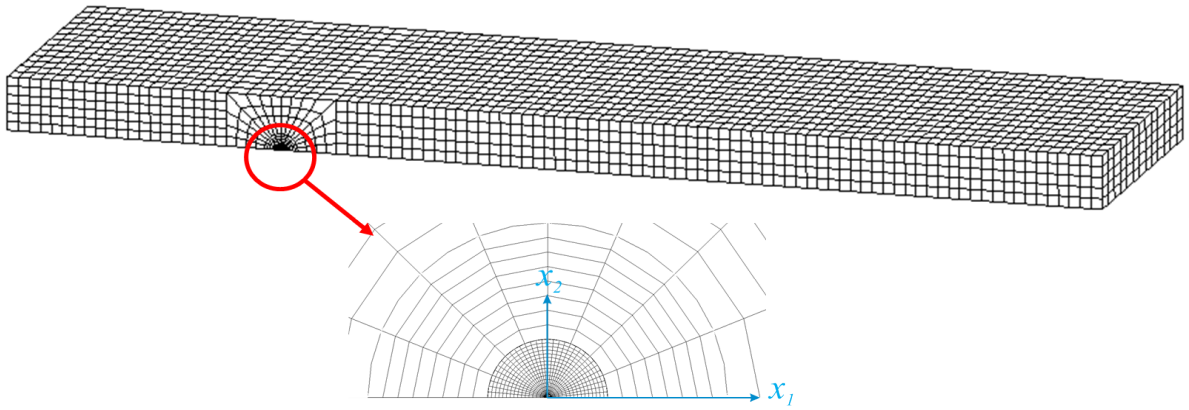

(a)

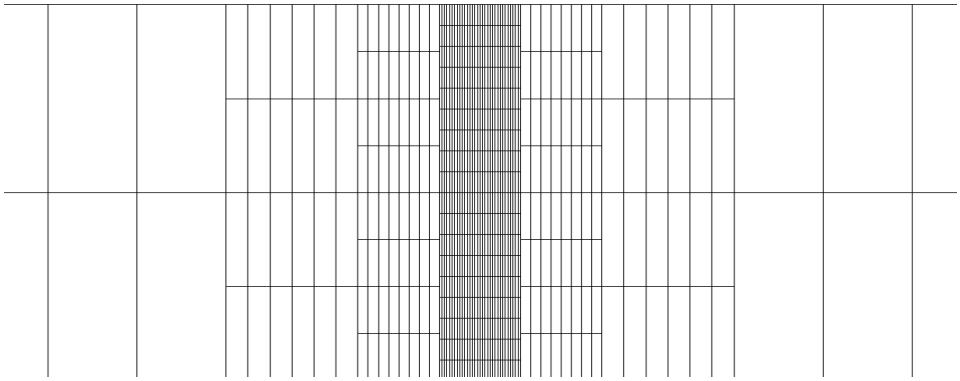

(b)

Figure 4.6: The mesh quality and transition in the three-dimensional model. (a) isometric and front view (b) bottom view.

all, K_{I} convergence is highly dependent on the $\frac{B}{H}$ ratio where only for the ratios more than 8, K_{I} relative error from the FEM and theory converges to less than a percent. Figure 4.7 summaries the above-mentioned lines.

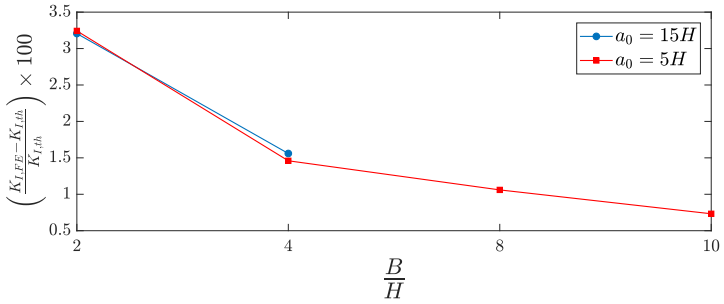

Figure 4.7: K_{I} mesh convergence for different $\frac{B}{H}$ ratios and two pre-crcak length, $a_0 = 15H$ and $a_0 = 5H$. The last two values of the relative error are not given due to negative values of K_{I} at the free surface.

The same number of elements along the crack ligament from the two-dimensional model

will be used and only the number of elements along the crack front varies. The mesh convergence study is presented in table 4.1 and figure 4.8. Here, *ne* refers to a cylinder with the radius of $0.02H$ and a height equal to the specimen width.

Table 4.1: The Mode I mesh convergence in three-dimensions.

ne	$\left\lvert\frac{K_{\mathrm{I,th}}-K_{\mathrm{I,FE}}}{K_{\mathrm{I,th}}}\right\rvert \times 100$	$\lvert\nu - T_z\rvert$	$u_2/u_{2,th}$ **relative error [%] in the middle**	$u_2/u_{2,th}$ **relative error [%] at the free surface**
204800	0.7324	0.0114	-	-
256000	0.5891	0.0190	0.1619	0.0052
341248	0.7324	0.0180	0.1588	0.0005

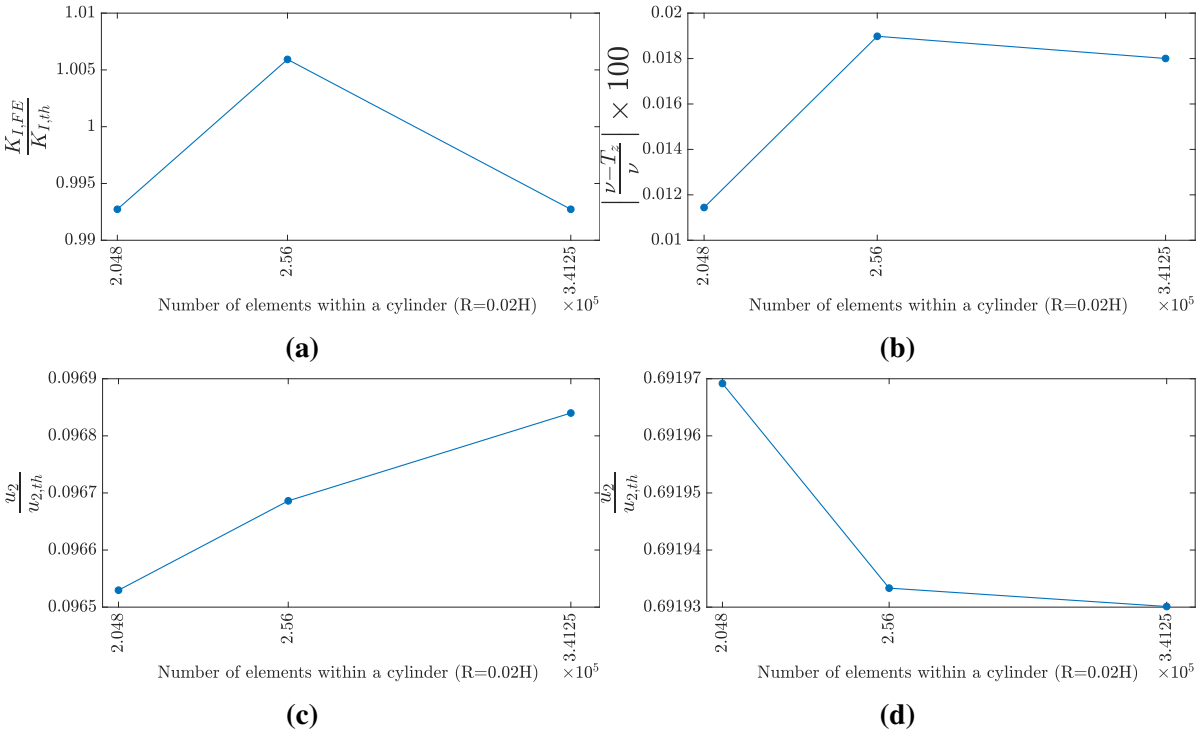

Figure 4.8: Mode I mesh convergence in the three-dimensional. (a) K_{I} (b) ν and T_z relative error (c) u_2 and $u_{2,th}$ at the free surface ($x_3 = \frac{B}{2}$), x_1=0.02H and θ=0 (d) u_2 and $u_{2,th}$ at the center ($x_3 = 0$), x_1=0.02H and θ=0.

As mentioned at the beginning of this section, T_z can provide the quality of the mesh at the free surface. Having plotted the T_z along the crack front for various *ne*, figure 4.9, one can observe more elements are required at the free surface (red box) due to the jump in T_z for the last element. T_z is constant and approximately close to the Poisson's ratio along the 90% of the width; however, by reaching the free surface the plane stress condition becomes pronounced and T_z drops. ABAQUS could not manage the model with higher mesh density since the number of output parameters exceeds the software defaults; hence, the mesh with *ne*=341248 is accepted for the mode I FE analysis.

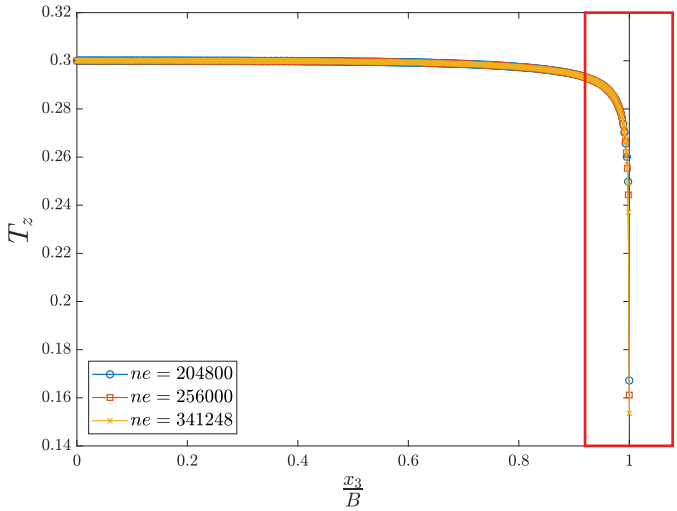

Figure 4.9: Distribution of T_z through the specimen width in mode I ($x_1 = 3.125\mu$m, $x_2 = 0$).

4.1.4.3 Element size

The smallest element dimensions, available at the crack front, are given in table 4.2. Figure 4.10 illustrates the element dimensions.

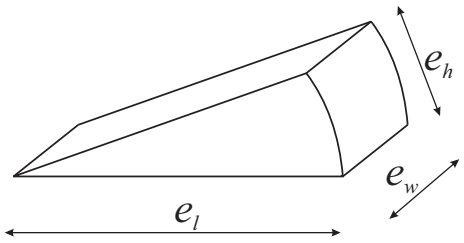

Figure 4.10: The geometry and dimension of the collapsed element at the crack front in three-dimensions.

Table 4.2: Three-dimensional mode I smallest element dimensions.

Parameter	Dimension
e_h[mm]	1.227E-03
e_h/H	1.227E-04
e_w[mm]	75.00E-03
e_w/H	0.0075
e_l[mm]	12.50E-03
e_l/H	0.0013
e_h/e_l	0.0982
e_w/e_l	6.000
e_h/e_w	0.0164

4.1.5 Result and discussion

The procedure of calculating $K_{\mathrm{I,th}}$ follows the same formulation mentioned in the two-dimensional analysis. The results are presented in table 4.3. Pure mode I is achieved and the normalized SIF together with the stress components are plotted along the normalized crack width in figure 4.11.

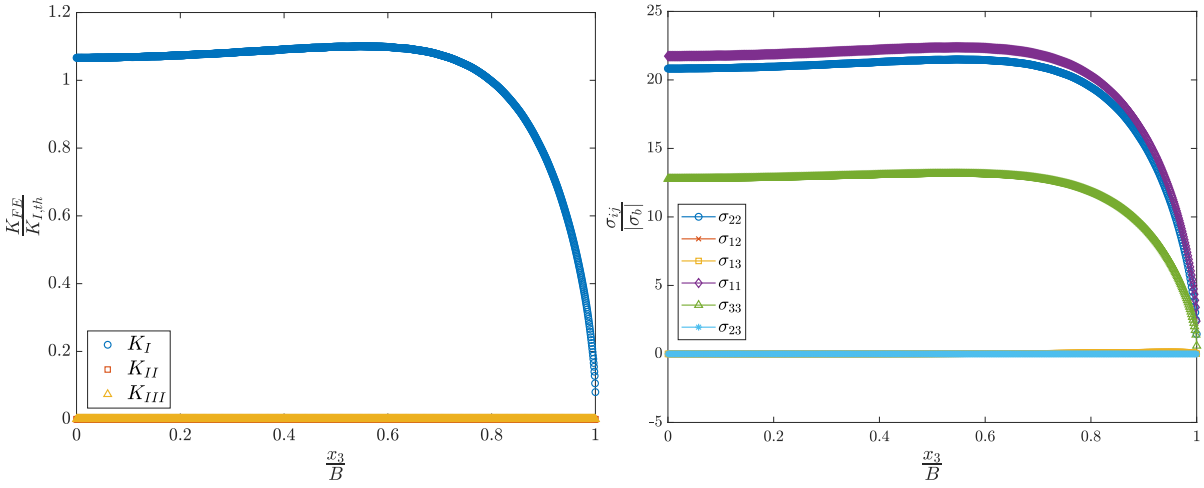

(a) **(b)**

Figure 4.11: (a) SIF (b) stress components (at $x_1 = 3.125\mu$m and $x_2 = 0$) along the crack front for mode I.

Table 4.3: The J integral and SIF values for the three-dimensional mode I.

$J/\sigma_b L$	$K_{\mathrm{I,th}}/K_{\mathrm{I,FE}}$	K_{II}	K_{III}
0.0018	0.9996	0	0

The stresses in figure 4.11 are extracted at the distance of $3.125\mu m$ ahead of the crack. Looking at σ_{11} and σ_{22} reveals that the K-dominated zone size is much smaller than $0.01H$ predicted by Charalambides et al. (1992) and $4\mu m$ reported by Pook et al. (2014). Another study was performed to find the exact size of the K-dominated zone where $\sigma_{11} = \sigma_{22}$ and it was concluded that even at the distance of $1.66\mu m$, σ_{11} and σ_{22} are not equal. In the present work, it is assumed that the K-dominated zone is achieved when $|\sigma_{11} - \sigma_{22}| < 10\%$ which is accomplished within the distance of $x_1 = 3.125\mu$m.

The asymptotic and the logarithmic normalized σ_{22} along the normalized crack ligament are plotted in figures 4.12 and 4.13. There are several noteworthy observations regarding these plots:

- At the normalized distance of 0.005 from the crack tip in figure 4.12(a), σ_{22} is compressive and therefore, in the corresponding logarithmic scale, the negative σ_{22} does not appear.

- Unfortunately, it is impossible to increase the number of elements in the x_3-direction due to the previous issue with the number of outputs and exceeding the allowable number of elements (a million).
- Another limitation is the width to the height ratio which resembles the specimen to a plate rather than a beam.

At the center, however, there is no compression. Another important observation is the dramatic drop in σ_{22} at the mid-nodes of the collapsed elements at both the free surface and center. This might be attributed to the quarter point shift in the mid-nodes of the first row of the elements at the crack front. Surprisingly, the mide-node of the first element value corresponds to the theoretical σ_{22}.

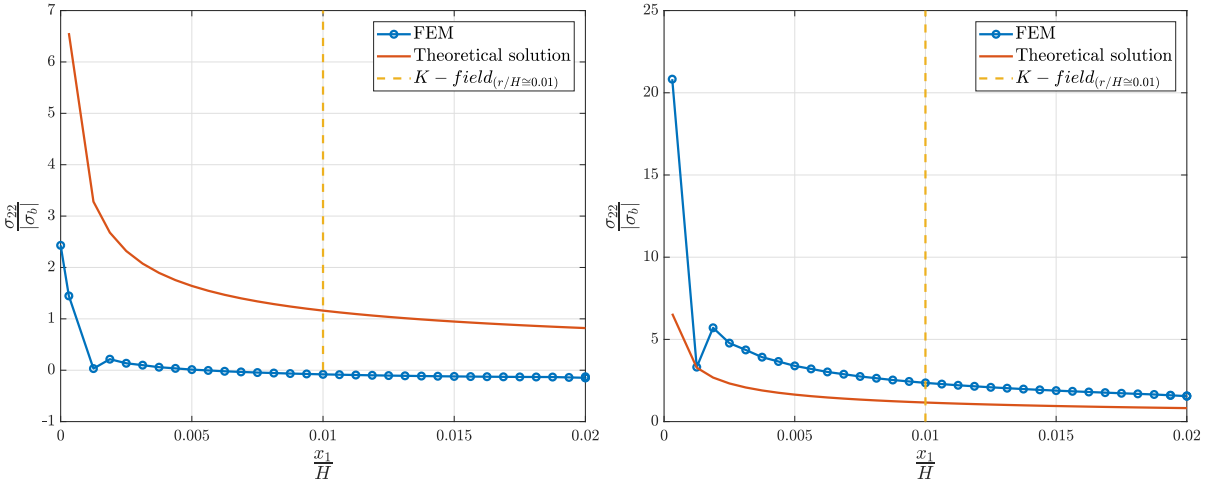

Figure 4.12: Asymptotic σ_{22} (a) at the free surface ($x_3 = \frac{B}{2}$) (b) in the center ($x_3 = 0$) along the crack ligament ($\theta = 0$).

The singularity exponent is extracted from a power curve fit to σ_{22} along the crack ligament at the free surface and in the center (figure 4.13) wherein the former corresponds to the plane stress and the latter to the plane strain. As shown in table 4.4, the singular field is achieved in the center in contrast to the free surface. Another study can determine the exact distance from the free surface where the singular field breaks and of course is out of the scope of the present project.

Table 4.4: λ values for three-dimensional Mode I at $\theta = 0$ (free surface and center correspond to $x_3 = \frac{B}{2}$ and $x_3 = 0$, respectively).

Free surface	Center
-2.010	-0.5242

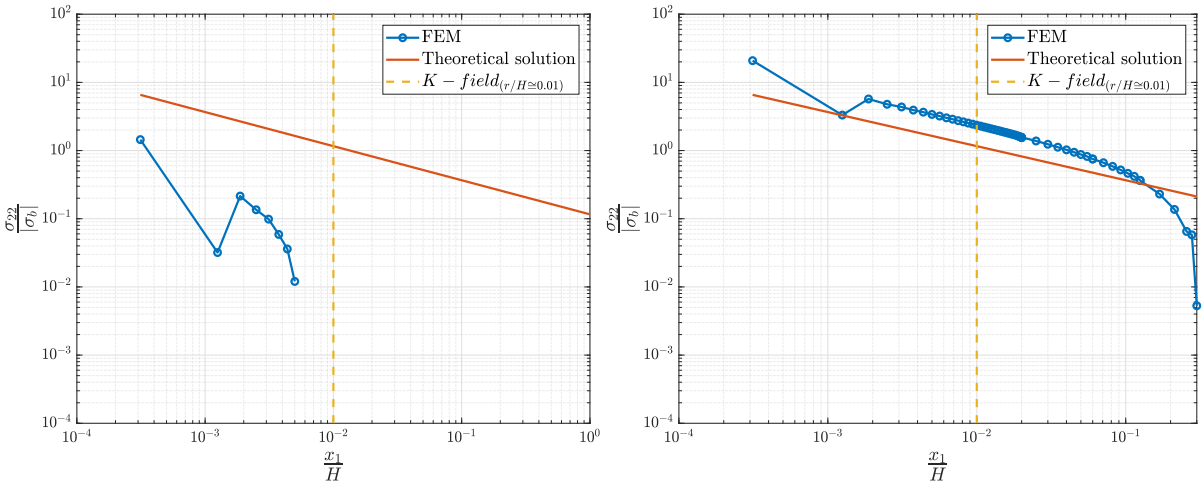

Figure 4.13: Logarithmic σ_{22} (a) at the free surface ($x_3 = \frac{B}{2}$) (b) in the center ($x_3 = 0$) along the crack ligament ($\theta = 0$).

The σ_{22} contours, figure 4.14, show higher stress values due to higher stress triaxiality compared to the free surface (lower triaxiality) (T.L.Anderson, 2004).

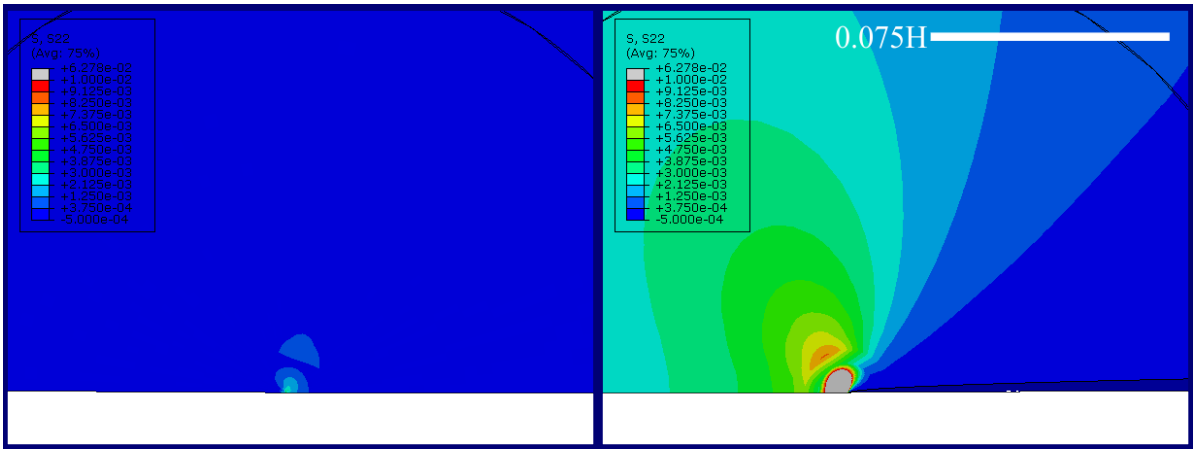

Figure 4.14: Mode I σ_{22} contours at the free surface ($x_3 = \frac{B}{2}$, left) and in the center ($x_3 = 0$, right).

4.2 Mode II

4.2.1 Finite Element Modeling

The complete mode II model is shown in figure 4.15. Because of the symmetry in the geometry, half of the specimen suffices the FE modeling (figure 4.16). To fulfill the symmetry, the specimen is chopped into half in the x_3-direction and clamped at the right end like a

cantilever beam. The dimensions are $a_0 = 15H$, $L = 30H$ and $B = 2H$. After the successful mesh convergence for the half-model, the complete model will be used for extracting the SIF and stress plots. The material and elements remain the same as mode I.

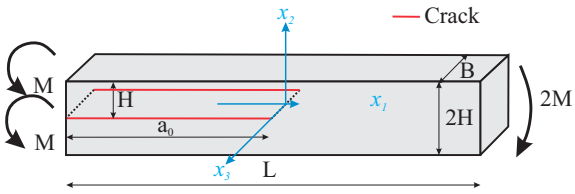

Figure 4.15: The geometry and loading of the three-dimensional DCB specimen under mode II.

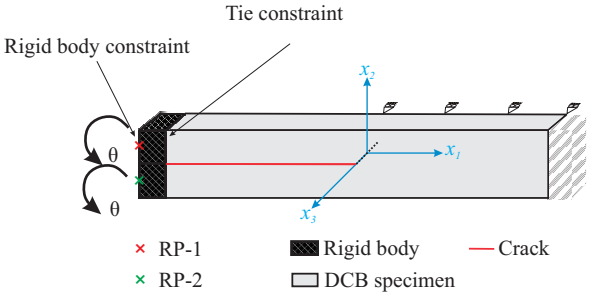

Figure 4.16: The three-dimensional DCB specimen FE model under mode II.

4.2.2 Mesh

4.2.2.1 Mesh convergence

The mesh criteria in the three-dimensional model for mode II are similar to the tow-dimensional study; however, as mentioned earlier in this chapter, the "10% stress field" is replaced with the stress triaxiality coefficient, T_z. The mesh study plots are given in figure 4.17 and table 4.5.

Table 4.5: The Mode II mesh convergence in three-dimensions.

ne	$\left\lvert\frac{K_{\text{II,th}}-K_{\text{II,FE}}}{K_{\text{II,th}}}\right\rvert \times 100$	$\lvert\nu - T_z\rvert$	$\Delta u_1/\Delta u_{1,th}$ **relative error [%] in the middle**	$\Delta u_1/\Delta u_{1,th}$ **relative error [%] at the free surface**
81920	0.8980	0.0537	-	-
102400	0.8912	0.0540	0.0124	0.0504
136704	0.4821	0.0539	0.0227	0.0140
204800	0.8958	0.0540	0.0410	0.0012
409600	0.8911	0.0540	0.0671	0.0145
819200	0.8961	0.0541	0.0147	0.0058

Although the mesh size can be immediately determined from figure 4.17 and table 4.5, the mesh quality at the free surface is another essential requirement for the final decision. To this end, T_z is plotted for different number of elements, *ne*, at the angle of $\theta = 90^o$ along the crack front. As demonstrated in figure 4.18 some of the element sizes, i.e., *ne*=81920, *ne*=102400 and *ne*=136704 are incapable of capturing the stress at the free surface. Concerning the obtained result, *ne*=204800 is chosen for the mode II FE analysis.

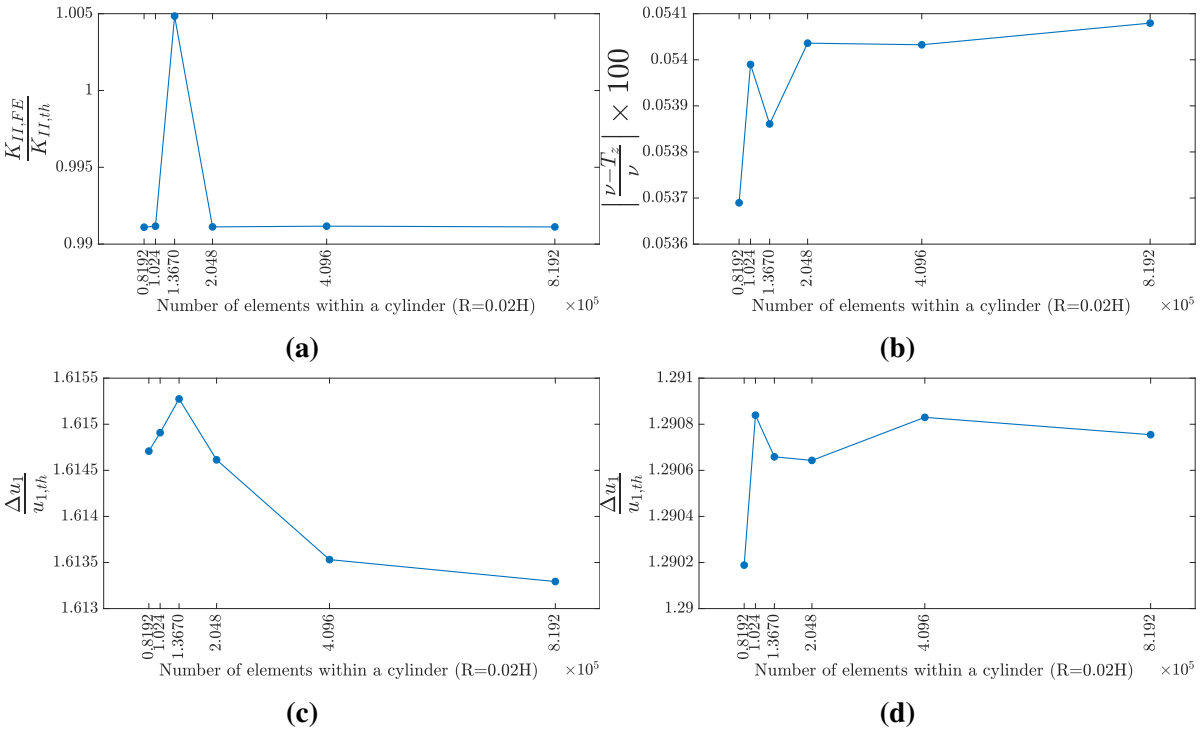

Figure 4.17: Mode II mesh convergence in the three-dimensional. (a) K_{II} (b) ν and T_z relative error (c) Δu_1 and $u_{1,th}$ at the free surface ($x_3 = \frac{B}{2}$), x_1=0.02H and θ=0 (d) Δu_1 and $u_{1,th}$ at the center ($x_3 = 0$) x_1=0.02H and θ=0.

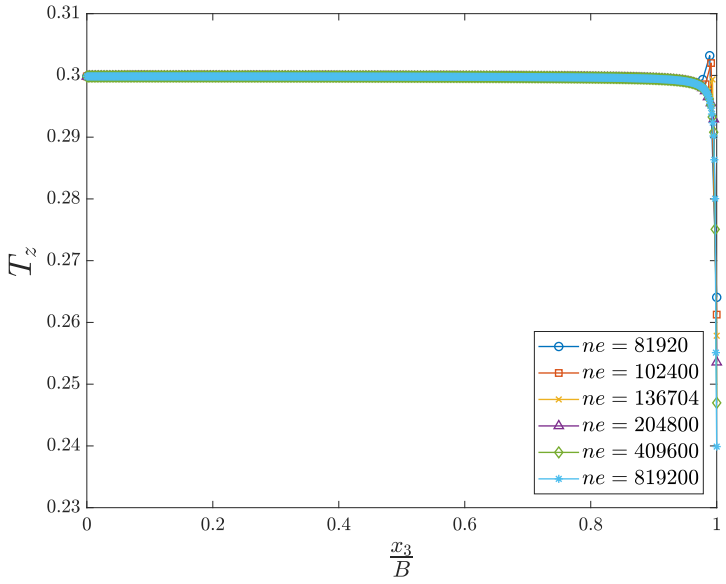

Figure 4.18: Distribution of T_z through the specimen width in mode II ($x_1 = 3.125\mu$m, $x_2 = 0$).

4.2.2.2 Elements size

Table 4.6 summarizes the dimensions of the smallest element size, present at the crack front, for mode II.

Table 4.6: Three-dimensional mode II smallest element dimensions.

Parameter	Dimension
e_h[mm]	12.50E-03
e_h/H	12.50E-04
e_w[mm]	50.00E-03
e_w/H	0.0050
e_l[mm]	1.227E-03
e_l/H	1.227E-04
e_h/e_l	10.19
e_w/e_l	40.75
e_h/e_w	0.2500

4.2.3 Result and discussion

To calculate $K_{\mathrm{II,th}}$, the same steps from figure 3.23 apply. The SIF and stress components along the crack front are plotted in figure 4.19.

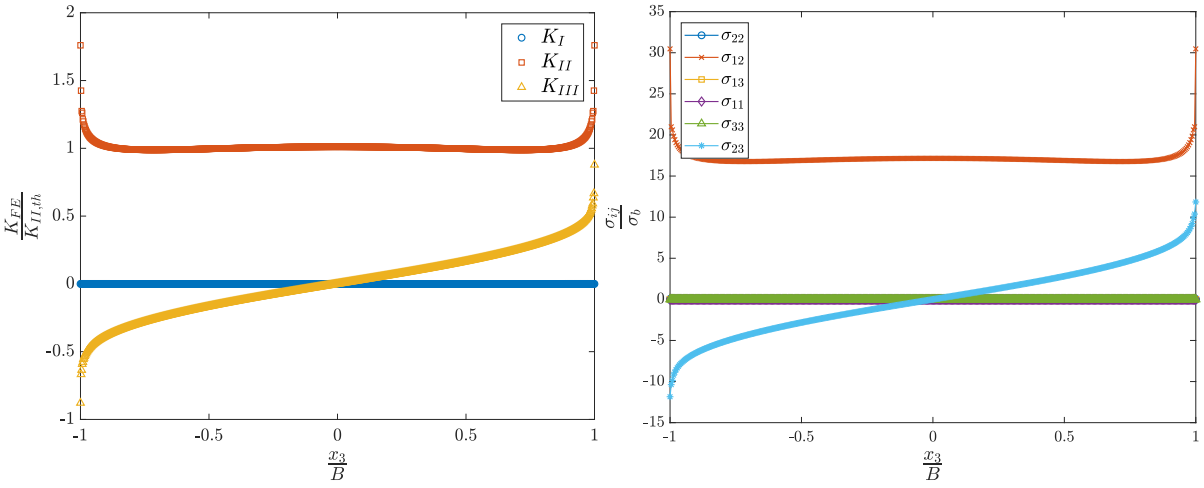

(a) **(b)**

Figure 4.19: (a) SIF (b) stress components (at $x_1 = 3.125\mu$m and $x_2 = 0$) along the crack front for mode II.

The mode-mixity with the predominant mode II is visible. $K_{\mathrm{II,FE}}$ is constant along the crack front and escalates at the free surfaces. $K_{\mathrm{III,FE}}$ also has its maximum value at the free surfaces and changes sign due to the sign shift in σ_{23}. The normalized values for the J integral as well as the SIF are provided in table 4.7.

Table 4.7: The J integral and SIF values for the three-dimensional mode II.

$J/\sigma_b L$	$K_{\mathrm{I,FE}}/K_{\mathrm{II,FE}}$	$K_{\mathrm{II,FE}}/K_{\mathrm{II,th}}$	$K_{\mathrm{III,FE}}/K_{\mathrm{II,FE}}$
3.976e-04	-4.953e-04	1.009	0.1815

Mode I is negative and negligible whereas the ratio of mode III to mode II in FEM is 18.15%. The asymptotic and logarithmic plots for σ_{12} through the crack front at the free surface and center are provided in figures 4.20 and 4.21. σ_{12} is positive along the crack ligament. The linear behavior can be seen both at the free surface and the specimen center which brings the fact that the K-field is approximately constant along the crack front for mode II.

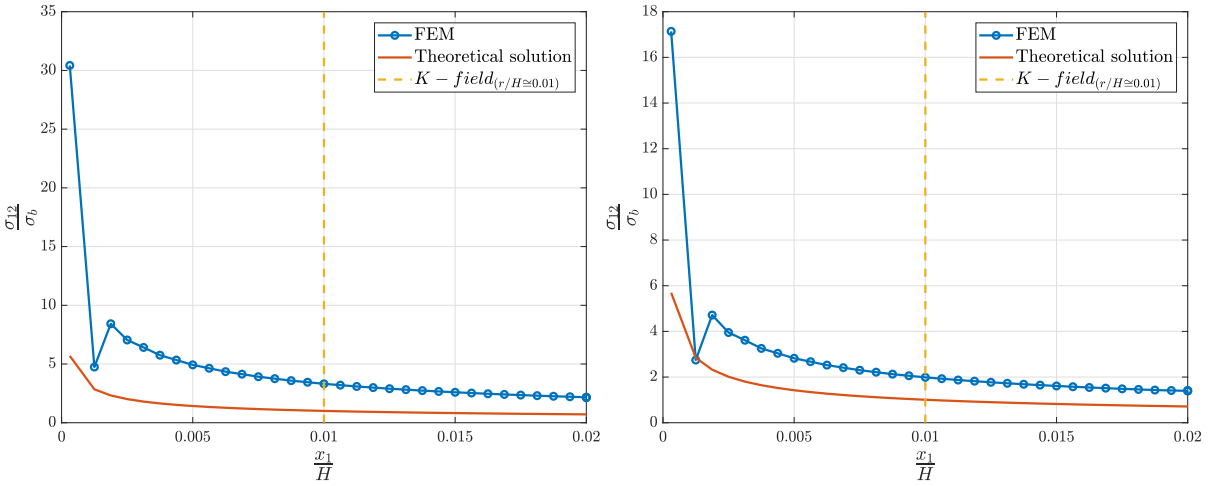

Figure 4.20: Asymptotic σ_{12} (a) at the free surface ($x_3 = \frac{B}{2}$) (b) in the center ($x_3 = 0$) along the crack ligament ($\theta = 0$).

λ values, table 4.8, implies successful $1/\sqrt{r}$-singularity both in the center and at the free surface.

Table 4.8: λ values for three-dimensional mode II at $\theta = 0$ (free surface and center correspond to $x_3 = \frac{B}{2}$ and $x_3 = 0$, respectively).

Free surface	**Center**
-0.5572	-0.5227

Figure 4.22 depicts σ_{12} contours at the free surface and center of the specimen. σ_{12} has higher values at the free surface and by moving towards the middle of the specimen this values reduces. Unlike the mode I, it appears that the crack in mode II tends to open from the edges rather than the center.

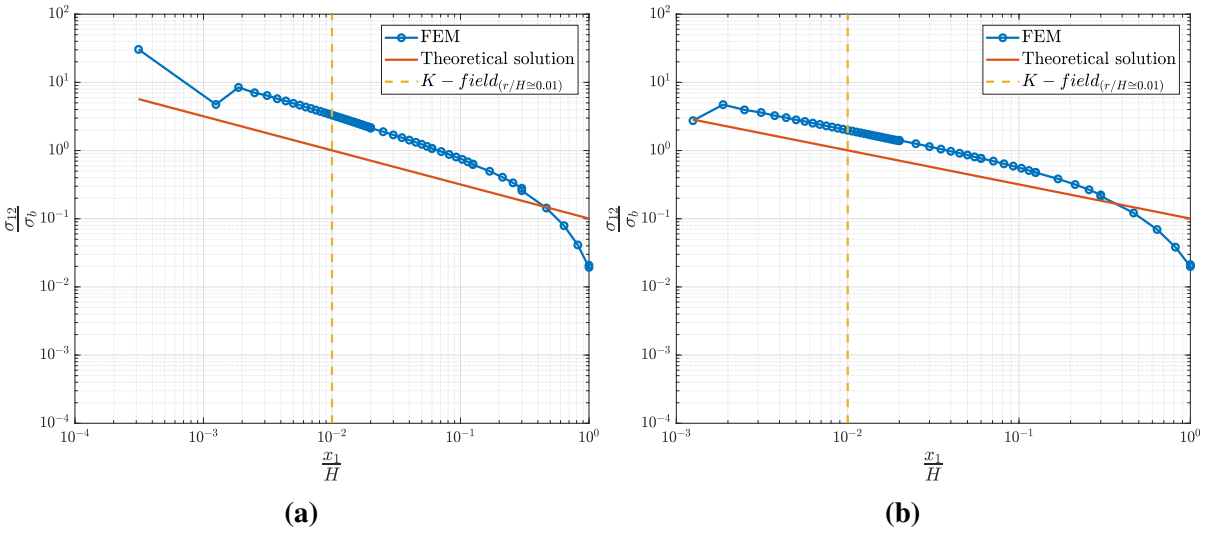

Figure 4.21: Logarithmic σ_{12} (a) at the free surface ($x_3 = \frac{B}{2}$) (b) in the center ($x_3 = 0$) along the crack ligament ($\theta = 0$)

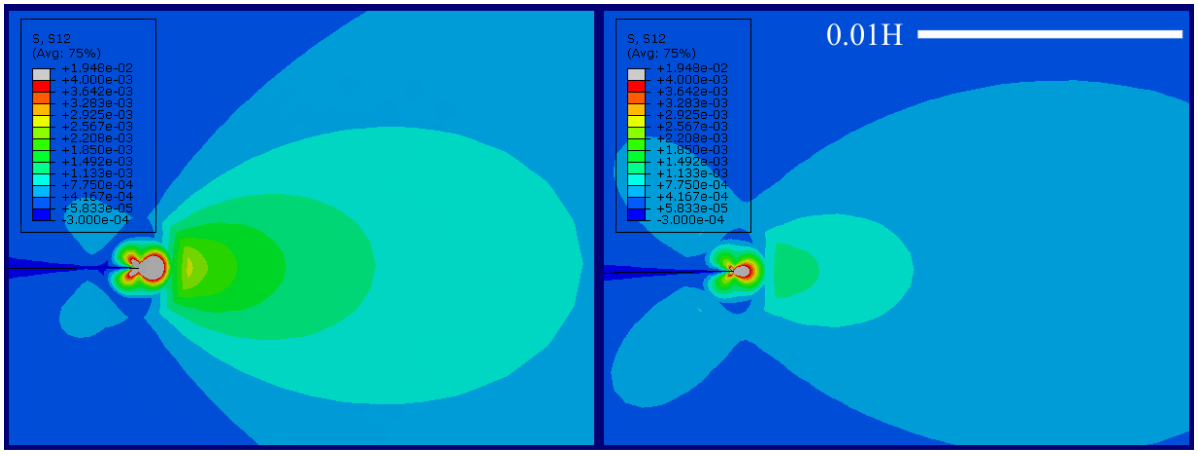

Figure 4.22: Mode II σ_{12} contours at the free surface ($x_3 = \frac{B}{2}$, left) and in the center ($x_3 = 0$, right).

An important observation is regarding the presence of σ_{23} at the free surface where it is expected to be zero. There are two point of views for this phenomenon. The former is regarding Benthem (1977), Pook et al. (2014) and Pook et al. (2015) where they believe that the SIF is a two-dimensional concept and it loses its meaning when it reaches the free surface; therefore, discussing the stress components in x_3-direction (σ_{13}, σ_{23} and σ_{33}) is futile and makes no sense. The latter belongs to Murakami and Natsume (2002). They believe that this increase in σ_{23} is due to the peculiarity of FEM calculation and with a very fine mesh at the crack, σ_{23} vanishes. To investigate the result from Murakami and Natsume (2002), the distribution of σ_{23} are extracted for two different coordinates, x_1=3.125μm and x_1=12.5μm (figure 4.23) in the crack plane. σ_{23} drops dramatically at x_1=12.5μm ahead of the crack. Therefore, it is observed that σ_{23} decays by moving in the direction ahead of the crack.

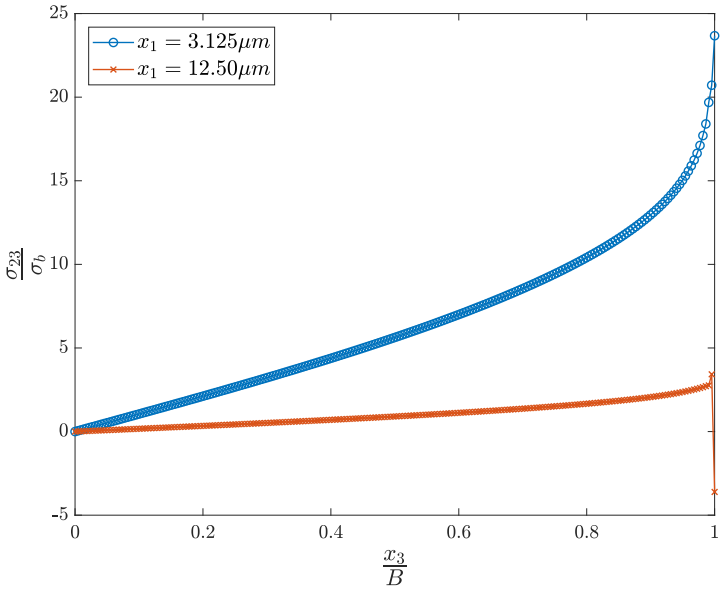

Figure 4.23: σ_{12} along the crack front at the distances x_1=3.125μm and x_1=12.50μm from the crack tip along the crack plane ($\theta = 0$).

4.3 Conclusion

Achieving a sophisticated model with the correct element types at the crack is an essential and fundamental part of mode III analysis. The findings through the analysis of mode I and II in two-dimensions and three-dimensions are summarized below.

- The triangular (collapsed) elements are preferred at the crack tip/front. The rectangular (non-collapsed) elements only produce the singularity on the side of the element that is normal to the crack plane. Furthermore, the singularity is created by only four of the rectangular elements (manually the mid-point is distorted to the quarter point in the crack tip direction) which makes the use of the rectangular (non-collapsed) elements undesired.
- Thin specimens ($\frac{B}{H} > 8$) with short pre-crack length ($\frac{a_0}{H} = 5$) are suitable for mode I LEFM study. The findings from Caprino (1990) also approves the application of thin specimens for mode I interlaminar fracture toughness testing. However, at the free surface ($x_3 = \frac{B}{2}$), σ_{22} becomes negative after few elements ahead of the crack which makes the observation of the linear behavior of σ_{22} along the crack ligament in the logarithmic scale impossible. Further study is necessary in the three-dimensional mode I with higher mesh densities at the surface since the current results are only based on the limitation of a million elements.
- In order to capture the stress, a denser mesh is required at the free surface. This is also possible through a biased mesh strategy where the maximum element length in the x_3-direction is available in the middle of the specimen. The element length decreases by

moving from the center to the free surface. An illustration is presented in figure 4.24. Reducing the computational cost due to lower number of elements is the privilege of this approach while due to the segmentation of the DCB specimen, the mesh transition from one segment to another requires further effert and consideration.

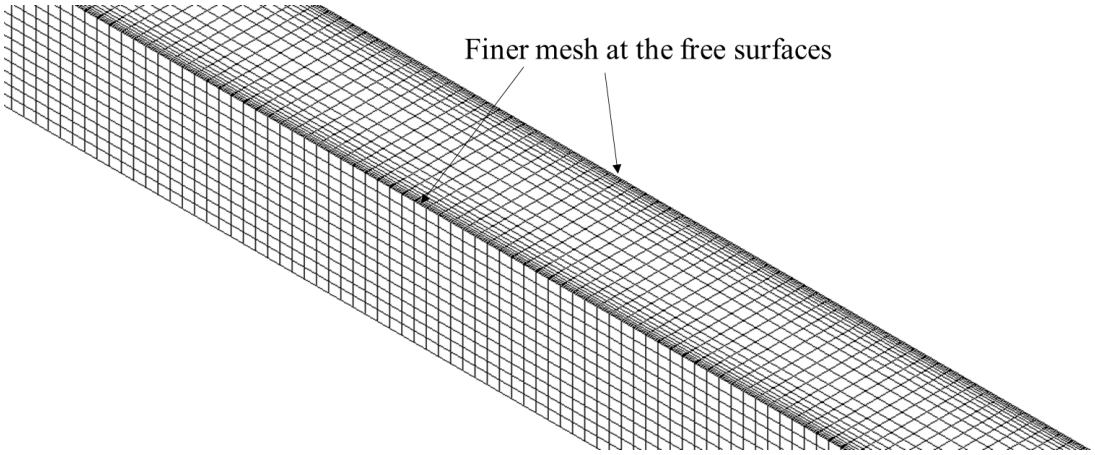

Figure 4.24: Biased mesh strategy in mode II. Denser elements are created at the free surface.

- In the DCB specimen, the K-dominated zone is much smaller than $0.01H$ (for the current model, $0.01H$=100μm) measured by Charalambides et al. (1992). Similar to the obtained results from figure 3.31, there is a difference between $\sigma_{11,FE}$ and $\sigma_{22,FE}$ where the difference is not vanished but reduced by smaller element size in the x_1-direction. Regarding the limitation in the maximum number of elements, the minimum difference between $\sigma_{11,FE}$ and $\sigma_{22,FE}$ could be obtained at 1.66μm that shows still $\sigma_{11,FE} \neq \sigma_{22,FE}$ in the K-dominated zone along the crack plane ($\theta = 0$).

- The obtained result for the SIF show a coupling between mode II and III (Pook, 2013) which requires a separate study and a model with a higher mesh density at the free surface.

- The non-vanishing σ_{23} at $x_3 = \frac{B}{2}$ and $x_3 = \frac{-B}{2}$ is discussed and it is concluded that this topic might be due to the insufficiently-fine mesh at the free surfaces and requires further studies.

- Under LEFM condition, ABAQUS calculates K_{I}, K_{II} and K_{III} from the J integral by Eq.(2.4) (ABAQUS, 2017). The J integral itself is calculated by the surface integral and rings of elements. In addition, σ_{23} decays further away from the crack tip. Therefore, it is expected that the effect of σ_{23} (which has its maximum value in the first ring of the elements and the smallest area during the surface integration) becomes very small for the J integral extracted from the 10th contour. As a result, K_{III} should have a very small value when not extracted from the 1st and 2nd contours. The author has no clear explanation for this observation.

- Based on the observations so far, it appears that the first element at the crack tip is unable to provide correct stress calculation which might be due to the distortion of the mid-nodes. Currently, by the development of the computational techniques, a separate research is recommended between the distorted and non-distorted elements at the crack tip to investigate the effect of the non-distorted elements on the obtained results, more specifically the singularity at the free surface.

CHAPTER 5
Effect of Width and Height Ratio on K_{III}

After succeeding a robust FE model in the previous two chapters, in the current and the next three chapters, the effect of several parameters will be studied to determine if the pure mode III is possible to achieve with the available theory and tools. This chapter focuses on the effect of width and height on K_{III} which provides the opportunity of monitoring both the thick and thin specimens under mode III.

5.1 Finite Element Model

The full DCB specimen for mode III is shown in figure 5.1. For the FEM, the specimen is fully modeled (figure 5.2) like a cantilever beam where the prescribed rotations are applied at the end of the specimen to create the anti-plane loading. Similar to the mode II, the length of the pre-existing crack, $a_0 = 15H$, the total beam length, $L = 30H$, and the specimen width is $B = 2H$.

The material, elements, crack definition and mesh strategy are similar to the three-dimensional mode I and II.

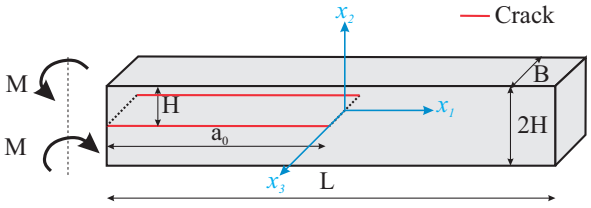

Figure 5.1: The geometry and loading of the DCB specimen under mode III.

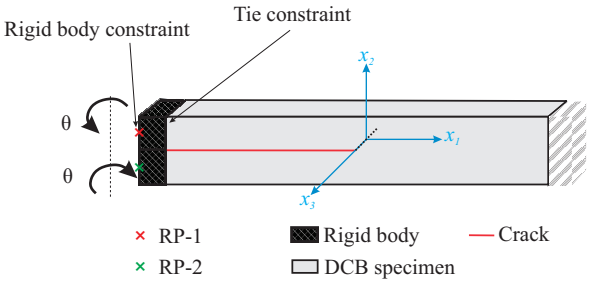

Figure 5.2: The DCB specimen FE model under mode III.

5.2 Elements Size

The smallest element dimensions according to figure 4.5 are listed in table 5.1.

Parameter	Dimension
e_h[mm]	1.227E-03
e_h/H	1.227E-04
e_w[mm]	125E-03
e_w/H	0.0125
e_l[mm]	12.50E-03
e_l/H	0.0013
e_h/e_l	0.1000
e_w/e_l	10.00
e_h/e_w	0.0098

Table 5.1: Mode III smallest element size.

Despite the poor aspect ratios which originates from the triangular (collapsed) elements at the crack front that is more pronounced for the element height to length and element height to width ratios, analyses from chapter 4 have shown the element dimensions in table 5.1 are capable of providing reasonable results ($ne = 81920$ in table 4.5 and figure 4.17); however, in the case of achieving mode III, the suitable mesh size will be determined by the mesh convergence.

5.3 The J integral

The same methodology as mentioned for the three-dimensional mode I and II is utilized to determine the theoretical mode III SIF, $K_{\mathrm{III,th}}$. The steps are illustrated in figure 5.3. The J integral under pure mode III evaluated along the external boundaries can be calculated by Eq.(5.1). The derivation is provided in Appendix E for an isotropic material.

$$J_{\mathrm{III}} = \frac{12M^2}{EB^4H} \tag{5.1}$$

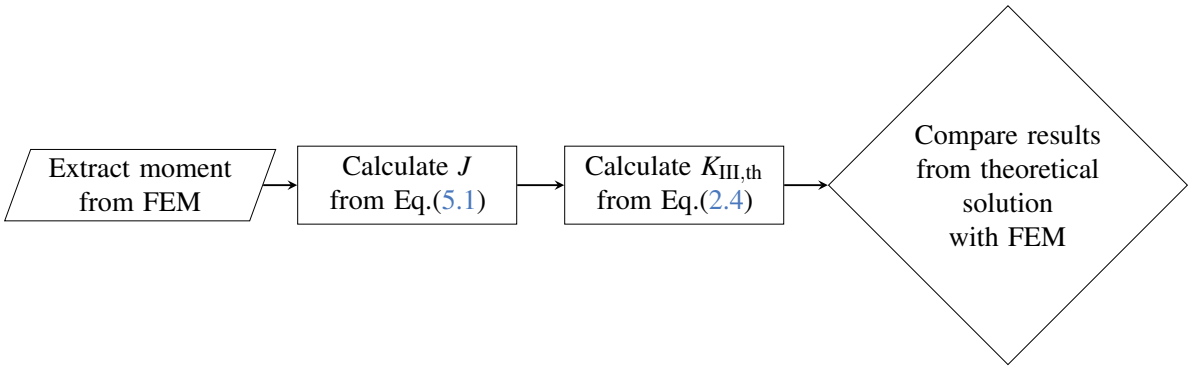

Figure 5.3: The flowchart for calculating $K_{\mathrm{III,th}}$ from the J integral.

5.4 Effect of Width

In this section, the height of the specimen is kept constant and the specimen width varies. The distribution of K_{II} and K_{III} through the specimen thickness for the ratios of $\frac{B}{H}$ =1, 2, 4 and 8 are shown in figure 5.4. The plots show that K_{II} and K_{III} vary across the width of the specimen (x_3-direction) but the results are nearly independent of the $\frac{B}{H}$ ratio.

Because of the negligible K_{I} values, only K_{II} and K_{III} from FEM will be plotted from now on. The coupling between K_{II} and K_{III} with dominantly mode II is visible. This time, K_{II} changes sign, due to σ_{12}, along the crack front and is virtually two times larger than K_{III} at the free surface.

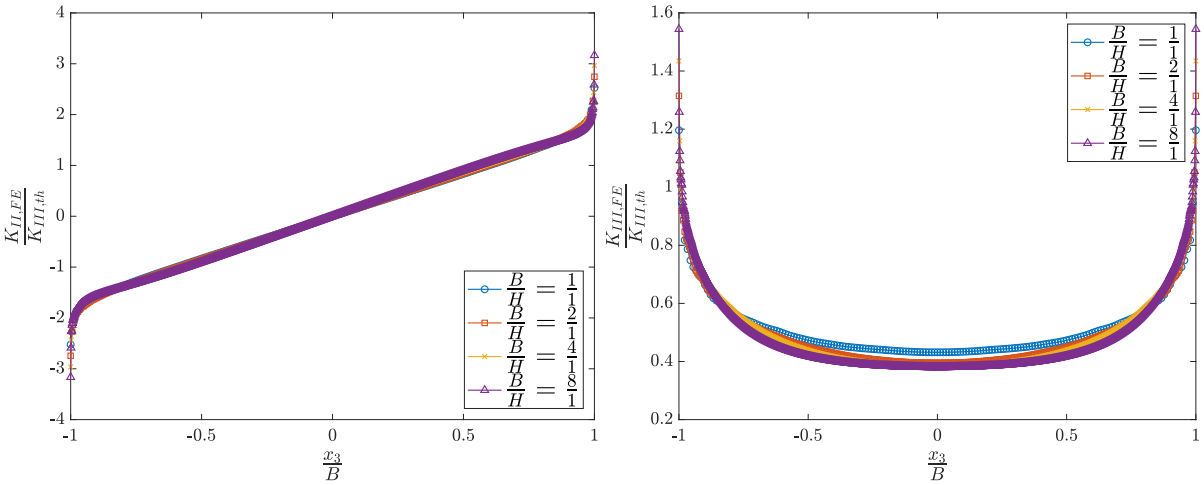

(a) **(b)**

Figure 5.4: Mode III-Effect of width: Distribution of (a) $K_{\mathrm{II,FE}}$ (b) $K_{\mathrm{III,FE}}$ through the crack front for different $\frac{B}{H}$ ratios.

The SIF and stress components have been plotted along the crack front for all the $\frac{B}{H}$ ratios. They all follow the similar behavior. Therefore, only the plots for $\frac{B}{H}$ =4 are illustrated in figure 5.5.

The asymptotic and logarithmic σ_{23} plots for $\frac{B}{H} = \frac{4}{1}$ are demonstrated in figures 5.6 and 5.7. It is evident that σ_{23} for the first element has a negative value in figure 5.6(a); thus, another analysis with a finer mesh in the vicinity of the crack in the x_1-direction does not improve the result and the negative σ_{23} is still available. Surprisingly, by extracting the $K_{\mathrm{III,FE}}$ from the 2nd contour, non of the K_{III} values are negative whereas it was expected that at least for the free surface K_{III} becomes negative.

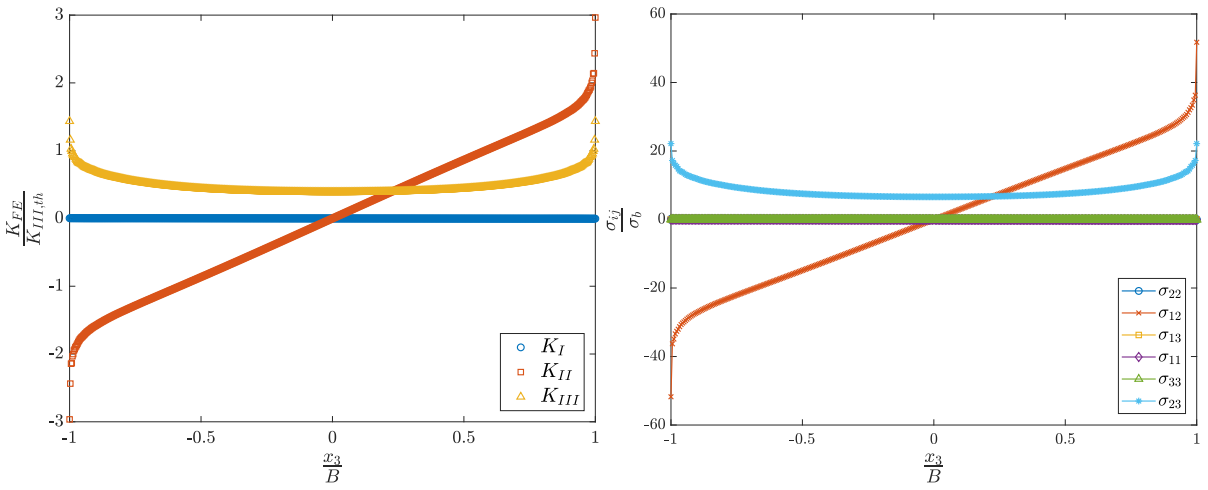

(a) **(b)**

Figure 5.5: Mode III-Effect of width: (a) SIF (b) stress (at $x_1 = 3.125\mu$m and $x_2 = 0$) components along the crack front for $\frac{B}{H}$ =4.

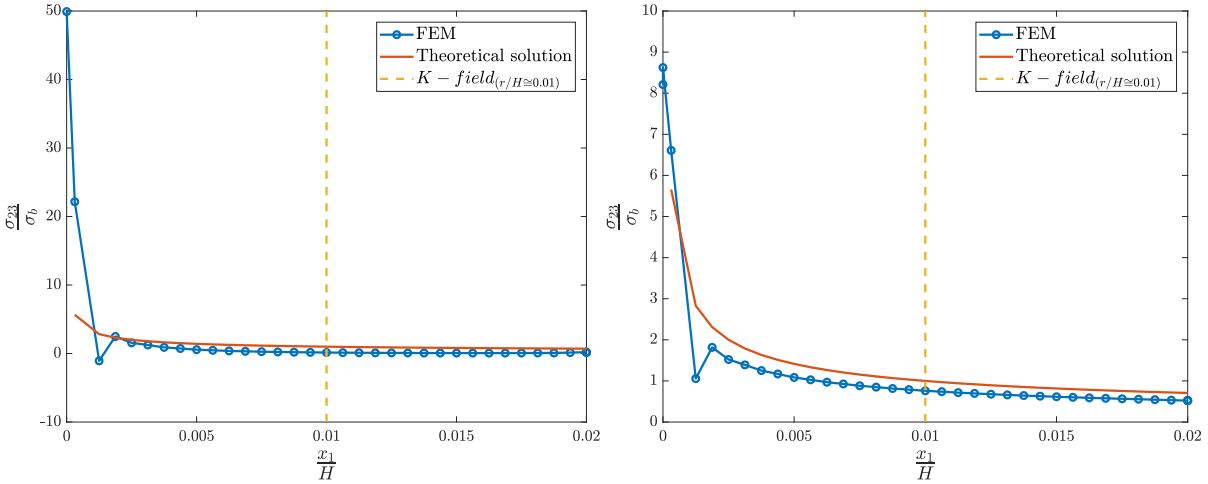

(a) **(b)**

Figure 5.6: Mode III-Effect of width: Asymptotic σ_{23} (a) at the free surface ($x_3 = \frac{B}{2}$) (b) in the center ($x_3 = 0$) along the crack ligament ($\theta = 0$) for $\frac{B}{H}$ =4.

Eq.(5.2) gives the formula for mode III singularity exponent. The calculated λ values by fitting a power curve for various $\frac{B}{H}$ ratios are listed in table 5.2. The $1/\sqrt{r}$-singularity cannot be accomplished at the free surface by increasing the specimen width, there is only a very narrow thickness in the center where the K-dominated zone is obtained.

$$\sigma_{23} = pr^{\lambda} \tag{5.2}$$

Despite having achieved the asymptotic behavior at the free surface, increasing the width,

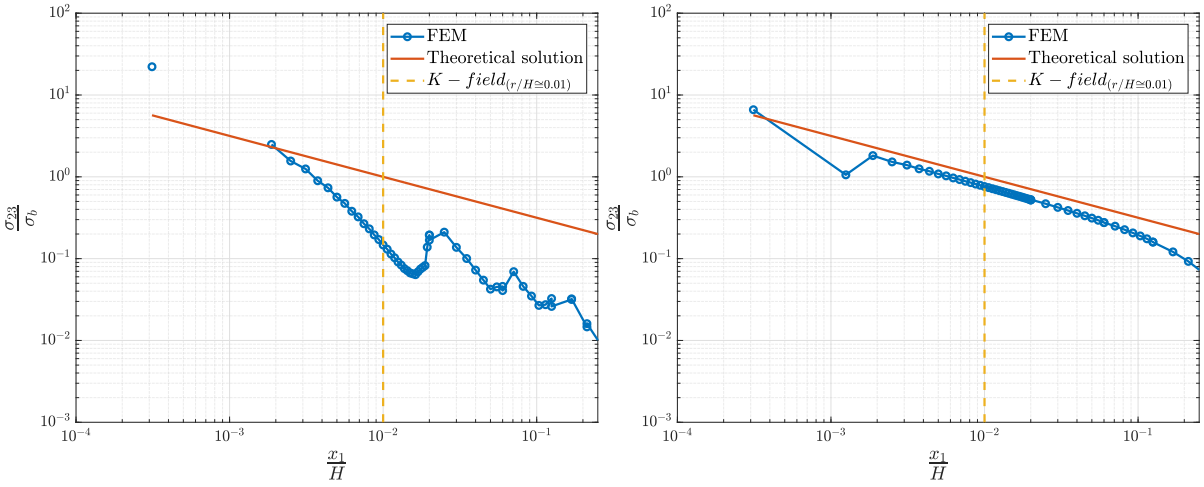

(a) **(b)**

Figure 5.7: Mode III-Effect of width: Logarithmic σ_{23} (a) at the free surface ($x_3 = \frac{B}{2}$) (b) in the center ($x_3 = 0$) along the crack ligament ($\theta = 0$) for $\frac{B}{H}$ =4.

Table 5.2: Mode III-Effect of width: λ values for different $\frac{B}{H}$ ratios at $\theta = 0$ (free surface and center correspond to $x_3 = \frac{B}{2}$ and $x_3 = 0$, respectively).

$\frac{B}{H}$	λ	
	Free surface	**Center**
1	-1.636	-0.5402
2	-1.822	-0.5317
4	-1.954	-0.5258
8	-2.049	-0.5229

λ deviates much from -0.5. On the contrary, in the middle, for all the ratios the singular field is obtained. Furthermore, λ is converging to -0.5.

The pre-crack part of the DCB specimen is divided into two parts: (a) the vicinity and (b) far from the crack tip (table 5.3). In each part, the dominant mode can be differentiated which provides useful information especially for the CZM. The beam displacements behind the crack, u_1, u_2 and u_3; at the free surface and center are normalized with the maximum beam deflection, δ_{max}, and is calculated from Eq.(5.3). u_1, u_2 and u_3 correspond to mode II, mode I and mode III displacements, respectively (figure 5.9).

$$\delta_{max} = \frac{M{a_0}^2}{2EI} \tag{5.3}$$

where M is the moment, a_0 is the pre-crack length and I is the second moment of area.

σ_{23} contours (figure 5.8) shows higher σ_{23} values at the free surface. As a result, the deformation are more pronounced at the edges.

Table 5.3: Mode III-Effect of width: Dominant modes in the vicinity and far from the crack behind the crack tip at $\theta = -\pi$ for $\frac{B}{H}$ =4 (free surface and center correspond to $x_3 = \frac{B}{2}$ and $x_3 = 0$, respectively).

	The vicinity of the crack tip	**Far from the crack tip**
Free surface	Mode II	Mode III
Center	Mode III	Mode III

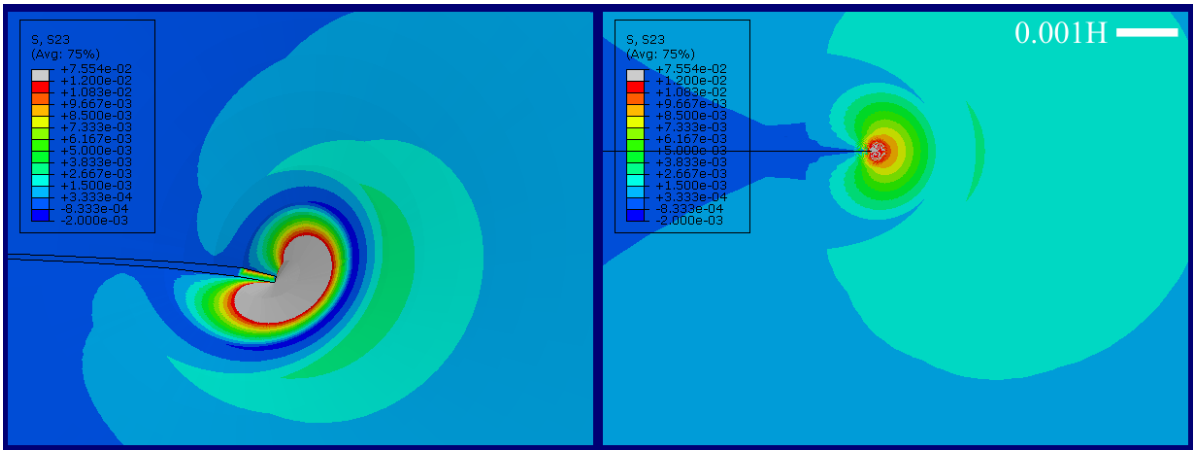

Figure 5.8: Mode III-Effect of width: Mode III σ_{23} contours at the free surface ($x_3 = \frac{B}{2}$, left) and in the center ($x_3 = 0$, right) for $\frac{B}{H}$ =4.

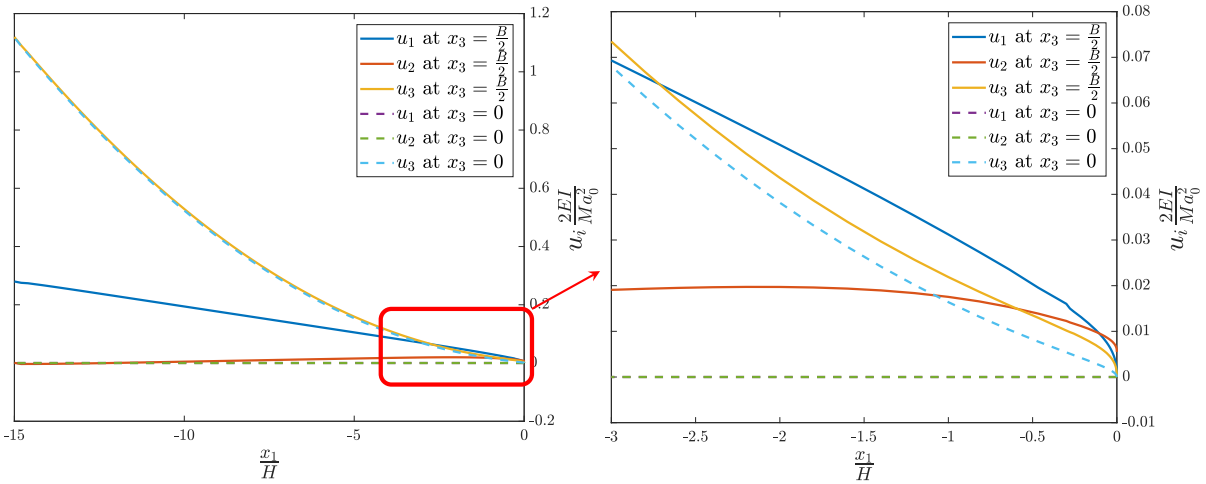

(a) **(b)**

Figure 5.9: Mode III-Effect of width: Specimen displacements behind the crack tip ($\theta = -\pi$) (a) away from the crack tip (b) in the vicinity of the crack tip for $\frac{B}{H}$ =4.

5.5 Effect of Height

In this section, the effect of the specimen height on mode III for four different ratios of $\frac{H}{B}$ will be analyzed. The K_{II} and K_{III} distribution through the crack for the various height scenarios are given in figure 5.10. Similar to the effect of width, K_{II} is independent of the specimen geometry while the thinnest specimen, $\frac{H}{B}$ =8 gives the highest value of K_{III}.

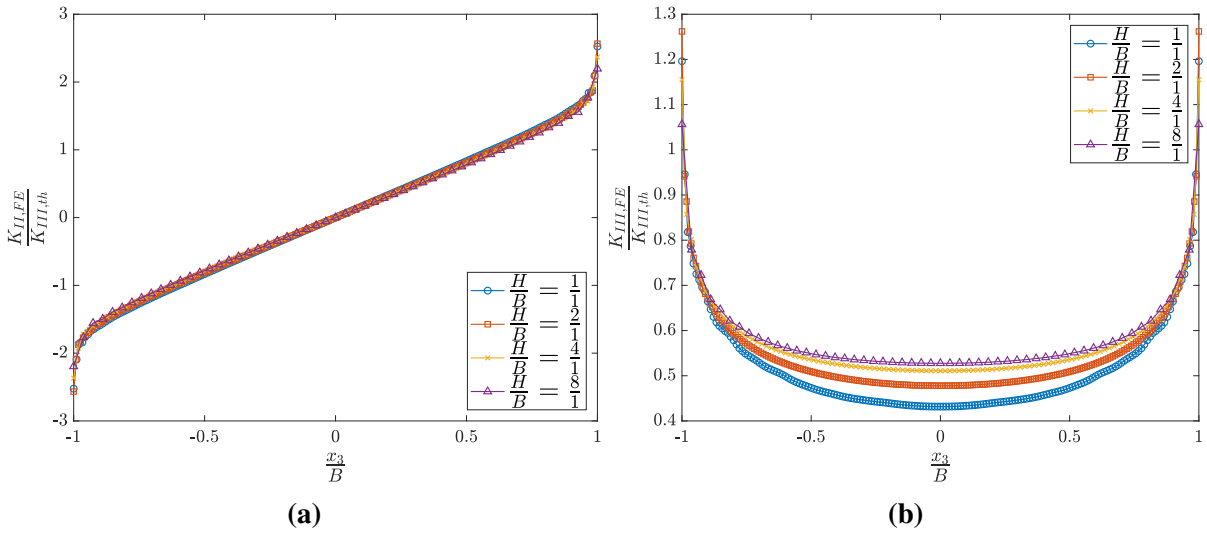

(a) **(b)**

Figure 5.10: Mode III-Effect of height: Distribution of (a) $K_{\mathrm{II,FE}}$ (b) $K_{\mathrm{III,FE}}$ through the crack front for different $\frac{H}{B}$ ratios.

To illustrate the SIF and stress components distribution along the crack front, only the result for $\frac{H}{B}$ =4 are illustrated in figure 5.11. The rest follows the same trend. Similar observations from the effect of width applies.

Surprisingly, by plotting σ_{23} for $\frac{H}{B}$ =4 in figure 5.12(b), one can see the reduced number of elements which stays within the $0.01H$ criterion (Charalambides et al., 1992) for the size of the K-dominated zone. This is interesting since the element size along the x_3-direction is the same for all the elements at the crack front. This might raises to the fact of removing the K-dominated zone in the specimen center by reducing the specimen width. The logarithmic plots for σ_{23} along the crack ligament are given in figure 5.13.

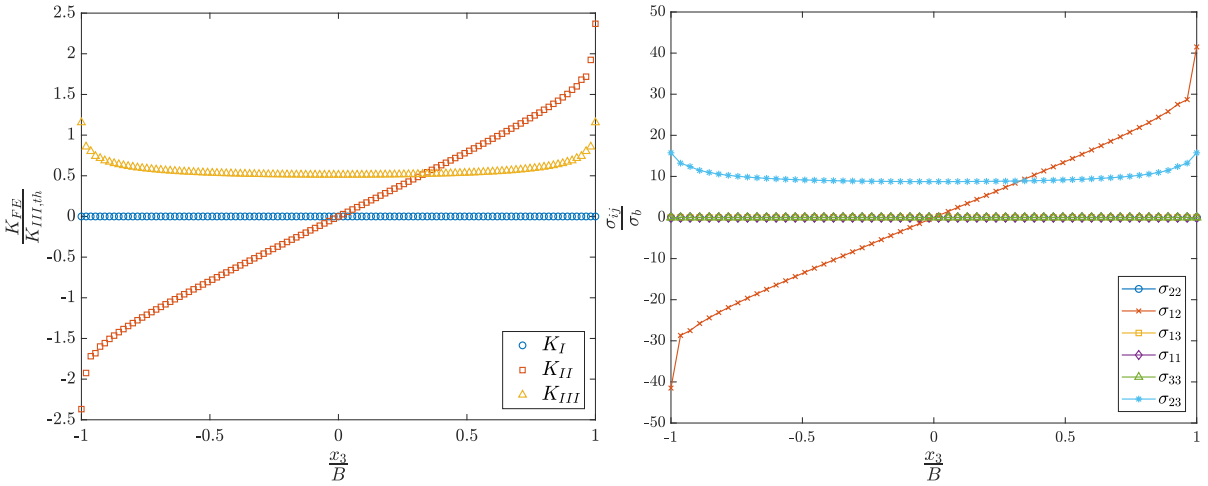

(a) **(b)**

Figure 5.11: Mode III-Effect of height: (a) SIF (b) stress components along the crack front for $\frac{H}{B} = 4$.

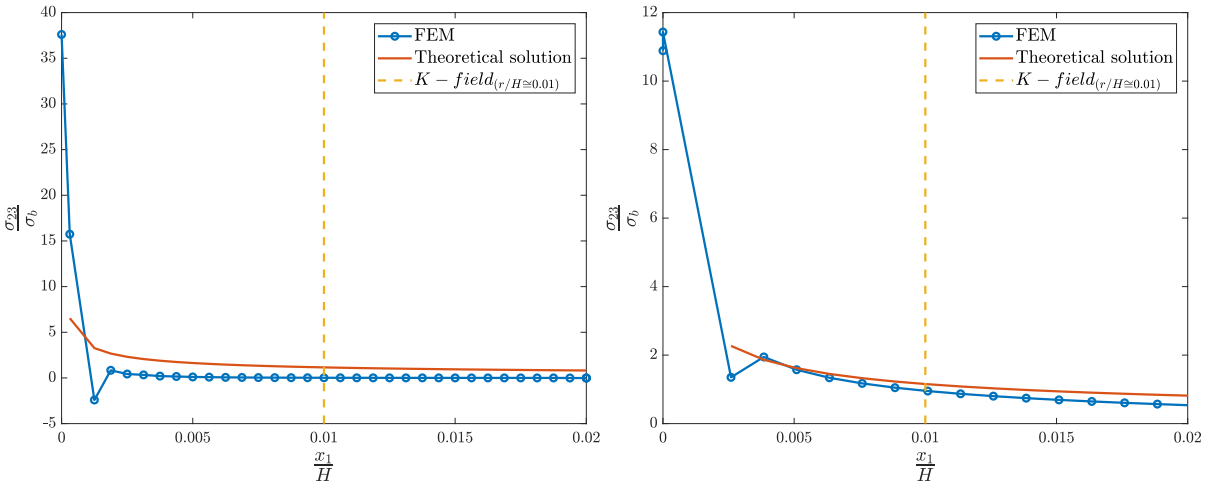

(a) **(b)**

Figure 5.12: Mode III-Effect of height: Asymptotic σ_{23} (a) at the free surface ($x_3 = \frac{B}{2}$) (b) in the center ($x_3 = 0$) along the crack ligament ($\theta = 0$) for $\frac{H}{B}$ =4.

The values of λ, table 5.4, in the center further approve destroying the K-dominated zone in the specimen center by reducing the specimen width. Another study with a finer mesh in the x_3 and x_1-directions could not make any improvement to λ values. It is likely that for the larger $\frac{H}{B}$ the specimen width controls the size of the K-dominated zone.

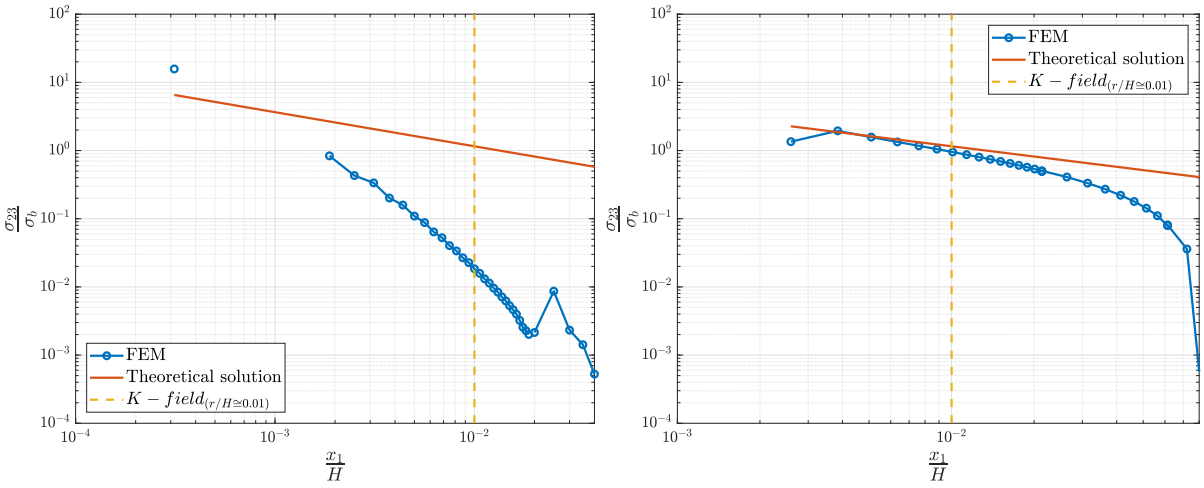

(a) **(b)**

Figure 5.13: Mode III-Effect of height: Logarithmic σ_{23} (a) at the free surface ($x_3 = \frac{B}{2}$) (b) in the center ($x_3 = 0$) along the crack ligament ($\theta = 0$) for $\frac{H}{B}$ =4.

Table 5.4: Mode III-Effect of height: λ values for different $\frac{H}{B}$ ratios at $\theta = 0$ (free surface and center correspond to $x_3 = \frac{B}{2}$ and $x_3 = 0$, respectively).

$\frac{H}{B}$	λ	
	Free surface	**Center**
1	-1.636	-0.5402
2	-1.843	-0.5845
4	-1.858	-0.7756
8	-1.902	-0.8098

The dominant modes behind the crack tip, table 5.5 and figure 5.14, are identical to the effect of height; however, the size of the predominantly mode II in the vicinity of the crack is noticeably reduced.

Table 5.5: Mode III-Effect of height: Dominant modes in the vicinity and far from the crack behind the crack tip at $\theta = -\pi$ for $\frac{H}{B}$ =4 (free surface and center correspond to $x_3 = \frac{B}{2}$ and $x_3 = 0$, respectively).

	The vicinity of the crack tip	**Far from crack tip**
Free surface	Mode II	Mode III
Center	Mode III	Mode III

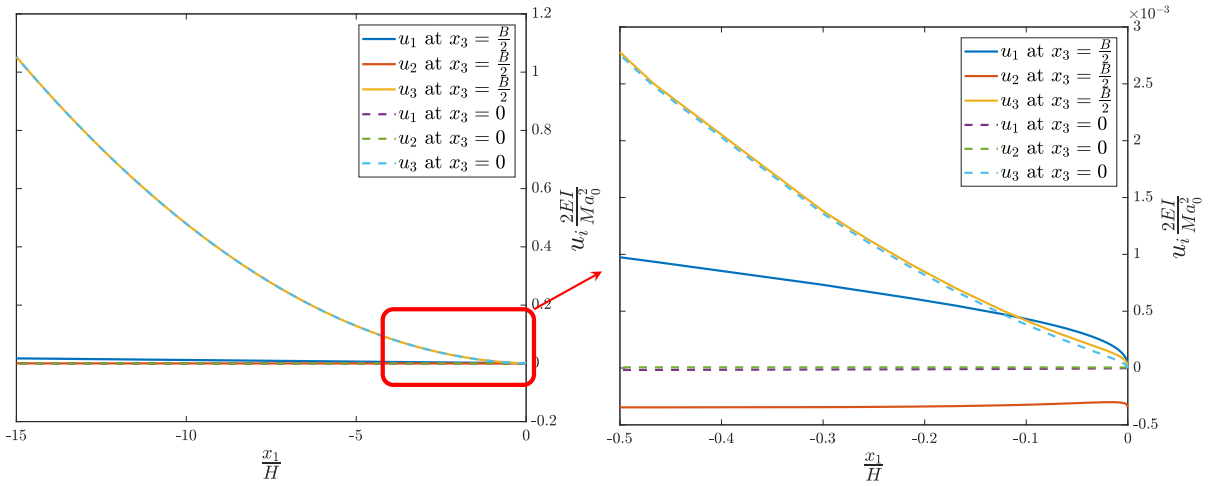

Figure 5.14: Mode III-Effect of height: Specimen displacements behind the crack tip ($\theta = -\pi$) (a) away from the crack tip (b) in the vicinity of the crack tip for $\frac{H}{B}$ =4

Figure 5.15 demonstrates the σ_{23} contour plots. σ_{23} has an approximately constant size and value at both the free surface and center of the specimen which is caused by reducing the specimen width.

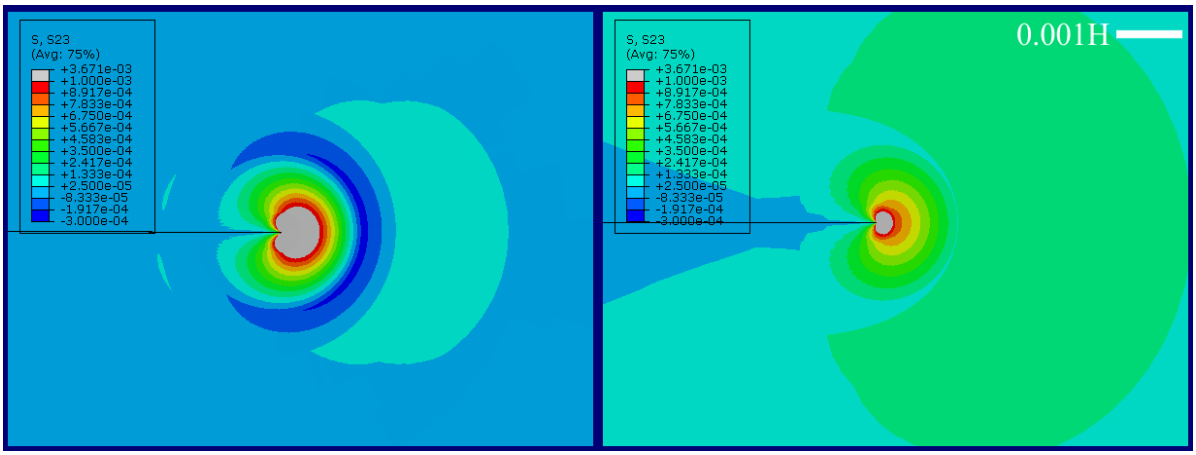

Figure 5.15: Mode III-Effect of height: Mode III σ_{23} contours at the free surface ($x_3 = \frac{B}{2}$, left) and in the center ($x_3 = 0$, right) for $\frac{H}{B}$ =.

5.6 Conclusion

- It was shown by Benthem (1977) and Bažant and Estenssoro (1979) that the $r^{-\lambda}$-singularity at the free surface is a function of the Poisson's ratio and varies from 0 ($\nu = 0$) to 0.604

($\nu = 0.4$) for the mode II and III. When $\nu = 0.3$, the corresponding λ=0.598 which shows that the theory by Bažant and Estenssoro (1979) should be revisited with models with higher mesh densities at the free surface.

- The obtained results agree with the work of Pook et al. (2014) and Pook et al. (2015) who performed a dedicated study on a plate and a disk with different width and a very fine mesh under anti-plane loading using the commercial code, ANSYS. They found out that ahead of the crack, at the free surface σ_{23} increases as one moves towards the crack tip. σ_{12} is also maximum at the free surface and there is a coupling between σ_{23} and σ_{12}.

- Another study with a shorter pre-crack length ($a_0 = 5H$) is conducted to investigate whether the length of crack may affect the distribution of K_{III} along the crack front. It has been concluded that the thin specimens ($B >> H$) are not suitable for mode III fracture toughness testing. Especially, in the case of short pre-crack which result in a much likely plate rather than a beam specimen (figure 5.16). Higher $\frac{B}{H}$ ratios for the case of short crack causes K_{III} relative error and mode II portion to increase negatively and positively.

- Specimen with $H >> B$ forces the singular field at the center to vanish (It was shown that under the higher $\frac{H}{B}$ the size of the K-dominated zone is driven by the specimen width). In addition, with higher $\frac{H}{B}$ ratios, K_{III} relative error and $K_{\mathrm{II,FE}}$ decreases in negative and positive fashions (figure 5.17).

- As expected, K_{III} is independent from the initial crack length and geometry.

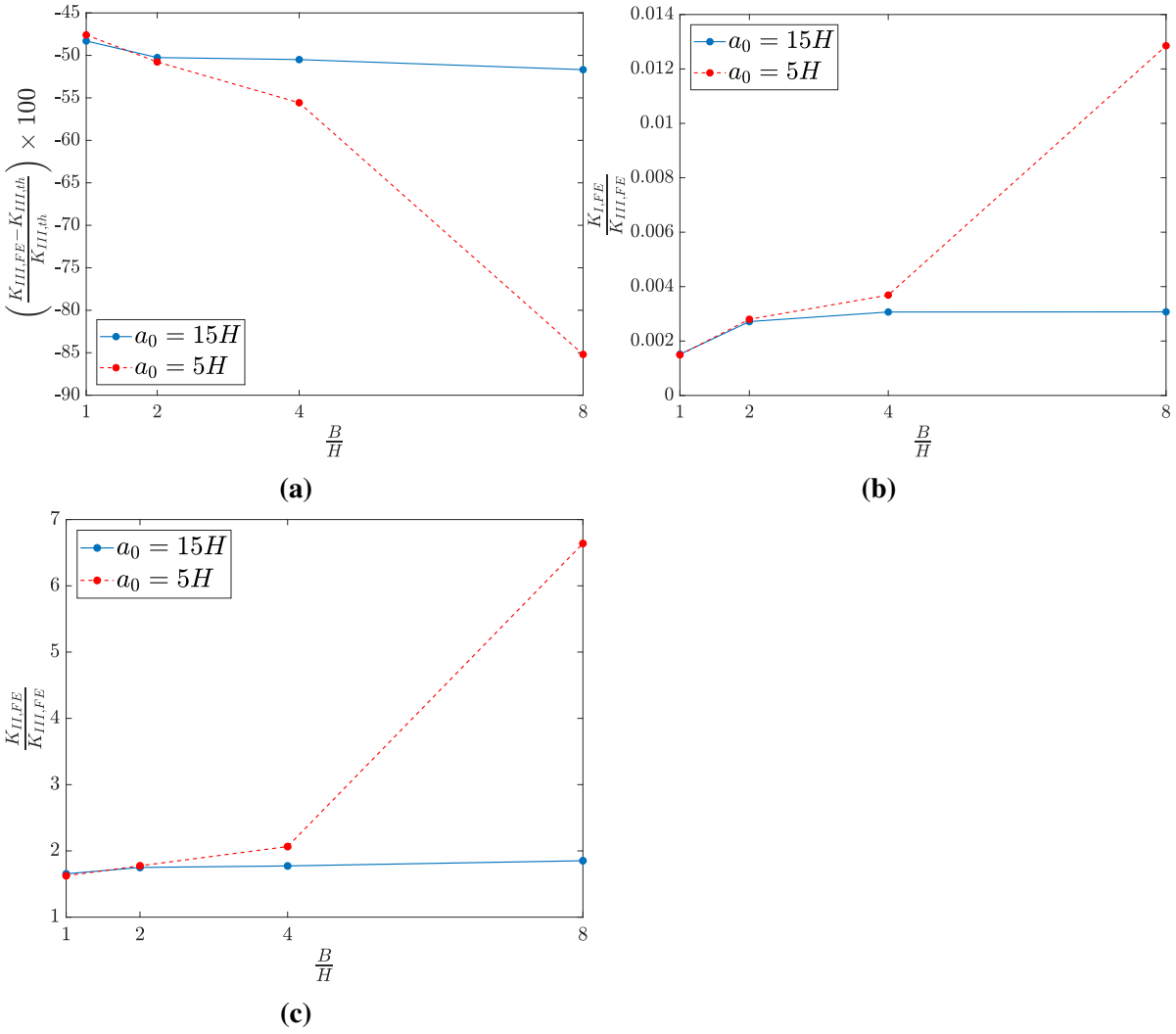

Figure 5.16: Mode III-Effect of width: Effect of the size of pre-crack and width on the mode III SIF. (a) $K_{\text{III,th}}$ and $K_{\text{III,FE}}$ relative error (b) $\frac{K_{\text{I,FE}}}{K_{\text{III,FE}}}$ (c) $\frac{K_{\text{II,FE}}}{K_{\text{III,FE}}}$.

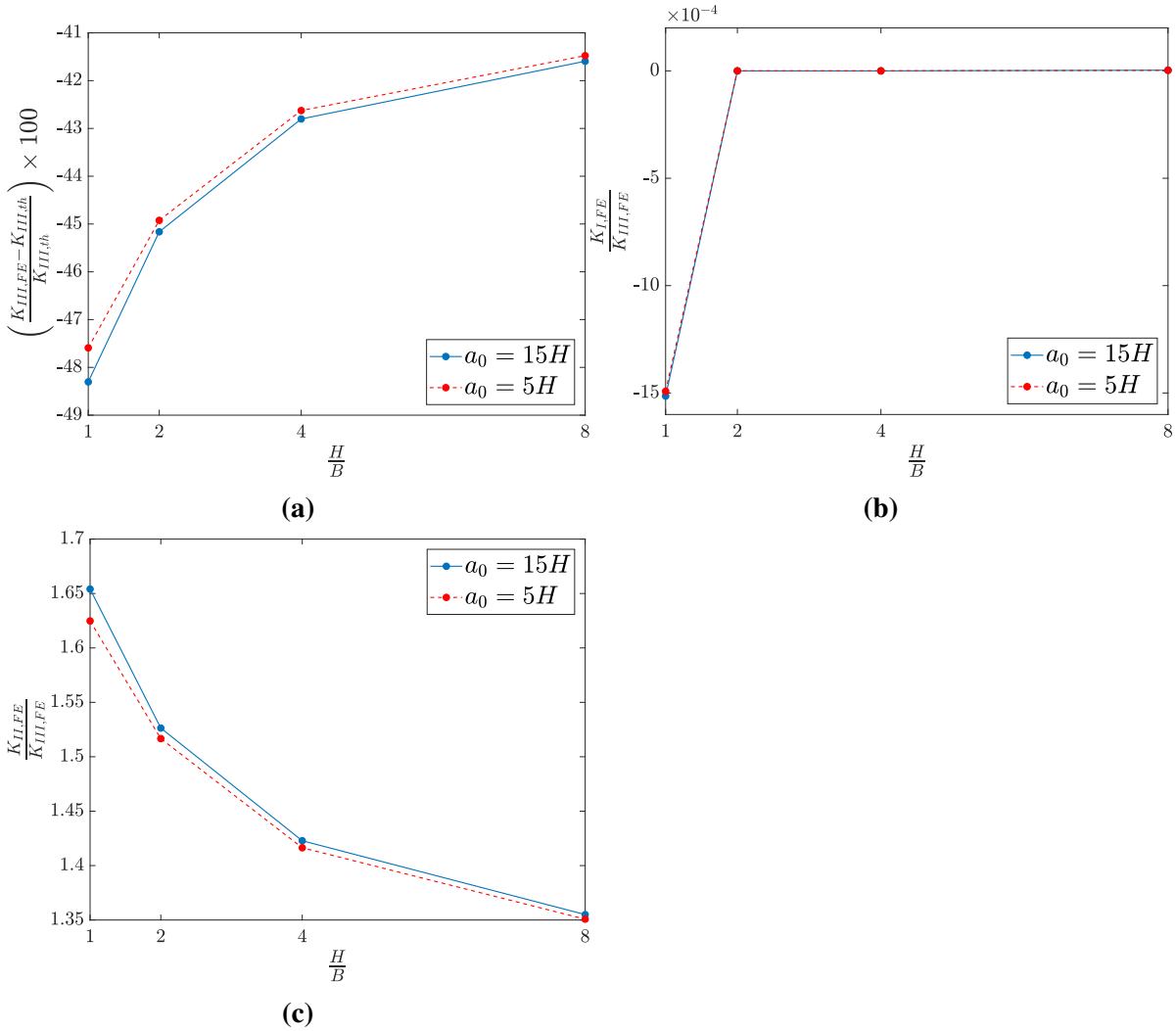

Figure 5.17: Mode III-Effect of height: Effect of the size of pre-crack and height on the mode III SIF. (a) $K_{\text{III,th}}$ and $K_{\text{III,FE}}$ relative error (b) $\frac{K_{\text{I,FE}}}{K_{\text{III,FE}}}$ (c) $\frac{K_{\text{II,FE}}}{K_{\text{III,FE}}}$.

CHAPTER 6
Effect of Side-grooves on K_{III}

In this chapter, the effect of side-grooves on K_{III} will be discussed. The side-grooves along the specimen length provide the opportunity of studying the effect of width variation and material removal or charge simultaneously on K_{III}.

6.1 Side-grooves

The possible strategies for the side-grooves are shown in figure 6.1. In the "Inward" strategy (figure 6.1(a)), the material is removed from the sides of the specimen resulting in sharp edges while for the "Outward" strategy (figure 6.1(b)), material is added to the sides. To reduce the possibility of stress concentration at the free surfaces of the Inward strategy, another sample with rounded edges is added to the list, the "Inward curve" as shown in figure 6.1(c).

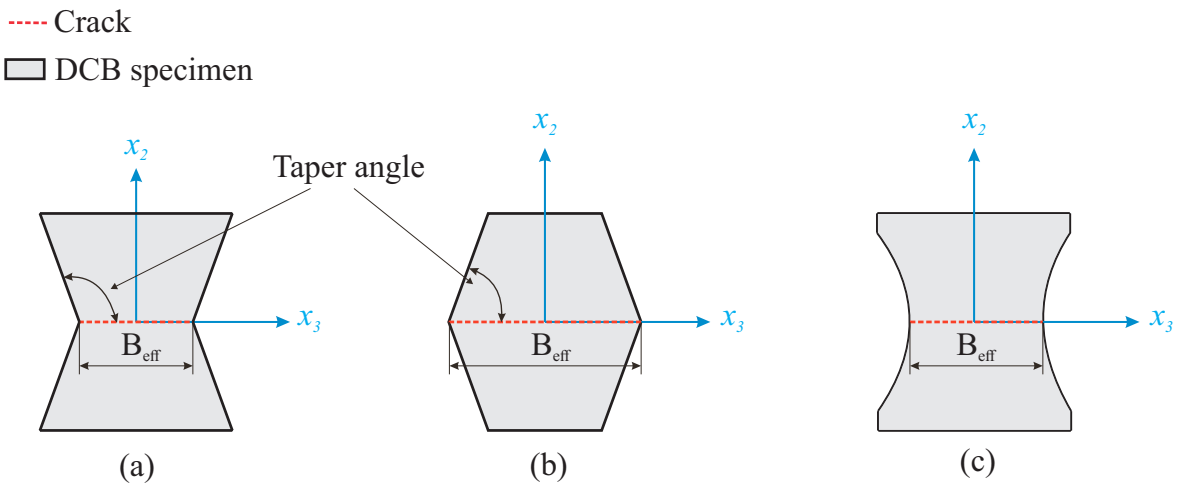

Figure 6.1: Mode III-Effect of side-grooves: Possible strategies (cross-sectional view). (a) Inward (b) Outward (c) Inward curve.

6.2 The J integral

The similar approach mentioned in section 5.3 is invoked to calculate $K_{III,th}$. The only difference is in the J integral equation. In order to reduce the effect of specimen width, B, Eq.(5.1) is replaced with Eq.(6.1). B is also changed to B_{eff} where B_{eff} is the length of the

crack front, shown with red dashed lines in figure 6.1. With this approach, the effect of specimen width is minimized.

$$J = \frac{M^2}{EB_{\text{eff}}I} \tag{6.1}$$

where M and I are the bending moment and the second moment of area, respectively.

6.3 Effect of Inward Side-grooves

The SIF and stress components distribution through the crack front for the Inward groove are plotted in figure 6.2 (the plots for the Inward curve strategy are identical). The coupling between mode II and mode III appears once more. Mode I is negligible compared to the other two modes but has higher values when is compared to a complete specimen from chapter 5.

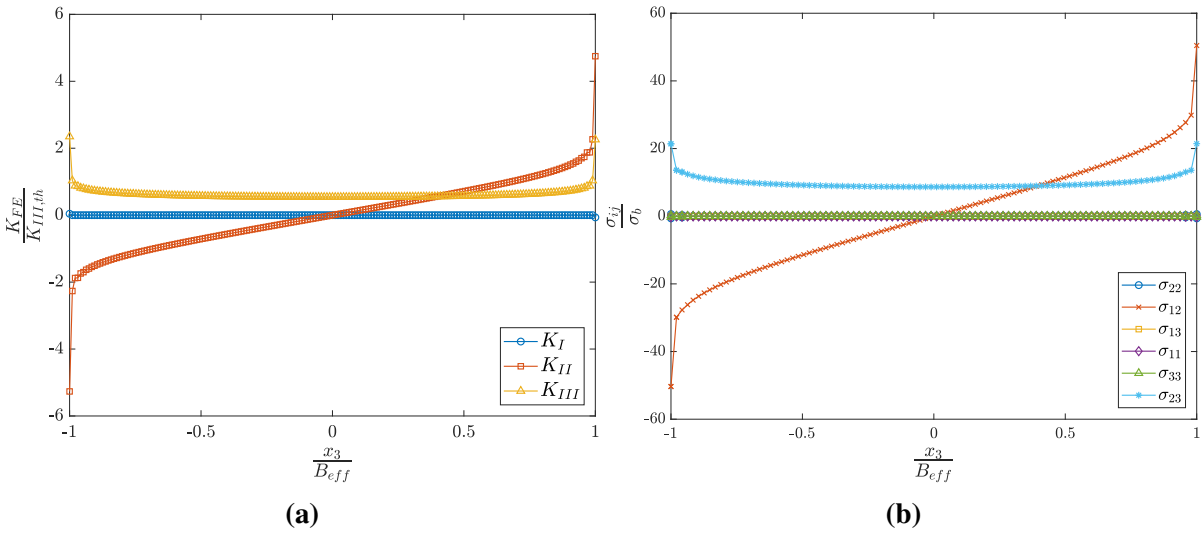

(a) **(b)**

Figure 6.2: Mode III-Effect of side-grooves: (a) SIF (b) stress (at $x_1 = 3.125\mu$m and $x_2 = 0$) components along the crack front for the Inward groove strategy.

Plotting the asymptotic σ_{23} along the ligament, figure 6.3, one is able to immediately recognize the fewer number of elements in the center, figure 6.3(b), compared to the free surface, figure 6.3(a), which is the effect of reducing the crack front length (here equal to B_{eff}) discussed in section 5.5 where in spite of the existence of the $1/\sqrt{r}$-singularity there are fewer elements that fits inside the $0.01H$ criterion for the K-dominated zone size which further indicates that this criterion for the size of the K-dominated zone can be influenced when the geometry of the DCB specimen is changed. The same plot for σ_{23} in the logarithmic scale, figure 6.3, gives the linear solution which is more pronounced in the center.

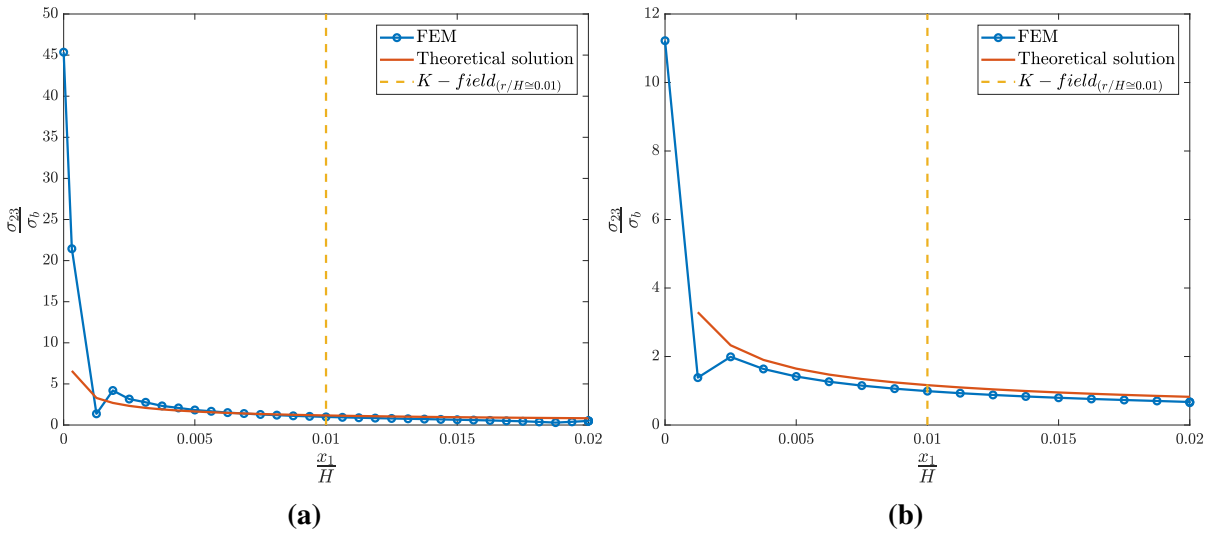

Figure 6.3: Mode III-Effect of Inward groove: Asymptotic σ_{23} (a) at the free surface ($x_3 = \frac{B_{\text{eff}}}{2}$) (b) in the center ($x_3 = 0$) along the crack ligament ($\theta = 0$).

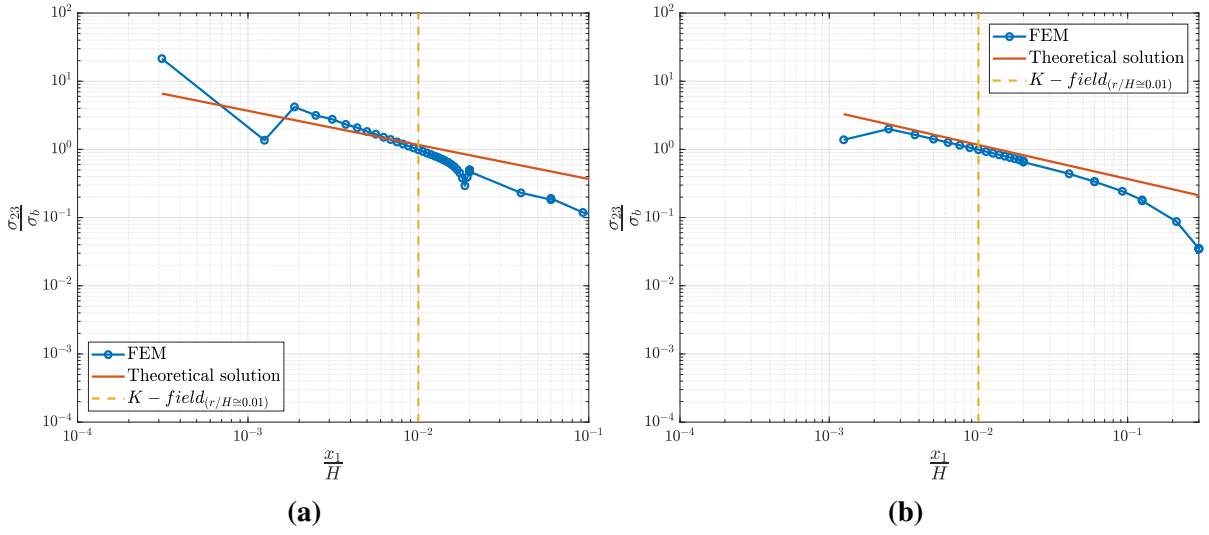

Figure 6.4: Mode III-Effect of Inward groove: Logarithmic σ_{23} (a) at the free surface ($x_3 = \frac{B_{\text{eff}}}{2}$) (b) in the center ($x_3 = 0$) along the crack ligament ($\theta = 0$).

6.4 Effect of Outward Side-grooves

In comparison with the Inward and Inward curve side-grooves, the Outward demonstrates an entirely different distribution of the SIF along the crack front. Figure 6.5 provides an overview of the SIF and stress components along the crack front. Both K_{II} and K_{III} suddenly change sign at the free surface (the green boxes in figure 6.5(a)). The result from another model with a finer mesh yielded the similar dramatic jump in K_{II} and K_{III}. It appears that the FEM cannot calculate the stress correctly and requires a mesh with a higher density. No clear

explanation has been found for this phenomenon.

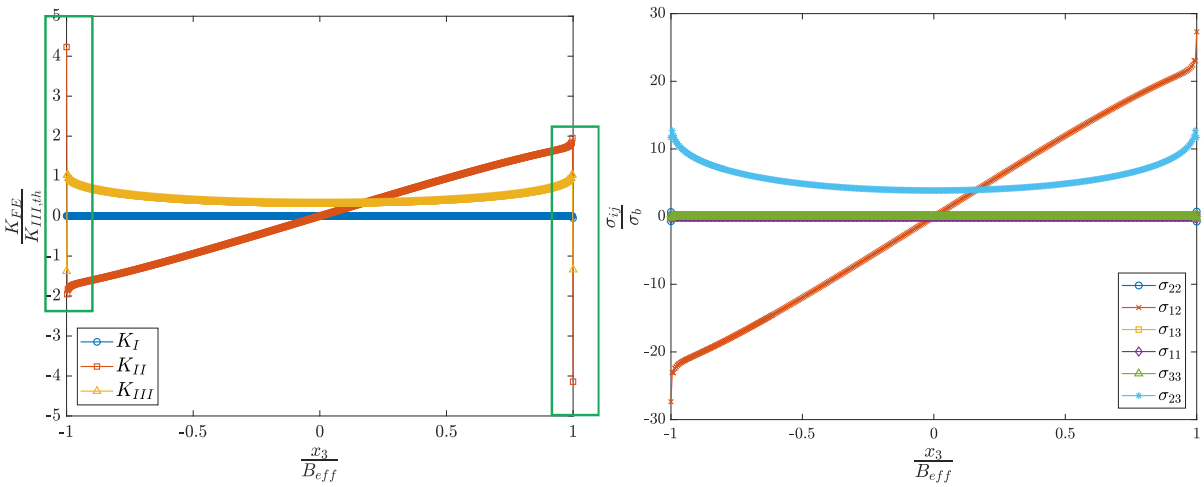

(a) **(b)**

Figure 6.5: Mode III-Effect of side-grooves: (a) SIF (b) stress (at $x_1 = 3.125\mu$m and $x_2 = 0$) components along the crack front for the Outward groove strategy.

The asymptotic, figure 6.6, and logarithmic, figure 6.7, plots of σ_{23} along the crack ligament show the failure of the linear solution at the free surface in logarithmic scale (figure 6.7(a)). σ_{23} is compressive at the free surface which leads to invalid values in the logarithmic plot. The negative σ_{23} was also observed in the effect of width and height; however, the only negative value belonged to the first element.

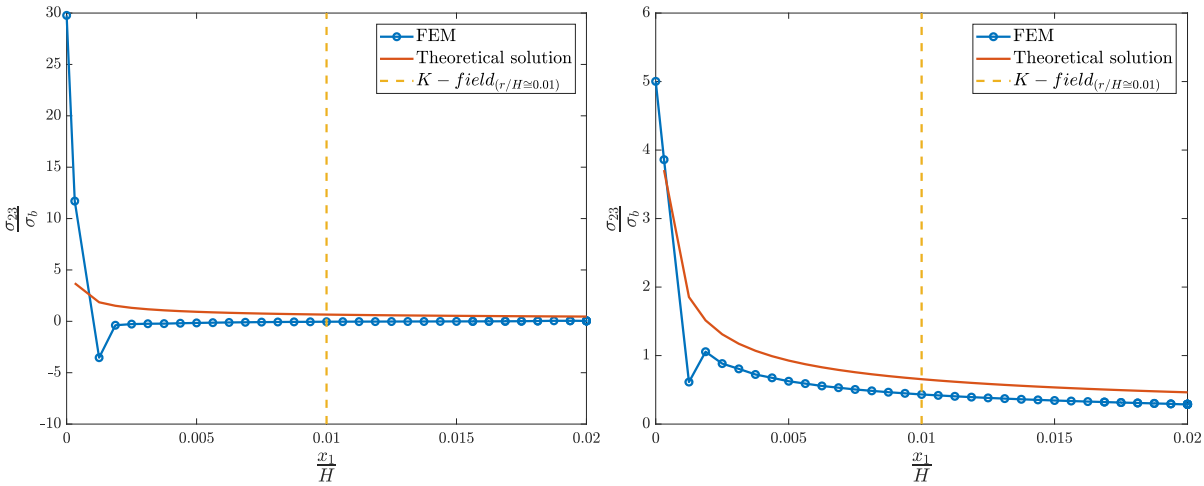

(a) **(b)**

Figure 6.6: Mode III-Effect of Outward groove: Asymptotic σ_{23} (a) at the free surface ($x_3 = \frac{B_{\text{eff}}}{2}$) (b) in the center ($x_3 = 0$) along the crack ligament ($\theta = 0$).

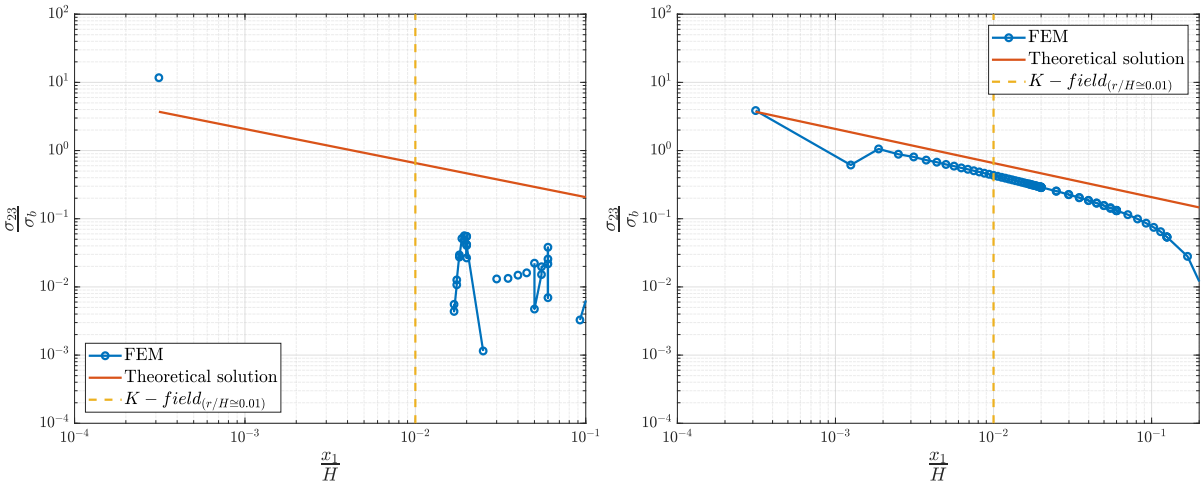

(a) **(b)**

Figure 6.7: Mode III-Effect of Outward groove: σ_{23} (a) at the free surface ($x_3 = \frac{B_{\text{eff}}}{2}$) (b) in the center ($x_3 = 0$) along the crack ligament ($\theta = 0$).

6.5 Inward against Outward Grooves

Figure 6.8 recap the FEM distributions of K_{II} and K_{III} for all the side-grooves. Table 6.1 summarizes λ values for the three side-groove strategies in the center and free surface of the specimen. As expected from figure 6.4, the best λ values are obtained by the Inward strategy. Comparing the obtained results from table 6.1 with Bogy (1971) shows that σ_{23} should be present on the vertex at the free surface for the Inward side-groove while there is no $1/\sqrt{r}$-singularity for the Outward side-groove. The λ values proposed by Bogy (1971) is also provided in table 6.1. The taper angle, shown in figure 6.1, from Bogy (1971) is different from the FE model for the Inward side-groove, however it still provide a good perspective.

Table 6.1: Mode III-Effect of side-grooves: λ values for different side-groove strategies at $\theta = 0$ (free surface and center correspond to $x_3 = \frac{B_{\text{eff}}}{2}$ and $x_3 = 0$, respectively).

Groove type	**λ proposed by Bogy (1971)**		**λ from current study**		
	Taper angle[deg]	**Free surface**	**Taper angle[deg]**	**Free surface**	**Center**
Inward	120	-0.384	112.5	-0.987	-0.5192
Outward	75	Not available	67.5	Not available	-0.5380
Inward curve	-	-	-	-1.528	-0.5301

Figure 6.9 shows σ_{23} contours where higher values occur at the free surface.

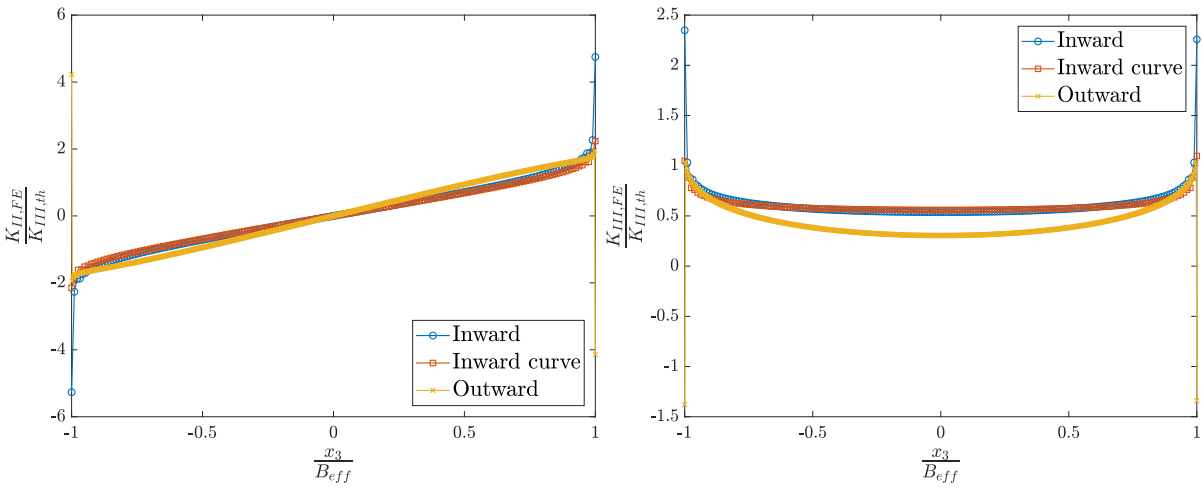

(a) **(b)**

Figure 6.8: Mode III-Effect of side-grooves: Distribution of (a) $K_{\mathrm{II,FE}}$ (b) $K_{\mathrm{III,FE}}$ through the crack front for side-groove strategies.

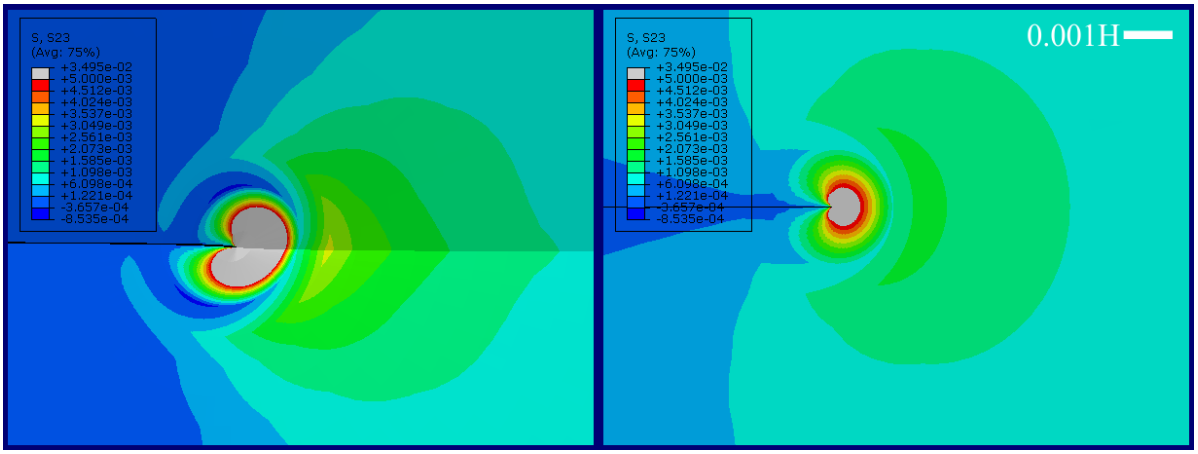

Figure 6.9: Mode III-Effect of side-grooves: Mode III σ_{23} contours at the free surface ($x_3 = \frac{B_{\mathrm{eff}}}{2}$, left) and in the center ($x_3 = 0$, right) for the Inward groove strategy.

Figure 6.10 and table 6.2 summarizes the dominant mode behind the crack in the vicinity and away from the crack tip.

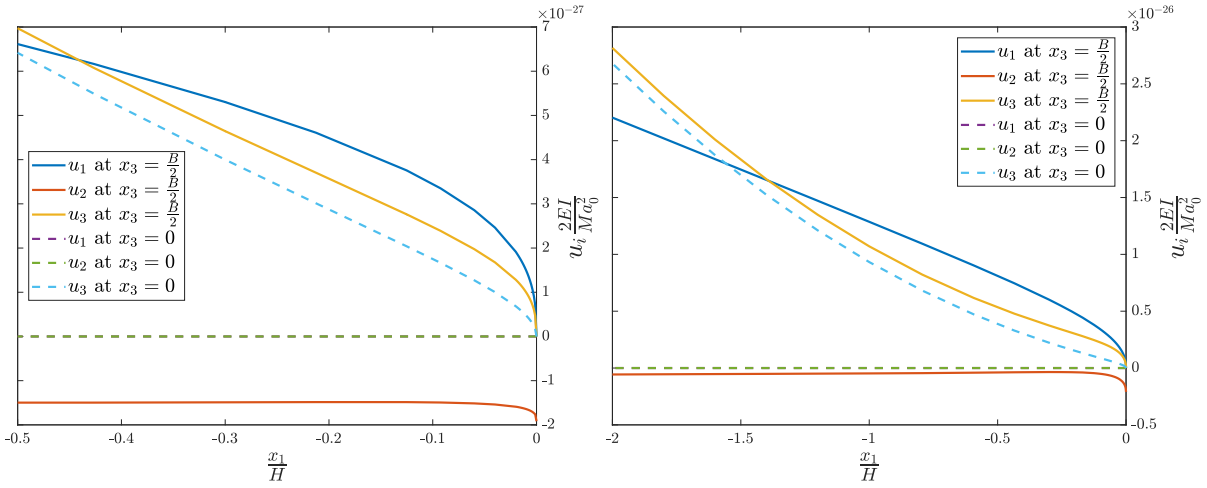

(a) **(b)**

Figure 6.10: Mode III-Effect of side-grooves: Specimen displacements behind the crack tip ($\theta = -\pi$) in the vicinity of the crack tip. (a) Inward (b) Outward side-grooves.

Table 6.2: Mode III-Effect of width: Dominant modes in the vicinity and far from the crack behind the crack tip at $\theta = -\pi$ for the side-groove strategies (free surface and center correspond to $x_3 = \frac{B_{\text{eff}}}{2}$ and $x_3 = 0$, respectively).

Side-groove type		The vicinity of the crack tip	Far from the crack tip
Inward	Free surface	Mode II	Mode III
	Center	Mode III	Mode III
Outward	Free surface	Mode II	Mode III
	Center	Mode III	Mode III
Inward curve	Free surface	Mode II	Mode III
	Center	Mode III	Mode III

6.6 Conclusion

- Shrinking the whole DCB specimen to a cylinder shown in figure 6.11 reveals admittedly that as long as there is a free surface, a coupling between mode II and III exist. Kotousov et al. (2013) named this coupling term as the "coupling mode II^c".
- According to the obtained result; in practice, if possible, material should be removed from the sides of the specimen. Adding material to the specimen in mode III fracture toughness testing specimens removes the $1/\sqrt{r}$-singularity. Figure 6.12 summaries the mode III SIF relative error and the portion of mode I and II w.r.t the mode III SIF obtained from FEM.

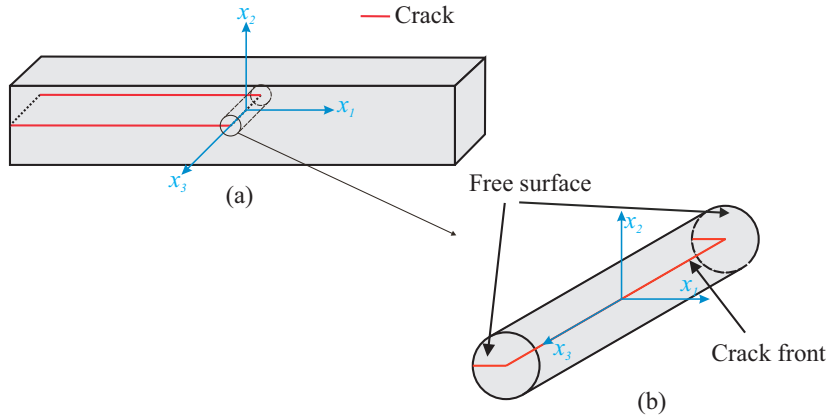

Figure 6.11: (a) Full (b) shrunken DCB model.

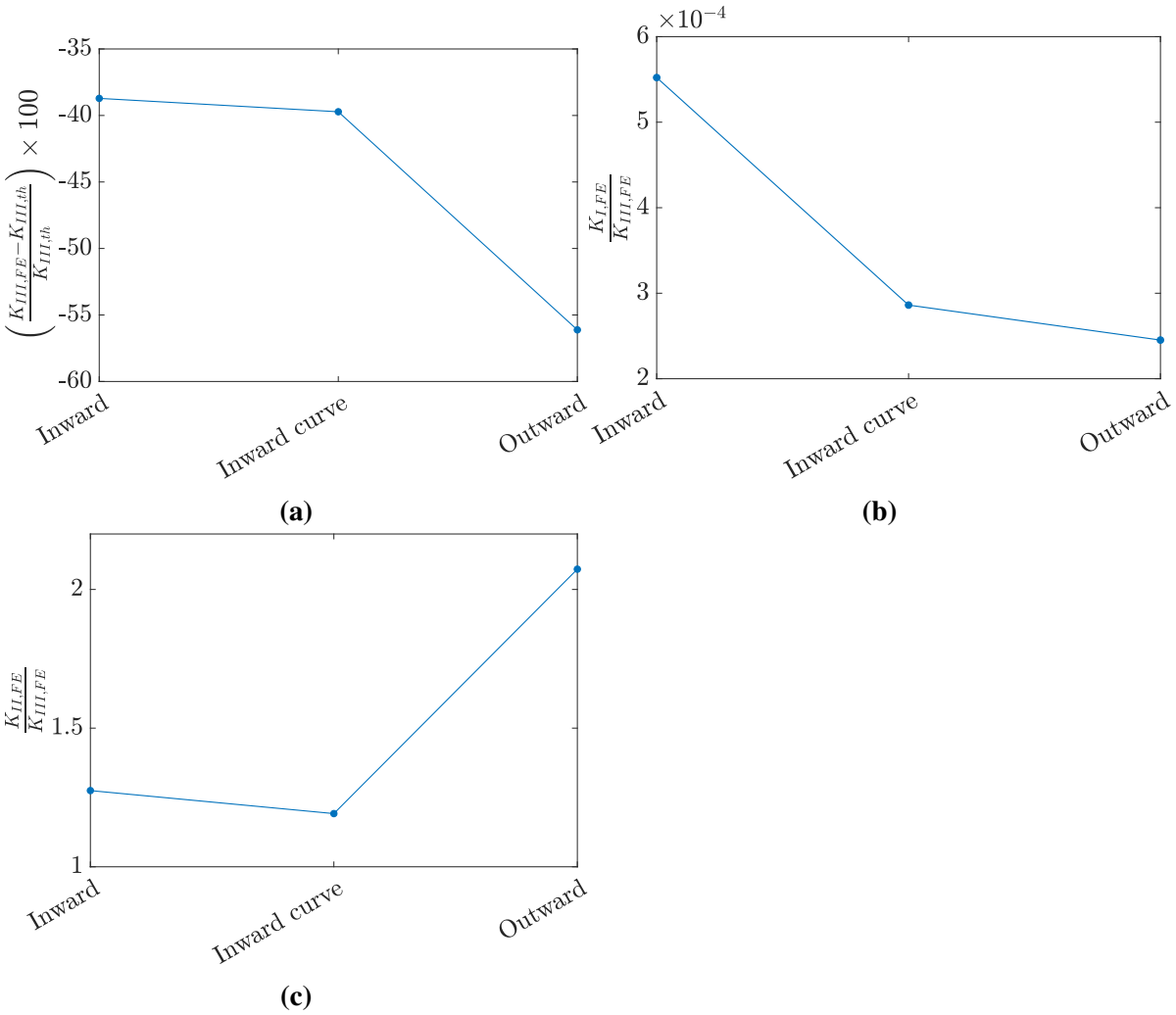

Figure 6.12: Mode III-Effect of side-grooves: Overview of the various side-groove strategies. (a) $K_{\mathrm{III,th}}$ and $K_{\mathrm{III,FE}}$ relative error (b) $\frac{K_{\mathrm{I,FE}}}{K_{\mathrm{III,FE}}}$ (c) $\frac{K_{\mathrm{II,FE}}}{K_{\mathrm{III,FE}}}$.

CHAPTER 7
Effect of Added Beams on K_{III}

So far it has been concluded that there is always a coupling mode II when the specimen undergoes the anti-plane loading. To reduce the effect of coupling mode II, in the present and next chapter several measures are taken into account. The current chapter is divided into two main sections. In the first, the effect of the elastic property of the added beams will be investigated. In the second, neutral axis of the DCB specimen is manipulated to study its effect on the coupling mode II.

7.1 Added Elastic Beams

The configurations of the added elastic beams are shown in figure 7.1. In the horizontal case (figure 7.1(a)), the elastic beams are added to the sides in the direction of shear loading. In the vertical case (figure 7.1(b)), the DCB specimen is sandwiched between two identical elastic beams. For the last case, the width of the horizontal beam changes while the elastic behavior is kept the same as the DCB specimen. The purpose of the third case is to shift the neutral axis in the x_3-direction to the added beams.

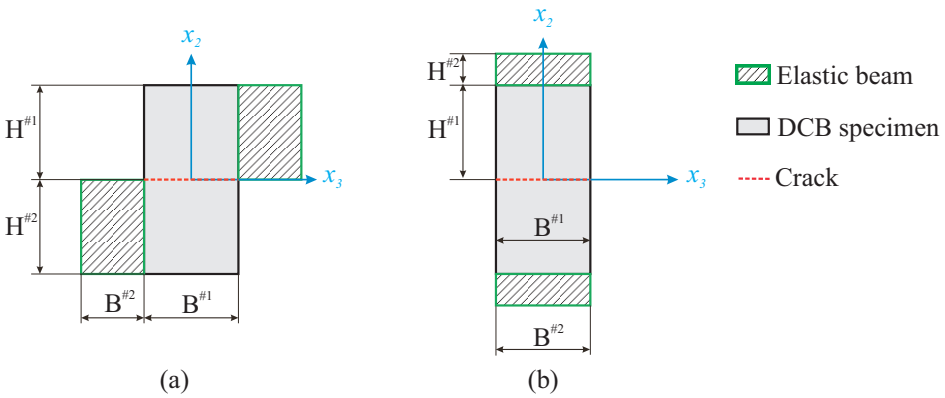

Figure 7.1: Mode III-Effect of added beams: Possible strategies (cross-sectional view). (a) Horizontal beams (b) Vertical beams (superscripts #1 and #2 refer to the DCB specimen and the elastic beam, respectively).

7.2 Finite Element Model

The previous method by the **Reference Point (RP)** and **Rigid body constraint** for the applied moments at the end of the specimen, cannot be utilized for the elastic beams because of

not generating the pure out-of-plane shear loading which is due to the difference in the elastic properties between the DCB specimen and elastic beams. As a result, the reaction moments around the x_1 and x_3 are non-zero. Instead, the prescribed displacement is exploited. In this approach, the **RP** and **Rigid body constraint** are replaced with the displacements shown in figure 7.2(a) and (b) at the specimen end. Two local coordinate systems are created on the top and bottom part of the cracked section of the specimen as illustrated in figure 7.2(a) and (b). Then, the displacement is applied by a line equation, $x_1 = mx_3$, where m is the magnitude. The applied displacements will cause the crack to open. The specimen dimensions and mechanical properties remain the same. The length and height of the elastic beams are similar to the DCB specimen while the elastic beam width is only half of the specimen. The Poisson's ratio for the elastic beam ,$\nu^{\#2}$, is assumed 0.28.

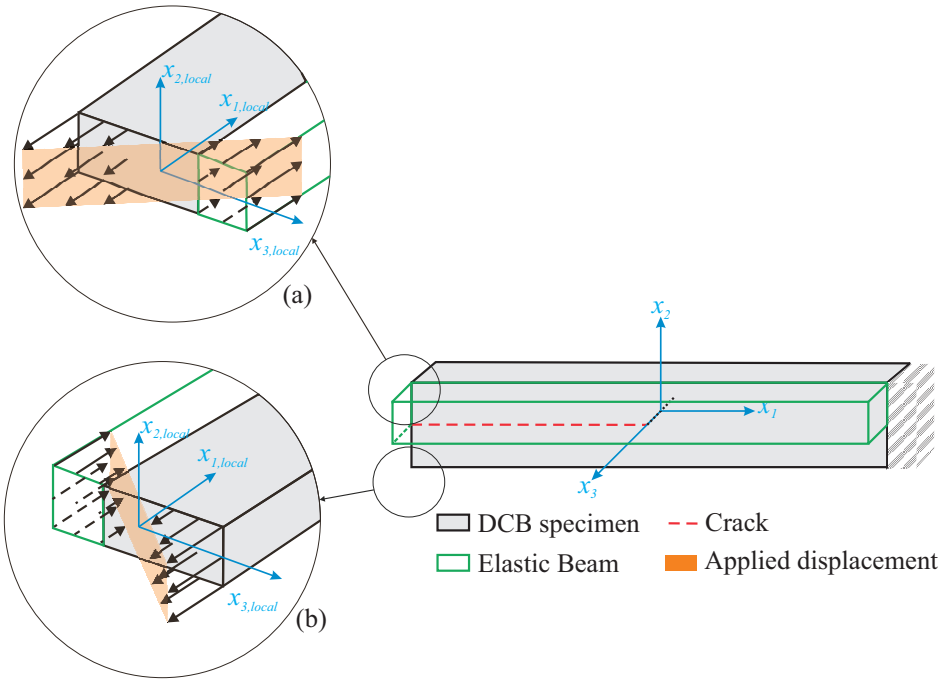

Figure 7.2: The DCB and horizontal elastic beam FE model under mode III using prescribed displacement. (a) Isometric view of the top configuration (b) Isometric view of the bottom configuration.

7.3 The J integral

Due to the prescribed displacements, the reaction moments are not valid in the ABAQUS output file. This is because of the zero values for the slopes in the nodal displacement vector. The method shown in figure 7.3 is used to calculate the reaction moment and J integral. According to the flowchart, u_3 in the position of $x_3 = \dfrac{B^{\#1}}{2}$ behind the crack ($\theta = -\pi$) in the x_1x_3 plane is extracted from FEM ($B^{\#1}$ is the DCB specimen width). Then, using a MATLAB script by Chernov (2018), a circle is fitted to u_3 based on Pratt (1987) method so that the radius of the curvature, ρ, can be determined. Next, the curvature, κ, is calculated from Eq.(7.1).

$$\kappa = \frac{1}{(\rho + B^{\#1} - \bar{x}_3)} \tag{7.1}$$

where $\bar{x}_3$ is the neural axis position along the x_3-direction calculated by shifting the coordinate system to $x_3 = -\dfrac{B^{\#1}}{2}$ for the ease of calculation. For the horizontal beam configuration, $\bar{x}_3$ is

$$\bar{x}_3 = \frac{E^{\#1}\left(\dfrac{B^{\#1}}{2}\right)B^{\#1}H^{\#1} + E^{\#2}\left(B^{\#1} + \dfrac{B^{\#2}}{2}\right)B^{\#2}H^{\#2}}{E^{\#1}B^{\#1}H^{\#1} + E^{\#2}B^{\#2}H^{\#2}} \tag{7.2}$$

and for the vertical configuration

$$\bar{x}_3 = \frac{E^{\#1}\left(\dfrac{B^{\#1}}{2}\right)B^{\#1}H^{\#1} + E^{\#2}\left(\dfrac{B^{\#2}}{2}\right)B^{\#2}H^{\#2}}{E^{\#1}B^{\#1}H^{\#1} + E^{\#2}B^{\#2}H^{\#2}} \tag{7.3}$$

The superscripts #1 and #2 denote the DCB and the elastic beam, respectively. After that, The equivalent cross-sectional second moment of area, I, is calculated from Eq.(7.4). In the second moment of area calculation, the coordinate system is set back to its original position in the middle of the DCB specimen.

$$\begin{aligned} I^{\#1} &= \frac{1}{12}H^{\#1}{B^{\#1}}^3 + H^{\#1}B^{\#1}\left(\bar{x}_3 - \frac{B}{2}\right)^2 \\ I^{\#2} &= \frac{1}{12}\left(\frac{E^{\#2}}{E^{\#1}}H^{\#2}\right){B^{\#2}}^3 + \left(\frac{E^{\#2}}{E^{\#1}}H^{\#2}\right)B^{\#2}\left(B^{\#1} + \frac{B^{\#2}}{2} - \bar{x}_3\right)^2 \\ I &= I^{\#1} + I^{\#2} \end{aligned} \tag{7.4}$$

The moment, M, for the J integral is determined from Eq.(7.5) and when inserted into Eq.(5.1), the width and height are converted in the form of second moment of area, the J integral can be written as Eq.(7.6).

$$M = \kappa E^{\#1} I \tag{7.5}$$

$$J = \frac{12M^2}{E^{\#1}{B^{\#1}}^4 H} = \frac{M^2}{E^{\#1}B^{\#1}I} \tag{7.6}$$

Finally, $K_{\mathrm{III,th}}$ is calculated from the procedure explained in figure 5.3.

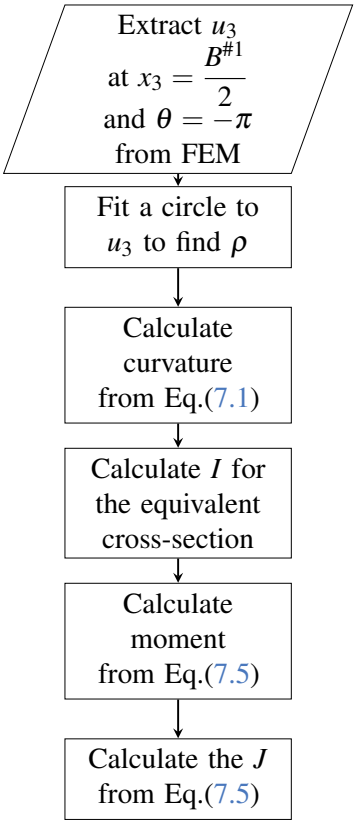

Figure 7.3: The effect of added elastic beams: The flowchart for calculating the J integral.

7.4 Effect of Added Horizontal Elastic Beams

The ABAQUS J integral code terminates if there exists a wedge element (figure 7.4(b)) inside the contour integral. By mirroring the mesh from the DCB specimen to the elastic beam, wedge elements (C3D15) are generated at the vertex of the elastic beam where it is connected to the DCB specimen $\left(x_3 = \pm\frac{B^{\#1}}{2}\right)$ as demonstrated in figure 7.4(a). Therefore, ABAQUS J integral terminates the analysis. ABAQUS is able to create the quadratic elements (C3D20) in the presence of the collapsed elements when the mid-nodes are shifted to the quarter point in the crack definition dialogue box in the ABAQUS CAE[1], unless the wedge elements are created. A good mesh transition from the DCB specimen to the elastic beam requires manual modifications in the ABAQUS input file that is beyond the scope of this study. Consequently, in the following, because of the above-mentioned issue, the beams are meshed with quadratic elements (C3D20) in the form of cubes which along with the different elastic properties of the DCB specimen and the elastic beam make the calculation of the stresses on the free surfaces $\left(x_3 = \pm\frac{B^{\#1}}{2}\right)$ difficult for ABAQUS. As a result, σ_{23} instead of the free surface is extracted in from a plane within a distance of d=0.0625mm from the free surface

[1] ABAQUS CAE is the ABAQUS Graphic User Interface (GUI).

$\left(x_3 = \pm\frac{B^{\#1}}{2} \mp 0.0625\text{mm}\right)$ as illustrated in figure 7.5. $x_3 = \pm\frac{B^{\#1}}{2} \mp 0.0625$mm in the mid-node of the first row of the elements at the free surface shown in figure 7.5.

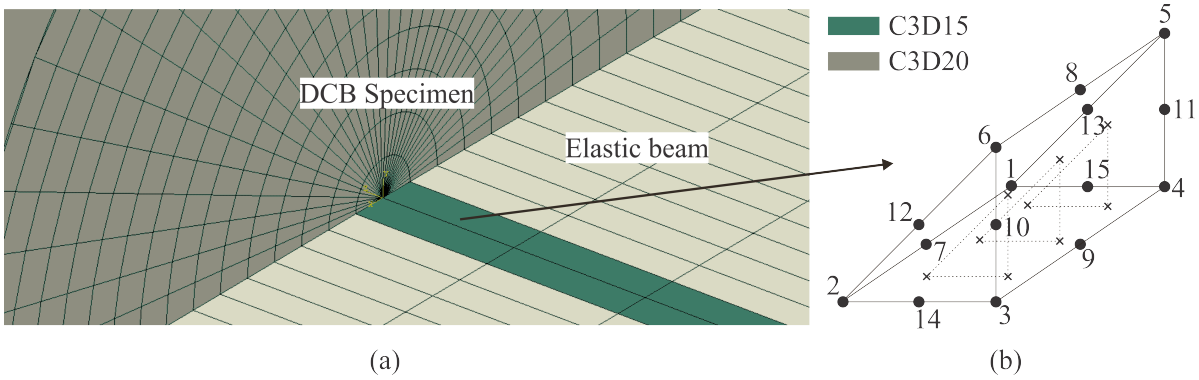

Figure 7.4: (a) The wedge elements (C3D15) inside the elastic beam created at the vertex of the DCB specimen (b) C3D15 element which has 15 nodes and 9 integration points terminates the ABAQUS *J* integral.

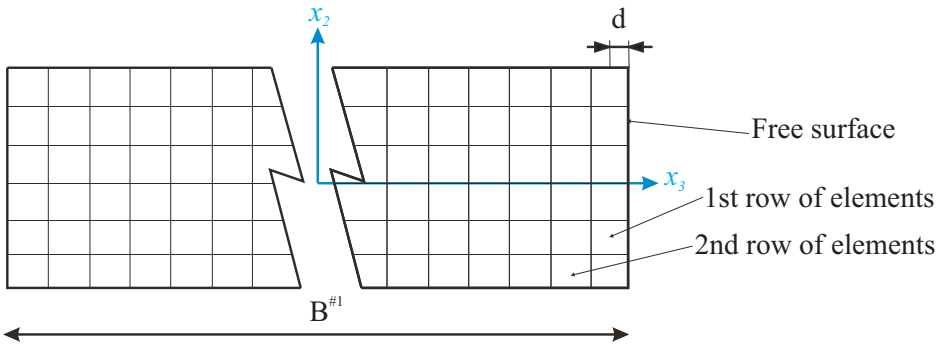

Figure 7.5: Schematic of the distance from the free surface, d.

The elastic behavior of the horizontal beams is influenced by increasing their Young's modulus. The analyses have been conducted for the $\frac{E^{\#2}}{E^{\#1}}$ ratios of 2, 3, 4 and 5. Although the obtained results are similar, the differences will be explained accordingly. The distribution of the SIF and stresses through the specimen width are shown in figure 7.6. The obtained results show the non-zero and larger σ_{22} compared to the previous scenarios; however, $K_{\text{I,FE}}$ is negative that is $K_{\text{I,FE}}$=0.

The asymptotic, figure 7.7, and logarithmic, figure 7.8, plots from FEM show a good agreement with the theoretical solution both at the free surface and center compared to the previously obtained results.

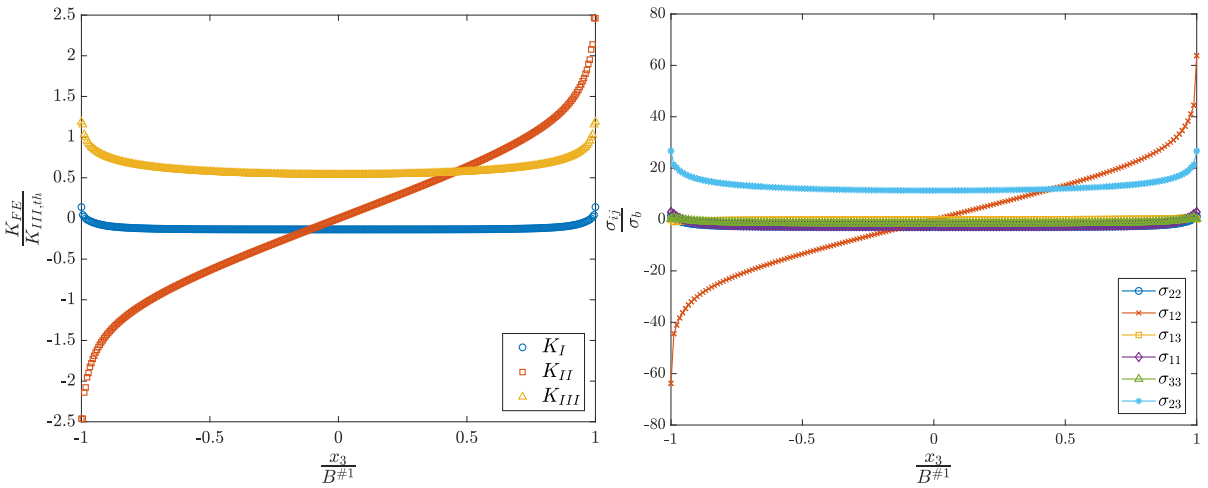

(a) **(b)**

Figure 7.6: Mode III-Effect of horizontal elastic beams: (a) SIF (b) stress (at $x_1 = 3.125\mu$m and $x_2 = 0$) components along the crack front for $\frac{E^{\#2}}{E^{\#1}}$=2 and $\frac{B^{\#2}}{B^{\#1}} = \frac{1}{2}$.

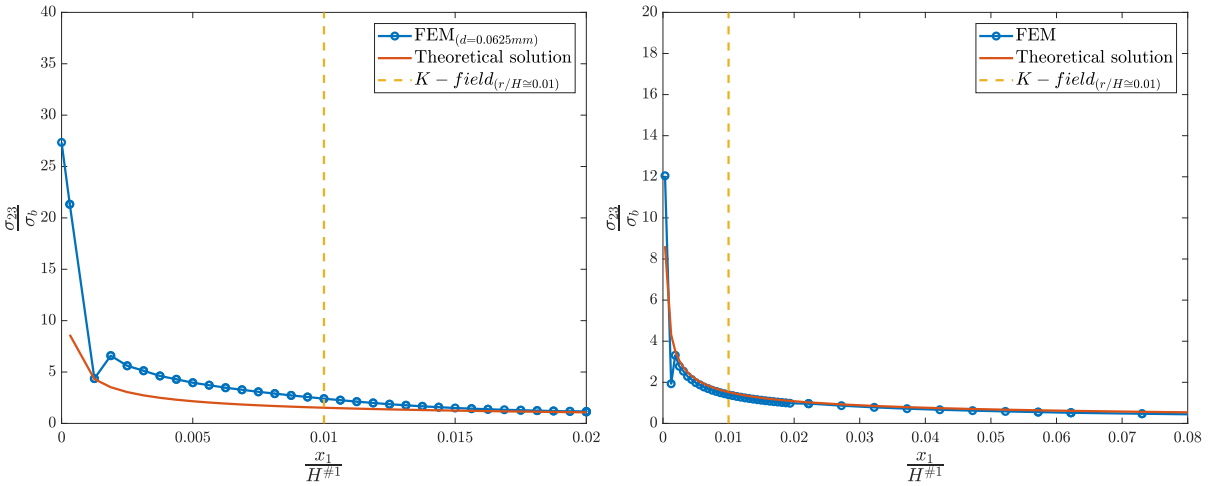

(a) **(b)**

Figure 7.7: Mode III-Effect of horizontal elastic beams: Asymptotic σ_{23} (a) near the free surface ($x_3 = \frac{B^{\#1}}{2} -$ 0.0625mm) (b) in the center ($x_3 = 0$) along the crack ligament ($\theta = 0$) for $\frac{E^{\#2}}{E^{\#1}}$=2 and $\frac{B^{\#2}}{B^{\#1}} = \frac{1}{2}$.

Another interesting observation occurs when the neutral axis in the x_3-direction is located inside the elastic beam. The $0.01H$ criterion for the K-dominated zone size by Charalambides et al. (1992) is influenced which brings this fact that it cannot provide an estimation of the K-dominated zone size when the neutral axis in the x_3-direction is outside the DCB specimen (figure 7.9). For the $\frac{E^{\#2}}{E^{\#1}}$ ratios which shifts the neural axis outside the DCB specimen, the

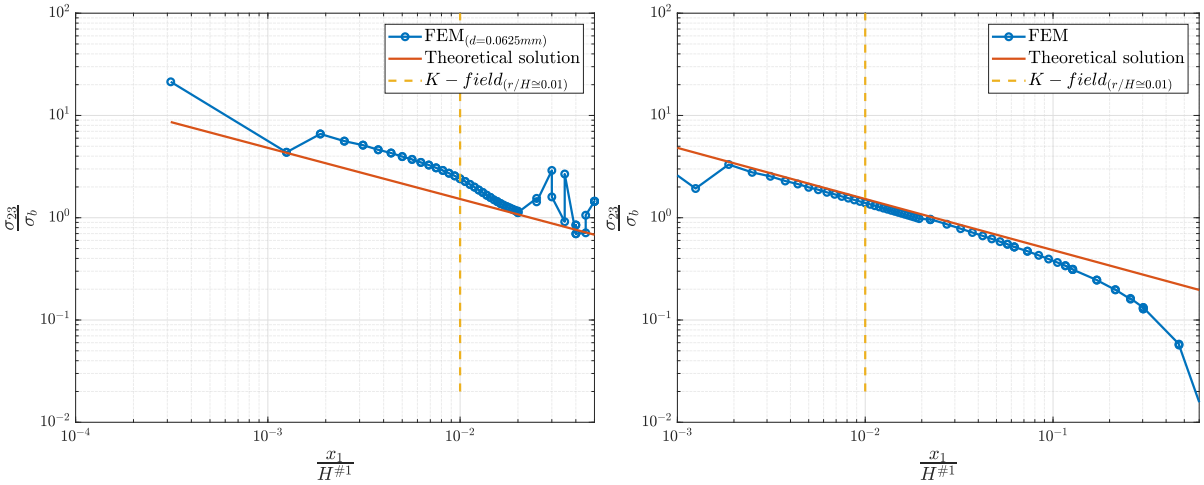

(a) **(b)**

Figure 7.8: Mode III-Effect of horizontal elastic beams: Logarithmic σ_{23} (a) near the free surface ($x_3 = \frac{B^{\#1}}{2} -$ 0.0625mm) (b) in the center ($x_3 = 0$) along the crack ligament ($\theta = 0$) for $\frac{E^{\#2}}{E^{\#1}}$=2 and $\frac{B^{\#2}}{B^{\#1}} = \frac{1}{2}$.

FEM requires a finer mesh in the x_1-direction focused at the crack tip. The lower number of elements inside the K-field$_{(\mathrm{r/H}\cong 0.01)}$ is visible in figure 7.9.

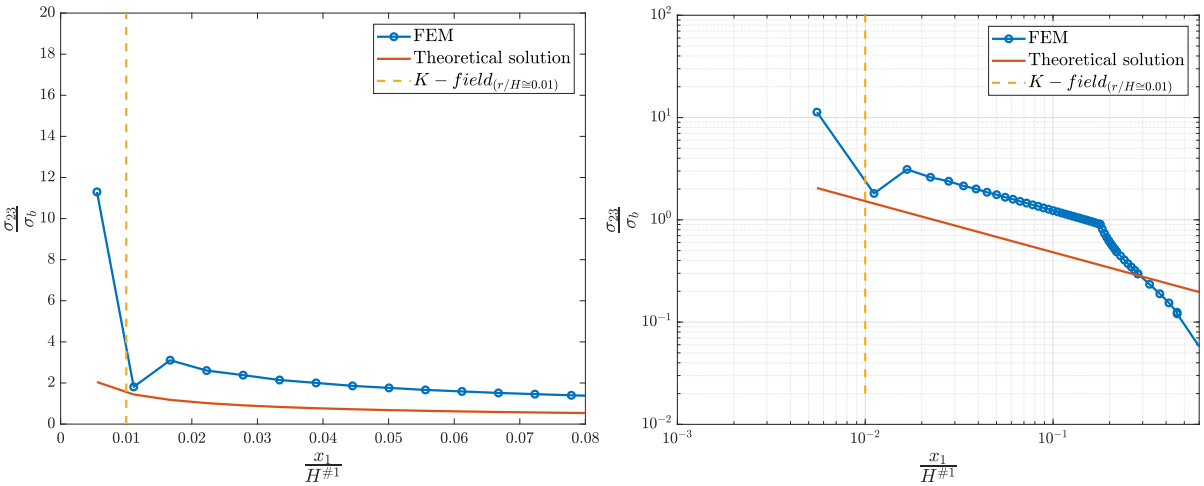

(a) **(b)**

Figure 7.9: Mode III-Effect of horizontal elastic beams: (a) Asymptotic (b) logarithmic σ_{23} along the crack ligament ($\theta = 0$) in the specimen center ($x_3 = 0$) for $\frac{E^{\#2}}{E^{\#1}}$=5 and $\frac{B^{\#2}}{B^{\#1}} = \frac{1}{2}$.

Plotting the distribution of K_{II} and K_{III} along the crack width, figure 7.10, make it difficult to observe any improvement made by increasing the beam elastic property.

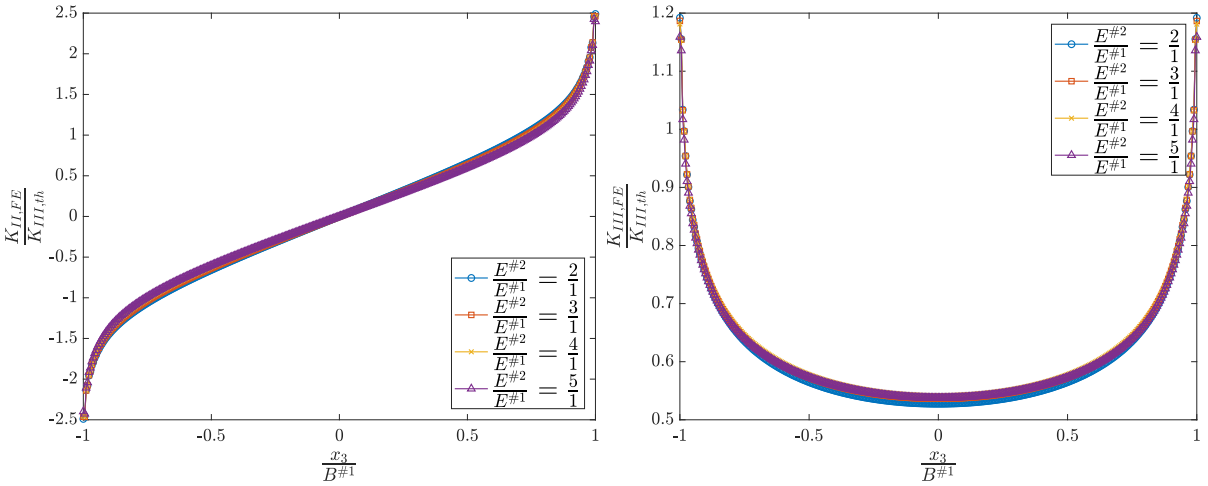

(a) **(b)**

Figure 7.10: Mode III-Effect of horizontal elastic beams: Distribution of (a) $K_{\text{II,FE}}$ (b) $K_{\text{III,FE}}$ through the crack front for different $\frac{E^{\#2}}{E^{\#1}}$ ratios, $\frac{B^{\#2}}{B^{\#1}} = \frac{1}{2}$.

7.5 Effect of Added Vertical Elastic Beams

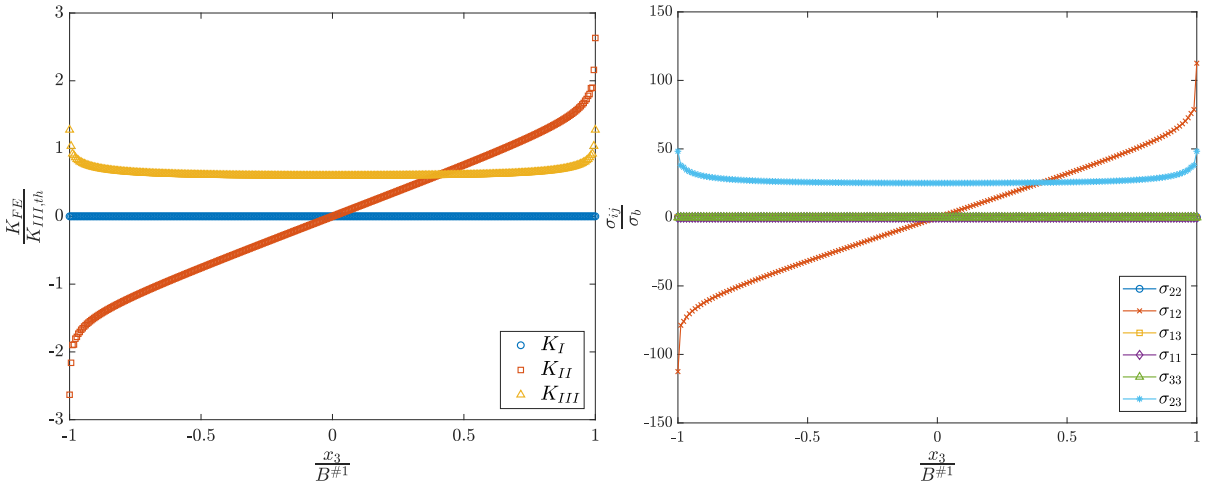

(a) **(b)**

Figure 7.11: Mode III-Effect of vertical elastic beams: (a) SIF (b) stress (at $x_1 = 3.125\mu$m and $x_2 = 0$) components along the crack front for $\frac{E^{\#2}}{E^{\#1}}$=5 and $\frac{H^{\#2}}{H^{\#1}} = 1$.

In the following, the results for the $\frac{E^{\#2}}{E^{\#1}}$=5 will be discussed. The distribution of the SIF and stresses along the crack front, figure 7.11, is similar to the horizontal beams case. From the asymptotic and logarithmic plots (figures 7.12 and 7.13), once more it can be seen that by increasing the $\frac{E^{\#2}}{E^{\#1}}$ ratio, there are fewer elements that remains within the K-field$_{(\text{r/H}\cong 0.01)}$

criterion; thus, by increasing the elastic beam Young's modulus, the FEM demands a model with a higher mesh density at the crack front in the x_3-direction.

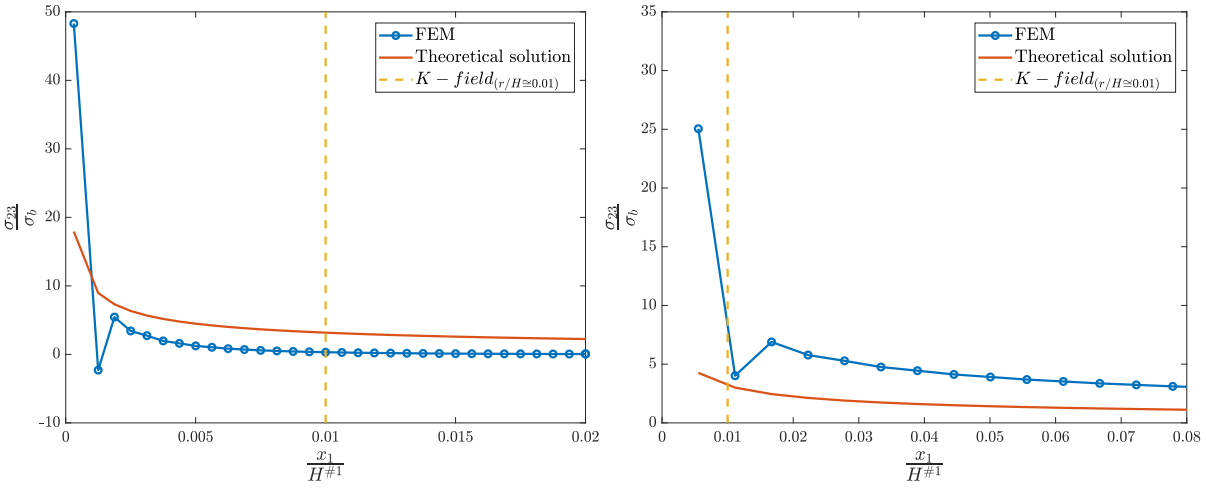

Figure 7.12: Mode III-Effect of vertical elastic beams: Asymptotic σ_{23} (a) at the free surface ($x_3 = \frac{B^{\#1}}{2}$) (b) in the center ($x_3 = 0$) along the crack ligament ($\theta = 0$) for $\frac{E^{\#2}}{E^{\#1}}$=5 and $\frac{H^{\#2}}{H^{\#1}} = 1$.

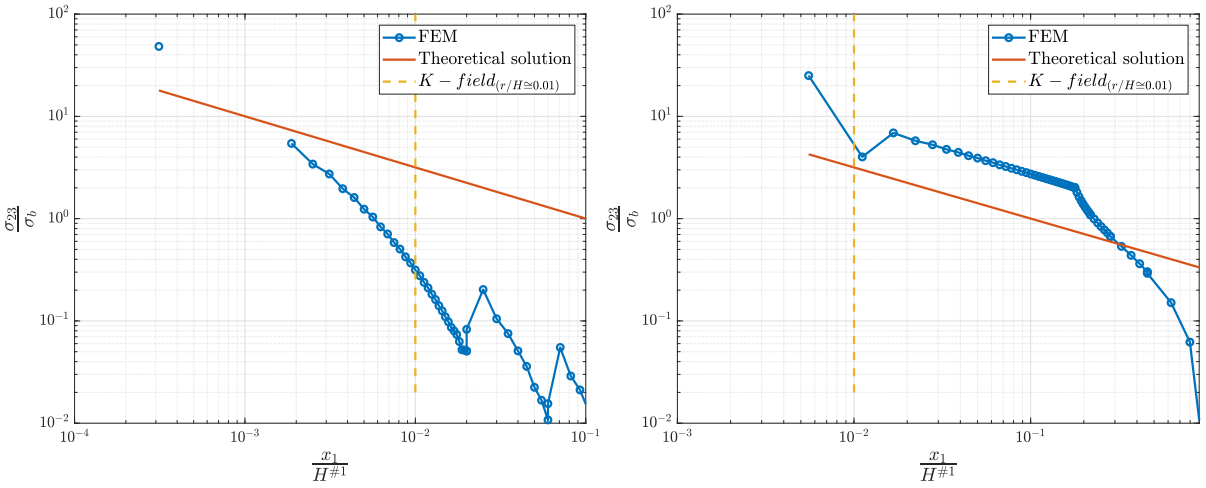

Figure 7.13: Mode III-Effect of vertical elastic beams: Logarithmic σ_{23} (a) at the free surface ($x_3 = \frac{B^{\#1}}{2}$) (b) in the center ($x_3 = 0$) along the crack ligament ($\theta = 0$) for $\frac{E^{\#2}}{E^{\#1}}$=5 and $\frac{H^{\#2}}{H^{\#1}} = 1$.

To provide a comparison between the horizontal and vertical cases for the elastic beams, σ_{23} is also extracted from a distance of d=0.0625mm from the free surface for the vertical elastic beams so that the singularity exponent, λ, can be compared at the free surface and a

distance close to that. Figure 7.14 illustrates the difference in the two aforementioned locations. Very close to the free surface, σ_{23} is always positive in the vicinity of the crack and the linear behavior in the logarithmic scale is much pronounced. Table 7.1 summarizes the λ values at the free surface ($x_3 = \frac{B^{\#1}}{2}$), d=0.0625mm from the free surface (demonstrated in figure 7.5) and center ($x_3 = 0$). There is a remarkable drop in λ from approximately -1.9 evaluated at $x_3 = \frac{B^{\#1}}{2}$ to approximately -0.72 at $x_3 = \frac{B^{\#1}}{2} - 0.0625$mm. To sum up, it appears that singularity exponent might differ from $x_3 = \frac{B^{\#1}}{2}$ to $x_3 = \frac{B^{\#1}}{2} - 0.0625$mm which requires a dedicated model with a very fine mesh at the free surface in the x_3-direction.

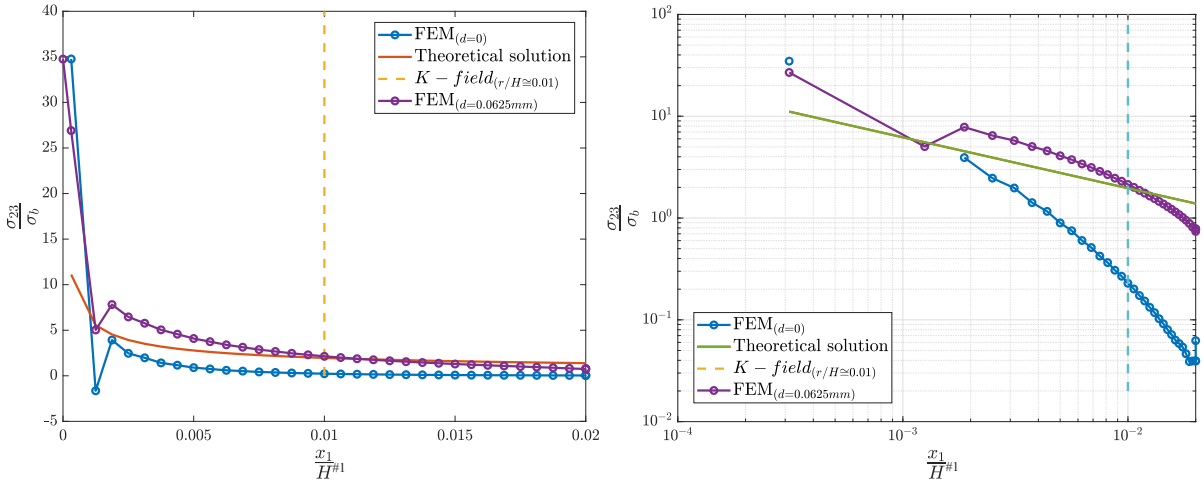

Figure 7.14: Mode III-Effect of vertical elastic beams: (a) Asymptotic (b) logarithmic σ_{23} along the crack ligament ($\theta = 0$) at $x_3 = \frac{B^{\#1}}{2}$ and $x_3 = \frac{B^{\#1}}{2} - 0.0625$mm for $\frac{E^{\#2}}{E^{\#1}}$=5 and $\frac{H^{\#2}}{H^{\#1}} = 1$.

Table 7.1: Mode III-Effect of added elastic beams: λ values for different $\frac{E^{\#2}}{E^{\#1}}$ ratios at $\theta = 0$ (free surface and center correspond to $x_3 = \frac{B^{\#1}}{2}$ and $x_3 = 0$, respectively). For the horizontal elastic beams, $\frac{B^{\#2}}{B^{\#1}} = \frac{1}{2}$ and for the vertical elastic beams, $\frac{H^{\#2}}{H^{\#1}} = 1$.

$\frac{E^{\#2}}{E^{\#1}}$	λ(Horizontal elastic beams)			λ(Vertical elastic beams)		
	Free surface	**d=0.0625mm**	**Center**	**Free surface**	**d=0.0625mm**	**Center**
2	-	-0.6446	-0.5245	-1.941	-0.7263	-0.5263
3	-	-0.6388	-0.5239	-1.944	-0.7269	-0.5250
4	-	-0.6354	-0.5241	-1.946	-0.7275	-0.5241
5	-	-0.6332	-0.5239	-1.947	-0.7279	-0.5234

The FE distribution of K_{II} and K_{III} for various elastic ratios is given in figure 7.15. K_{II} remains unchanged whereas, K_{III} distribution in the 50% of the middle span steps up.

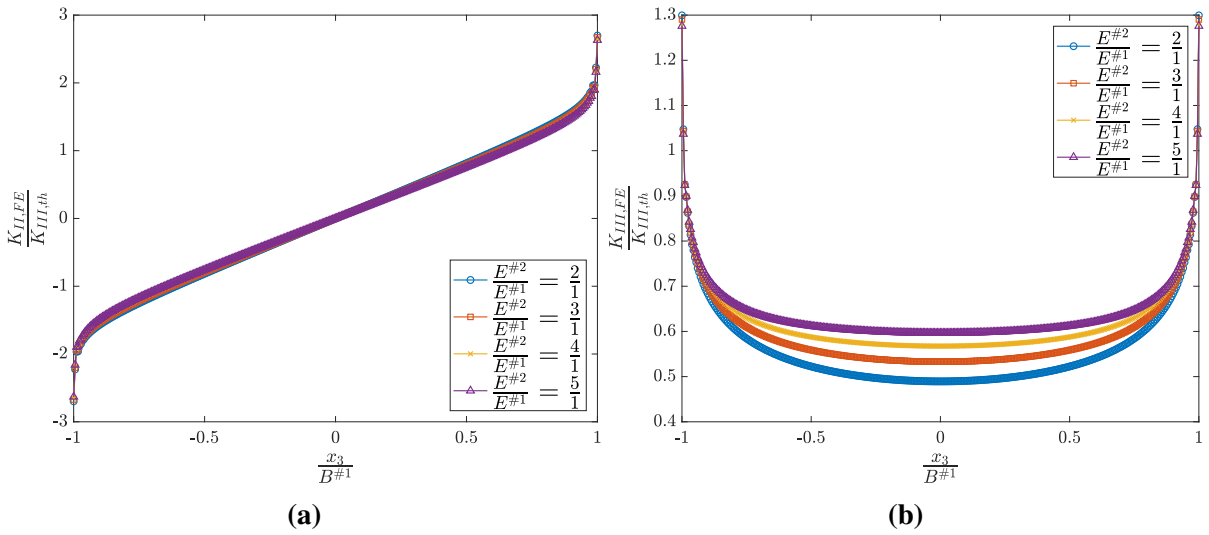

Figure 7.15: Mode III-Effect of vertical elastic beams: Distribution of (a) $K_{\text{II,FE}}$ (b) $K_{\text{III,FE}}$ through the crack front for different $\frac{E^{\#2}}{E^{\#1}}$ ratios, $\frac{H^{\#2}}{H^{\#1}} = 1$.

7.6 Effect of Added Horizontal Varying Width Beams

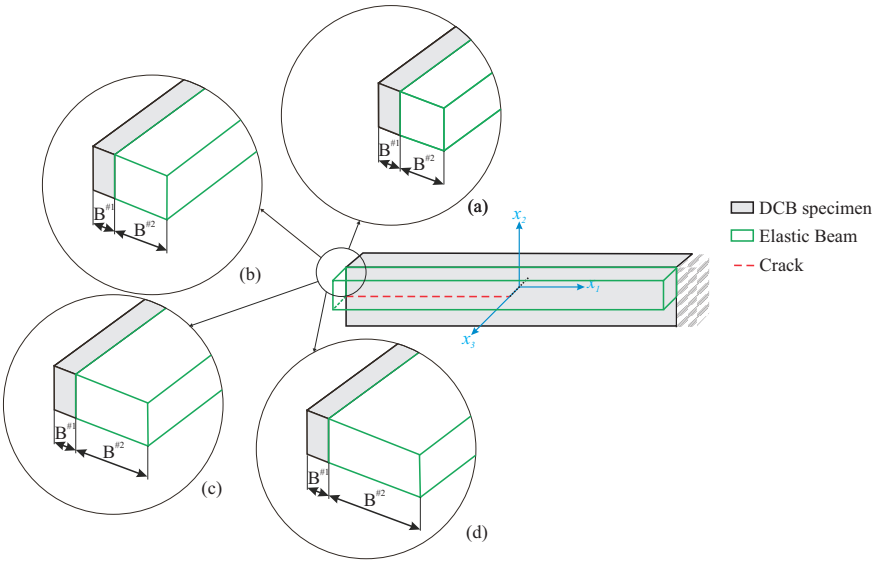

Figure 7.16: Mode III-Effect of horizontal varying width: The DCB and horizontal elastic beams. For all the cases $\frac{E^{\#2}}{E^{\#1}} = 1$ and $\frac{H^{\#2}}{H^{\#1}} = 1$. (a) $\frac{B^{\#2}}{B^{\#1}} = 2$ (b) $\frac{B^{\#2}}{B^{\#1}} = 3$ (c) $\frac{B^{\#2}}{B^{\#1}} = 4$ (d) $\frac{B^{\#2}}{B^{\#1}} = 5$.

"Horizontal Varying Width Beams" refers to the similar added horizontal beams that their elastic behaviour is constant (for all the cases $\frac{E^{\#2}}{E^{\#1}}$=1) while their width w.r.t to the DCB spec-

imen , $\frac{B^{\#2}}{B^{\#1}}$, along the x_3-direction changes from 2 to 5. Figure 7.16 illustrates all the strategies for the "Horizontal Varying Width Beams".

The distribution of the SIF and different stress components through the crack width is shown in figure 7.17. The first noticeable difference compared to the horizontal and vertical elastic beams is the higher σ_{22} values which are negative except for a distance close to the free surface. Another worth-mentioning observation is the constant σ_{23} along the width. There is a drop in σ_{23} at the free surface that does not vanish with a very fine mesh, in the x_3-direction, near the free surfaces. The coupling mode II prevails as before.

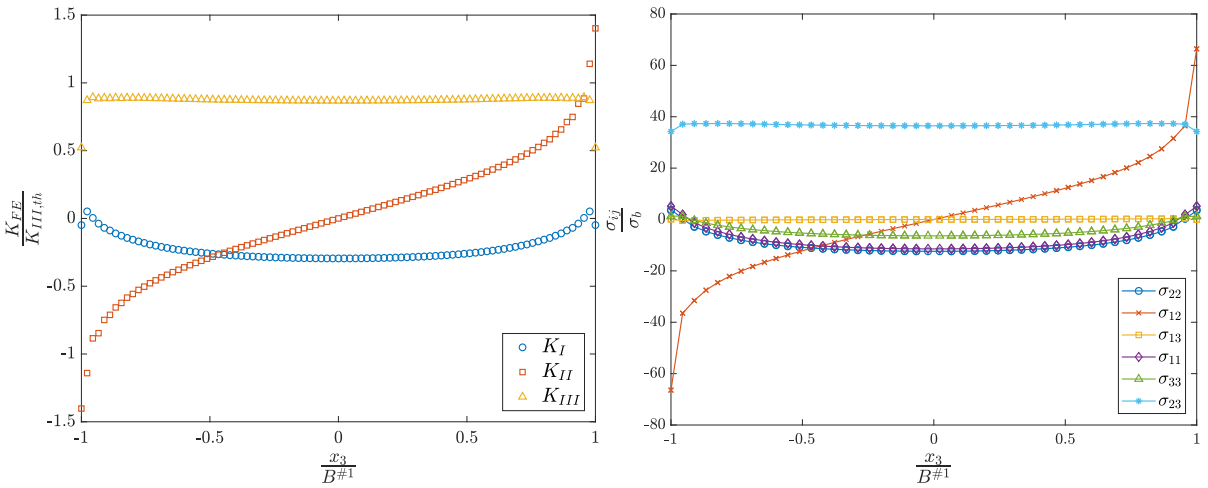

(a) **(b)**

Figure 7.17: Mode III-Effect of horizontal varying width: (a) SIF (b) stress (at $x_1 = 3.125\mu$m and $x_2 = 0$) components along the crack front for $\frac{B^{\#2}}{B^{\#1}}$=5 and $\frac{E^{\#2}}{E^{\#1}} = 1$.

Due to the oscillatory behavior of σ_{23} along the ligament, the corresponding values are extracted from a distance of d=0.0111mm from the free surface. Once more, few elements are fitted in the K-field$_{(r/H\cong 0.01)}$ criterion. The size of the K-dominated zone seems to become larger in the center (figures 7.18 and 7.19).

Plotting the distribution of the K_{II}, 7.20(a), for various $\frac{B^{\#2}}{B^{\#1}}$ ratios, it appears on the surface that the coupling mode II effect vanishes when $B^{\#2}$ goes to infinity. However, the non-normalized plots show that the coupling mode is not affected at all and the increase in $K_{III,th}$ makes this illusion. For all the cases in figure 7.20(b), a sudden drop in $K_{III,FE}$ is clearly visible at the free surfaces.

λ values for the case of horizontal varying width are given in table 7.2. The horizontal varying width case provides better results for the singularity exponent than the horizontal elastic beams.

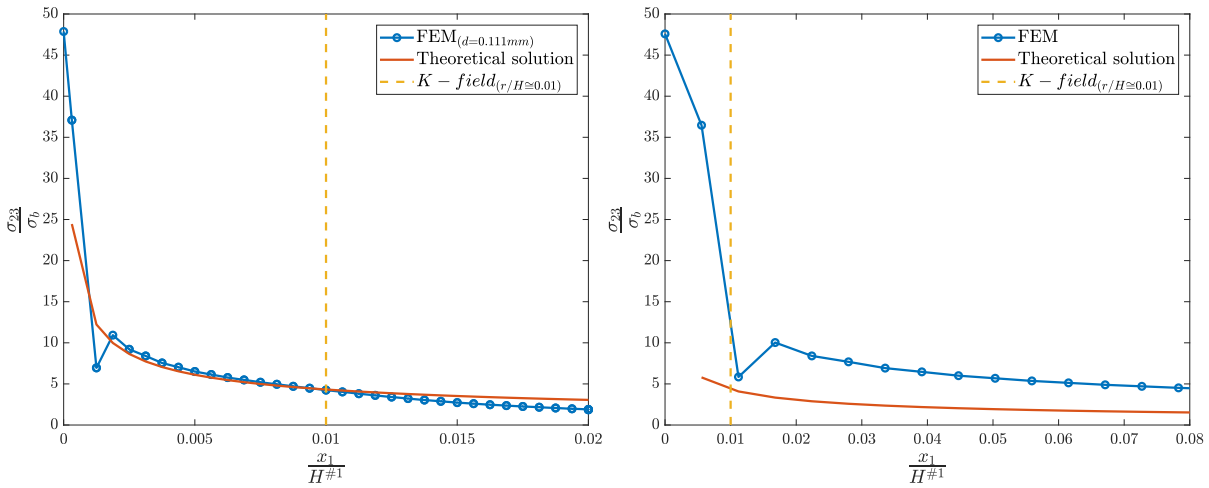

(a) **(b)**

Figure 7.18: Mode III-Effect of horizontal varying width: Asymptotic σ_{23} (a) near the free surface ($x_3 = \frac{B^{\#1}}{2} - 0.0111$mm) (b) in the center ($x_3 = 0$) along the crack ligament ($\theta = 0$) for $\frac{B^{\#2}}{B^{\#1}}$=5 and $\frac{E^{\#2}}{E^{\#1}} = 1$.

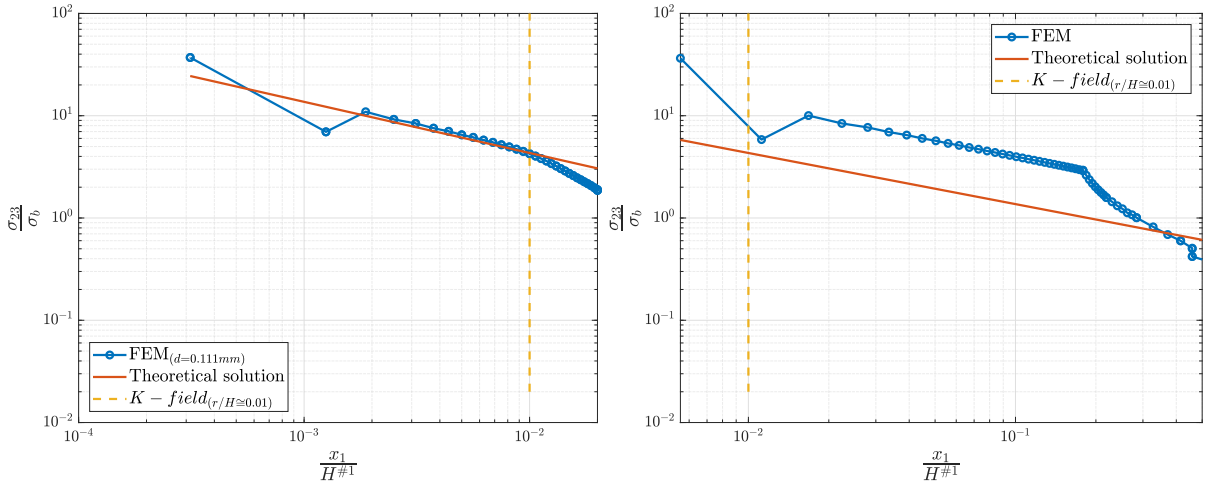

(a) **(b)**

Figure 7.19: Mode III-Effect of horizontal varying width: Logarithmic σ_{23} (a) near the free surface ($x_3 = \frac{B^{\#1}}{2} - 0.0111$mm) (b) in the center ($x_3 = 0$) along the crack ligament ($\theta = 0$) for $\frac{B^{\#2}}{B^{\#1}}$=5 and $\frac{E^{\#2}}{E^{\#1}} = 1$.

Table 7.2: Mode III-Effect of horizontal varying width: λ values for different $\frac{B^{\#2}}{B^{\#1}}$ ratios at $\theta = 0$, $\frac{E^{\#2}}{E^{\#1}} = 1$ (free surface and center correspond to $x_3 = \frac{B^{\#1}}{2}$ and $x_3 = 0$, respectively).

$\frac{B^{\#2}}{B^{\#1}}$	λ		
	Free surface	***d*=0.111mm**	**Center**
2	-	-0.6923	-0.5279
3	-	-0.6899	-0.5257
4	-	-0.6871	-0.5125
5	-	-0.6865	-0.5115

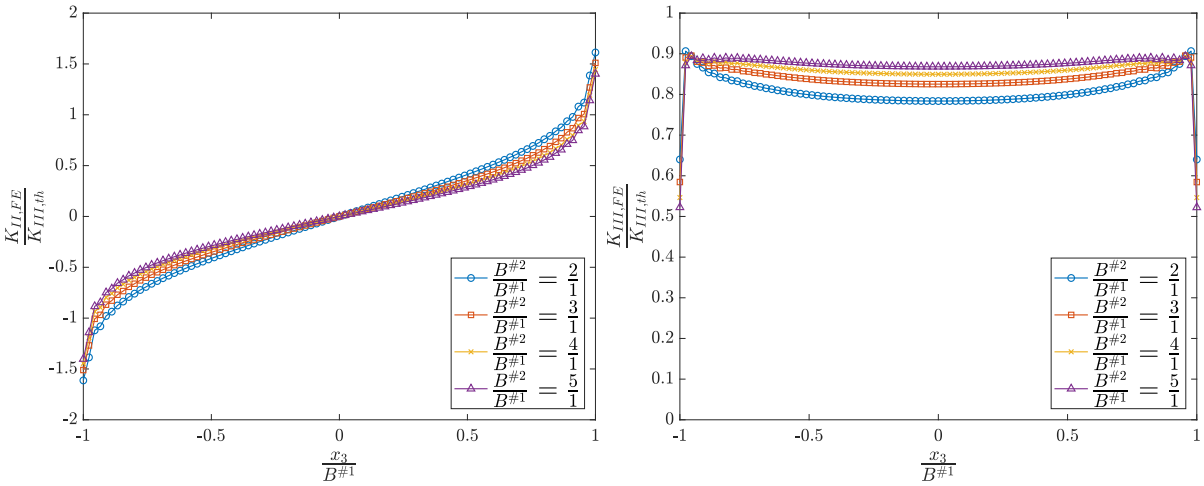

(a) **(b)**

Figure 7.20: Mode III-Effect of vertical elastic beams: Distribution of (a) $K_{\mathrm{II,FE}}$ (b) $K_{\mathrm{III,FE}}$ through the crack front for different $\frac{B^{\#2}}{B^{\#1}}$ ratios, $\frac{E^{\#2}}{E^{\#1}} = 1$.

7.7 Stress Contours and Dominant Modes

The σ_{23} contours for all the strategies, figure 7.21 to 7.23, show higher stress at the free surface which indicates that the elastic beam did not change the way of crack opening. According to figures 7.21 to 7.23, the region where the specimen experience the higher stress value (gray-shaded area in figures 7.21 to 7.23) is larger at the free surface than the specimen center; therefore, the crack propagates from the edges to the specimen center.

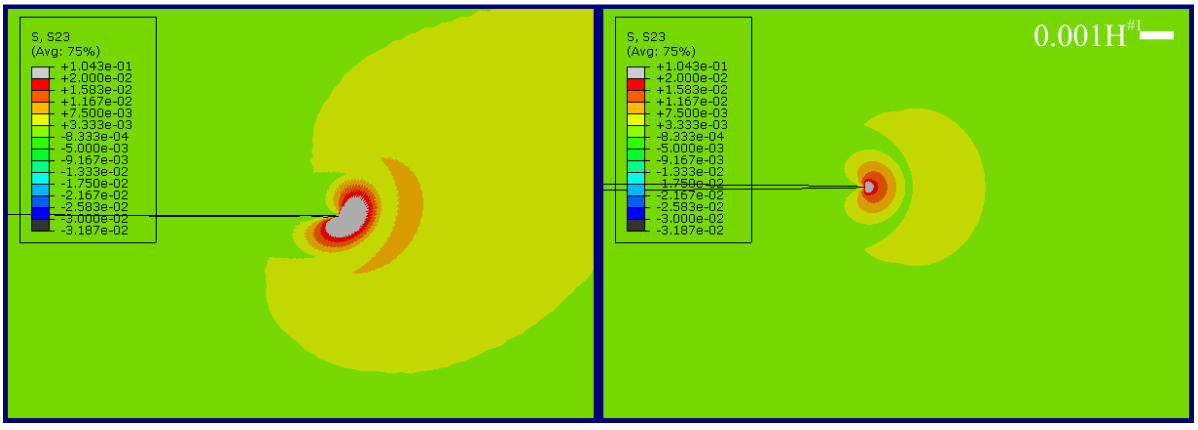

Figure 7.21: Mode III-Effect of horizontal elastic beams: Mode III σ_{23} contours close to the free surface ($x_3 = \frac{B^{\#1}}{2} - 0.0625$mm, left) and in the center ($x_3 = 0$, right) for $\left(\frac{E^{\#2}}{E^{\#1}} = 5, \frac{B^{\#2}}{B^{\#1}} = \frac{1}{2}\right)$.

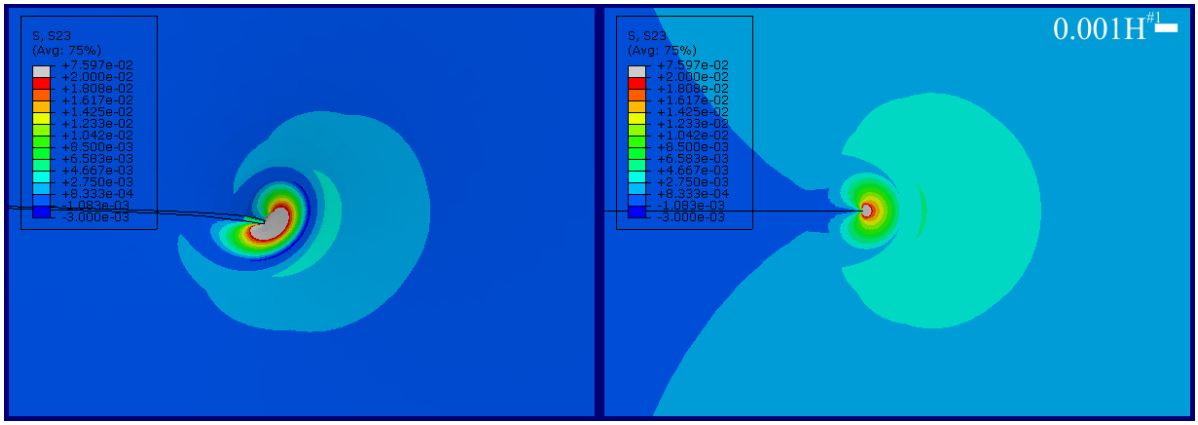

Figure 7.22: Mode III-Effect of vertical elastic beams: Mode III σ_{23} contours at the free surface ($x_3 = \frac{B^{\#1}}{2}$, left) and in the center ($x_3 = 0$, right) for $\left(\frac{E^{\#2}}{E^{\#1}} = 5, \frac{H^{\#2}}{H^{\#1}} = 1\right)$.

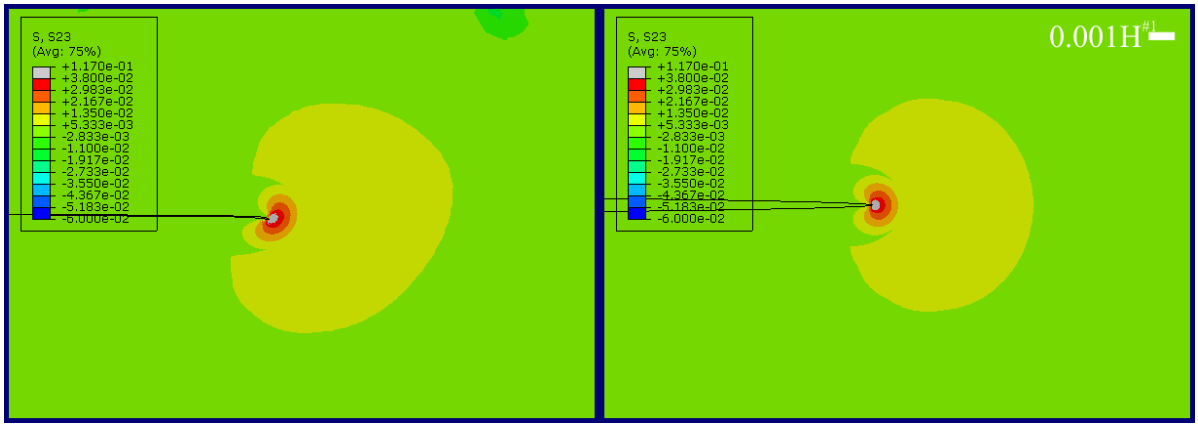

Figure 7.23: Mode III-Effect of horizontal varying width: Mode III σ_{23} contours close to the free surface ($x_3 = \frac{B^{\#1}}{2} - 0.0111\text{mm}$, left) and in the center ($x_3 = 0$, right) for $\left(\frac{B^{\#2}}{B^{\#1}} = 5, \frac{E^{\#2}}{E^{\#1}} = 1\right)$.

The dominant modes in the vicinity, figure 7.24, and far from the crack are summarized in table 7.3.

Table 7.3: Mode III-Effect of added beams: Dominant modes in the vicinity and far from the crack behind the crack tip at $\theta = -\pi$ (free surface and center correspond to $x_3 = \frac{B^{\#1}}{2}$ and $x_3 = 0$, respectively).

Strategy		**The vicinity of the crack tip**	**Far from the crack tip**
Horizontal beams	Free surface	Mode II	Mode III
	Center	Mode III	Mode III
Vertical beams	Free surface	Mode II	Mode III
	Center	Mode III	Mode III
Horizontal varying width	Free surface	Mode II	Mode III
	Center	Mode III	Mode III

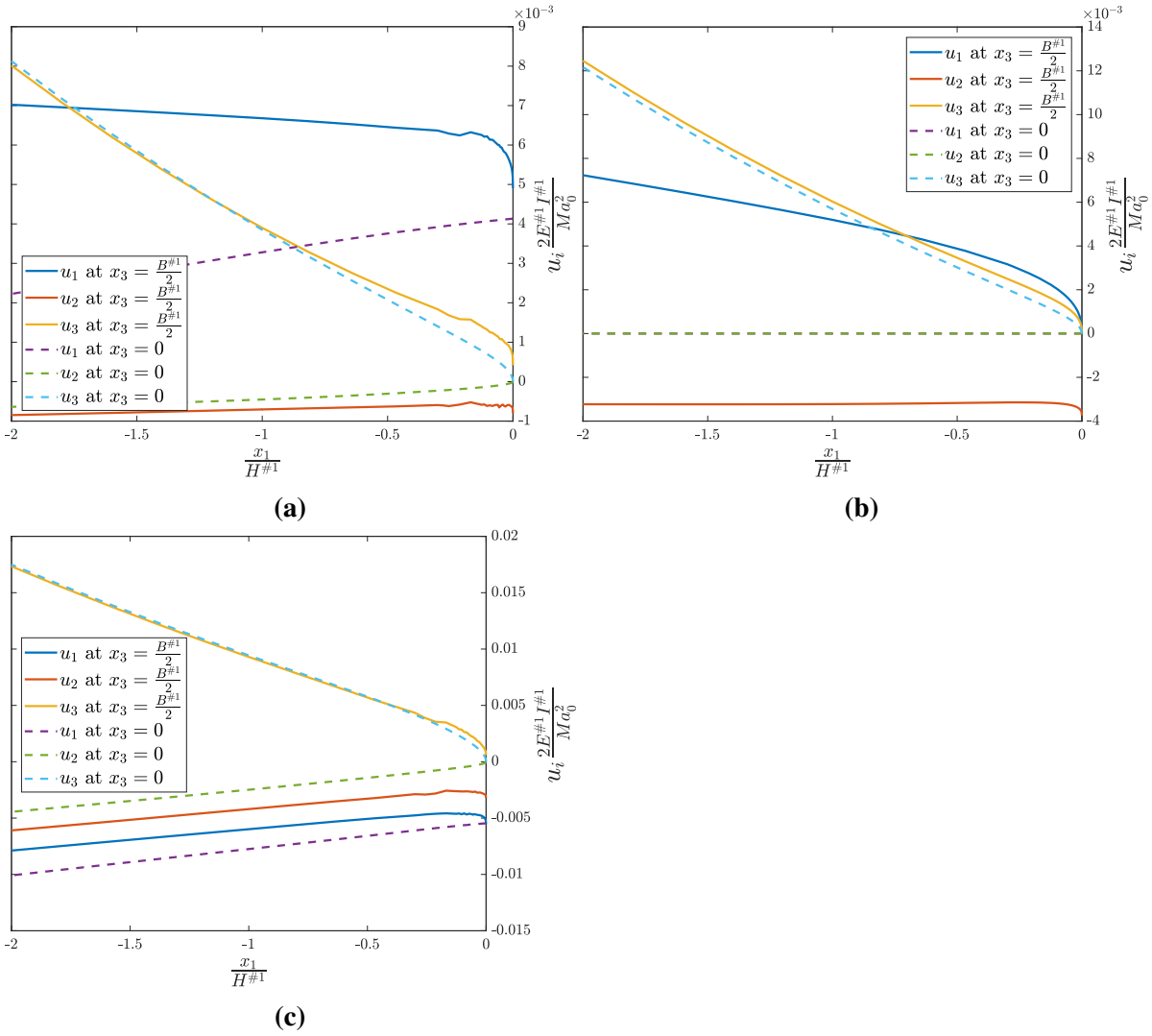

Figure 7.24: Mode III-Effect of added beams: Specimen displacements behind the crack tip ($\theta = -\pi$) in the vicinity of the crack tip. (a) Horizontal elastic beams $\left(\frac{E^{\#2}}{E^{\#1}} = 5, \frac{B^{\#2}}{B^{\#1}} = \frac{1}{2}\right)$ (b) Vertical elastic beams $\left(\frac{E^{\#2}}{E^{\#1}} = 5, \frac{H^{\#2}}{H^{\#1}} = 1\right)$ (c) Horizontal varying width $\left(\frac{B^{\#2}}{B^{\#1}} = 5, \frac{E^{\#2}}{E^{\#1}} = 1\right)$.

7.8 Conclusion

- The coupling mode II, II^c, is an inseparable part of the mode III. The elastic behavior of the horizontal or vertical beams along with the neutral axis in the x_3-direction and second moment of area do not influence II^c.
- The singularity term power, λ, are found at the free surface, $x_3 = \frac{B^{\#1}}{2}$, an a distance close to that, $x_3 = \frac{B^{\#1}}{2} - 0.0625\text{mm}$, for the vertical elastic beams where λ shows a

remarkable difference. Theses different obtained values for the singularity exponent requires further models with extremely fine mesh with good transition from the DCB specimen to the beams before reaching a conclusion.

- The K-field$_{(\mathrm{r/H}\cong 0.01)}$ criterion for the K-dominated zone comes from a DCB specimen with the regular geometry. When the DCB specimen is sandwiched between the horizontal and vertical beams, the K-field$_{(\mathrm{r/H}\cong 0.01)}$ criterion is affected.
- By increasing the elastic beam Young's modulus and shifting the neutral axis in the x_3-direction outside the DCB specimen, the FE models should be equipped with a higher mesh density in the x_1-direction (the direction of the crack ligament).
- The effect of the wider horizontal beams leads to the maximum mode III, figure 7.25.

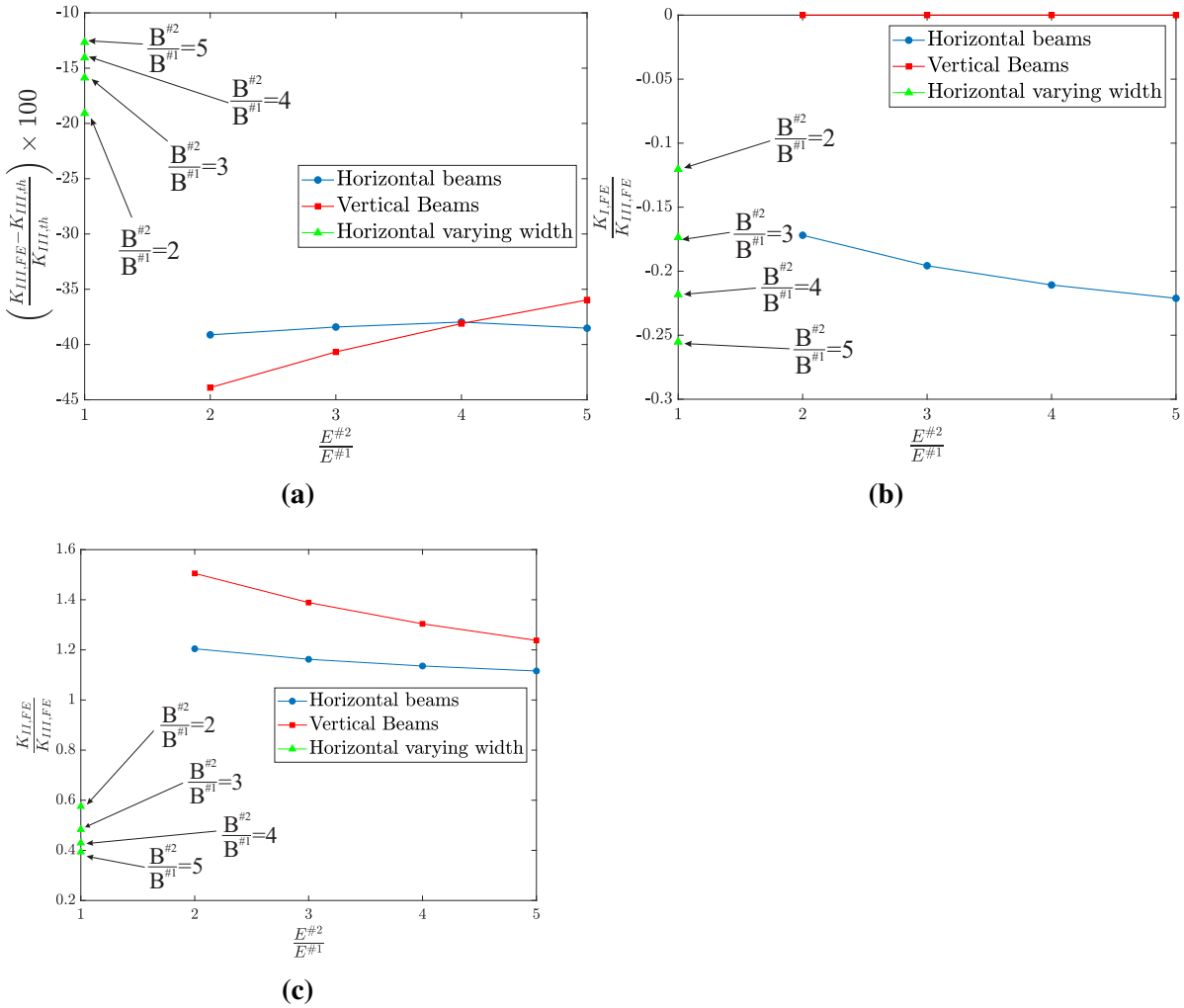

Figure 7.25: Mode III-Effect of added beams: Effect of the added beam elastic behavior and width on the mode III SIF. (a) $K_{\mathrm{III,th}}$ and $K_{\mathrm{III,FE}}$ relative error (b) $\frac{K_{\mathrm{I,FE}}}{K_{\mathrm{III,FE}}}$ (c) $\frac{K_{\mathrm{II,FE}}}{K_{\mathrm{III,FE}}}$.

CHAPTER 8
Effect of Orthotropy on K_{III}

For the final chapter of studying the effect of different parameters on K_{III}, the isotropic material is replaced with an orthotropic material. The specimen is loaded in its strongest direction; therefore, the effect of increasing the longitudinal Young's modulus, in the unidirectional composite laminate (typical layup for wind turbine blades and most aerospace structures) on K_{III} is the topic of the present chapter.

8.1 Material

In this section, two unidirectional laminates, according to table 8.1 are selected for the effect of orthotropy. The former is a Glass/Epoxy (Bak et al., 2013) and the latter is a Carbon/Epoxy laminate (Tsai and Hahn, 1980).

Table 8.1: Mechanical properties of unidirectional laminates.

Property	Symbol	Unit	Glass/Epoxy	Carbon/Epoxy
Fiber volume fraction	V_f	-	0.5	0.7
Longitudinal Young's modulus	E_{11}	GPa	39.5	181.0
Transverse Young's modulus	E_{22}	GPa	12.1	10.3
In-plane Poisson's ratio	ν_{12}	-	0.2750	0.2800
Out-of-plane Poisson's ratio	ν_{23}	-	0.3329	0.2800
In-plane shear modulus	G_{12}	GPa	4.54	7.17
Out-of-plane shear modulus	G_{23}	GPa	4.54	7.17

As can be seen from the above table, for the Glass/Epoxy composite laminate, $\frac{E_{11}}{E_{22}}$ is approximately 3 and the same ratio is around 17 for the Carbon/Epoxy laminate. It is assumed that $E_{33} = E_{22}$, $\nu_{13} = \nu_{23}$ and $G_{13} = G_{23}$ (transverse isotropy).

8.2 Specimen Dimensions

The stress in an orthotropic material depends on the elastic constants. For all the analyses in this chapter, the specimen longitudinal axis coincides with the fiber direction; thus, the specimen is loaded in its strongest direction. For the tow-dimensional (plane) problems, Z. Suo and FAN (1992) suggested a rescaling technique using a scaling parameter, Λ, whereby the end-zone length or the length of the pre-crack should be multiplied by $\Lambda^{-1/4}$. In other words,

a longer specimen is required for the orthotropic fracture test specimens compared to the isotropic. Λ can be determined from Eq.(8.1).

$$\Lambda = \frac{E_{22}}{E_{11}} \tag{8.1}$$

where E_{11} and E_{22} denote the longitudinal and transverse Young's modulus, respectively. Table 8.2 compares the dimensions of the isotropic and orthotropic specimens used in this project. For both specimens, a_0 and L are multiplied by $\Lambda^{-1/4}$. It is worth-mentioning that the rescaling approach is based on the tow-dimensional compatibility equations for the orthotropic materials (Z. Suo and FAN, 1992) and it is unclear if it remains correct for the three-dimensional problems.

Table 8.2: The DCB specimen dimensions with an isotropic material against an orthotropic material.

Dimension	Symbol	Unit	Isotropic	Glass/Epoxy	Carbon/Epoxy
Pre-existing crack length	a_0	mm	150	210	330
Specimen length	L	mm	300	420	660
Scaling factor	$\Lambda^{-1/4}$	-	1	1.34	2.05

8.3 Element Dimensions

Due to the change of material and also the complexity which originates from the orthotropy, the regular mesh size from table 5.1 is not able to provide the correct values of the SIF (some of the values become zero along the crack front). Table 8.3 summarizes the smallest element size used at the crack tip for the study of orthotropy.

Table 8.3: Mode III-Effect of orthotropy: Smallest element size.

Parameter	Dimension
e_h[mm]	5.450E-04
e_h/H	5.450E-05
e_w[mm]	125E-03
e_w/H	0.0125
e_l[mm]	8.333E-03
e_l/H	8.333E-04
e_h/e_l	0.0654
e_w/e_l	15.00
e_h/e_w	0.0044

8.4 The J integral

The J integral, assuming pure mode III, can be calculated from Eq.(8.2). Detailed derivation is given in appendix F.

$$J_{\mathrm{III}} = \frac{12M^2}{E_{11}B^4H} \tag{8.2}$$

The compliance matrix, $\boldsymbol{S}$, for an orthotropic material is

$$\boldsymbol{S} = \begin{bmatrix} S_{11} & S_{12} & S_{13} & 0 & 0 & 0 \\ S_{21} & S_{22} & S_{23} & 0 & 0 & 0 \\ S_{31} & S_{32} & S_{33} & 0 & 0 & 0 \\ 0 & 0 & 0 & S_{44} & 0 & 0 \\ 0 & 0 & 0 & 0 & S_{55} & 0 \\ 0 & 0 & 0 & 0 & 0 & S_{66} \end{bmatrix} = \begin{bmatrix} \frac{1}{E_{11}} & -\frac{\nu_{12}}{E_{11}} & -\frac{\nu_{13}}{E_{11}} & 0 & 0 & 0 \\ -\frac{\nu_{21}}{E_{22}} & \frac{1}{E_{22}} & -\frac{\nu_{23}}{E_{22}} & 0 & 0 & 0 \\ -\frac{\nu_{31}}{E_{33}} & -\frac{\nu_{32}}{E_{33}} & \frac{1}{E_{33}} & 0 & 0 & 0 \\ 0 & 0 & 0 & \frac{1}{G_{23}} & 0 & 0 \\ 0 & 0 & 0 & 0 & \frac{1}{G_{31}} & 0 \\ 0 & 0 & 0 & 0 & 0 & \frac{1}{G_{12}} \end{bmatrix} \tag{8.3}$$

where the Poisson's ratios are determined from Eq.(8.4).

$$\nu_{ij} = \nu_{ji}\frac{E_i}{E_j} \quad \text{for} \quad i \neq j \quad \text{and} \quad i,j = 1,2,3 \tag{8.4}$$

Another compliance matrix, $\boldsymbol{S'}$, is built according to Eq.(8.5) (Banks-Sills et al., 2005).

$$S'_{ij} = S_{ij} - \frac{S_{i3}S_{3j}}{S_{33}} \quad \text{where} \quad i,j = 1,2,4,5,6 \tag{8.5}$$

$\boldsymbol{S'}$ is a symmetric matrix and $S'_{i3} = S'_{3i} = 0$. For the plane strain, the J integral and SIF for all three modes are related through Eq.(8.6) (Banks-Sills et al., 2005).

$$J = \frac{D_0}{2}\left(\sqrt{S'_{22}}K_{\mathrm{I}}^2 + \sqrt{S'_{11}}K_{\mathrm{II}}^2\right) + \frac{1}{2}\sqrt{S'_{44}S'_{55} - {S'_{45}}^2}K_{\mathrm{III}}^2 \tag{8.6}$$

where

$$D_0 = \sqrt{2\sqrt{S'_{11}S'_{22}} + 2S'_{12} + S'_{66}} \tag{8.7}$$

For the plane stress, Eq.(8.8) correlates the J integral and SIF (Paris and Sih, 1965).

$$J = \left(\sqrt{\frac{S_{11}S_{22}}{2}}\sqrt{\sqrt{\frac{S_{22}}{S_{11}}} + \frac{2S_{12}+S_{66}}{2S_{11}}}\right)K_{\mathrm{I}}^2 + \left(\frac{S_{11}}{\sqrt{2}}\sqrt{\sqrt{\frac{S_{22}}{S_{11}}} + \frac{2S_{12}+S_{66}}{2S_{11}}}\right)K_{\mathrm{II}}^2 + \frac{1}{2}\sqrt{S_{44}S_{55}}K_{\mathrm{III}}^2 \tag{8.8}$$

In order to calculate σ_{23} along the crack ligament for an orthotropic material Eq.(8.9) is exploited.

$$\sigma_{23} = \frac{K_{III}}{\sqrt{2\pi x_3}} \mathrm{Re}\left(\frac{1}{\sqrt{\cos(\theta)+s_3\sin(\theta)}}\right) \tag{8.9}$$

where s_3 is the conjugate root of the below equation.

$$S_{55}s_3^2 - 2S_{45}s_3 + S_{44} = 0 \tag{8.10}$$

Since σ_{23} is extracted along crack plane (θ=0), the real part of Eq.(8.9) is 1 and the same equation for the isotropic material will be obtained. Next, Eq.(8.6) will be used for $K_{III,th}$.

8.5 Effect of Orthotropy

The obtained results are identical for both cases. In the following, the plots for the Glass/Epoxy laminate will be presented. Figure 8.1 illustrates the distribution of the SIF and various stress components along the crack front. Similar to the isotropic material, the coupling mode II is present and the maximum K_{II} and K_{III} occurs at the free surface.

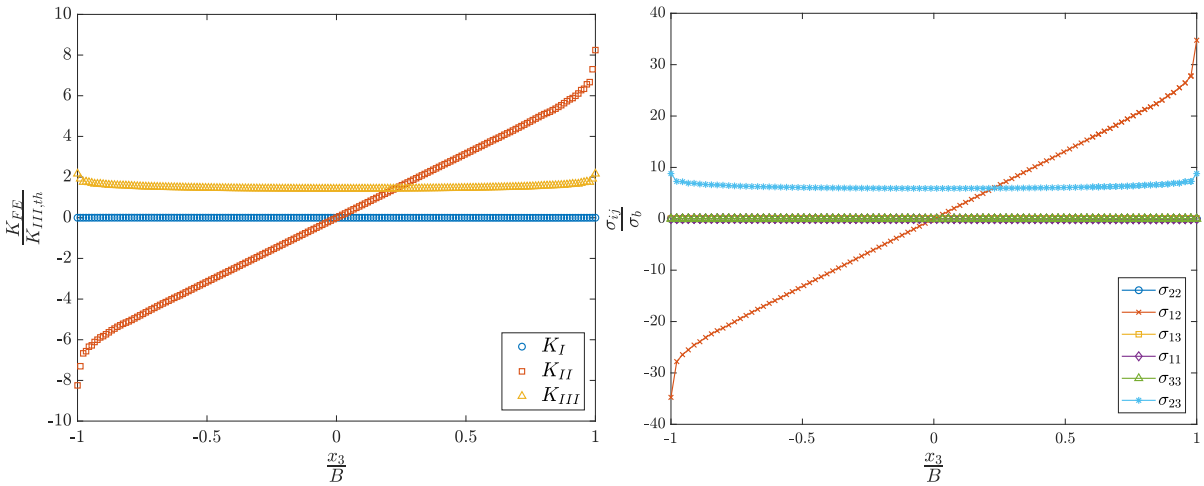

(a) **(b)**

Figure 8.1: Mode III-Effect of orthotropy: (a) SIF (b) stress (at $x_1 = 2.083\mu$m and $x_2 = 0$) components along the crack front for the Glass/Epoxy laminate.

The asymptotic, figure 8.2, and logarithmic scale, figure 8.3, show the singularity in the specimen center.

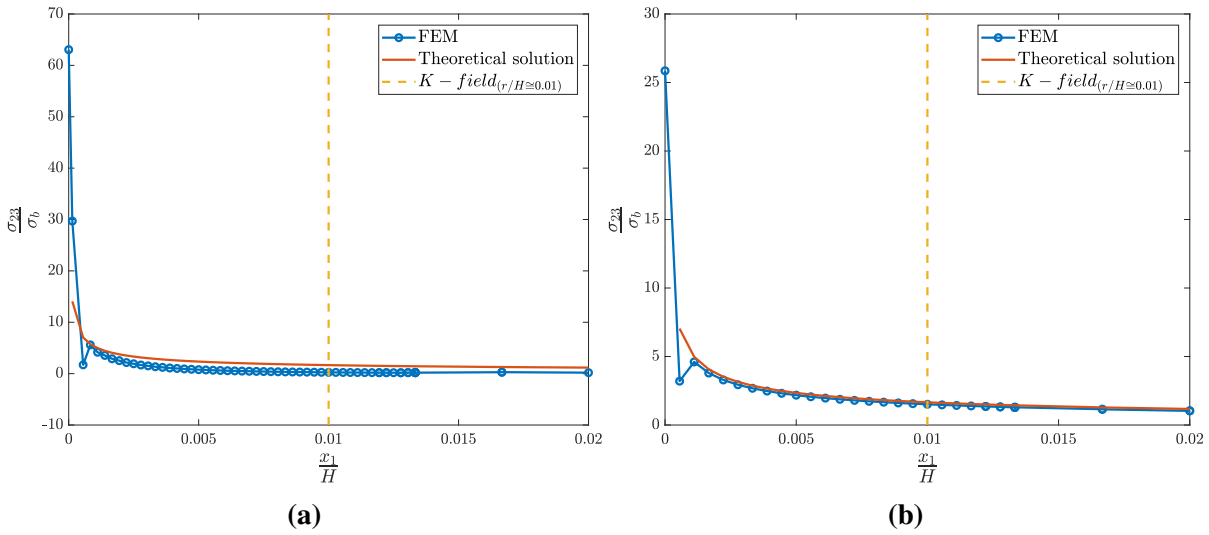

Figure 8.2: Mode III-Effect of orthotropy: Asymptotic σ_{23} (a) at the free surface ($x_3 = \frac{B}{2}$) (b) in the center ($x_3 = 0$) along the crack ligament ($\theta = 0$).

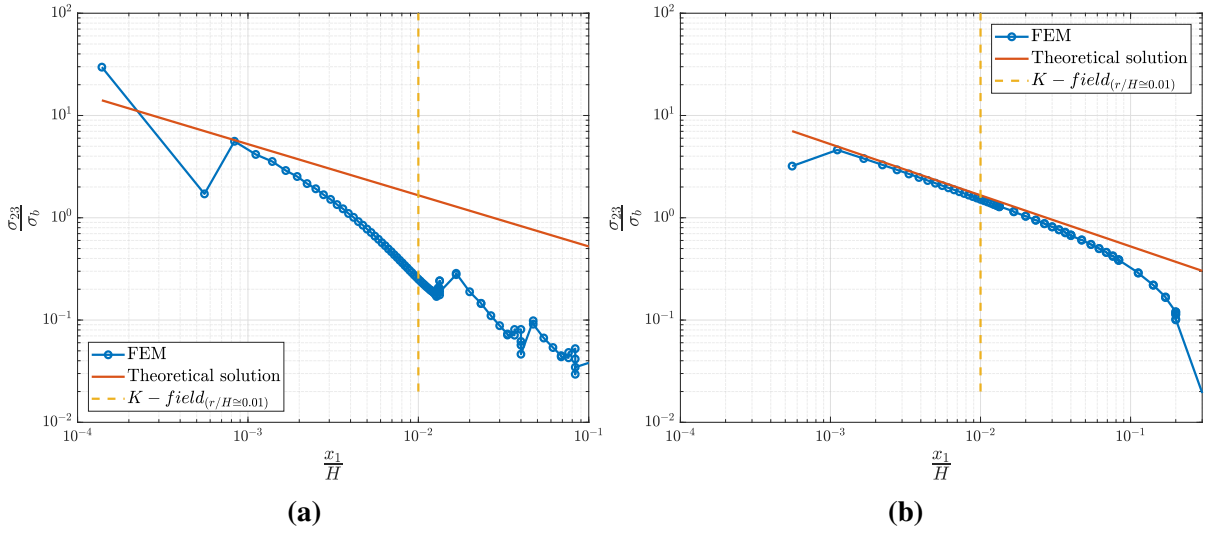

Figure 8.3: Mode III-Effect of orthotropy: Logarithmic σ_{23} (a) at the free surface ($x_3 = \frac{B}{2}$) (b) in the center ($x_3 = 0$) along the crack ligament ($\theta = 0$).

Comparing the distribution of K_{III} through the specimen width, figure 8.4(b), show a convex shape for the Carbon/Epoxy laminate. At the first sight, it appears to be the effect of scaling parameter mentioned in section 8.2; however, scaling the specimen width and height by $\Lambda^{-1/4}$, the convex shape of K_{III} is not influenced.

λ values are given in table 8.4. The singularity is accomplished in the center.

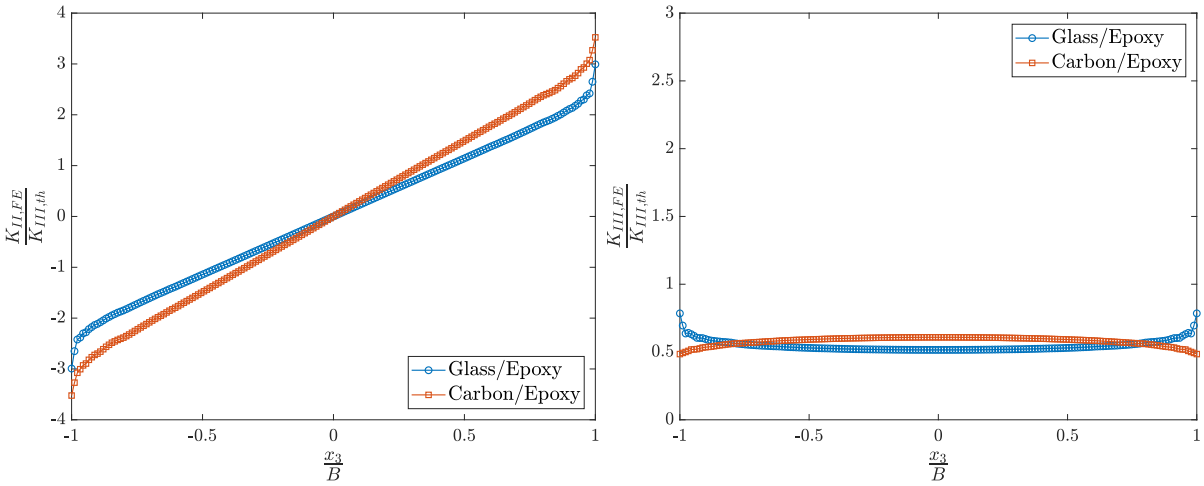

(a) **(b)**

Figure 8.4: Mode III-Effect of orthotropy: Distribution of (a) $K_{\mathrm{II,FE}}$ (b) $K_{\mathrm{III,FE}}$ through the crack front for the Glass/Epoxy and Carbon/Epoxy composite laminates.

Table 8.4: Mode III-Effect of orthotropy: λ values for the two unidirectional composite laminates at $\theta = 0$ (free surface and center correspond to $x_3 = \frac{B}{2}$ and $x_3 = 0$, respectively).

Unidirectional laminate	λ	
	Free surface	**Center**
Glass/Epoxy	-1.030	-0.4998
Carbon/Epoxy	-1.046	-0.4975

Table 8.5 summarizes the dominant modes in the vicinity and far from the crack. A comparison of the dominant modes close to crack is illustrated in figure 8.5 for both composite laminates.

Table 8.5: Mode III-Effect of orthotropy: Dominant modes in the vicinity and far from the crack behind the crack tip at $\theta = -\pi$ (free surface and center correspond to $x_3 = \frac{B}{2}$ and $x_3 = 0$, respectively).

Composite laminate		**The vicinity of the crack tip**	**Far from the crack tip**
Glass/Epoxy	Free surface	Mode II	Mode III
	Center	Mode III	Mode III
Carbon/Epoxy	Free surface	Mode II	Mode III
	Center	Mode III	Mode III

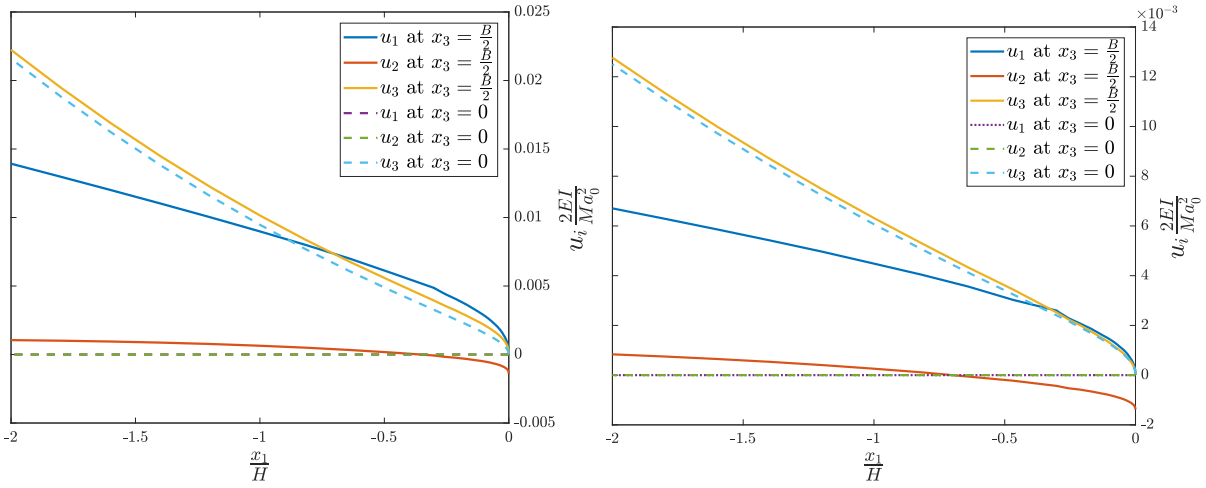

Figure 8.5: Mode III-Effect of orthotropy: Specimen displacements behind the crack tip ($\theta = -\pi$) in the vicinity of the crack tip. (a) Glass/Epoxy (b) Carbon/Epoxy.

The σ_{23} stress contours are also shown in figure 8.6. σ_{23} in higher at the free surface.

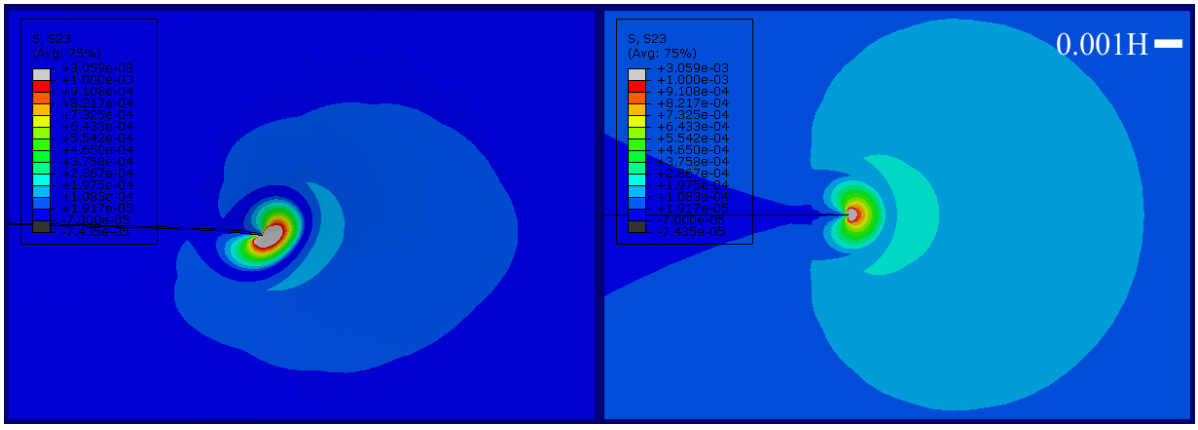

Figure 8.6: Mode III-Effect of orthotropy: Mode III σ_{23} contours at the free surface ($x_3 = \frac{B}{2}$, left) and in the center ($x_3 = 0$, right) for the Glass/Epoxy laminate.

8.6 Conclusion

- Similar results to the isotropic material are obtained for the orthotropic materials; therefore, all the geometrical modifications discussed from chapter 5 to 7 can be extended to the unidirectional laminates on the assumption that the crack growth direction and crack tip displacements are less important than the intensity of the stresses at the crack tip/front when the crack initiates (Parhizgar, 1979). Figure 8.7 illustrates the relative error as well as the portion of $K_{\mathrm{I,FE}}$ and $K_{\mathrm{II,FE}}$.

- The elastic constant have no influence on the coupling mode II.
- The FE model with the orthotropic properties requires a finer mesh in the x_1-direction (in the direction of the crack ligament) compared to its identical isotropic model.

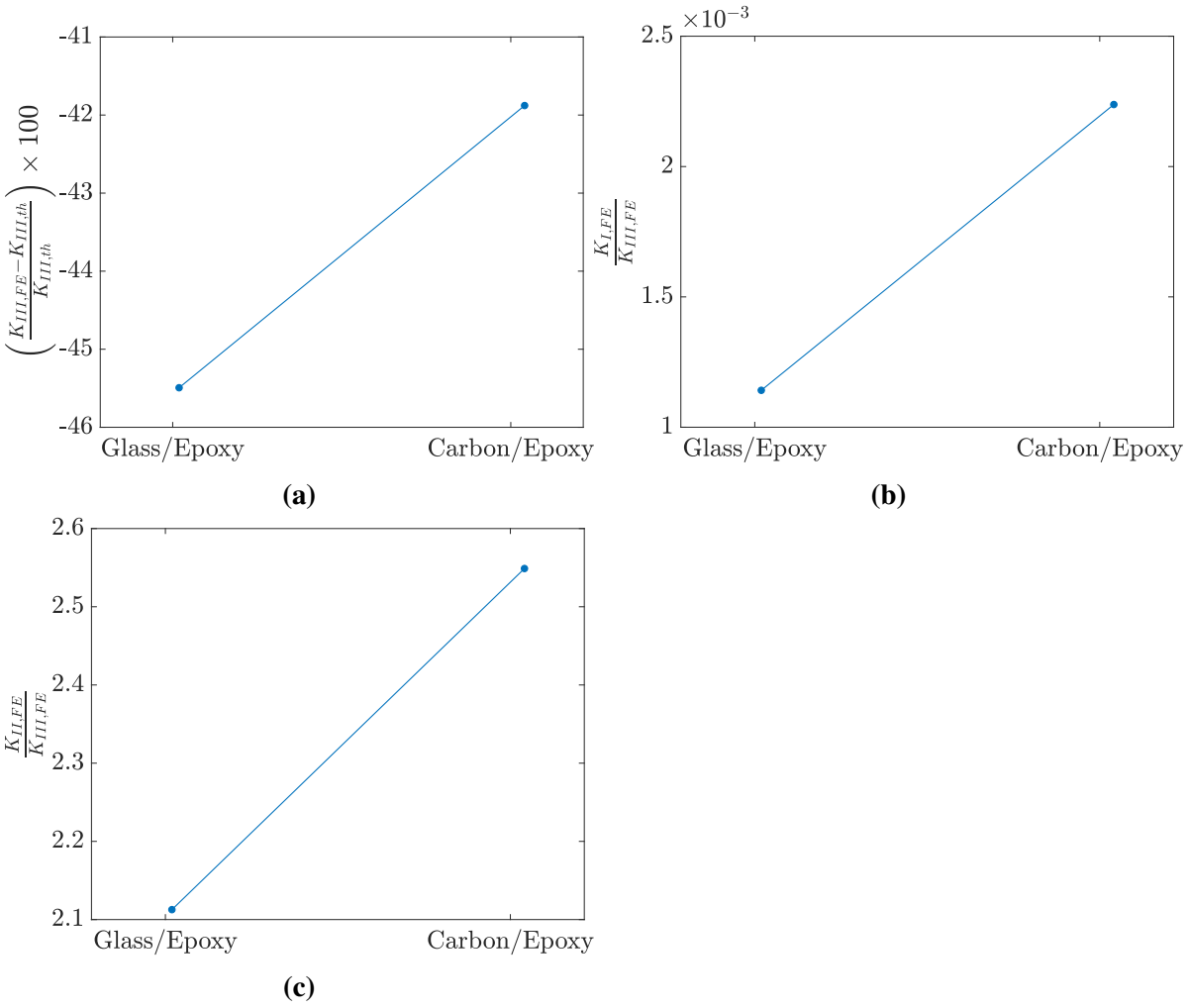

Figure 8.7: Mode III-Effect of orthotropy: Effect of $\frac{E_{11}}{E_{22}}$ on the mode III SIF. (a) $K_{\mathrm{III,th}}$ and $K_{\mathrm{III,FE}}$ relative error (b) $\frac{K_{\mathrm{I,FE}}}{K_{\mathrm{III,FE}}}$ (c) $\frac{K_{\mathrm{II,FE}}}{K_{\mathrm{III,FE}}}$.

CHAPTER 9
Cohesive Zone Modeling

The second part in the Progressive Failure Analysis, damage evolution in the form of crack growth, is the main topic of this chapter. Delamination is simulated by the defined cohesive law and parameters in ABAQUS. As a result, the dissipated energy for the crack extension is extracted from the solver and finally used in the validation step of the cohesive law. Therefore, this chapter is divided into two sections. The former is the CZM and the latter is the cohesive law determination.

9.1 Finite Element Model

As mentioned earlier in chapter 2, in the CZM, in addition to the bulk materials, there exist other self-destructive elements or the so-called "cohesive elements". The cohesive elements, indicated by red color in figure 9.1, are placed between the top and bottom parts of the DCB specimen. The local coordinate system of the cohesive elements is also shown in red with the capital letter X_i where i=1 ,2 ,3.

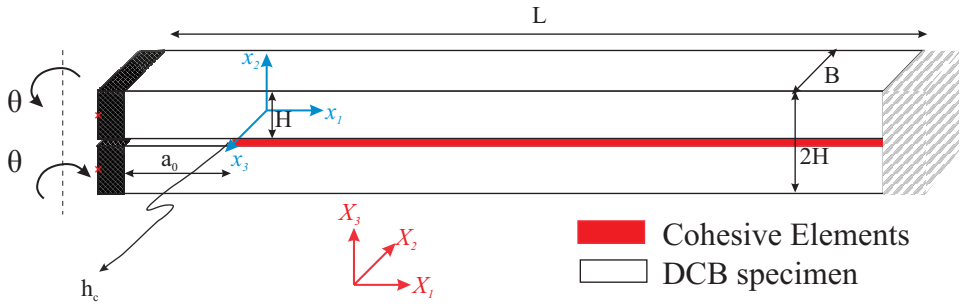

Figure 9.1: The CZM of the DCB specimen in ABAQUS. The blue color shows the global coordinate system (DCB) while the red indicates the local cohesive element coordinate system.

For the crack growth simulation, a longer specimen ($L >> a_0$) is required. The dimensions are $a_0 = 5H$, $B = 2H$ and $L = 75H$. Bear in mind that the choice of the short pre-crack length in figure 9.1 does not cause any issue since the study does not concern with the LEFM.

The bulk material is the same isotropic material with $E = 200$GPa, $G = 80$GPa and $\nu = 0.3$.

9.2 Defining the cohesive law

There are three main steps for defining each cohesive law:

- The elastic formulation
- Damage initiation criterion
- Damage evolution

9.2.1 The elastic formulation

In this section, the elastic properties for the elastic regime (the green area in figure 2.8) will be defined. The elasticity matrix is (units in MPa)

$$\boldsymbol{E} = \begin{bmatrix} E_{nn} & E_{ns} & E_{nt} \\ E_{ns} & E_{ss} & E_{st} \\ E_{nt} & E_{st} & E_{tt} \end{bmatrix} = \begin{bmatrix} 25 & 0 & 0 \\ 0 & 25 & 0 \\ 0 & 0 & 25 \end{bmatrix}$$

and the cohesive strength vector is (units in MPa)

$$\boldsymbol{T_c} = \begin{Bmatrix} T_{n,c} \\ T_{s,c} \\ T_{t,c} \end{Bmatrix} = \begin{Bmatrix} 1.2 \\ 1.2 \\ 1.2 \end{Bmatrix}$$

where the superscripts n, s and t denote the normal, the first and second transverse directions corresponding to the X_2, X_1 and X_3 axes in figure 9.1.

9.2.2 Damage initiation criterion

After increasing the load to a certain level, for instance the cohesive strength, the damage starts. Therefore, a damage initiation criterion is required for the solver. Several damage initiation criteria are implemented in ABAQUS. Among which the common **Quadratic nominal stress** is chosen. According to the **Quadratic nominal stress**, crack opens when Eq.(9.1) holds.

$$\left\{ \frac{\langle T_n \rangle}{T_{n,c}} \right\}^2 + \left\{ \frac{T_s}{T_{s,c}} \right\}^2 + \left\{ \frac{T_t}{T_{t,c}} \right\}^2 = 1 \tag{9.1}$$

T_n in Eq.(9.1) is placed between two angles, $\langle\rangle$, that is T_n is effective when its value is positive (tension). If T_n becomes negative then it is replaced with zero in Eq.(9.1) since the crack closure occurs.

9.2.3 Damage evolution

This section covers the red area in figure 2.7. ABAQUS is equipped with the linear and exponential damage evolution unless otherwise a user-subroutine can be substituted. The cohesive law exploited in this project is a bilinear law which has a linear damage evolution shape. In practice, it was shown that the fracture energy, J_c, and the cohesive strength, $\boldsymbol{T_c}$, can better describe this part of the cohesive law (Schwalbe et al., 2012). The critical separation, δ_c, is calculated by ABAQUS according to the damage evolution shape. The fracture energy is set to 1.2 $\frac{\mathrm{J}}{\mathrm{mm}^2}$. δ_c is determined from Eq.(9.2) (units in mm).

$$\boldsymbol{\delta_c} = \frac{2J_c}{\boldsymbol{T_c}} = \frac{2 \times 1.2}{\begin{Bmatrix} 1.2 \\ 1.2 \\ 1.2 \end{Bmatrix}} = \begin{Bmatrix} 2 \\ 2 \\ 2 \end{Bmatrix} \tag{9.2}$$

The damage evolution follows the set of the equations below.

$$\begin{aligned} T_n &= \begin{cases} (1-D)\overline{T}_n & \text{if } \overline{T}_n \leq 0 \\ \overline{T}_n & \text{if } \overline{T}_n < 0 \end{cases} \\ T_t &= (1-D)\overline{T}_t \\ T_s &= (1-D)\overline{T}_s \end{aligned} \tag{9.3}$$

where $\overline{T}$ is the calculated traction from Eq.(2.10) or the traction components from the elastic cohesive law without damage and D is the damage. When D=1 the material is separated.

9.2.4 Element

The model includes two element types. The first belongs to the bulk material while the second is the cohesive element. Since the damage, D, is unavailable in the post-processing when quadratic elements are selected for the bulk material, the linear element, C3D8R, is chosen (figure 9.2(b)). C3D8R is the reduced version of the C3D8 element which has one integration point. Enough number of C3D8R is assured in the width and height. The displacements are of paramount importance in this study and are accurately calculated in the nodes. The element dimensions for the bulk material are given in table 9.1 The linear cohesive element, COH3D8, is illustrated in figure 9.2(a) with its local coordinate system. There is only one layer of the cohesive elements between the two parts of the bulk material.

9.3 Mesh

The mesh criteria from Schwalbe et al. (2012) are utilized in the present study. Also the mesh is fine enough to cater the known mesh strategies in section 2.5.1 for the CZM. To this end, the cohesive element height, h_c, is set to $0.01H$.

Table 9.1: Bulk material element (C3D8R) dimensions for the CZM.

Parameter	Dimension
e_h[mm]	2E-03
e_h/H	2E-04
e_w[mm]	2E-03
e_w/H	2E-04
e_l[mm]	2E-03
e_l/H	2E-04
e_h/e_l	1
e_w/e_l	1
e_h/e_w	1

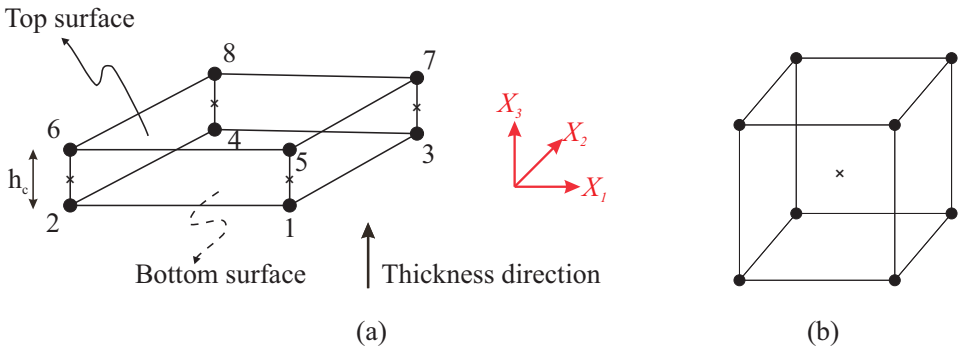

Figure 9.2: (a) COH3D8 (b) C3D8R element.

- The cohesive element width and height are set to 2mm; hence, h_c is negligible compared to the element area (0.1mm$<<$ 4mm^2).
- $h_c << \delta_c$ (0.1mm$<<$ 2mm)
- h_c is incomparable with other geometrical dimensions, e.g, H, W, L and a_0.

9.4 Result and Discussion

The damaged specimen is shown in figure 9.3.

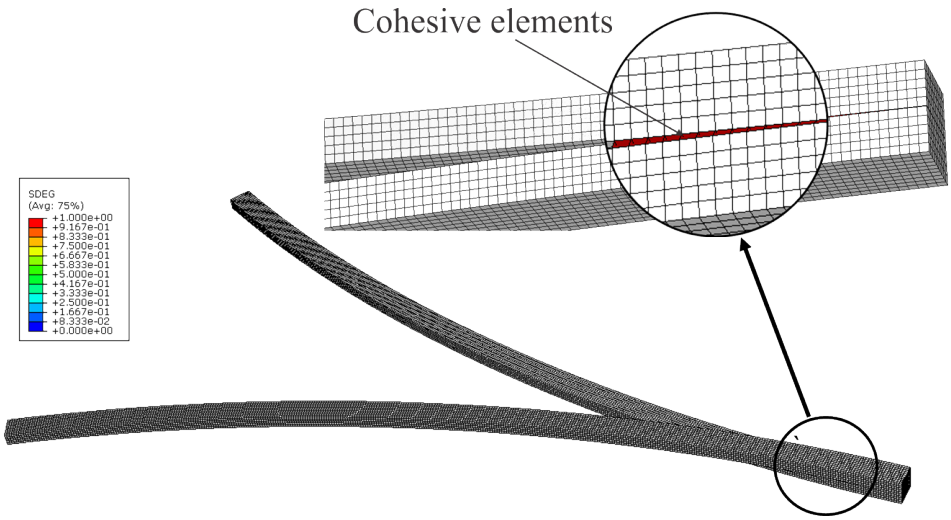

Figure 9.3: The damaged DCB specimen by the CZM.

When the specimen is loaded, the value of the left-hand side of Eq.(9.1) will increase, as illustrated by the blue curve in figure 9.4(a), until it equals 1 where the crack starts growing. Before the crack initiation, the material degradation is zero (red curve in figure 9.4). The high values in the elasticity matrix prevent the crack from opening at this level. As soon as the crack extension starts, the material degrades and its corresponding value in ABAQUS rises gradually to 1. At this point, the energy in the form of resistance acquires a constant value and is refered as the steady state, J_{ss}. The FPZ is easily transferred through the specimen in a self-similar fashion meaning that the FPZ attains a self-similar opening, δ_c, and length, L_c, as demonstrated in figure 9.4(b).

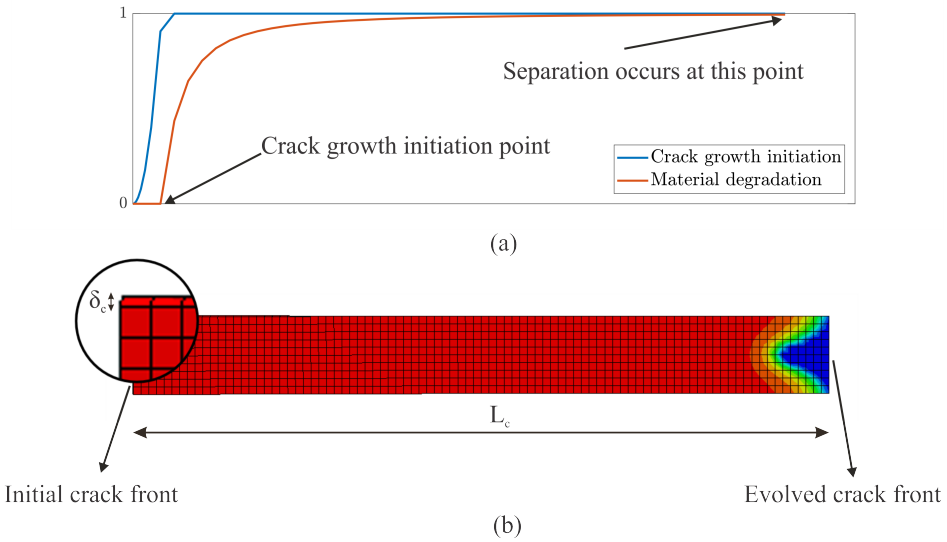

Figure 9.4: (a) The crack growth initiation and material degradation plots (b) The initial and evolved crack fronts when the FPZ takes a self-similar opening profile.

The coordinates in the x_1x_3 plane along with the displacements on the top and bottom

surfaces of the cohesive elements are extracted from ABAQUS. The local opening for each element is calculated from Eq.(9.4).

$$\delta_n{}^* = \begin{Bmatrix} U_n^5 - U_n^1 \\ U_n^6 - U_n^2 \\ U_n^7 - U_n^3 \\ U_n^8 - U_n^4 \end{Bmatrix} \quad \delta_s{}^* = \begin{Bmatrix} U_s^5 - U_s^1 \\ U_s^6 - U_s^2 \\ U_s^7 - U_s^3 \\ U_s^8 - U_s^4 \end{Bmatrix} \quad \delta_t{}^* = \begin{Bmatrix} U_t^5 - U_t^1 \\ U_t^6 - U_t^2 \\ U_t^7 - U_t^3 \\ U_t^8 - U_t^4 \end{Bmatrix} \tag{9.4}$$

The superscripts refer to the node numbers in figure 9.2 and U is the local displacement of the cohesive element. The local openings normalized with the critical opening, $\boldsymbol{\delta_c}$, along the X_2, X_1 and X_3 directions are plotted in figure 9.5. According to the plots, the mode III is dominated far from the evolved crack front, $\delta_t{}^* \approx 4\delta_s{}^*$. The mode I is negligible w.r.t to other two modes. In conclusion, mode III is accomplished under LSB condition. Next, the implemented cohesive law needs to be verified.

9.5 Cohesive Law validation

The FE model is identical to figure 9.1. Only two points shown in green in figure 9.6 are added on the sides of the specimen at $x_3 = \dfrac{B}{2}$ to record the local openings.

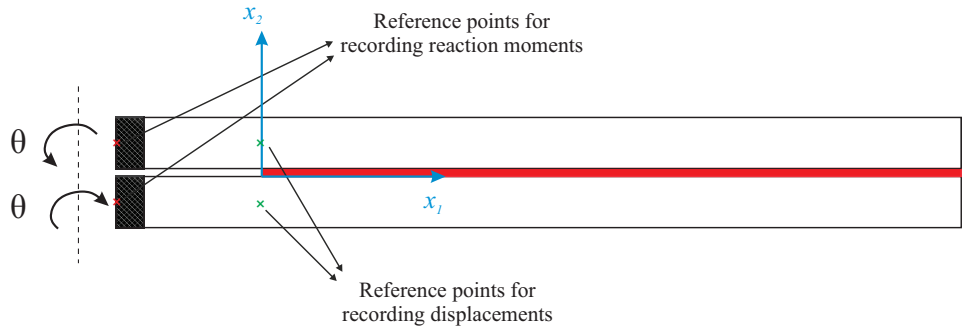

Figure 9.6: The FE model used for extracting the applied moments and separation in the CZM.

The J integral values in the form of resistance, J_R, can be determined by Eq.(5.1) and are plotted against the opening in figure 9.7(a). The normalized J_R with the critical fracture energy, J_c, increases with the end-opening and reaches the steady-state, J_{ss}, at the normalized distance, $\dfrac{\delta_t{}^*}{\delta_{t,c}}$=1. To find the corresponding traction values for the mode III, T_t, Eq.(2.13) is invoked under the assumption that the contribution of mode II is negligible. The definition of derivation, Eq.(9.5), is used to calculate the derivative of the J_R w.r.t to the tangential end-opening, $\delta_t{}^*$.

$$T_{t,ii}(\delta_t{}^*) = \frac{\partial J_R}{\partial \delta_t{}^*} = \frac{J_{R,ii} - J_{R,(ii-1)}}{\delta^*{}_{t,ii} - \delta^*{}_{t,(ii-1)}} \tag{9.5}$$

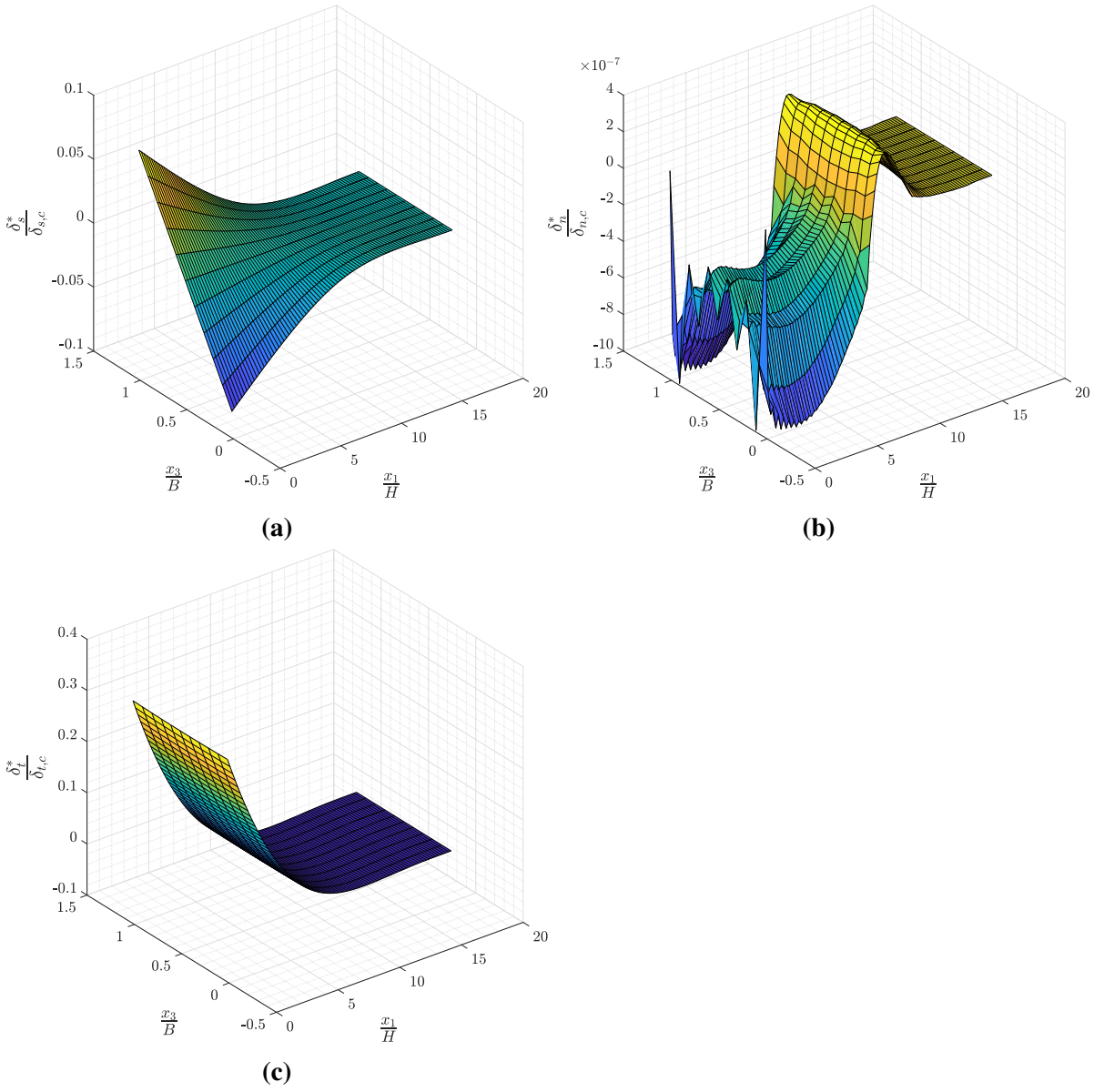

Figure 9.5: (a) $\delta_1{}^*$ in the x_1x_3 plane corresponding to the sliding opening (Mode II). (b) $\delta_2{}^*$ in the x_1x_3 plane corresponding to the normal opening (Mode I). (c) $\delta_3{}^*$ in the x_1x_3 plane corresponding to the tangential opening (Mode III).

where *ii* indicates the increment in the applied moment and $\delta^*{}_t$ is extracted from $x_3 = \frac{B}{2}$. The corresponding derived traction for mode III, T_t, versus the local opening is shown in figure 9.7(b). There exists enough number of elements both in the elastic and damage evolution regions. The implemented cohesive law is also plotted which show a good agreement with the FEM result. Therefore, from the FEM, the implemented cohesive law is verified and can be used for the LSB problem under mode III delamination.

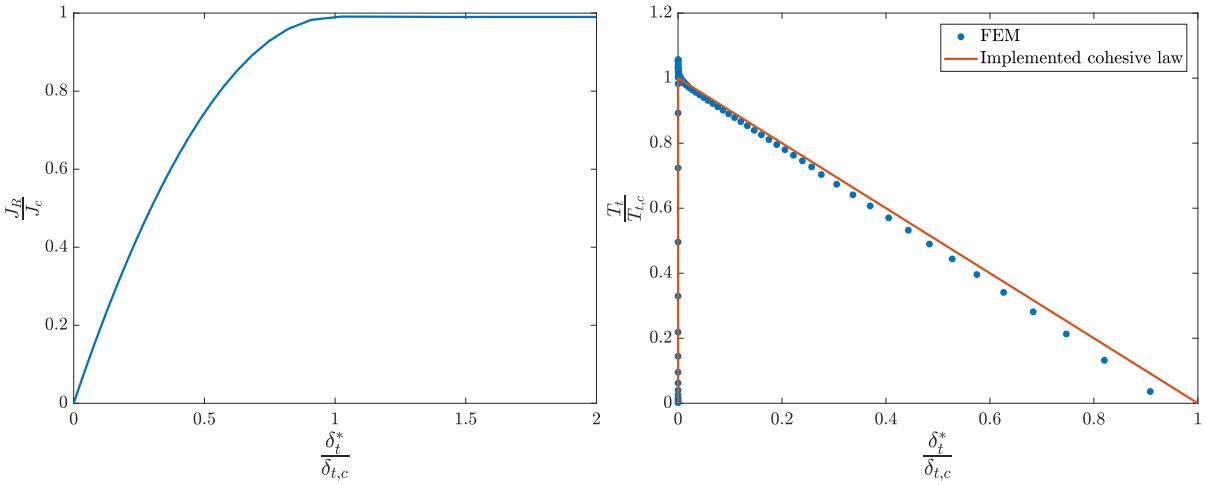

(a) (b)

Figure 9.7: (a) Fracture resistance, J_R, versus tangential end-opening, δ_t^* (b) tangential traction, T_t, versus tangential end-opening, δ_t^*.

9.6 Cohesive Law Parameter Study

The use of a bilinear Traction-Separation Law (TSL) due to maximum two required parameters (two out of $\boldsymbol{T_c}$, $\boldsymbol{\delta_c}$ and $\boldsymbol{J_c}$) for the definition of the cohesive law (here $\boldsymbol{T_c}$ and $\boldsymbol{J_c}$) provides the opportunity of examining the cohesive parameters under LSB condition. In this section, the effect of the critical separation, δ_c, which indirectly gives a measure of the active cohesive zone size will be investigated. In addition to the implemented cohesive law from the previous section (TSL06 in table 9.2), seven other cohesive laws (TSL01 to TSL05, TSL07 and TSL08) are examined as listed in table 9.2. For all the cohesive law the elastic behavior is the same as explained in section 9.2.1. Using the cohesive elements in ABAQUS, one should know that all the cohesive zone parameters must be the same, unless otherwise, the work of the separation becomes path dependent (Goutianos and Sørensen, 2012).

Table 9.2: Effect of cohesive parameters: Different traction-separation laws for the cohesive law parameter study ($\boldsymbol{E}$ is the elasticity matrix and the values are given in section 9.2.1).

TSL#	$\frac{\boldsymbol{T_c}}{\boldsymbol{E}}$	$\frac{\boldsymbol{\delta_c}}{H}$	$\frac{1}{2}\left(\frac{\boldsymbol{T_c}\boldsymbol{\delta_c}}{EH}\right)$
TSL01	3.072	3.125E-03	0.0048
TSL02	1.536	6.250E-03	0.0048
TSL03	0.768	1.250E-02	0.0048
TSL04	0.384	2.500E-02	0.0048
TSL05	0.192	5.000E-02	0.0048
TSL06	0.048	2.000E-01	0.0048
TSL07	0.024	4.000E-01	0.0048
TSL08	0.012	8.000E-01	0.0048

Plotting the R-curve from the reaction moment according to Eq.(5.1) in figure 9.8(a), one is able to identify coupling mode II and mode III with predominantly coupling mode II for lower δ_c where the size of the active cohesive zone is small. By increasing δ_c, the FPZ undergoes mode III, the effect of the coupling mode II becomes less and the assumption for determination of the cohesive law from Eq.(9.5) is applicable. This observation also confirms the results from chapter 5 to 8 whereby under Small-Scaled Fracture Process Zone (LEFM) there is a contribution of the coupled mode II. Suppose the coupled mode II and mode III are incorporated in calculating resistance, then J_R is a function of both sliding end-opening, ${\delta_s}^*$, and tangential end-opening, ${\delta_t}^*$. It can be written as

$$J_R({\delta_s}^*, {\delta_t}^*) = \int_0^{{\delta_s}^*} T_s(\delta_s, \delta_t) d\delta_s + \int_0^{{\delta_t}^*} T_t(\delta_s, \delta_t) d\delta_t \tag{9.6}$$

Consequently, assuming that the cohesive laws are differentiable from J_R, the cohesive traction can be determined from the equations below.

$$T_s({\delta_s}^*, {\delta_t}^*) = \frac{\partial J_R({\delta_s}^*, {\delta_t}^*)}{\partial {\delta_s}^*} \quad , \quad T_t({\delta_s}^*, {\delta_t}^*) = \frac{\partial J_R({\delta_s}^*, {\delta_t}^*)}{\partial {\delta_t}^*} \tag{9.7}$$

Figure 9.8(b) provides an overview of J_R against the tangential end-opening. For TSL02 and more clearly TSL01, ${\delta_t}^* > \delta_{t,c}$.

In the following, by ignoring the contribution of the coupled mode II in TSL01 to TSL05, i.e., assuming that it is a pure mode III problem, the derived traction-separation plots together with the implemented cohesive laws are demonstrated in figure 9.9(a). It can be seen that by decreasing δ_c, there would be a difference between the implemented cohesive law and the results obtained from FEM. Conversely, the implemented cohesive laws agree with the FEM results as the size of the active cohesive zone enlarges , i.e. , TSL06 to TSL08 in figure 9.9(b).

It is also advantageous to compare the cohesive parameters obtained from FEM with the implemented cohesive parameters. To this end, T_t at the crack initiation and complete separation, δ_c, along with the area under the curve which is equal to the work of separation, J_c, are extracted from FEM. The second column in table 9.3 shows the peak tangential traction, $T_{t,c}$, normalized by the corresponding implemented cohesive strength from FEM. The difference for all the TSLs except TSL01 is around 5%. The second column provides the cohesive traction (normalized by the corresponding cohesive traction) calculated at δ_c where it is expected that T_t=0. The last column in table 9.3 gives J_c normalized by the implemented fracture energy. The values should be close to 1. It is noteworthy to mention that the number of elements play a key role for the results obtained in table 9.3 (especially for TSL05, the green plot in figure 9.8(b)); however, by increasing δ_c, the difference between the implemented and FEM cohesive laws reduces.

Table 9.3: Effect of cohesive parameters: The difference between the obtained values of T_c and J_c from both the implemented cohesive and FEM results for various cohesive laws.

TSL#	Normalized $T_{(t,c)_{FE}}$	Normalized $T_{t,FE}$ at δ_c	Normalized $J_{c,FE}$
TSL01	0.8522	0.1065	1.025
TSL02	0.9546	0.0318	0.993
TSL03	1.0254	0.0219	1.004
TSL04	1.0510	0.0355	0.909
TSL05	1.0521	0.0881	0.684
TSL06	1.0569	0.0362	0.940
TSL07	1.0541	0.0346	0.957
TSL08	1.0582	0.0242	0.948

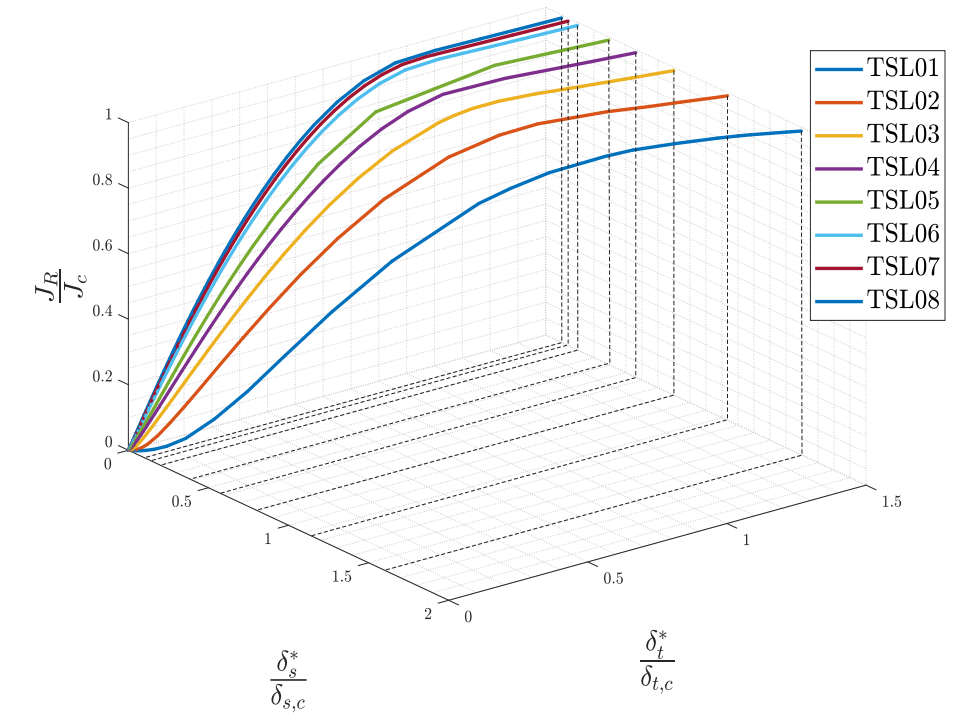

(a)

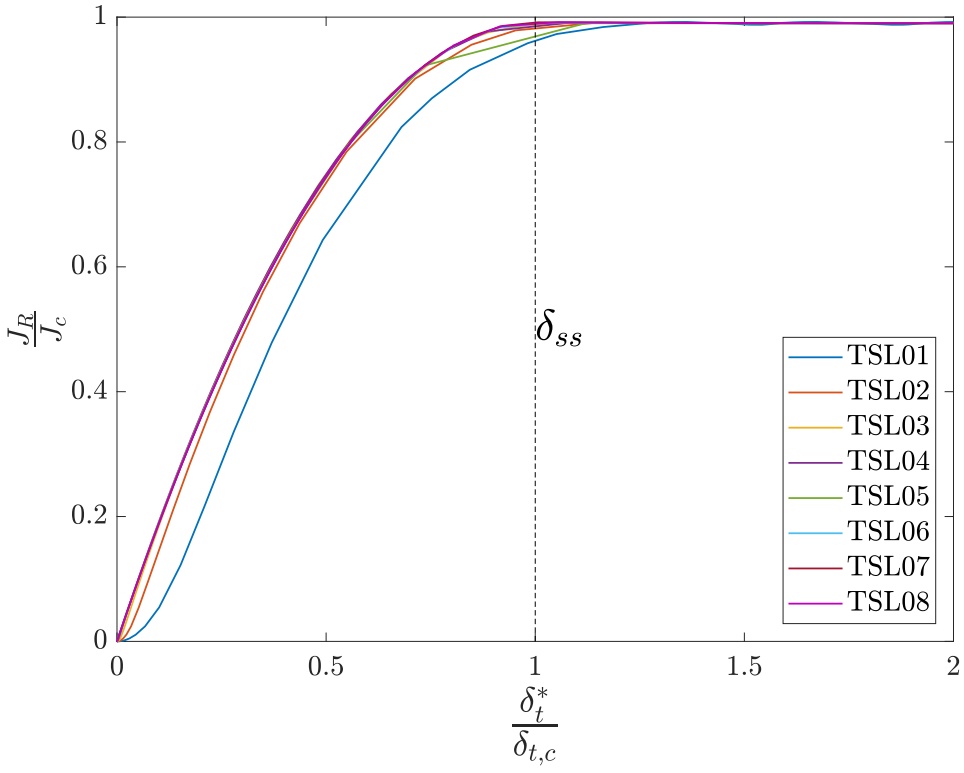

(b)

Figure 9.8: Effect of cohesive parameters: (a) Fracture resistance, J_R, versus sliding, $\delta_s{}^*$, and tangential end-opening, $\delta_t{}^*$ (b) Fracture resistance, J_R, versus tangential end-opening, $\delta_t{}^*$ for different cohesive laws in table 9.2.

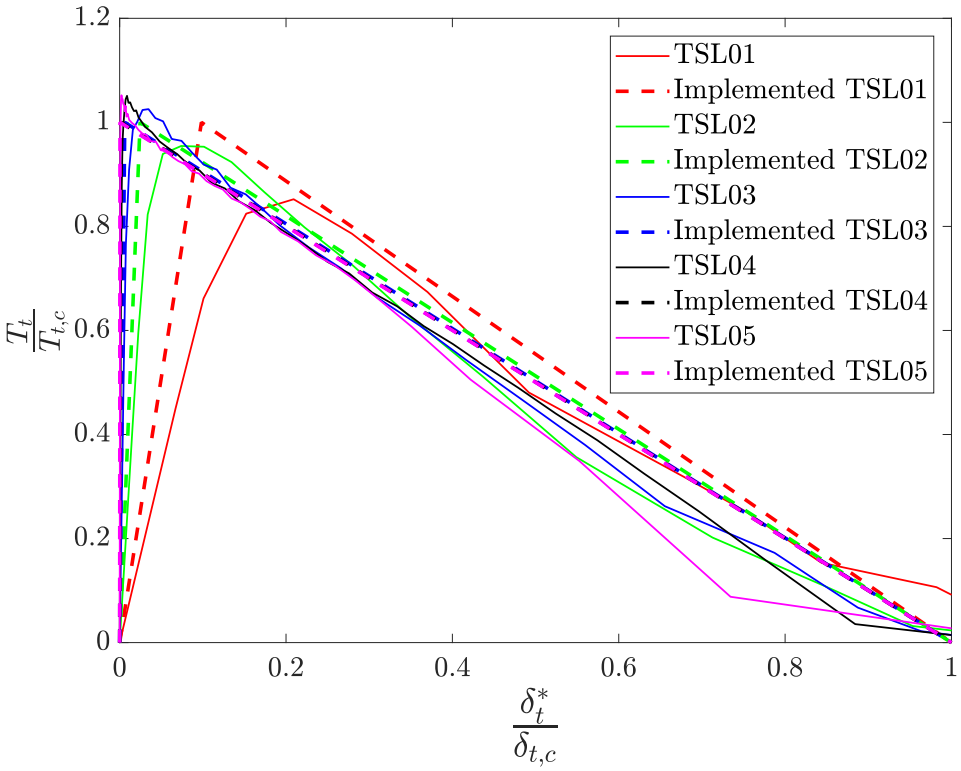

(a)

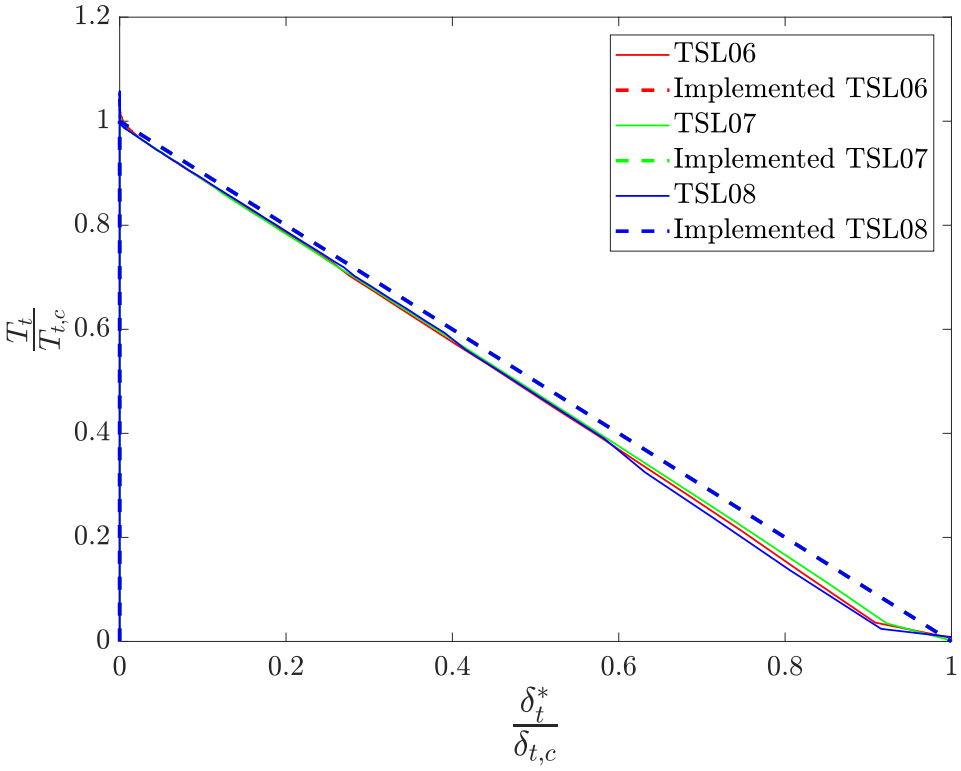

(b)

Figure 9.9: Effect of cohesive parameters: Tangential traction, T_t, versus tangential end-opening for (a) TSL01 to TSL05 (b) TSL06 to TSL08.

CHAPTER 10
Conclusion and Future Perspective

The Double Cantilever Beam (DCB) specimen under mode I, mode II and mode III is analyzed by FEM and compared with the theory. For the FEM, ABAQUS as a reliable Finite Element package is utilized; therefore, all the conclusions are based on the results obtained from this commercial code.

- The two-dimensional mode I and II results from the LEFM Finite Element model agree with the theory for both the plane stress and plane strain conditions; however, the primary weakness appears in the three-dimensional analysis. In the three-dimensional mode I, the Finite Element model is unable to provide enough number of points for the normal stress, σ_{22}, along the crack ligament at the free surface. The insufficient number of points originates from inadequate number of elements in the specimen longitudinal direction due to exceeding a million number of elements for the whole model and limitation in computational time. The smaller specimens for the mode II and III allow a finer mesh at the free surface; however, the $1/\sqrt{r}$-singularity is not still accomplished. Furthermore, a noticeable difference between the singularity exponent, λ, is observed at the free surface and the plane very close to the free surface. The results are in agreement with the obtained from Pook et al. (2014) and Pook et al. (2015) who had an element size virtually ten times smaller than the elements used in this study.

- In LEFM, the effect of the mid-node distortion in the elements at the crack tip should be investigated thoroughly since the stress is not calculated correctly in these elements. With the improvement in the computational power, it might be unnecessary to move the mid-nodes to the quarter point since there is a possibility of influencing the stress calculation at the free surface by such elements. Overall, it is believed that a Finite Element model with a very fine mesh at the free surface is needed before commenting on whether the $1/\sqrt{r}$-singularity at the free surface exists or the distorted elements at the crack tip may affect the stresses at the free surface.

- The three-dimensional LEFM analysis of mode II reveals a coupling mode III, due to the presence of shear stress, σ_{23}, at the crack tip and the first ring of the elements where the mid-nodes are shifted to the quarter point. ABAQUS uses the surface integral to calculate the J integral and K is determined from the J values. Using the surface integral and sufficiently fine mesh (element size of 0.013% specimen height in the specimen longitudinal direction with aspect ratios no more than 10) the effect of the first and the

second contour in the surface integral becomes negligible. Next, a user subroutine in the post-processing can extract the J values by ignoring the first and second contours during the surface integral which may remove the decaying σ_{23} in mode II and mode III at the free surface.

- The importance of the collapsed elements (the element type whereby the nodes at one of the sides of the element coinciding the crack tip have similar coordinates) at the crack tip/front is explicitly discussed in LEFM. It is shown that despite providing good result for the Stress Intensity Factor by the non-collapsed elements, they can only produce singularity on the element boundary and are not recommended for the LEFM analyses. Furthermore, there can be only four non-collapsed elements at the crack tip/front which makes the stress calculation for different angles around the crack difficult for these elements.
- In LEFM, the size of the K-dominated zone in the DCB-type specimens is very small (less than 0.013% of the specimen height) and by moving from the center to the edges, its size shrinks.
- Based on the obtained results, in LEFM, there is always a coupling mode II, II^{c}, under anti-plane loading which induces the mode III. Therefore, the pure mode III, in the form of what usually is expected, is not achievable and of course is not limited only to case studies in the present project. For Small Fracture Process Zone, the coupling mode II is dominant in the vicinity of the crack. Further away from the crack, for the Large Fracture Process Zone, i.e, Large-Scale Bridging condition; the specimen acts like a beam under anti-plane loading.
- The DCB specimens with low thickness are not suitable for mode III delamination toughness testing in LEFM. By reducing the thickness, the singularity field inside the specimen vanishes.
- Among several LEFM case studies for the suitable cross-section for mode III delamination toughness testing, the horizontal beams on the side of the applied rotation with the width five times larger than the DCB specimen is capable of generating mode III although the coupled mode II cannot be vanished. The cross-section is illustrated in figure 10.1.

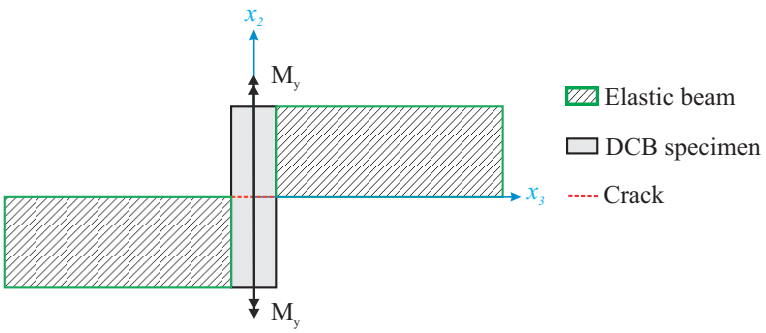

Figure 10.1: The optimum cross-section for mode III delamination toughness testing.

- Unlike the mode I where the crack opens from the center to the edges, in mode II and III the crack extends from the edges to the center. The result from the Cohesive Zone Modeling also confirms this observation for mode III.
- The bilinear cohesive law under the assumption of neglecting mode II can be utilized for the Large-Scale Bridging problems and the crack evolution for the DCB specimen with the isotropic material. For Large Fracture Process Zone, far from the evolved crack front is predominated by the mode III. The DCB specimen exhibits a stable crack growth. The validation of the cohesive law using the J integral works well with the DCB specimen which makes it a suitable specimen for the Large Fracture Process Zone modeling under anti-plane loading. The result from the Cohesive Zone Modeling can be extended to the DCB specimen with the unidirectional fibers. The next step is to evaluate the FEM with the result from a lab specimen.
- For the Large-Scale Bridging condition, A cohesive parameter study using a bilinear cohesive law has been performed. It is shown that by increasing the critical separation, $\boldsymbol{\delta_c}$, the specimen undergoes mode III and the effect of the coupled mode II becomes negligible unless, another cohesive law is required that cover both the sliding (mode II) and tangential (mode III) separation.

10.1 Recommendations for Further Studies

- Further studies is required for the three-dimensional mode I to clarify: (a) the reason for negative normal stress, σ_{22}, very close to the crack tip at the free surface, (b) existence of the $1/\sqrt{r}$-singularity at the free surface and (c) the effect of pre-crack length on the mode I Stress Intensity Factor, K_{I}.
- The Finite Element mesh transition both in the specimen longitudinal and in the direction of height and width can be optimized.
- The Finite Element model from chapter 7, Effect of Added Beams on K_{III}, needs to be improved in mesh transition from the specimen to the elastic beams.
- A separate study among the fracture mechanics FE packages is necessary for the LEFM to compare different codes.

10.2 Limitations

There has been more than 50 Finite Element Analyses with models from 10000 to 900000 elements. The computational time for a Finite Element model with 500000 elements and 20 Cores each with the frequency of 2.8 GHz is about 60 hours. Furthermore, the maximum number of elements, a million, and the variety of the cases does not give the chance of creating a model with extremely fine mesh; however, the present work can be used as a guideline for the detailed studies of each case in the future.

APPENDIX A

LEFM stress and displacement fields for an isotropic material

The stress fields for mode I are

$$\begin{Bmatrix}\sigma_{11}\\ \sigma_{22}\\ \sigma_{12}\end{Bmatrix} = \frac{K_{\mathrm{I}}}{\sqrt{2\pi r}}\cos\left(\frac{\theta}{2}\right)\begin{Bmatrix}1-\sin\left(\frac{\theta}{2}\right)\sin\left(\frac{3\theta}{2}\right)\\ 1+\sin\left(\frac{\theta}{2}\right)\sin\left(\frac{3\theta}{2}\right)\\ \sin\left(\frac{\theta}{2}\right)\cos\left(\frac{3\theta}{2}\right)\end{Bmatrix} \tag{A.1}$$

$$\begin{Bmatrix}\sigma_{33}\\ \sigma_{23}\\ \sigma_{31}\end{Bmatrix} = \begin{Bmatrix}\text{For plane stress: } 0 \text{ and for plane strain: } \nu(\sigma_{11}+\sigma_{22})\\ 0\\ 0\end{Bmatrix}$$

For mode II

$$\begin{Bmatrix}\sigma_{11}\\ \sigma_{22}\\ \sigma_{12}\end{Bmatrix} = \begin{Bmatrix}-\frac{K_{\mathrm{II}}}{\sqrt{2\pi r}}\sin\left(\frac{\theta}{2}\right)\left(2+\cos\left(\frac{\theta}{2}\right)\cos\left(\frac{3\theta}{2}\right)\right)\\ \frac{K_{\mathrm{II}}}{\sqrt{2\pi r}}\sin\left(\frac{\theta}{2}\right)\cos\left(\frac{\theta}{2}\right)\cos\left(\frac{3\theta}{2}\right)\\ \frac{K_{\mathrm{II}}}{\sqrt{2\pi r}}\cos\left(\frac{\theta}{2}\right)\left(1-\sin\left(\frac{\theta}{2}\right)\sin\left(\frac{3\theta}{2}\right)\right)\end{Bmatrix} \tag{A.2}$$

$$\begin{Bmatrix}\sigma_{33}\\ \sigma_{23}\\ \sigma_{31}\end{Bmatrix} = \begin{Bmatrix}\text{For plane stress: } 0 \text{ and for plane strain: } \nu(\sigma_{11}+\sigma_{22})\\ 0\\ 0\end{Bmatrix}$$

And for mode III

$$\begin{Bmatrix} \sigma_{11} \\ \sigma_{22} \\ \sigma_{12} \end{Bmatrix} = \begin{Bmatrix} 0 \\ 0 \\ 0 \end{Bmatrix}$$
$$\begin{Bmatrix} \sigma_{33} \\ \sigma_{23} \\ \sigma_{31} \end{Bmatrix} = \begin{Bmatrix} 0 \\ -\frac{K_{III}}{\sqrt{2\pi r}}\cos\left(\frac{\theta}{2}\right) \\ \frac{K_{III}}{\sqrt{2\pi r}}\sin\left(\frac{\theta}{2}\right) \end{Bmatrix} \tag{A.3}$$

in which r and θ are the polar coordinates as shown in figure 2.2, σ is the stress, subscripts 1, 2 and 3 denotes the x_1, x_2 and x_3 directions and ν is the Poisson's ratio.

The displacement fields for mode I are

$$\begin{Bmatrix} u_1 \\ u_2 \\ u_3 \end{Bmatrix} = \begin{Bmatrix} \frac{K_I}{G}\sqrt{\frac{r}{2\pi}}\cos\left(\frac{\theta}{2}\right)\left(1-2\beta+\sin^2\left(\frac{\theta}{2}\right)\right) \\ \frac{K_I}{G}\sqrt{\frac{r}{2\pi}}\sin\left(\frac{\theta}{2}\right)\left(2-2\beta-\cos^2\left(\frac{\theta}{2}\right)\right) \\ 0 \end{Bmatrix} \tag{A.4}$$

For mode II

$$\begin{Bmatrix} u_1 \\ u_2 \\ u_3 \end{Bmatrix} = \begin{Bmatrix} \frac{K_{II}}{G}\sqrt{\frac{r}{2\pi}}\sin\left(\frac{\theta}{2}\right)\left(2-2\beta+\cos^2\left(\frac{\theta}{2}\right)\right) \\ \frac{K_{II}}{G}\sqrt{\frac{r}{2\pi}}\cos\left(\frac{\theta}{2}\right)\left(-1+2\beta+\sin^2\left(\frac{\theta}{2}\right)\right) \\ 0 \end{Bmatrix} \tag{A.5}$$

where

$$\begin{cases} \beta = \dfrac{\nu}{1+\nu} & \text{For plane stress} \\ \beta = \nu & \text{For plane strain} \end{cases}$$

And for mode III

$$\begin{Bmatrix} u_1 \\ u_2 \\ u_3 \end{Bmatrix} = \begin{Bmatrix} 0 \\ 0 \\ \frac{K_{III}}{G}\sqrt{\frac{2r}{\pi}}\sin\left(\frac{\theta}{2}\right) \end{Bmatrix} \tag{A.6}$$

G is the shear modulus and u denotes the displacement.

APPENDIX B

Cohesive traction determination from J integral

B.1 J integral for the CZM

Integrating Eq.(2.3) along the path Γ shown in figure 2.9, the first term in the J integral drops (dx_2=0) and the equation is written as

$$J = -\int_{\Gamma} \sigma_{ij} n_j \frac{\partial u_i}{\partial x_1} dx_1 = -\int_0^{L_c} \sigma_{ij} n_j \frac{\partial u_i}{\partial x_1} dx_1 \tag{B.1}$$

where $T(\delta) = -\sigma_{ij} n_j$, u_i and L_c are replaced by δ and δ^*, respectively. Rewriting the above equation gives

$$J = \int_0^{\delta^*} T(\delta) \frac{\partial \delta}{\partial x_1} dx_1 \tag{B.2}$$

Since $\frac{\partial \delta}{\partial x_1} dx_1 = d\delta$, the J integral for the cohesive model will be

$$J_c = \int_0^{\delta^*} T(\delta) d\delta \tag{B.3}$$

B.2 Cohesive law derivation from the J integral

Differentiating Eq.(2.12) w.r.t δ^* gives

$$\frac{dJ_R}{d\delta^*} = \frac{d}{d\delta^*} \left(\int_0^{\delta^*} T(\delta) d\delta \right) \tag{B.4}$$

When differentiating, the J_{tip} is removed since it is not a function of δ^*. According to the Leibniz's rule for differentiation

$$\frac{d}{dx} \left(\int_{g(x)}^{h(x)} f(x,t) dt \right) = f(x,h(x)) \frac{d}{dx} h(x) - f(x,g(x)) \frac{d}{dx} g(x) + \int_{g(x)}^{h(x)} \frac{\partial}{\partial x} f(x,t) dt \tag{B.5}$$

The Eq.(B.4) by matching each term from the Leibniz's rule can be written as

$$\frac{d}{d\delta^*}\left(\int_0^{\delta^*} T(\delta^*,\delta)d\delta\right) = T(\delta^*,\delta^*)\frac{d\delta^*}{d\delta^*} - T(\delta^*,0)\frac{d(0)}{d\delta^*} + \int_0^{\delta^*}\frac{\partial T(\delta^*,\delta)}{\partial\delta^*}d\delta \tag{B.6}$$

The second term on the right hand side of the Eq.(B.6) is zero. Furthermore, $T(\delta^*,\delta) = T(\delta)$; thus, $\frac{\partial T(\delta)}{\partial\delta^*} = 0$ and the third term on the right hand side vanishes. Eq.(B.6) reduces to

$$\frac{d}{d\delta^*}\left(\int_0^{\delta^*} T(\delta^*,\delta)d\delta\right) = T(\delta^*,\delta^*)\frac{d\delta^*}{d\delta^*} \tag{B.7}$$

Rewriting Eq.(B.7) gives

$$\frac{dJ_R}{d\delta^*} = T(\delta^*) \tag{B.8}$$

APPENDIX C

J integral solution for pure mode I

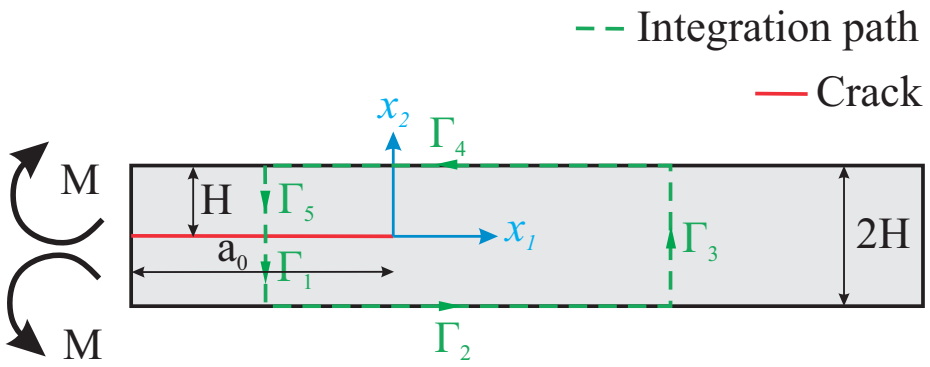

Figure C.1: The DCB specimen configuration for mode I and the integration path for the J integral.

The fracture surfaces are assumed traction free. Hence the J integral is the contributions from Γ_1 to Γ_5

$$J = J_1 + J_2 + J_3 + J_4 + J_5 \tag{C.1}$$

The first term in Eq.(2.3) for Γ_2 and Γ_4 is zero since $dx_2 = 0$. The only present stress component is σ_{11}. Calculating the traction according to $T_i = \sigma_{ij} n_j$ also makes the second term in the J integral for Γ_2 and Γ_4 zero. Γ_3 is also stress free and therefore $J_3 = 0$. In conclusion, Eq.(C.1) reduces to the summation of J_1 and J_5. Because of symmetry the J integral for both Γ_1 and Γ_5 will be the same. In the following, the derivation will be explained for the J_5. The same steps applies to J_1. According to Eq.(2.3)

$$J_5 = \int_{\Gamma_5} \left(W dx_2 - \sigma_{ij} n_j \frac{\partial u_i}{\partial x_1} dS \right) \tag{C.2}$$

By Assuming the linear elasticity, the strain energy density, W, can be written as

$$W = \frac{1}{2} \sigma_{11} \varepsilon_{11} \tag{C.3}$$

n_1=-1, $dS = -dx_2$, $\dfrac{\partial u_1}{\partial x_1} = \varepsilon_{11}$ and the integration limit is from H to zero. Assuming $a_0 >> H$ and a long specimen, the beam theory applies and the bending stress w.r.t to the defined coordinate system, can be written as

$$\sigma_{11} = \frac{M\left(x_2 - \frac{H}{2}\right)}{I} \quad \text{where} \quad I = \frac{1}{12}BH^3$$

Substituting the above-values in Eq.(C.2) leads to

$$J_5 = \int_H^0 (\frac{1}{2}\sigma_{11}\varepsilon_{11} - \sigma_{11}\varepsilon_{11})dx_2 = \frac{1}{2}\int_0^H (\sigma_{11}\varepsilon_{11})dx_2 \tag{C.4}$$

Applying the Hooke's law, $\sigma_{11} = E\varepsilon_{11}$

$$\begin{aligned}
J_5 &= \frac{1}{2E}\int_0^H \sigma_{11}^2 dx_2 \\
&= \frac{1}{2E}\int_0^H \left(\frac{M\left(x_2 - \frac{H}{2}\right)}{I}\right)^2 dx_2 \\
&= \frac{M^2}{2EI^2}\int_0^H \left(x_2 - \frac{H}{2}\right)^2 dx_2 \\
&= \frac{M^2}{2EI^2}\int_0^H \left(x_2^2 + \frac{H^2}{4} - Hx_2\right) dx_2 \\
&= \frac{M^2}{2EI^2}\left(\frac{x_2^3}{3} + \frac{H^2}{4}x_2 - H\frac{x_2^2}{2}\right)\Bigg|_0^H = \frac{M^2H^3}{24EI^2} \\
&= \frac{M^2H^3}{24E\frac{1}{144}B^2H^6} = \frac{6M^2}{EB^2H^3}
\end{aligned} \tag{C.5}$$

Following the same methodology for Γ_1 yields the same resultas the J_5. Finally

$$J = J_1 + J_5 = \frac{6M^2}{EB^2H^3} + \frac{6M^2}{EB^2H^3} = \frac{12M^2}{EB^2H^3} \tag{C.6}$$

APPENDIX D

J integral solution for pure mode II

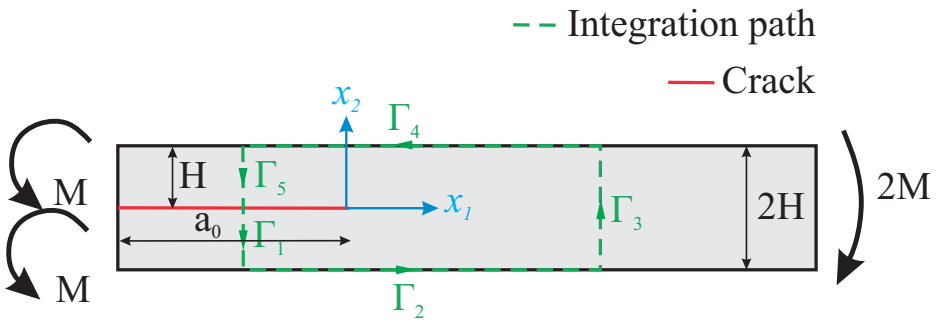

Figure D.1: The DCB specimen configuration for mode II and the integration path for the J integral.

Assuming traction free fracture surfaces, the J integral can be written as

$$J = J_1 + J_2 + J_3 + J_4 + J_5 \tag{D.1}$$

The first term in the J integral (Eq.(2.3)) for Γ_2 and Γ_4 is zero. Due to the applied loading and boundary condition, the only present stress component is σ_{11} and the normal vector for both Γ_2 and Γ_4 is $n_2 = \pm 1$. As a result, the resultant traction for both Γ_2 and Γ_4 becomes zero. The second term in the J integral equation vanishes for both Γ_2 and Γ_4 and $J_2 = J_4 = 0$. Rewriting Eq.(D.1) gives

$$J = J_1 + J_3 + J_5 \tag{D.2}$$

Because of symmetry, the derivation of the J_1 and J_5 will be the same and only the steps for J_1 will be presented.

According to Eq.(2.3)

$$J_1 = \int_{\Gamma_1} \left(W dx_2 - \sigma_{ij} n_j \frac{\partial u_i}{\partial x_1} dS \right) \tag{D.3}$$

Assuming linear elasticity, the strain energy density, W, will be

$$W = \frac{1}{2} \sigma_{11} \varepsilon_{11} \tag{D.4}$$

n_1=-1, $dS = -dx_2$, $\dfrac{\partial u_1}{\partial x_1} = \varepsilon_{11}$ and the integration limit is from zero to $-H$. Assuming $a_0 >> H$ and a long specimen, the beam theory applies and the bending stress w.r.t to the defined coordinate system, can be written as

$$\sigma_{11} = \frac{M\left(x_2 + \dfrac{H}{2}\right)}{I} \quad \text{where} \quad I = \frac{1}{12}BH^3 \tag{D.5}$$

Substituting Eq.(D.4) and Eq.(D.5) along with all the above-mentioned parameters in Ep.(D.3) yields

$$J_1 = \int_0^{-H} (\frac{1}{2}\sigma_{11}\varepsilon_{11} - \sigma_{11}\varepsilon_{11})dx_2 = \frac{1}{2}\int_{-H}^{0} (\sigma_{11}\varepsilon_{11})dx_2 \tag{D.6}$$

Assuming the Hooke's law, $\sigma_{11} = E\varepsilon_{11}$

$$\begin{aligned}
J_1 &= \frac{1}{2E}\int_{-H}^{0} \sigma_{11}^2 dx_2 \\
&= \frac{1}{2E}\int_{-H}^{0} \left(\frac{M\left(x_2 + \dfrac{H}{2}\right)}{I}\right)^2 dx_2 \\
&= \frac{M^2}{2EI^2}\int_{-H}^{0} \left(x_2 + \frac{H}{2}\right)^2 dx_2 \\
&= \frac{M^2}{2EI^2}\int_{-H}^{0} \left(x_2^2 + \frac{H^2}{4} + Hx_2\right) dx_2 \\
&= \frac{M^2}{2EI^2}\left(\frac{x_2^3}{3} + \frac{H^2}{4}x_2 + H\frac{x_2^2}{2}\right)\Bigg|_{-H}^{0} = \frac{M^2H^3}{24EI^2} \\
&= \frac{M^2H^3}{24E\dfrac{1}{144}B^2H^6} = \frac{6M^2}{EB^2H^3}
\end{aligned} \tag{D.7}$$

The J integral for Γ_3 is

$$J_3 = \int_{\Gamma_1} \left(W dx_2 - \sigma_{ij}n_j\frac{\partial u_i}{\partial x_1}dS\right) \tag{D.8}$$

where n_1=1, $dS = dx_2$, $\dfrac{\partial u_1}{\partial x_1} = \varepsilon_{11}$ and the integration limit is from $-H$ to H. Applying the beam theory, the bending stress is

$$\sigma_{11} = \frac{-2Mx_2}{I} \quad \text{where} \quad I = \frac{1}{12}B(2H)^3 \tag{D.9}$$

Substituting Eq.(D.4), Eq.(D.9) and the above parameters in Eq.(D.8) provides

$$J_3 = \int_{-H}^{H} (\frac{1}{2}\sigma_{11}\varepsilon_{11} - \sigma_{11}\varepsilon_{11})dx_2 = -\int_{0}^{H} (\sigma_{11}\varepsilon_{11})dx_2 \tag{D.10}$$

Applying the Hooke's law, $\sigma_{11} = E\varepsilon_{11}$

$$\begin{aligned} J_3 &= -\frac{1}{E}\int_0^H \sigma_{11}^2 dx_2 \\ &= -\frac{1}{E}\int_0^H \left(\frac{-2Mx_2}{I}\right)^2 dx_2 \\ &= -\frac{4M^2}{EI^2}\int_0^H x_2^2 dx_2 \\ &= -\frac{4M^2}{EI^2}\left(\frac{x_2^3}{3}\right)\Big|_0^H = -\frac{4M^2H^3}{3EI^2} \\ &= -\frac{4M^2H^3}{3E\frac{1}{144}B^2(2H)^6} = -\frac{3M^2}{EB^2H^3} \end{aligned} \tag{D.11}$$

Rewriting Eq.(D.2) yield the final J value for pure mode II

$$J = J_1 + J_3 + J_5 = \frac{6M^2}{EB^2H^3} + \frac{6M^2}{EB^2H^3} - \frac{3M^2}{EB^2H^3} = \frac{9M^2}{EB^2H^3} \tag{D.12}$$

APPENDIX E

J integral solution for pure mode III

A three-dimensional model of the DCB specimen along with the integral contour is shown in figure E.1.

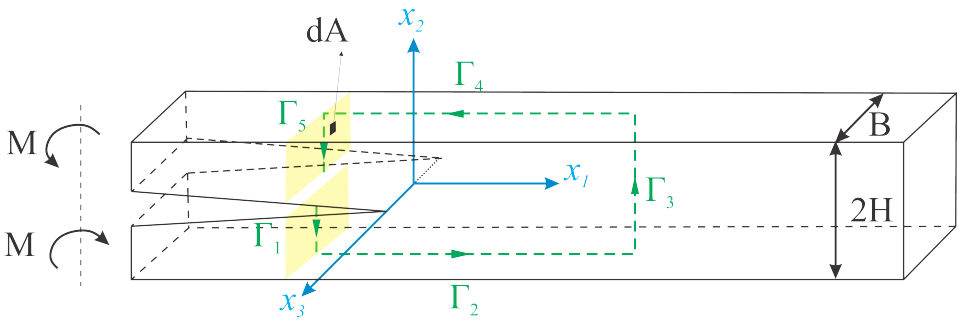

Figure E.1: The DCB specimen configuration for mode III and the integration path for the J integral.

According to figures E.1, the J integral can be written as

$$J = J_1 + J_2 + J_3 + J_4 + J_5 \tag{E.1}$$

Since the only present stress is σ_{11}, the traction for the Γ_6 and Γ_7 will be zero and Eq.(2.8) is applicable. Expanding the J integral from this equation, one have

$$\begin{aligned} J = \frac{1}{2B}\int_{\Gamma}(\sigma_{11}\varepsilon_{11} + \sigma_{22}\varepsilon_{22} + \sigma_{33}\varepsilon_{33} + \sigma_{12}\gamma_{12} + \sigma_{32}\gamma_{32} + \sigma_{31}\gamma_{31})dx_2 \\ - \int_{\Gamma}(\sigma_{11}n_1 + \sigma_{12}n_2 + \sigma_{23}n_3)\frac{\partial u_1}{\partial x}dA \\ - \int_{\Gamma}(\sigma_{12}n_1 + \sigma_{22}n_2 + \sigma_{23}n_3)\frac{\partial u_2}{\partial x}dA \\ - \int_{\Gamma}(\sigma_{13}n_1 + \sigma_{32}n_2 + \sigma_{33}n_3)\frac{\partial u_3}{\partial x}dA \end{aligned} \tag{E.2}$$

Under the assumption of pure mode III and symmetry, the only present stress component is σ_{11}. Calculating the traction for the $\Gamma_2, \Gamma_3, \Gamma_4$ reveal that these paths are traction free. $dx_2 = 0$ for the Γ_2 and Γ_4 and the Γ_3 is stress free. In conclusion, the J integral for the DCB specimen reduces to

$$J = J_1 + J_5 \tag{E.3}$$

Derivation for Γ_5 , due to symmetry, will be done in the following. The same is applicable to Γ_1.

$$J_5 = \frac{1}{B}\int_{\Gamma_5}\left(Wn_1 - T_i\frac{\partial u_i}{\partial x_1}\right)dA \tag{E.4}$$

The strain energy density, W, (the first term in Eq.(E.2)) by assuming the linear elasticity is

$$W = \frac{1}{2}\sigma_{11}\varepsilon_{11} \tag{E.5}$$

The outward vector for Γ_5, n_1=$\begin{Bmatrix}-1\\0\\0\end{Bmatrix}$, $\dfrac{\partial u_1}{\partial x_1} = \varepsilon_{11}$ and $T = -\sigma_{11}$. Rewriting Eq.(E.2) for Γ_5 and integrating in both the x_2 and x_3 directions at the same time, gives

$$\begin{aligned}
J_5 &= \frac{1}{B}\int_{-B/2}^{B/2}\int_0^H\left(\frac{-1}{2}\sigma_{11}\varepsilon_{11} + \sigma_{11}\varepsilon_{11}\right)dx_2dx_3\\
&= \frac{1}{B}\int_{-B/2}^{B/2}\left(\frac{-1}{2}\sigma_{11}\varepsilon_{11} + \sigma_{11}\varepsilon_{11}\right)Hdx_3\\
&= \frac{2H}{B}\int_0^{B/2}\left(\frac{1}{2}\sigma_{11}\varepsilon_{11}\right)dx_3\\
&= \frac{H}{B}\int_0^{B/2}(\sigma_{11}\varepsilon_{11})dx_3
\end{aligned} \tag{E.6}$$

According to Hook's law

$$\sigma_{11} = E\varepsilon_{11} \tag{E.7}$$

Substituting Eq.(E.7) in Eq.(E.6) and rewriting the J_5

$$J_5 = \frac{H}{EB}\int_0^{B/2}\sigma_{11}^2 dx_3 \tag{E.8}$$

where the bending stress, σ_{11} is

$$\sigma_{11} = \frac{Mx_3}{I} \quad \text{and} \quad I = \frac{1}{12}HB^3 \tag{E.9}$$

Plugging Eq.(E.9) into Eq.(E.8) yields

$$
\begin{aligned}
J_5 &= \frac{H}{EB}\int_0^{B/2}\left(\frac{Mx_3}{I}\right)^2 dx_3 \\
&= \frac{M^2H}{EBI^2}\int_0^{B/2} x_3^2 dx_3 \\
&= \frac{M^2H}{EBI^2}\left(\frac{x_2^3}{3}\right)\Bigg|_0^{B/2} \\
&= \frac{144M^2B^3H}{24EB^7H^2} \\
&= \frac{6M^2}{EB^4H}
\end{aligned}
\tag{E.10}
$$

Following the same procedure for Γ_1 gives the same equation as Eq.(E.10). The final value for J is

$$
J = \frac{12M^2}{EB^4H} \tag{E.11}
$$

APPENDIX F

J integral solution for pure mode III for an orthotropic material

The integration contour is similar to the contour illustrated in figure E.1. Due to the same geometry and loading condition both Eq.(E.3) and Eq.(E.4) hold. The derivation will be explained for Γ_5. The J_1 follows the same steps.

The stress-strain for an orthotropic material by assuming linear elasticity, can be related through the below equation set.

$$\begin{aligned}
\varepsilon_{11} &= \frac{1}{E_{11}}\sigma_{11} - \frac{\nu_{12}}{E_{11}}\sigma_{22} - \frac{\nu_{13}}{E_{11}}\sigma_{33} \\
\varepsilon_{22} &= -\frac{\nu_{21}}{E_{22}}\sigma_{11} + \frac{1}{E_{22}}\sigma_{22} - \frac{\nu_{23}}{E_{22}}\sigma_{33} \\
\varepsilon_{33} &= -\frac{\nu_{31}}{E_{33}}\sigma_{11} - \frac{\nu_{32}}{E_{33}}\sigma_{22} + \frac{1}{E_{33}}\sigma_{33} \\
\gamma_{23} &= \frac{1}{G_{23}}\sigma_{23} \\
\gamma_{31} &= \frac{1}{G_{31}}\sigma_{31} \\
\gamma_{12} &= \frac{1}{G_{12}}\sigma_{12}
\end{aligned} \tag{F.1}$$

Next, strain energy density, W, is can be written as

$$\begin{aligned}
W &= \frac{1}{2}(\sigma_{11}\varepsilon_{11} + \sigma_{22}\varepsilon_{22} + \sigma_{33}\varepsilon_{33} + \sigma_{23}\gamma_{23} + \sigma_{31}\gamma_{31} + \sigma_{12}\gamma_{12}) \\
&= \frac{1}{2}\left(\frac{\sigma_{11}^2}{E_{11}} + \frac{\sigma_{22}^2}{E_{22}} + \frac{\sigma_{33}^2}{E_{33}} - \frac{2\nu_{12}}{E_{11}}\sigma_{11}\sigma_{22} - \frac{2\nu_{13}}{E_{11}}\sigma_{11}\sigma_{33} - \frac{2\nu_{23}}{E_{22}}\sigma_{22}\sigma_{33} + \frac{\sigma_{23}^2}{G_{23}} + \frac{\sigma_{31}^2}{G_{31}} + \frac{\sigma_{12}^2}{G_{12}}\right)
\end{aligned} \tag{F.2}$$

Since σ_{11} is the only present stress component, Eq.(F.2), reduces to:

$$W = \frac{1}{2}\left(\frac{\sigma_{11}^2}{E_{11}}\right) \tag{F.3}$$

By implementing Eq.(F.3) in Eq.(E.4) and with regard to what explained for the J integral in Appendix E for the rest of terms, one can find the J_5.

$$\begin{aligned} J_5 &= \frac{1}{B}\int_{-B/2}^{B/2}(\frac{-1}{2}\frac{\sigma_{11}^2}{E_{11}}+\frac{\sigma_{11}^2}{E_{11}})Hdx_3 \\ &= \frac{2H}{B}\int_0^{B/2}(\frac{1}{2}\frac{\sigma_{11}^2}{E_{11}})dx_3 \\ &= \frac{H}{E_{11}B}\int_0^{B/2}\sigma_{11}^2 dx_3 \end{aligned} \tag{F.4}$$

σ_{11} is replaced from Eq.(E.9)

$$\begin{aligned} J_5 &= \frac{H}{E_{11}B}\int_0^{B/2}\left(\frac{Mx_3}{I}\right)^2 dx_3 \\ &= \frac{M^2H}{E_{11}BI^2}\int_0^{B/2}x_3^2 dx_3 \\ &= \frac{M^2H}{E_{11}BI^2}\left(\frac{x_2^3}{3}\right)\Big|_0^{B/2} \\ &= \frac{144M^2B^3H}{24E_{11}B^7H^2} \\ &= \frac{6M^2}{E_{11}B^4H} \end{aligned} \tag{F.5}$$

$$\begin{aligned} J_5 &= \frac{144M^2B^3H}{24E_{11}B^7H^2} \\ &= \frac{6M^2}{E_{11}B^4H} \end{aligned} \tag{F.6}$$

Following the same steps for the J_1 will give the same equation as Eq.(F.6). Finally, by summing up both J_1 and J_5, the final value of the J is derived.

$$J = J_1 + J_5 = \frac{12M^2}{E_{11}B^4H} \tag{F.7}$$

APPENDIX G

Prescribed Rotation against Prescribed Displacement

In all the plots, "pr" and "pd" denote the prescribed rotation and prescribed displacement.

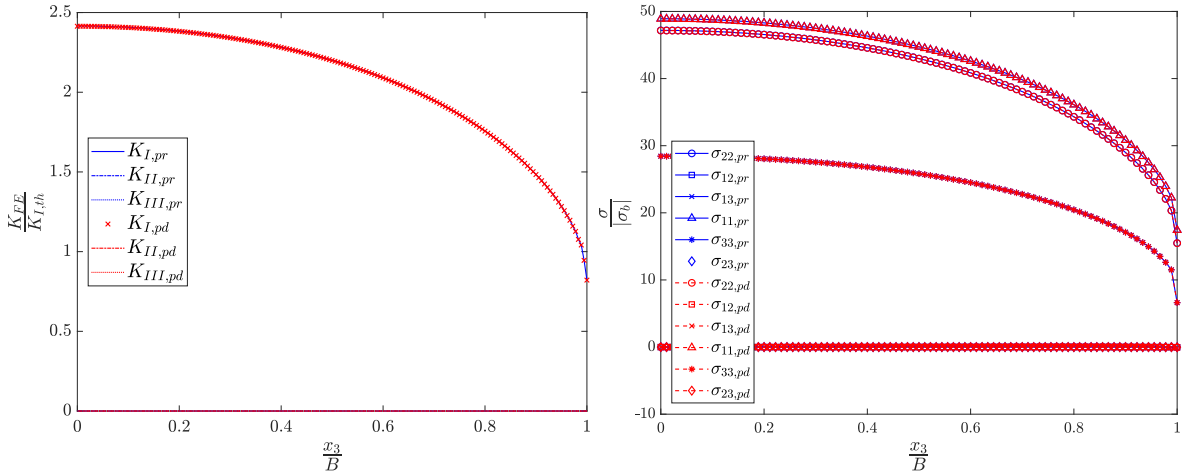

(a) **(b)**

Figure G.1: Mode 1-Comparison between the prescribed rotation and displacement: Distribution of (a) SIF (b) stress components (at $x_1 = 3.125\mu$m and $x_2 = 0$) along the crack front.

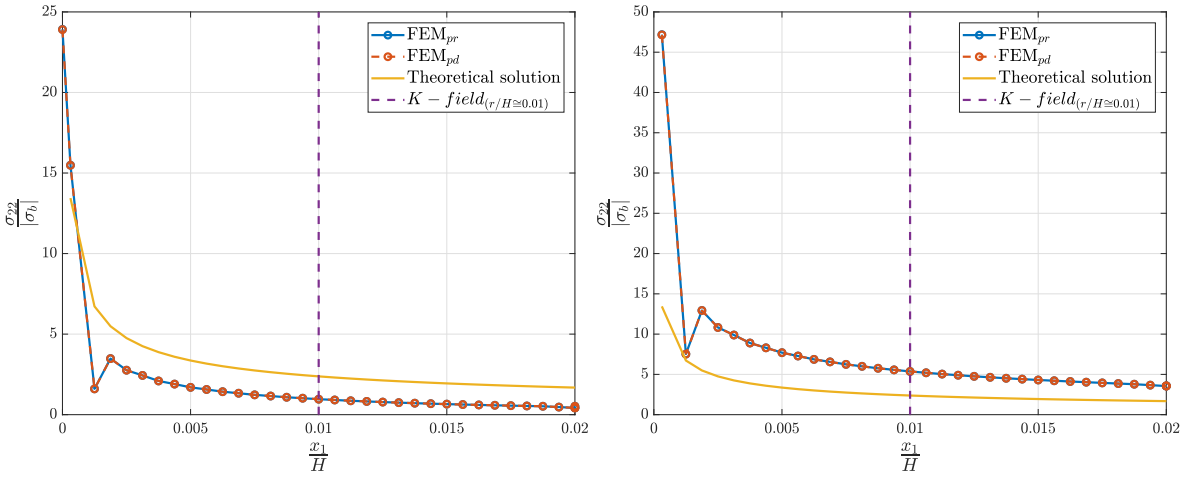

(a) **(b)**

Figure G.2: Mode 1-Comparison between the prescribed rotation and displacement: Distribution of σ_{22} along the crack ligament ($\theta = 0$) (a) at the free surface ($x_3 = \frac{B}{2}$) (b) in the center ($x_3 = 0$).

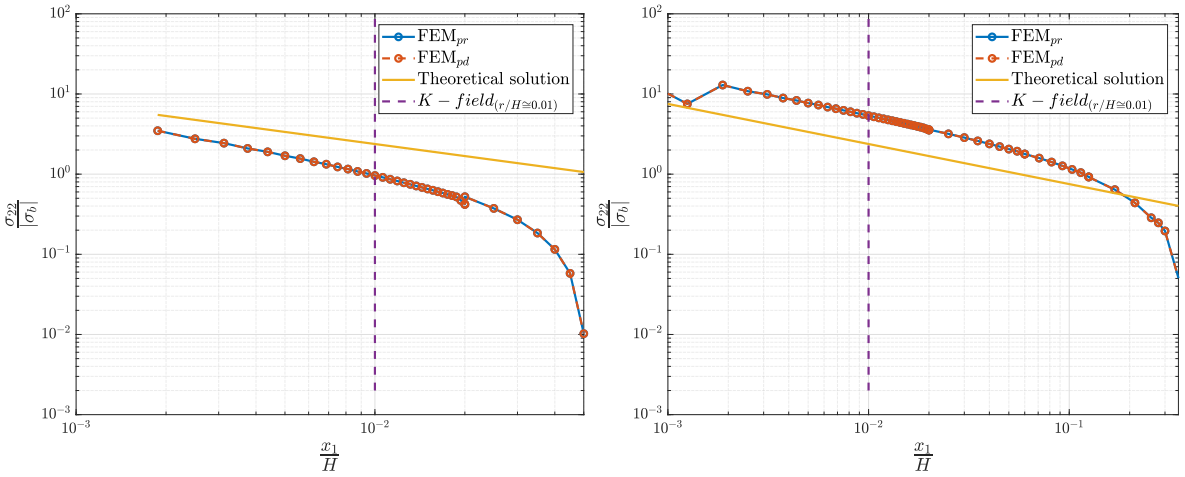

(a) **(b)**

Figure G.3: Mode 1-Comparison between the prescribed rotation and displacement: Distribution of σ_{22} along the crack ligament ($\theta = 0$) (a) at the free surface ($x_3 = \frac{B}{2}$) (b) in the center ($x_3 = 0$) in logarithmic scale.

Table G.1: Comparison of mode I result for applied moment through prescribed rotation and prescribed displacement

	$K_{\mathrm{I,th}}/K_{\mathrm{I,FE}}$
Prescribed rotation	1.032
Prescribed displacement	1.032

Bibliography

ABAQUS (2017). *ABAQUS/Standard User's Manual, Version 2017*. SIMULIA.

AIRBUS (2018). AIRBUS A380 - Technology. http://www.airbus.com/aircraft/passenger-aircraft/a380-family/technology.html#materials. [Online; accessed 05-February-2018].

Amestoy, M., Bui, H. D., and Labbens, R. (1981). On the definition of local path independent integrals in three-dimensional crack problems. *Mechanics Research Communications*, 8(4):231–236.

Anderson, T. (2005). *Fracture Mechanics: Fundamentals and Applications*, volume Third Edition. U.S:CRC Press.

ASTM D5528-01 (2014). Standard Test Method for Mode I Interlaminar Fracture Toughness of Unidirectional Fiber-Reinforced Polymer Matrix Composites. *American Standard of Testing Methods*, 03(Reapproved 2007):1–12.

Bak, C., Zahle, F., Bitsche, R., Yde, A., Henriksen, L. C., Nata, A., and Hansen, M. H. (2013). Description of the DTU 10 MW Reference Wind Turbine. *DTU Wind Energy Report-I-0092*, (July):1–138.

Bakker, A. (1984). *Ph.D. thesis: The Three-Dimensional J-Integral*. Delft,Delft University of Technology.

Banks-Sills, L., Hershkovitz, I., Wawrzynek, P. A., Eliasi, R., and Ingraffea, A. R. (2005). Methods for calculating stress intensity factors in anisotropic materials: Part I - z = 0 is a symmetric plane. *Engineering Fracture Mechanics*, 72(15):2328–2358.

Bao and Suo, Z. (1992). Remarks on crack-bridging concepts. *Journal of Applied Mechanics*, 45(8):355–366.

Barenblatt, G. I. (1962). The Mathematical Theory of Equilibrium of Crack in Brittle Fracture. *Adv. Appl. Mech.*, 7:55–129.

Barsoum, R. S. (1976). On the use of isoparemetric finite elements in linear fracture mechanics. *International Journal for Numerical Methods in Engineering*, 10(October 1974):25–37.

Barsoum, R. S. (1977). Triangular Quarter Point Elements as Elastic and Perfectly Plastic Crack Tip Elements. *Int. j. Numer. Meth. Engng.*, 11(December 1975):85.

Bažant, Z. P. and Estenssoro, L. F. (1979). Surface singularity and crack propagation. *International Journal of Solids and Structures*, 15(5):405–426.

Benthem, J. P. (1977). State of stress at the vertex of a quarter-infinite crack in a half-space. *International Journal of Solids and Structures*, 13(5):479–492.

Berto, F., Campagnolo, A., and Pook, L. P. (2015). Three-dimensional effects on cracked components under anti-plane loading. *Frattura ed Integrita Strutturale*, 9(33):17–24.

Boeing (2008). BOEING 787 FROM THE GROUND UP. http://www.boeing.com/commercial/aeromagazine/articles/qtr_4_06/article_04_2.html. [Online; accessed 05-February-2018].

Bogy, D. B. (1971). Two Edge-Bonded Elastic Wedges of Different Materials and Wedge Angles Under Surface Tractions. *Journal of Applied Mechanicsapplied mechanics*, 38(2):377–386.

Branner, Kim; Ghadirian, A. (2014). Database about blade faults. *Department of Wind Energy, DTU*, pages 8–13.

Broberg, K. B. (1999). *Cracks and Fracture*. Cambridge: Cambridge University Press.

Brocks, W., Cornec, A., and I., S. (2003). Computational Aspects of Nonlinear Fracture Mechanics. *Comprehensive Structural Integrity: Fracture of Material from Nano to Micro*, 3:127–209.

Browning, G., Carlsson, L. A., and Ratcliffe, J. G. (2010). Redesign of the ECT Test for Mode III Delamination Testing . Part I: Finite Element Analysis. *Journal of Composite Materials*, 44(15).

Browning, G., Carlsson, L. A., and Ratcliffe, J. G. (2011). Modification of the edge crack torsion specimen for mode III delamination testing . Part II experimental study. *Journal of Composite Materials*.

Campagnolo, A., Berto, F., and Pook, L. P. (2015). Three-dimensional effects on cracked discs and plates under nominal Mode III loading. *Frattura ed Integrita Strutturale*, 9(34):190–199.

Caprino, G. (1990). The use of thin DCB specimens for measuring mode I interlaminar fracture toughness of composite materials. *Composites Science and Technology*, 39(2):147–158.

Charalambides, M., Kinloch, A. J., Wang, Y., and Williams, J. G. (1992). On the analysis of mixed-mode failure. *International Journal of Fracture*, 54(3):269–291.

Chernov, N. (2018). Circle Fit (Pratt method). https://se.mathworks.com/matlabcentral/fileexchange/22643-circle-fit-pratt-method. [Online; accessed 10-July-2018].

Chiarelli, M. and Frediani, A. (1993). A computation of the three-dimensional J-integral for elastic materials with a view to applications in fracture mechanics. *Engineering Fracture Mechanics*, 44(5):763–788.

Cricrì, G. and Perrella, M. (2017). Investigation of mode III fracture behaviour in bonded pultruded GFRP composite joints. *Composites Part B: Engineering*, 112:176–184.

Cricrì, G., Perrella, M., Sessa, S., and Valoroso, N. (2015). A novel fixture for measuring mode III toughness of bonded assemblies. *Engineering Fracture Mechanics*, 138:1–18.

Dávila, C. G., Camanho, P. P., and de Moura, M. F. (2001). Mixed-Mode Decohesion Elements for Analyses of Progressive Delamination. *Proceedings of the 42nd AIAA/ASME/ASCE/AHS/ASC Structures, Structural Dynamics and Materials Conference*, (April 16-19).

Donaldson, S. L. (1988). Mode III interlaminar fracture characterization of composite materials. *Composites Science and Technology*, 32(3):225–249.

Dugdale, D. S. (1960). Yielding of steel. *J. Mech. Phys. Solids*, 8:100–104.

Eder, M., Bitsche, R., Nielsen, M., and Branner, K. (2014). A practical approach to fracture analysis at the trailing edge of wind turbine rotor blades. *Wind Energy*, 17:483–497.

Erdogan, F. and Sih, G. C. (1963). On the Crack Extension in Plates Under Plane Loading and Transverse Shear. *Journal of Basic Engineering*, 85(4):519.

Falk, M. L., Needleman, A., and Rice, J. R. (2001). A critical evaluation of dynamic fracture simulations using cohesive surfaces. *Journal de Physique IV, Proceedings 11(Pr.5)*, (March 5-8):43–50.

Ge, Y., Gong, X., Hurez, A., and De Luycker, E. (2016). Test methods for measuring pure mode III delamination toughness of composite. *Polymer Testing*, 55:261–268.

Goutianos, S. and Sørensen, B. F. (2012). Path dependence of truss-like mixed mode cohesive laws. *Engineering Fracture Mechanics*, 91:117–132.

Henshell, R. D. and Shaw, K. G. (1975). Crack tip finite elements are unnecessary. *International Journal for Numerical Methods in Engineering*, 9(3):495–507.

Hillerborg, A., Modéer, M., and Petersson, P. E. (1976). Analysis of crack formation and crack growth in concrete by means of fracture mechanics and finite elements. *Cement and Concrete Research*, 6(6):773–781.

Horner, A. L., Czabaj, M. W., Davidson, B. D., and Ratcliffe, J. G. (2015). Three-dimensional crack surface evolution in mode III delamination toughness tests. *Engineering Fracture Mechanics*, 149:313–325.

Hwang, S.-f. and Hu, C.-l. (2001). Tearing Mode lnterlaminar Fracture Toughness. *Polymer*, 22(7):57–64.

Irwin, G. R. (1957). Analysis of Stresses and Strains Near the End of a Crack Traversing a Plate. *J. Appl. Mech.*

Irwin, G. R. and Kies, J. A. (1954). Critical energy rate analysis of fracture strength. *Welding Research Supplement*, pages 193–198.

Israr, H., Wong, K., and Tamin, M. (2017). Cohesive zone modelling of Mode III delamination using the edge crack torsion test. *Journal of Mechanical Engineering and Sciences (JMES)*, 11(1):2526–2538.

Jamieson, P. (2011). *INNOVATION IN WIND TURBINE DESIGN*. United Kingdom:John Wiley & Sons.

Javier S. Millàn, Iñaki Armendàriz, J. G.-M. R. G. (2016). *Handbook of Materials Failure Analysis With Case Studies from the Aerospace and Automotive Industries*. United Kingdom:Elsevier.

Johnston, A. L. and Davidson, B. D. (2014). Intrinsic coupling of near-tip matrix crack formation to mode III delamination advance in laminated polymeric matrix composites Upper load. *International Journal of Solids and Structures*, 51(13):2360–2369.

Johnston, A. L., Davidson, B. D., and Simon, K. K. (2014). Assessment of split-beam-type tests for mode III delamination toughness determination. *International Journal of Fracture*, 185(1-2):31–48.

Kassapoglou, C. (2015). *Modeling the effect of damage in composite structures*. United Kingdom:John Wiley & Sons.

Khoshravan, M. R. and Moslemi, M. (2014). Investigation on mode III interlaminar fracture of glass/epoxy laminates using a modified split cantilever beam test. *Engineering Fracture Mechanics*, 127:267–279.

Kitagawa, H., Kisu, H., Nakagiri, S., Yuuki, R., and Ogura, K. (1980). Break-through and ductile fracture of reactor components with a surface crack. *Fourth International Conference on Pressure Vessel Technology*, 12(7):103–110.

Kotousov, A., Lazzarin, P., Berto, F., and Pook, L. P. (2013). Three-dimensional stress states at crack tip induced by shear and anti-plane loading. *Engineering Fracture Mechanics*, 108:65–74.

Kuna, M. (2013). *Finite Elements in Fracture Mechanics*, volume 201. New York, London:Springer Heidelberg, Dordrecht.

Lee, S. M. (1993). An Edge Crack Torsion Method for Mode III Delamination Fracture Testing. *Journal of Composites Technology & Research, JCTRER*, 15(3):193–201.

Li, V. C. and Ward, R. J. (1989). A novel testing technique for post peak tensile behaviour of cementitious materials. *Fracture Toughness and Fracture Energy*, pages 183–195.

López-Menéndez, A., Viña, J., Argüelles, A., Rubiera, S., and Mollón, V. (2016). A new method for testing composite materials under mode III fracture. *Journal of Composite Materials*, 50(28):3973–3980.

López-Menéndez, A., Viña, J., Argüelles, A., Viña, I., and Rubiera, S. (2017). Analysis of mode III interlaminar fracture toughness of laminated composites using a novel testing device. *Engineering Fracture Mechanics*, 173:55–63.

Mehrabadi, F. A. and Khoshravan, M. (2012). Mode III interlaminar fracture and damage characterization in woven fabric-reinforced glass / epoxy composite laminates. *Journal of Composite Materials*.

Millàn, J. S. and Armendàriz, I. (2015). *Damage Growth in Aerospace Composites*. Switzerland, Springer International Publishing.

Moës, N. and Belytschko, T. (2002). Extended finite element method for cohesive crack growth. *Engineering Fracture Mechanics*, 69(7):813–833.

Morais, A. B. D. and Pereira, A. B. (2009). Composites : Part A Mode III interlaminar fracture of carbon / epoxy laminates using a four-point bending plate test. *Composites Part A*, 40(11):1741–1746.

Murakami, Y. and Natsume, H. (2002). Stress Singularity at the Corner Point of 3-D Surface Crack under Mode II Loading *. *JSME international Journal*, 45(2):161–169.

Parhizgar, S. (1979). *Ph.D. thesis: Fracture mechanics of unidirectional composite materials*. Iowa, Iowa State University.

Paris, P. and Sih, G. (1965). Stress Analysis of Cracks. *Fracture Toughness Testing and its Applications*, pages 30–52.

PENNAS D., CANTWELL, W. J., and COMPSTON, P. (2007). The Influence of Strain Rate on the Mode III Interlaminar Fracture of Composite Materials. *Journal of Composite Materials*, 41(21).

Pereira, A. B., De Morais, A. B., and De Moura, M. F. S. F. (2011). Design and analysis of a new six-point edge crack torsion (6ECT) specimen for mode III interlaminar fracture characterisation. *Composites Part A: Applied Science and Manufacturing*, 42(2):131–139.

Pontjo Utomo and Hamid R. Nikraz (2007). Evaluation Of Finite Element Mesh Arrangements And Stress Intensity Factor Calculation Methods For Opening Mode Fracture Of Cracked-Cemented Materials. *Civil Engineering Dimension*, 9(1):25–32.

Pook, L. P. (2013). A 50-year retrospective review of three-dimensional effects at cracks and sharp notches. *Fatigue and Fracture of Engineering Materials and Structures*, 36(8):699–723.

Pook, L. P., Berto, F., Campagnolo, A., and Lazzarin, P. (2014). Coupled fracture mode of a cracked disc under anti-plane loading. *Engineering Fracture Mechanics*, 128:22–36.

Pook, L. P., Campagnolo, A., Berto, F., and Lazzarin, P. (2015). Coupled fracture mode of a cracked plate under anti-plane loading. *Engineering Fracture Mechanics*, 134:391–403.

Pratt, V. (1987). Direct least-squares fitting of algebraic surfaces. *SIGGRAPH '87 Proceedings of the 14th annual conference on Computer graphics and interactive techniques*, 21(4):145–152.

Rice, J. R. (1968a). A Path Independent Integral and the Approximate Analysis of Strain Concentration by Notches and Cracks. *Journal of Applied Mechanics*, 35(2):379.

Rice, J. R. (1968b). Mathematical Analysis in the Mechanics of Fracture. *Mathematical Fundamentals*, 2(B2):191–311.

Schwalbe, K.-H., Scheider, I., and Cornec, A. (2012). *Guidelines for Applying Cohesive Models to the Damage Behaviour of Engineering Materials and Structures*. New York, London:Springer Heidelberg, Dordrecht.

Sih, G. C., Paris, P. C., and Irwin, G. R. (1965). On cracks in Rectilinearly Anisotropic Bodies. *International Journal of Fracture Mechanics*, 1(6):189–203.

Sørensen, B. and Jacobsen, T. (2000). Crack growth in composites Applicability of R-curves and bridging laws. *Plastics, Rubber and Composites*, 29(3):119–133.

Sørensen, B. F. and Jacobsen, T. K. (2003). Determination of cohesive laws by the J integral approach. *Engineering Fracture Mechanics*, 70(14):1841–1858.

Sørensen, B. F., Jørgensen, E., Debel, C. P., Jensen, F. M., Jensen, H. M., Jacobsen, T. K., and Halling, K. M. (2004). *Improved design of large wind turbine blade of fibre composites based on studies of scale effects (Phase 1) - Summary Report*. Denmark, Risø:DTU Materials Research Department.

Sørensen, B. F. and Kirkegaard, P. (2006). Determination of mixed mode cohesive laws. *Engineering Fracture Mechanics*, 73(17):2642–2661.

Spearing, S. M. and Evans, A. G. (1992). THE ROLE OF FIBER BRIDGING IN THE DELAMINATION RESISTANCE OF FIBER-REINFORCED COMPOSITES. 40(9):2191–2199.

Suemasu, H. (1999). An experimental method to measure the mode-III interlaminar fracture toughness of composite laminates. *Composites Science and Technology*, 59(7):1015–1021.

Tada, H., Paris, P. C., and Irwin, G. R. (2000). *The stress analysis of cracks handbook*. New York:ASME Press.

T.L.Anderson (2004). *Fracture mechanics : fundamentals and applications*. U.S:CRC Press.

Toubal, A., Sahli, A., Kebdani, S., and Rahmani, O. (2013). Stress Intensity Solutions for Cracked Orthotropic Plates. *International Journal of Mechanics and Applications*, 3(5):122–130.

Tsai, S. W. and Hahn, H. T. (1980). *Introduction to Composite Materials*. USA:CRC Press.

Turon, A., Dávila, C., Camanho, P., and Costa, J. (2007). An engineering solution for mesh size eects in the simulation of delamination using cohesive zone models. *Engineering Fracture Mechanics*, 74(June 2005):1665–1682.

Tvergaard, V. and Hutchinson, J. W. (2008). Mode III effects on interface delamination. *Journal of the Mechanics and Physics of Solids*, 56(1):215–229.

Wang, S. S. (1983). *Fracture Mechanics for Delamination Problems in Composite Materials*, volume 17. Elsevier Science Publishers B.V.,.

Westergaard, H. M. (1939). Bearing Pressures and Cracks. *Journal of Applied Mechanics*, 6(1):49–53.

Williams, M. L. (1961). The Bending Stress Distribution at the Base of a Stationary Crack. *Journal of Applied Mechanics*, 28(1):78.

Z. Suo, G. B. and FAN, B. (1992). Delamination R-curve phenomena due to damage. *J. Mech. Phys. Solids*, 40:1–16.

Technical University of Denmark
Department of Wind Energy
Frederiksborgvej 399
2800 Kgs. Lyngby
Denmark
Telephone 46 77 50 85

info@vindenergi.dtu.dk
www.vindenergi.dtu.dk